

1999

Transport processes in directional solidification and their effects on microstructure development

Prantik Mazumder
Iowa State University

Follow this and additional works at: <https://lib.dr.iastate.edu/rtd>

 Part of the [Fluid Dynamics Commons](#), [Materials Science and Engineering Commons](#), [Mechanical Engineering Commons](#), and the [Plasma and Beam Physics Commons](#)

Recommended Citation

Mazumder, Prantik, "Transport processes in directional solidification and their effects on microstructure development " (1999). *Retrospective Theses and Dissertations*. 12193.
<https://lib.dr.iastate.edu/rtd/12193>

This Dissertation is brought to you for free and open access by the Iowa State University Capstones, Theses and Dissertations at Iowa State University Digital Repository. It has been accepted for inclusion in Retrospective Theses and Dissertations by an authorized administrator of Iowa State University Digital Repository. For more information, please contact digirep@iastate.edu.

INFORMATION TO USERS

This manuscript has been reproduced from the microfilm master. UMI films the text directly from the original or copy submitted. Thus, some thesis and dissertation copies are in typewriter face, while others may be from any type of computer printer.

The quality of this reproduction is dependent upon the quality of the copy submitted. Broken or indistinct print, colored or poor quality illustrations and photographs, print bleedthrough, substandard margins, and improper alignment can adversely affect reproduction.

In the unlikely event that the author did not send UMI a complete manuscript and there are missing pages, these will be noted. Also, if unauthorized copyright material had to be removed, a note will indicate the deletion.

Oversize materials (e.g., maps, drawings, charts) are reproduced by sectioning the original, beginning at the upper left-hand corner and continuing from left to right in equal sections with small overlaps. Each original is also photographed in one exposure and is included in reduced form at the back of the book.

Photographs included in the original manuscript have been reproduced xerographically in this copy. Higher quality 6" x 9" black and white photographic prints are available for any photographs or illustrations appearing in this copy for an additional charge. Contact UMI directly to order.

UMI[®]

Bell & Howell Information and Learning
300 North Zeeb Road, Ann Arbor, MI 48106-1346 USA
800-521-0600

Transport processes in directional solidification and their effects on microstructure
development

by

Prantik Mazumder

A dissertation submitted to the graduate faculty
in partial fulfillment of the requirements for the degree of
DOCTOR OF PHILOSOPHY

Major: Mechanical Engineering

Major Professors: Richard H. Pletcher, Rohit K. Trivedi

Iowa State University

Ames, Iowa

1999

Copyright © Prantik Mazumder, 1999. All rights reserved.

UMI Number: 9941783

**Copyright 1999 by
Mazumder, Prantik**

All rights reserved.

**UMI Microform 9941783
Copyright 1999, by UMI Company. All rights reserved.**

**This microform edition is protected against unauthorized
copying under Title 17, United States Code.**

UMI
300 North Zeeb Road
Ann Arbor, MI 48103

Graduate College
Iowa State University

This is to certify that the Doctoral dissertation of
Prantik Mazumder
has met the dissertation requirements of Iowa State University

Signature was redacted for privacy.

Co-major Professor

Signature was redacted for privacy.

Co-major Professor

Signature was redacted for privacy.

For the Major Department

Signature was redacted for privacy.

For the Graduate College

TABLE OF CONTENTS

	Page
CHAPTER 1: GENERAL INTRODUCTION	1
1.1 Introduction and Basic Principles of Directional Solidification	1
1.1.1 System and Methods	1
1.1.2 Basic Transport Mechanisms	4
1.1.3 One Dimensional Diffusive Model	7
1.1.4 One Dimensional Boundary Layer Model	10
1.2 Review of Relevant Research	13
1.2.1 Thermal Convection in Horizontal Configuration	15
1.2.2 Rayleigh-Benard Configuration in Vertical Configuration	15
1.2.3 Double Diffusive Convection in Vertical Configuration Due to Unstable Solute Gradient	17
1.2.4 Convection in Vertical Configuration Due to Radial Temperature Gradient	18
1.3 Objective of Thesis	21
1.4 Dissertation Organization	21
References	23
CHAPTER 2: A MODEL OF CONVECTION INDUCED OSCILLATORY STRUCTURE FORMATION IN PERITECTIC ALLOYS	27
Abstract	27
I. Introduction	28
II. Background	30
III. Natural Convection in Bridgman System	34
IV. Mechanism of Microstructure Development	37

V. Computational Model	40
A. Mathematical Model	41
B. Convective Velocity Components	42
B-1: Diffusion Dominated Transport	42
B-2: Steady Convection	42
B-3: Unsteady Convection	43
C. Numerical Analysis	43
VI. Results	44
A. Diffusive Transport	44
B. Steady Convection	45
C. Unsteady Convection	46
VII. Discussion	47
VIII. Conclusion	49
Acknowledgment	50
References	50
 CHAPTER 3: MECHANISMS OF LAYER STRUCTURE FORMATION IN PERITECTIC ALLOYS	 74
Abstract	74
Introduction	74
Experimental Results	77
Theoretical Model for Convection Induced Oscillatory Microstructure	78
Acknowledgment	80
References	82

CHAPTER 4: THE EFFECT OF CONVECTION ON DISORDER IN PRIMARY CELLULAR AND DENDRITIC ARRAYS	83
Abstract	83
1. Introduction	84
2. Experimental studies	86
A. Microstructures	86
B. Primary spacing analysis	88
3. Numerical modeling	91
A. Model	92
B. Numerical results	95
4. Discussion	97
A. Experimental results	97
B. Convection effects	98
C. Array disorder	99
5. Conclusions	100
Acknowledgments	101
References	101
 CHAPTER 5: UNSTEADY THERMO-SOLUTAL CONVECTION IN VERTICAL BRIDGMAN SYSTEM AND PATTERN FORMATION IN SOLID PHASE: MODELING, DYNAMICS AND MICROSTRUCTURE EVOLUTION	 126
Abstract	126
1. Introduction	127
2. Background	129
2.1 Convection in Vertical Bridgman System	129
2.1.1 Double Diffusive Convection in Vertical configuration Due to Unstable Solute Gradient	129

2.1.2 Convection in Vertical Configuration Due to Radial Temperature Gradient	143
2.2 Layered Structure Formation in Peritectic Alloys	132
3. Objective	136
4. Mathematical Formulation	136
4.1 Boundary Condition at Top and Bottom Surfaces	143
4.2 Grid System and Numerical Scheme	143
5. Benchmarking With Published Results	145
5.1 Case Study 1	145
5.2 Case Study 2	146
5.3 Case Study 3	146
5.4 Case Study 4	147
6. Effect of Thermal Conductivities of Solid and Liquid on the Thermal, Flow and Segregation Patterns	148
7. Thermal Characterization: Determination of Boundary Conditions and Biot Numbers	150
8. Background or Base Flow	151
9. Thermo-Solutal Convection During Solidification	154
9.1 Steady State Thermo-Solutal Convection for Small Ra_T	155
9.2 Oscillatory Convection for $Ra_T > 23000$	157
9.3 Vortex Shedding, Intermittent Oscillation-Relaxation	161
10. Mechanism of Layered Structure Formation	163
10.1 Thin Tubes	163
10.2 Large tubes	164
10.3 Effect of Growth Rate on Layer Thickness and Spacing	167
Acknowledgment	168

References	168
CHAPTER 6: GENERAL CONCLUSIONS	210

CHAPTER 1: GENERAL INTRODUCTION

1.1 Introduction and Basic Principles of Directional Solidification

Directional solidification is one of the key techniques for processing a myriad of semiconductor and metallic alloys. The unique mechanical, thermal, electrical, optical and magnetic properties of these solidified materials depend strongly on the microstructures of the solid phase. The microstructures are strongly related to the details of the processing conditions and by the thermodynamic properties of the phase diagrams. Consequently, to obtain a product which meets specific requirements, it is important to identify the processing parameters for a given alloy that give the desired microstructure [1,2].

The development of microstructure depends on the manner in which the latent heat of fusion is carried away from the advancing solid-liquid interface. Two distinctly different heat flow conditions may be present which give rise to either the free growth or the constrained growth behavior [3-4]. In free growth, where solidification occurs in an undercooled melt, the latent heat is dissipated through the liquid. In constrained growth the latent heat is carried away through the solid and the temperature gradient in the liquid ahead of the interface is positive. This constrained growth gives rise to directional solidification (DS). The following are the reviews of classical theories of directional solidification [3-4].

1.1.1 System and Methods

A schematic of the directional-solidification apparatus is shown in Figure 1.1. The facility mainly consists of a 1) three-zone thermal assembly surrounding a cylindrical ampoule inside which the liquid metal is solidified, and 2) a mechanism for solidifying the alloy. The method will be briefly described in the following paragraph.

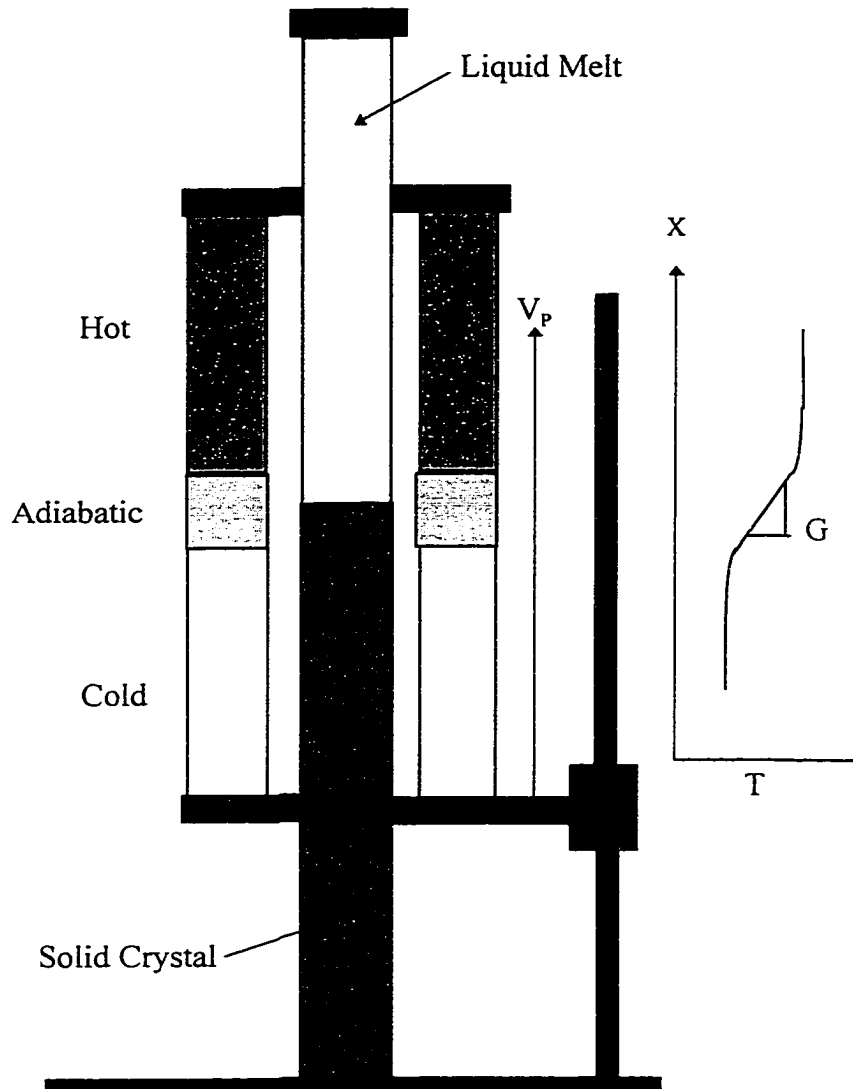


Figure 1.1 : Schematic of Vertical Bridgman System

Solid binary alloy of a specific composition is placed inside an ampoule made from a material that does not react with the alloy. A three zone thermal assembly is set up around the ampoule. The assembly consists of a heating furnace, an insulator and a cooling unit as shown in the Figure 1.1. The hot, adiabatic and cold zones are stacked over each other, to establish a high vertical temperature gradient. Since temperature is increasing axially upwards, this arrangement is stabilizing for the hydrostatic condition, since lighter liquid overlays heavier liquid. Since the temperatures of the heating and cooling zones are kept much higher and lower, respectively, than the melting temperature of the alloy, part of the sample in the heating zone is liquid, whereas the part in the cooling region is solid. It is expected that the solid-liquid interface will reside somewhere in the adiabatic zone. The purpose of using the insulator in between the heating and cooling regions is to minimize the radial temperature variation at and near the interface. If properly designed, the three zone assembly should provide a unidirectional heat flow profile such that the heat flow lines are downwards and parallel to the axis of the sample tube near the interface. Once the desired temperature gradient is established, the solidification of the alloy is achieved by one of the following techniques: (1) the tube which contains the alloy is moved downwards into the cold chamber at a constant rate. (2) The alloy is held stationary, and the thermal assembly is moved upwards at a constant rate. (3) Both the alloy tube and the thermal assembly are held stationary, but the temperature of the furnace and the cold chamber are reduced synchronously at a constant rate such that the temperature gradient is not altered. All the experimental studies mentioned in this thesis are done in a system which follows the second technique, and it is described in detail by Mason [6]. This technique is better than the first technique since the mechanical disturbance induced in the sample during translation is minimized. In the third technique the axial temperature gradient may not remain constant with time, and proper monitoring of the temperature gradient and post-experiment analysis of the transport processes, especially thermo-solutal convection becomes difficult.

As the thermal assembly is moved upwards with constant velocity, the isotherms move upwards following the motion of the thermal assembly and the liquid starts freezing.

After some initial transient, the solid-liquid interface can move at the same rate as the thermal assembly, in which case a steady state growth is attained. It is also possible for the interface velocity to oscillate about the pulling velocity such that the mean growth rate is equal to the pulling velocity.

The parameters which could be externally varied are the temperatures of the heating furnace (T_H) and the cooling unit (T_C), the thickness of the adiabatic or insulating zone, the linear speed of the thermal assembly (V_p), and the initial composition of the binary alloy (C_0). The temperatures T_H and T_C , and the length of the insulator could be varied to obtain the desired vertical temperature gradient (G_v) at the interface. Since in the DS process all the external parameters can be varied independently, this technique is a very powerful tool to study the fundamental aspects of the correlation between the microstructure and the processing variables. Through precise control of temperature gradient and growth rate, a high degree of microstructural control is achieved in DS technique. Thus, the DS technique is ideally suited for the growth of single crystals.

Depending on the values of G_v , C_0 , and V_p , the solid-liquid interface can be planar, cellular or dendritic as shown in Figure 1.2. For large G_v and low V_p , usually a planar interface growth is achieved which allows the crystal to form with uniform composition in the absence of convection in the melt. In this thesis we are mainly concerned with growth conditions where the interface is always planar, except in Chapter 6 where we investigate the primary spacings of cellular and dendritic morphologies in presence of fluid flow.

1.1.2 Basic Transport Mechanisms

The equilibrium between a crystalline solid and a liquid is conveniently represented by a binary phase diagram by means of two lines, the liquidus line, above which the liquid is stable, and the solidus line, below which the solid is stable [3]. A schematic phase-diagram of a binary alloy is shown in Figure 1.3. For simplicity, the equilibrium curves are assumed

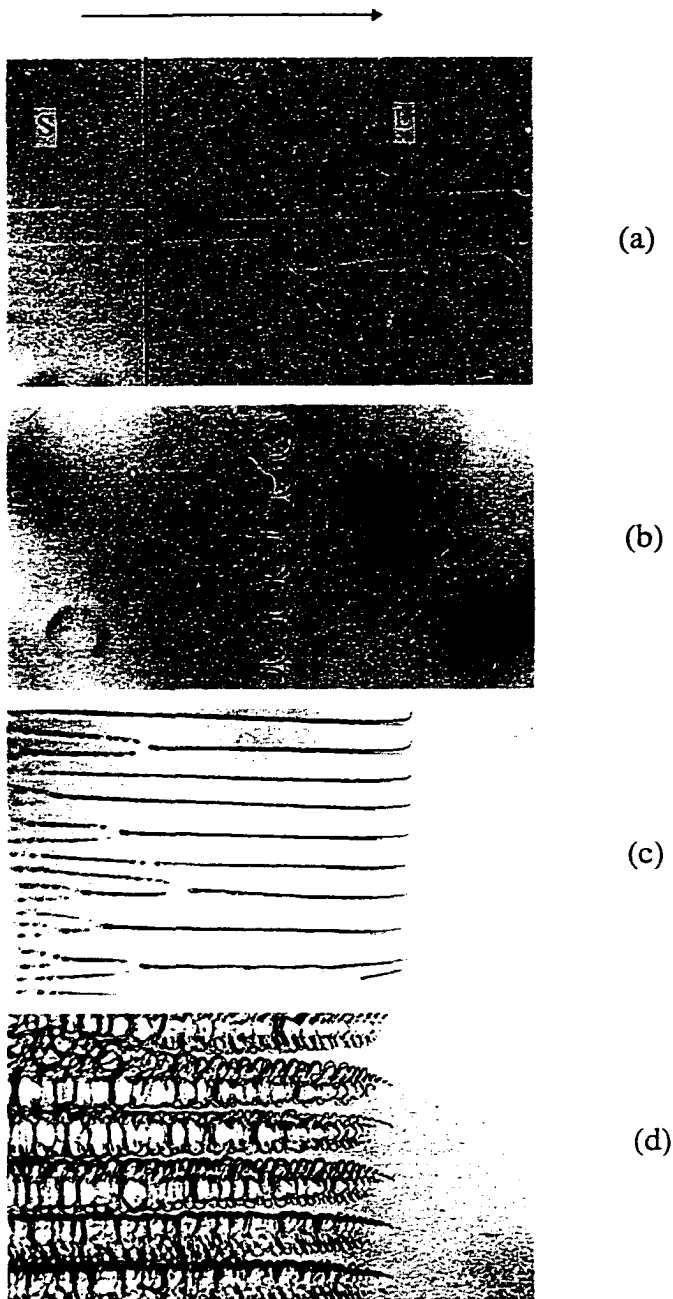


Figure 1.2: Morphologies of solid-liquid interface during directional solidification. The arrow shows the direction of freezing in all the samples. The solid (S) is on the left and the liquid (L) is on the right. (a) Planar interface (b) Shallow cells, (c) Deep cells, (d) Dendrites.

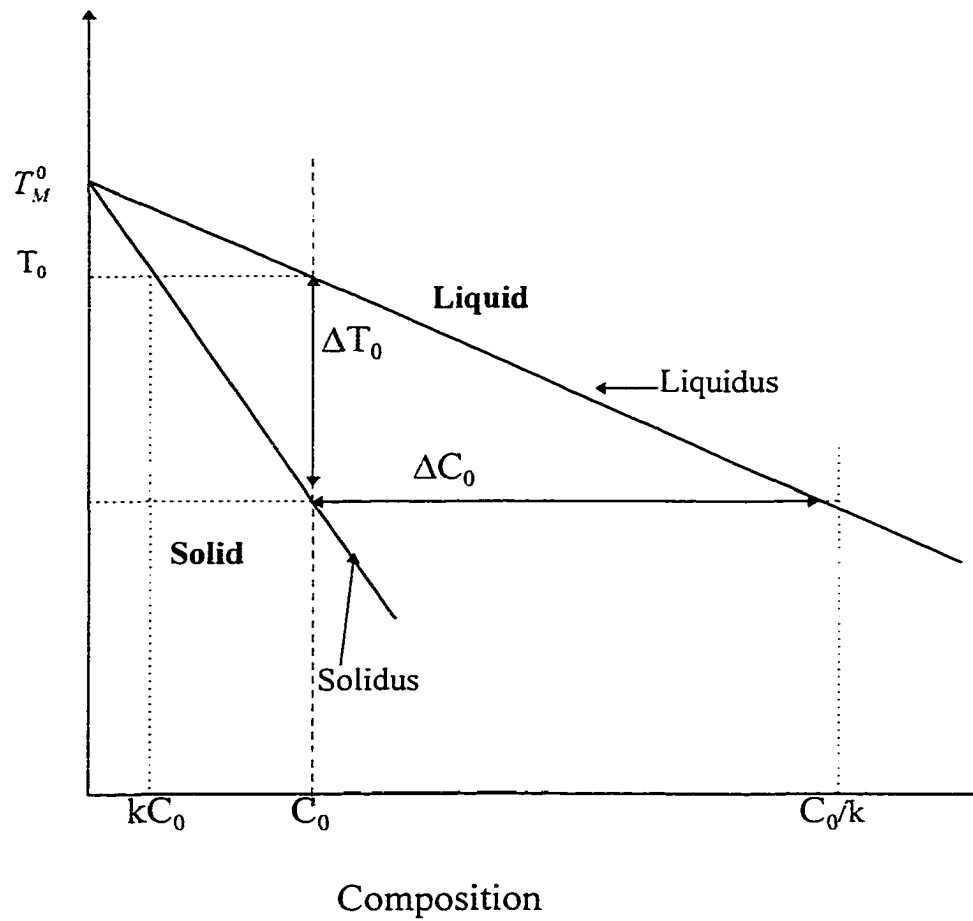


Figure 1.3: Solidification of an alloy of initial composition C_0 . Phase diagram, equilibrium compositions at steady state.

to be straight lines. The equilibrium relation between the solid and liquid compositions are described in terms of an equilibrium partition coefficient k , as

$$k = \frac{c_s^i}{c_l^i} = \frac{m_s}{m_l}$$

where c_s^i and c_l^i are the solid and liquid compositions at the solid-liquid interface; m_s and m_l are the slopes of the solidus and liquidus curves. For straight solidus and liquidus lines, k is constant. When solidification starts, the composition of the liquid is at C_0 , and the initial small amount of solid forms with composition kC_0 at temperature T_0 (Figure 1.3). Since, the composition of the solidified volume is less after solidification, solute must be rejected from the advancing solid front into the liquid. This raises the composition of the liquid at the interface and thus lowers the equilibrium freezing temperature. Since, the solid composition at the interface is tied with the liquid composition due to local equilibrium, the solid composition also increases in response to increase in liquid composition. This leads to gradual solidification, where the liquid and solid compositions and the temperature at the interface move along the liquidus and solidus lines, with local equilibrium maintained throughout the event. The solute rejected into the liquid is transported by two mechanisms, molecular diffusion and convection in the liquid.

1.1.3 One-Dimensional Diffusive Model (Tiller et al.[7])

In the absence of any fluid motion, the transport of solute in the melt is solely due to molecular diffusion. Tiller et al. [7] developed a simple analytical model for the steady state composition profile in the binary melt with the solid composition C_0 far from the flat solid-liquid interface located at $\bar{x} = 0$. The one-dimensional diffusion equation written in terms of a reference frame fixed with the interface moving with constant growth rate \bar{V}_p is given as

$$D_l \frac{\partial^2 \bar{c}_l}{\partial \bar{x}^2} + \bar{V}_p = 0 \quad (1)$$

where \bar{x} is the distance from the interface, D_l is the diffusion coefficient of solute in liquid, and \bar{V}_p is the constant growth rate of interface. The far field boundary condition is that of the unperturbed homogeneous melt, or,

$$\bar{c}_l = C_0, \text{ at } \bar{x} \rightarrow \infty \quad (2)$$

The solute flux-balance condition at the interface is

$$-D_l \left. \frac{\partial \bar{c}_l}{\partial \bar{x}} \right|_{\bar{x}=0} = \bar{V}_p (1-k) \bar{c}_l \Big|_{\bar{x}=0} \quad (3)$$

where k is the equilibrium partition coefficient. The solution of (1), (2), and (3), as given by Tiller et. al [7], is

$$\bar{c}_l(\bar{x}) = C_0 \left[1 + \frac{1-k}{k} e^{-\bar{V}_p \bar{x} / D_l} \right] \quad (4)$$

The solution (4) implies the existence of an exponential boundary layer next to the interface with characteristic *diffusion length scale*, $\bar{l}_{dif} = D_l / \bar{V}_p$. A schematic composition profile during steady-state solidification is shown in Figure 1.4. During steady-state solidification the solute composition at interface remains fixed at C_0 / k and C_0 in the liquid and solid phases respectively. Only under steady-state condition, solid of uniform composition C_0 grows from the melt. Although, this model can be applied only during steady-state solidification, Tiller et al.[7] developed an approximate analytical model for the initial

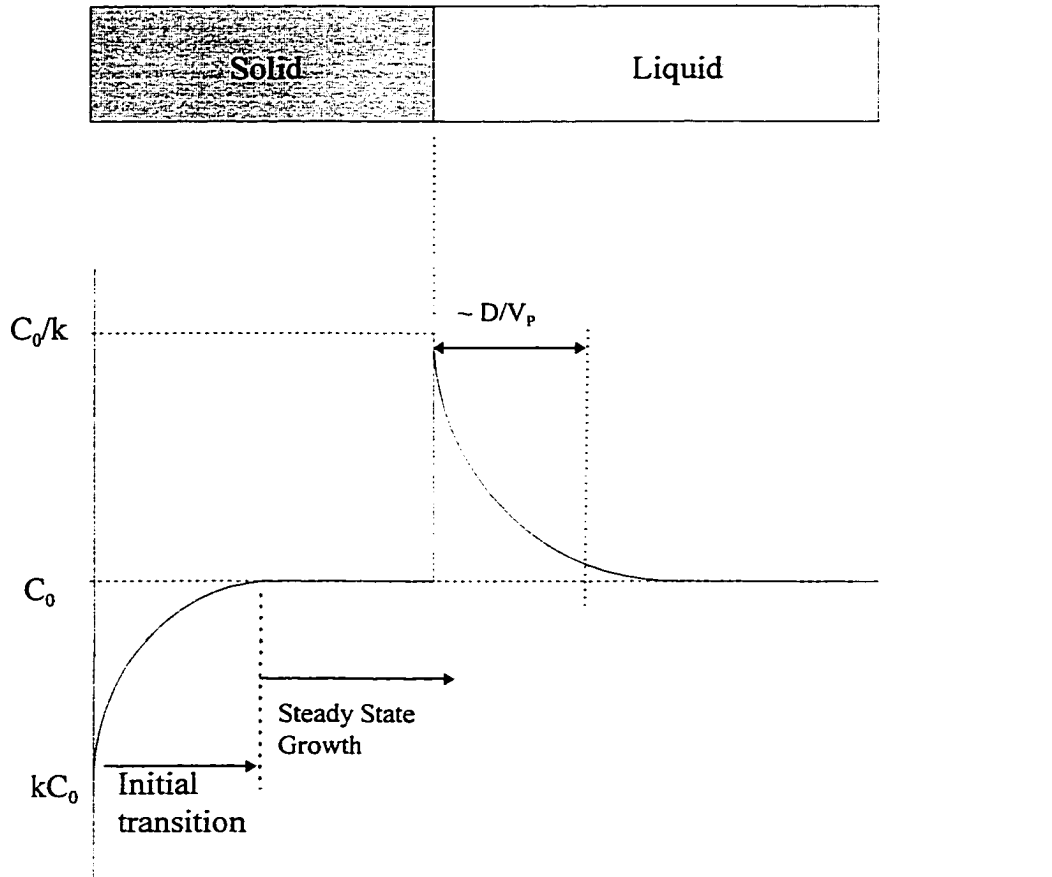


Figure 1.4: Steady State Composition Profile During Diffusive Growth

transient. They assumed that during the initial transient the rate of approach of interface composition towards the steady state composition was proportional to the instantaneous difference between those two values. With this assumption, they developed the expression for solute profile within the initial transient distance as,

$$\bar{c}_s(\tilde{x}) = C_0 [1 - (1 - k) e^{-k \bar{V}_p \tilde{x} / D_l}] \quad (5)$$

where, composition of the solid \bar{c}_s was given as a function of the distance from the start of solidification \tilde{x} . In this analysis, it was assumed that even during the initial transient, equation (3) was valid. This implies that the solid-liquid interface instantaneously reaches the imposed growth velocity as soon as solidification begins and remains constant throughout the event of solidification. In reality, the actual interface velocity should start from zero and gradually increase during the initial transient until it equals the growth rate. The actual dynamics of the interface and hence the composition profile in the solidified sample should also depend on the imposed temperature gradient G . This is not predicted in (5) due to the assumption of constant velocity of interface from the start of solidification..

1.1.4 One-Dimensional Boundary Layer Model For Convection In Melt (Burton et al. [8])

The assumption of solute transport only by molecular diffusion is very unlikely to be realized in any practical situation, since some convection is always present in the liquid melt. In fact, free convection is difficult to remove in the liquid metal alloys due to their low viscosity [9]. Convection in the melt causes mixing of solute and alters the diffusion boundary layers adjacent to the melt/crystal interface. The two or three dimensional spatial structures of the flow in turn establish a non-homogeneous composition field in the melt. In this text we will be mainly concerned with the one and two-dimensional nature of the transport processes. Although, the actual composition profile should vary both along the

axial (along the growth direction) and lateral (perpendicular to growth direction) directions, a simplified one-dimensional model for the effects of convection was originally developed by Burton, Prim, and Slichter [8] using the *stagnation film* concept proposed by Nernst [10]. According to this model, a diffusion boundary layer of constant thickness δ is assumed next to the solid-liquid interface. Inside this boundary layer, the transport of solute is due only to molecular diffusion along the growth direction, while outside the boundary layer the bulk liquid composition is uniform due to effective mixing by convective flow. The schematic of the model is shown in Figure 1.5. The solute transport equation inside the boundary layer is the same as (1). However the boundary condition (2) is modified as

$$\bar{c}_l = C_m, \text{ at } \bar{x} \geq \delta \quad (6)$$

The bulk composition C_m is equal to the initial composition C_0 for semi-infinite melt. For a finite melt, C_m is an increasing function of time. If the liquid melt is semi-infinite in extent, the bulk liquid composition is not altered by the solid forming and remains constant at C_0 . The steady-state solution of equations (1) and (6) for a semi-infinite melt is

$$\frac{\bar{c}(\bar{x})}{C_0} = \frac{k + (1 - k) \exp(-V_p \bar{x} / D)}{k + (1 - k) \exp(-V_p \delta / D)} \quad (7)$$

as originally given by Burton et al. [8]. For convenience, an *effective partition coefficient* k_{eff} is defined, which is the ratio of solid composition at the interface to the bulk liquid composition.

$$k_{\text{eff}} = \frac{k}{k + (1 - k) \exp(-V_p \delta / D)} \quad (8)$$

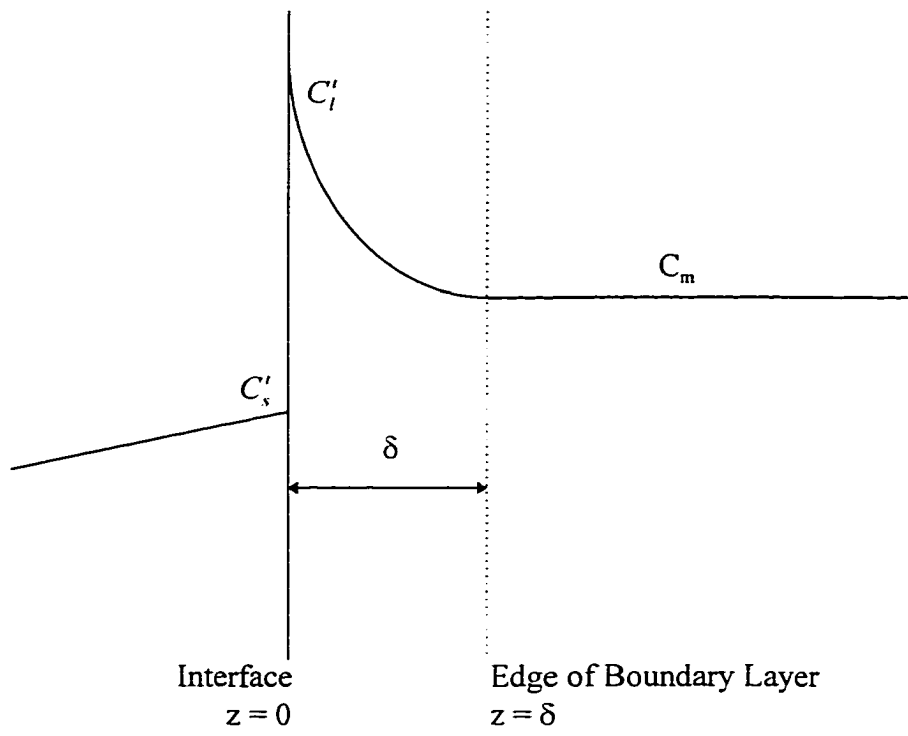


Figure 1.5: Schematic of the boundary layer model of Burton et al. [8]

Expression (8) is widely used to correlate experimental data and is usually highly successful for that purpose. However, one needs to find the proper value of boundary-layer thickness δ for good match between the data and the correlation. Despite its success in fitting a curve through the experimental data, this model hardly presents any physics of the fluid convection and the dynamical aspects of transport processes. Expression (8) could be rewritten for a finite length of the sample in terms of the fraction f of the sample solidified to give the normal freezing expression

$$\frac{\bar{c}(\bar{x})}{C_0} = k_{eff} (1 - f)^{(k_{eff}-1)} \quad (9)$$

For complete mixing in the fluid $\delta = 0$ and $k_{eff} = k$, where for diffusive growth $\delta \rightarrow \infty$ and $k_{eff} = 1$. The effect of convection on the solute profiles in the solid is schematically shown in Figure 1.6.

1.2 Review of Relevant Research

It has been well established that there is an immediate need for understanding the fundamental transport processes, especially the fluid flow effects, in crystal growth systems in order to have better control and predictability of the final microstructures, solute/dopant field, stress fields, and hence the thermo-mechanical, electrical and optical properties of the solid crystals [1,2]. This realization led to a large number of experimental, theoretical and numerical studies in the past fifteen years [11-50]. The volume of work can be classified in four major categories based on the system geometry and the direction of the buoyancy terms due to concentration and temperature gradients that lead to convection.

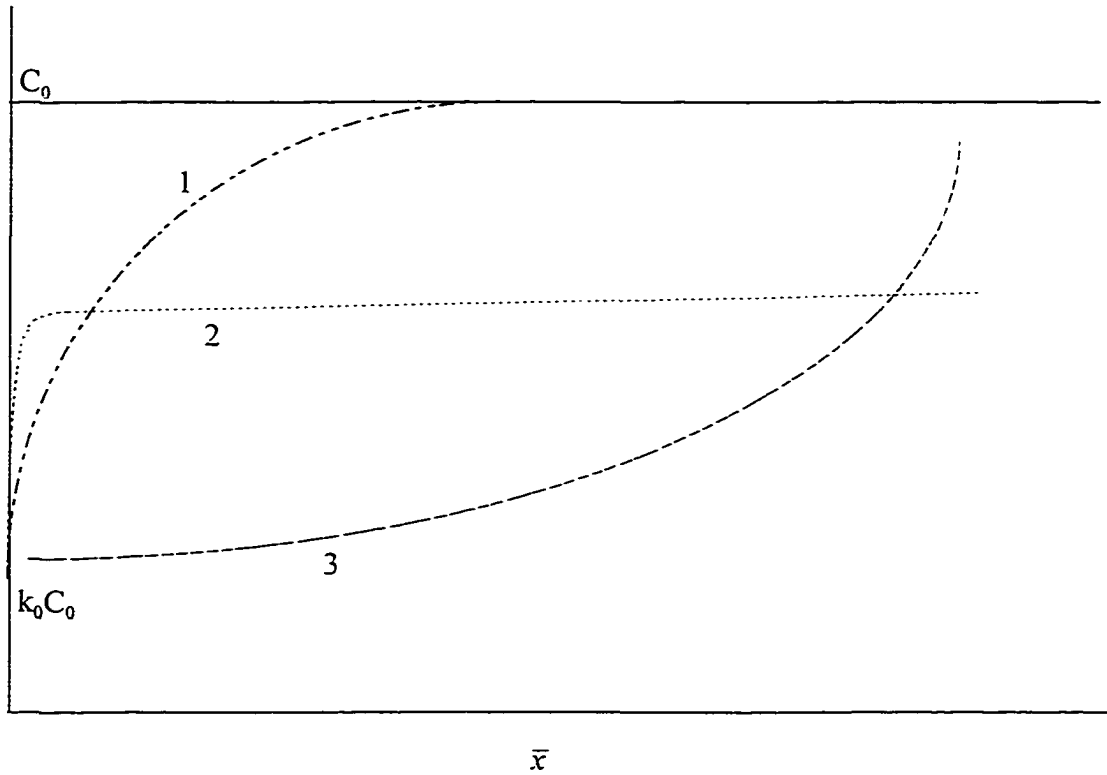


Figure 1.6: Solute profiles in solidified sample with (1) no convection (2) partial mixing (3) complete mixing [9]

1.2.1 Thermal Convection in Horizontal Configuration

The schematic of a horizontal Bridgman growth system is shown in Figure 1.7a. The solid crystal (filled rectangle) is grown from the melt by translating a temperature gradient G , along the sample length. The large horizontal temperature gradient leads to intense convection in the melt that has been investigated by numerous authors [11-29]. After the famous model experiment by Hurle et. al [12] with liquid Gallium, demonstrating critical conditions for the onset of oscillations in a parallelepiped container subject to a horizontal temperature gradient, several stability and numerical studies were carried out in order to interpret this behaviour. Recently, the stability and dynamics of the flow of low Prandtl number fluids ($Pr = 0$ and 0.015) in a 2D cavity with differentially heated walls, have been analyzed by a group of scientists in the GAMM workshop, Marseille, 1989 [13] in order to develop a solution database for code verifications and explore the bifurcation sequence from steady convection to complex time dependent convection. Within the range of Rayleigh numbers explored, multiple steady, periodic and quasi-periodic solutions were found that strongly depend on the boundary conditions. However, this configuration is the least stable in terms of achieving a no-flow condition in the melt, and is not of primary interest for fundamental studies on directional solidification.

1.2.2 Rayleigh-Benard Convection in Vertical Configuration

A schematic of the vertical configuration of Bridgman system is shown in Figure 1.7b, where the solid crystal is below the melt and the crystal is grown vertically upwards in the presence of a vertically stabilizing temperature gradient. A variation of this configuration, though not commonly used, is the downward solidification where the crystal is situated above the melt. The axial temperature gradient for the latter configuration is destabilizing (bottom heating) and the situation resembles the classic Rayleigh-Benard

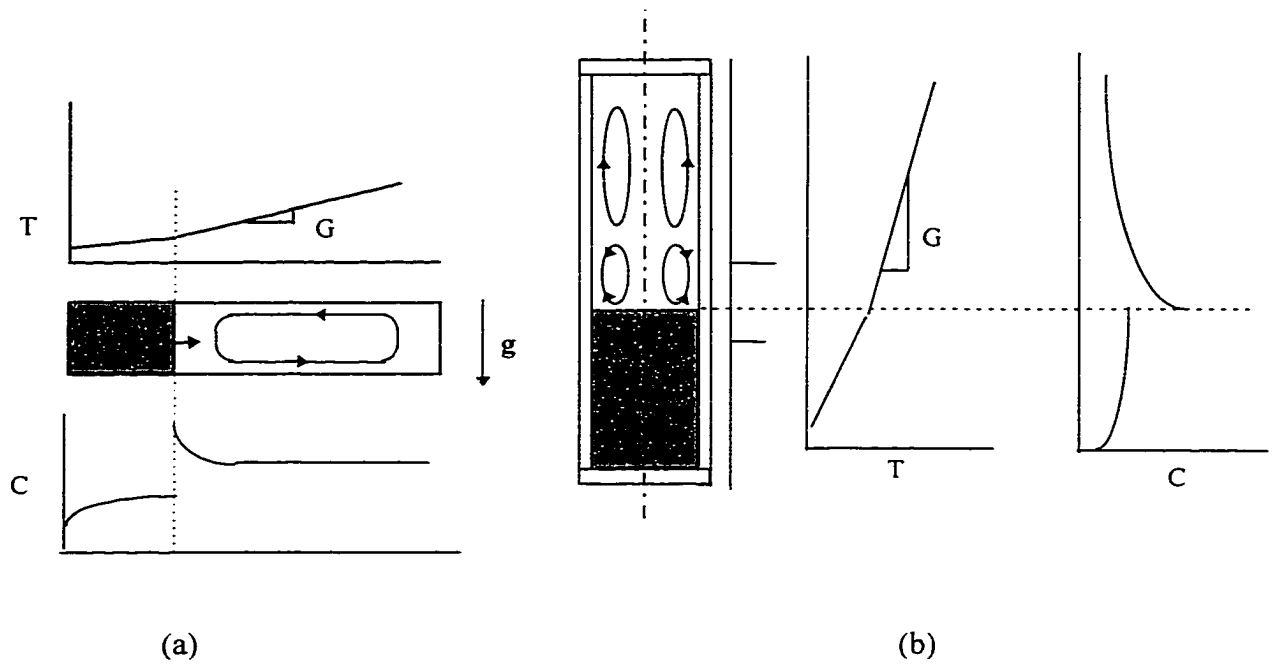


Figure 1.7: Schematic diagrams showing the arrangement, temperature and solute fields in commonly used Bridgman techniques for melt-crystal growth. (a) Horizontal Case (b) Vertical case.

configuration. As the thermal Rayleigh number exceeds the critical value, convection sets in as a bifurcation from the static state. For low Prandtl number fluids ($Pr \sim 0.01$) as in liquid metals, and solidification inside ampoules of moderate size, the convection is weakly turbulent, and the temperature, flow, and interface velocity fluctuations appear to give rise to striations and non-homogenities in the final crystal. This vertically downward solidification configuration is not widely used since it almost always leads to complex flow in the melt that is extremely difficult to control and characterize. A comprehensive review of other work with this geometry can be found in Chang and Brown [31], Muller and Ostrogorsky [32]

1.2.3 Double Diffusive Convection in Vertical Configuration Due to Unstable Solute Gradient

Coriell et al. [33] and McFadden et al. [34] pioneered the quantitative analysis of thermo-solutal convection during vertically upwards solidification of binary alloys, where the flow is driven by an unstable solute field in the presence of a stabilizing axial temperature gradient. The solute rejected at the interface was lighter than the solvent, or the solutal Rayleigh number was negative. No lateral temperature gradient was present in the system, and the only vertical temperature gradient was positive or stabilizing. This situation corresponds to the classic “double diffusive” configuration [51-55], where a no-flow equilibrium solution is possible for the equations of motion. However, this base static state becomes unstable above the critical values of the appropriate Rayleigh numbers, and double-diffusive convection sets in. Through linear stability analysis and numerical modeling, the critical solutal Rayleigh numbers were identified as a function of solidification velocity for fixed temperature gradients [33,34]. It was found that for thermal Rayleigh numbers less than 10, the temperature field has hardly any effect on the onset of instability. When the thermal Rayleigh number is much greater than 10, the thermal field becomes important. For a narrow solutal Rayleigh number range, the flow was found to be time periodic. After this

pioneering work, numerous studies were done on thermo-solutal convection in vertical solidification of binary alloys with a lighter solute in a heavier solvent [35-37].

However, none of these studies considered any lateral temperature variation and the sole mechanism for fluid flow was a double-diffusive instability from the stationary state. Although, these studies could be related to systems where the melt is solutally unstable (e.g. Pb-Sn, Pb-Bi) and the dominant driving force for convection is the solutal buoyancy even in the presence of thermal buoyancy due to lateral temperature gradient. the models cannot explain the flow processes in alloys where the solute is heavier than the solvent (e.g. Hg-Cd-Te, Ga-Ge, Al-Cu, Sn-Cd). In these cases, considering vertical gradients of temperature and concentration only, no convection should be expected, since both the vertical gradients produce stable density stratification. However, it has been experimentally observed that convection effects were dominant even in these systems where the solute is heavier than the solvent [56-67]. The driving force for convection in these samples is the radial temperature gradient that ubiquitously exists in all Bridgman systems due to its design (heating and cooling from side) and imperfections. The analytical solution of the heat conduction equations with boundary conditions as in Bridgman system clearly showed that a significant lateral temperature gradient exists in the sample due to the nature of the boundary conditions [68]. The magnitude of the gradient depends on the heat transfer coefficients or the Biot numbers between the furnace and the ampoule, and the thermal conductivity of the ampoule and sample material. The lateral temperature gradient, however small, always gives rise to free or natural convection in the melt.

1.2.4 Convection in Vertical Configuration Due to Radial Temperature Gradient

Realizing the need for developing a more physically realistic model Chang and Brown [38] first carried out the pioneering work where the thermal convection due to a lateral temperature gradient was investigated. The prototype model consisted of vertical solidification of a binary alloy with neutral solutal buoyancy (that is density of the melt is

not a function of the concentration) inside a cylindrical ampoule. The temperature field was prescribed along the edge of the sample and consisted of isothermal hot and cold zones separated by an adiabatic zone. This implied that the ampoule wall was extremely thin so that no temperature gradient existed within the wall along the radial direction, and the heat transfer coefficient between the furnace and the ampoule outer wall was infinite, so that the temperature of the furnace was directly impressed on the ampoule wall. The calculations demonstrated intense convection even in the presence of a vertically stabilizing temperature gradient, driven by a large radial temperature gradient near the adiabatic-hot junction. The radial temperature gradient was a consequence of the nonuniform temperature distribution along the ampoule boundary. The temperature was greater near the wall and lower at the center and this temperature gradient led to torroidal steady flows where the flow is up along the warmer wall and down along the cooler center. The radial segregation at the interface was found to be as large as 60% of the mean composition at certain cases. The study proved the coarseness of the constant thickness boundary layer type model [8] and substantiated the necessity of full scale modeling of the flow processes for precise characterization of the solute/dopant distribution.

Adornato and Brown [39] improved this model by considering a finite thickness of the ampoule and also taking into account a finite heat transfer coefficient between the ampoule and the furnace. The temperature of the furnace was hence not directly impressed on the outer ampoule wall, and instead was modeled by Newton's law of cooling. This apparently small difference in the heat transfer environment however substantially changed the flow features in the melt. Instead of the single torroidal cell flowing down along the centerline and up along the ampoule wall [38], there were two axially stacked counter-rotating cells, with the cell nearest to the interface moving downwards along the wall and up along the centerline (Figure 1.7 b). The model could predict the steady state (or quasi-steady state) interface shape, thermal, flow and solute field in the melt. It was found that the radial segregation was a nonlinear function of the thermal Rayleigh number and the maximum segregation occurred where the diffusive and convective rates of transport were of the same

orders of magnitude. Inclusion of solutal buoyancy, or positive solutal Rayleigh number seemed to dampen the thermal convection. For certain combinations of thermal and solutal Rayleigh number and the growth rate, sideways diffusive instability was observed due to the interaction of lateral temperature gradient with the stabilizing axial solute gradient as predicted by Hart [69].

The success of these models inspired a large number of numerical studies of the vertical Bridgman system [40-50]. These models closely simulated the real Bridgman system, taking into account the heat transfer from the furnace to the ampoule of finite thickness, conduction through the ampoule and the solid crystal, and conduction and convection in the melt. However, most of these models were restricted to steady and/or quasi-steady state analysis of either only thermal convection, or both thermal and solutal convections only in a narrow Rayleigh number range for a few specific semi-conductor alloys. Although in a few cases the initial transient and the transient effects due to finite sample size have been explored for the same materials, the flow instabilities and transition of steady convection to oscillatory or chaotic convections have not been explored in terms of microstructure evolution. Moreover, since the alloys with specific thermo-physical characteristics were considered, the results could not be generally applied to other systems. For example, it was consistently reported that the generic structure of the flow in the system consisted of two torroidal cells stacked over each other, which rotated in opposite sense. We found that this was due particularly to the lower thermal conductivity of the solid than the liquid for the semiconductor alloys considered, and hence could not be generalized [70]. For alloys in which the solid phase has higher thermal conductivity than the liquid phase, the counter-rotating cells are replaced by co-rotating cells stacked over each other (Figure 1.7 b).

Although significant quantitative analysis has been done on steady state and quasi-steady state solute and temperature distributions, interface curvature, axial and radial segregation, the flow instabilities and transition of steady convection to oscillatory or chaotic convections have not been explored in these configurations. However, it has been experimentally observed that even for samples with stabilizing vertical solute gradients,

oscillating microstructures could develop in the large samples [67]. When the same experiments are done in thin samples the oscillating structures disappear. Using semi-analytical and numerical models, we have shown that oscillatory convection in the liquid melt gave rise to oscillating layered structure [70-74]. Extensive computations encompassing broad parameter space, conclusively showed the presence of time dependent flows (periodic, quasi-periodic, non-periodic) in the melt, that lead to spatial patterns in the solid sample.

1.3 Objective of Thesis

The major objectives of this research are to (i) propose new physical mechanisms for the formation of oscillatory tree-like structure formation in the two-phase peritectic alloys that could not be explained with the existing theories, (ii) develop realistic numerical models of the vertical Bridgman growth system, in which time-dependent fluid flow will be precisely characterized, and its influence on the solidification microstructure will be established, (iii) discover novel microstructures that arise solely due to the fluid flow, and which cannot be accessed in the diffusive regime, and (iv) investigate the fundamental mechanisms and onsets of various flow instabilities and the nonlinear dynamics following the instabilities in a precisely characterized prototype model of the vertical Bridgman system.

1.4 Dissertation Organization

The dissertation is written in an alternate format composed of five original manuscripts, preceded by a general introduction. References cited in each manuscript are placed immediately after the manuscripts.

The first manuscript in Chapter 2, “A model of convection induced oscillatory structure formation in peritectic alloys” was submitted to the *Metallurgical and Materials Transactions*. A *novel physical mechanism* is proposed in this paper that explains the

oscillating structure formation in Peritectic alloys. It is proposed that a complex layered structure in the solid phase can form due to oscillating fluid flow in the melt. This physical mechanism is substantiated by a simple advection-diffusion model that uses prototype steady and time-periodic flows for the convection.

The second manuscript in Chapter 3, “Mechanisms of layer structure formation in peritectic alloys” is published in the Symposium Proceedings on *Phase Transformations and Systems Driven Far From Equilibrium*, TMS 98. A numerical model has been developed to investigate the characteristics of thermo-solutal convection due to an *imposed* lateral temperature gradient in a simplified system. A constant lateral temperature gradient is prescribed between the vertical walls of a rectangular cavity inside which a binary melt is solidified vertically upwards. The lateral temperature gradient is *externally imposed* to model the actual radial temperature gradient that exists in all vertical Bridgman systems that employ the three zone heating assemblies. The solution of the transport equations (momentum, mass and heat) showed that oscillatory convection sets in large samples (6 mm diameter) and produces oscillatory tree-like structure in the solid phase. In thin samples (0.6 mm diameter) the convection level is minimal and only α phase to β phase transition takes place.

The third manuscript in Chapter 4, “The effect of convection on disorder in primary cellular and dendritic arrays” has been submitted to the *Metallurgical and Materials Transactions*. The disorder in primary spacing of cellular and dendritic arrays on the solidification front is experimentally analyzed and quantified. The apparently puzzling behaviour of higher disorder in Al-Cu (low level of convection due to rejection of heavier solute in the melt) than that in Pb-Sn (high level of convection due to rejection of lighter solute in the melt) is explained by numerical analysis.

The fifth manuscript in Chapter 6, “Unsteady melt convection in vertical Bridgman system and pattern formation in the solid phase of peritectic alloys: modeling, dynamics and microstructure evolution” is to be submitted to the *Journal of Fluid Mechanics*.

References

1. Trivedi R. 1989, "Directional Solidification of Alloys", in Principles of Solidification and Materials Processing, 1, p33, Oxford and IBH Publ. Co. Pvt. Ltd.
2. Brown R. C. 1988, AIChE J., v 34, p 881
3. Chalmers B. 1964, Principles of Solidification. Wiley, New York
4. Flemings M. C. 1974 Solidification Processing, Mc-Graw Hill, New York
5. Kurz W. and Fisher D. J. 1986 Fundamentals of Solidification, Trans. Tech. Publ., Aedermannsdorf, Switzerland
6. Mason J. T. 1982 An Apparatus for Directional Solidification, IS-4817, UC-37
7. Tiller W. A., Jackson K. A., Rutter J. W., Chalmers B. 1953, Acta Met., v 1, p 428
8. Burton J. A., Prim R. C., Slichter W. P. 1953, J. Chem. Phys., v 21, p 1987
9. Verhoeven J. D. 1975 Fundamentals of Physical Metallurgy, John Wiley & Sons Inc.
10. Nenrst W. 1904, Z. Phys. Chem., v 47, p 52
11. Azouni M. A. 1981, PhysicoChemical Hydrodynamics, v 2, pp295-309
12. Hurle D. T. J., Jakeman E., Johnson C. P. 1974, J. Fluid Mech., v 64, p 565
13. Roux B., 1990, Numerical Simulation of Oscillatory Convection in Low Pr Fluids, Vieweg, Braunschweig
14. Hurle D. T. J. 1966, Phil. Mag., v 13, p 305
15. Muller A. and Wiehelm M. 1964, Z. Naturf. A, v 19, p 254
16. Hart J. 1972, J. Atm. Sci., v 29, p 687
17. Hart J. 1983, J. Fluid Mech., v 132, p 271
18. Gill A. E. 1974, J. Fluid Mech., v 64, p 577
19. Kuo H. P. and Korpela S. 1988, Phys. Fluids, v 31
20. Laure P. and Roux B. 1987, CRAS Ser. II, v305, p 1137
21. Birikh R. V. 1966, PMM, v 30, p 432

22. Cormack D. E., Leal L. G. and Imberger J. 1974, *J. Fluid Mech.*, v 209
23. Winters K. H. 1988, *Int. J. Numer. Methods Eng.*, v 25
24. Okada K. and Ozoe J. 1993, *J. Crystal Growth*, v 126
25. Pulicani J. P., Del Arco E. C., Randriamampianina A., Peyret R. 1990, *Int. J. Numer. Methods Fluids*, v 481
26. Del Arco E. C., Pulicani J. P., Randriamampianina A. 1989, *CRAS Ser. II* v309, p1869
27. Cliffe K. A. and Winters K. H. 1984, *J. Comp. Physics*, v 54
28. Riley D. S. and Winters K. H. 1990, *J. Fluid Mech.*, v 215
29. Skeldon A. C., Riley D. S., Cliffe K. A. 1996, *J. Crystal Growth*, v 162, p 95
30. Carruthers J. R. 1977, in *Preparation and properties of Solid State Materials*, eds. W R Wilcox and R A Lefever, Dekker. New York, NY
31. Chang C. J. and Brown R. A. 1984, *J. Comp. Physics*, v 53, p 1
32. Muller G. and Ostrogorsky A. 1994, in *Handbook of Crystal Growth*, v 2b, p 709
33. Coriell S. R., Cordes M. R., Boettinger W. J., Sekerka R. F. 1980, *J. Crystal Growth*. v 49, p 13
34. McFadden G. B., Rehm R. G., Coriell S. R., Clark W. and Morrish K. A. 1984, *Met. Trans.*, v A15, p 2125
35. Le Marec C, Guerin R. , Haldenwang P. 1996., *J. Crystal Growth*, v 169, p147
36. Le Marec C., Guerin R., Haldenwang P 1996., submitted to *Phys. Fluids*
37. Heinrich J. C. 1988, *Comp. Meth. App. Mech. and Engg.*, v 65, p 65
38. Chang C. J. and Brown R. A. 1983, *J. Crystal Growth*, v 63, p 343
39. Adornato P. M. and Brown R. A. 1987, *J. Crystal Growth*, v 80, p155
40. Carlson F. M., Fripp A. L., Crouch R. K. 1984, *J. Crystal Growth*, v 68, p 747
41. Ouyang H. and Shyy W. 1996, *Int. J. Heat and Mass Transfer*, v 39. p 2039
42. Ouyang H., Shyy W., Levit V. I., Kaufman M. J. 1997, *Int. J. Heat and Mass Transfer*, v 40, p 293
43. Ouyang H. and Shyy W. 1997, *J. Crystal Growth*, v 173, p 352

44. Kaddeche S., Garandet J. P., Barat C., Ben Hadid H., Henry D. 1996, *J. Crystal Growth*, v 158, p144
45. Kappurao S., Brandon S., Derby J. 1995, *J. Crystal Growth*, v 155, p 93
46. Kim D. H. and Brown R. A. 1989, *Journal of Crystal Growth*, v 96, p 609
47. Brown R. A. and Kim D. H. 1991, *Journal of Crystal Growth*, v 109, p 50
48. Kim D. H. and Brown R. A. 1991, *Journal of Crystal Growth*, v 109, p 50
49. Brown R. A. 1992, in *Heat and Mass Transfer in Materials Processing*, eds.. Tanasawa I and Lior N, p 137
50. Kappurao S., Brandon S. and Derby J. 1995, *Journal of Crystal Growth*, v 155, p 103
51. Veronis G. 1968, *J. Fluid Mech.* v 34, p 315
52. Turner J. S. 1985, *Ann. Rev. Fluid Mech.*, v 17, p 11
53. Turner J. S. 1973, *Buyoancy Effects in Fluids*, Cambridge University Press, London
54. Moore D. R. and Weiss N. O. 1990, *Phil. Trans. R. Soc. Lond. A* , v 121
55. Huppert E. 1976, *Nature*, v 263, p 20
56. Capper P., Jones C. L., Pearce E. J. and Quelch M. J. T. 1983 , *J Crystal Growth*. v 62. p 487
57. Klaren C. M., Verhoeven J. D. and Trivedi R. 1980, *Metall. Trans. A*, v 11, p 1853.
58. Mason J. T., Verhoeven J. D. and Trivedi R. 1982, *J. Crystal Growth*, v 59, p 516
59. Rouzaud A., Camel D., Favier J. J. 1985, *J. Crystal Growth*, v 73, p 73
60. Tewari S. N. and Trivedi R. 1991, *Int. J. Microgra. Res.IV/4* , p 240.
61. Tewari S. N., Shah R. and Chopra M. A. 1993, *Metall. Trans.* v 24A, p 1661
62. Tewari S. N. and Shah R. 1996, *Metall. Trans.*, v 27A, p1353
63. Tewari S. N. 1986, *Metall. Trans.*, v 17A, p 2279
64. Tewari S. N. 1990, *Mat. Sci. Eng.. A*, v 130, p 219
65. Tewari S. N. 1988, *Metall. Trans.*, v 19A, p 1351
66. Tewari S. N. and Chopra M. A. 1990, *Int. J. Microgra. Res.III*, p 99
67. Park J. S. and Trivedi R. 1998, *J. Cryst. Growth*, v 187, p 511

68. Naumann R. J. 1982, *J. Crystal Growth*, v 58, p 589
69. Hart J. E. 1971, *J. Fluid Mech.*, v 49, p 279
70. Mazumder P. and Trivedi R. 1999, in *Fluid Flow Phenomena in Metals Processing*, TMS 99, eds. Naggy al Kaddah, D G C Robertson, S T Johansen, V R Voller, p 459
71. Trivedi R., Mazumder P., Tewari S. N. 1999, submitted to *Met. Trans. A*
72. Trivedi R., Miyahara H., Mazumder P. and Tewari S. N. 1999, submitted to *Met. Trans. A*
73. Mazumder P., Trivedi R. and Karma A. 1998, *Met. Trans. A.*, in press
74. Mazumder P., Trivedi R., and Karma A. 1998, in *Phase Transformations and Systems Driven far From Equilibrium*, eds. E Ma, M Atzmon, P Bellon. R Trivedi, MRS, v 481. p 39

CHAPTER 2: A MODEL OF CONVECTION INDUCED OSCILLATORY STRUCTURE FORMATION IN PERITECTIC ALLOYS

A manuscript submitted to *Met. Trans. A*

P. Mazumder*, R. Trivedi** and A. Karma#

Ames Laboratory US-DOE, Iowa State University, Ames, IA 50011

*Department of Mechanical Engineering

**Department of Material Science and Engineering

Department of Physics, Northeastern University, Boston, MA

ABSTRACT

In the two phase region of a peritectic system, experimental studies have shown that the primary phase often forms a large tree-like structure which is surrounded by the peritectic phase. The formation of this novel structure has been attributed to the presence of convection in the liquid. Here, specific physical mechanisms of convection-induced tree-like structure formation are identified. A mathematical model based on advection-diffusion of solute, with *prototype flows* for advection, is presented, and solved numerically to show that an oscillating fluid motion can give rise to a complex oscillatory, tree-like, structure. Three different regimes are established: diffusive, steady convective and unsteady convective regimes. In the diffusive regime, a banded structure is predicted within a narrow composition range, and the spacing of the bands is dictated by the nucleation undercoolings of the two phases. Under steady convection, the primary phase transforms into the peritectic phase with a curved $\alpha:\beta$ interface. Finally in the presence of oscillating convection, a tree-like shape of the primary phase is predicted, as observed experimentally.

I. INTRODUCTION

Several experimental studies in the two-phase region of peritectic systems have shown the development of a so-called *banded structure* in which *bands* of the primary and peritectic phases form alternately normal to the growth direction [1-5]. Analytical models have recently been developed to explain the mechanism of layer structure formation under the assumption of diffusive growth [6] or strong convective growth which can be described by a boundary layer model [5]. Although these models offered insight into the possibility of inherent oscillatory dynamics of repeated nucleation and growth of two phase solids for specific situations, they could not explain many of the salient features observed in actual experiments [5, 7]. Through the comparison of experimental results with a boundary layer model, Karma et al. [5] showed that after the first nucleation of the peritectic phase, no nucleation of either of the phases occurs in the formation of layers, suggesting that the discrete bands observed in the plane of polish could indeed be continuous. Recently, Park and Trivedi [8] have carried out a systematic experimental study to show that the apparent *band* structure is in fact a continuous tree-like morphology of the primary phase that is surrounded by the peritectic phase. Through a systematic study of solidification in samples of different diameters, they have shown that this tree-like structure, observed in a larger diameter tube, disappears when the experiments are carried out under reduced convection conditions in very fine tubes of diameters 0.6 mm or less indicating that convection might have influenced the microstructure. Park and Trivedi [8] concluded that convection effects play a dominant role in all experiments carried out on layered structure formation in peritectic systems in sample diameters larger than 1 mm. However, discrete *band* formation was observed in very fine samples only for the composition range where banding was predicted by the diffusive model [6].

The aim of this paper is to first propose a physical mechanism of convection induced *oscillatory layered structure* formation in large samples as observed by Park and Trivedi [8]. The mechanism will then be supported by a 2D numerical model. In this simplified

numerical model, we solve the advection-diffusion equation for solute transport, where the advection terms are modeled by *prototype flows* [45] pertinent to natural convection inside 2D ampoules. We shall show that although the inherent oscillatory cycle of Trivedi [6] is valid in a diffusive growth regime, it is not operative in most experimental studies reported so far [1-5, 7]. We explain that when one considers the effects of fluid flow in the melt, the oscillatory cycle of repeated nucleation and growth is not absolutely required to form oscillating layered structures. One or two nucleation events and fluctuating interface composition profiles in response to unsteadiness in the fluid flow is sufficient to generate complex oscillatory structures. As we shall see, this model is able to explain almost all the intriguing features of experimental observations by Karma et al. [5]: (i) finite number of layers, (ii) interconnectedness of α layers, (iii) continuous β matrix, (iv) decaying width and thickness of α layers along the length of sample and, (v) the possibility of layer formation over almost the entire peritectic range.

The paper is arranged as follows. (1) We shall first review the experimental observations and the existing models of band formation, and show the inadequacy of the models to explain the experimental results. (2) We will then review the causes of natural convection in a vertical Bridgman system and show that significant convection is present in experimental studies. (3) Next, we will describe how the convection effects alter the composition field, and propose a physical mechanism for the oscillatory structure formation. (4) Finally, the numerical model and computational results will be presented to support the proposed mechanisms. The proposed theory predicts the complex geometric features of the experimentally observed tree-like microstructures, and at the same time, reproduces the results of the earlier theory of Trivedi [6] in the limit of no fluid motion.

II. BACKGROUND

Figure 1 shows schematically a typical peritectic phase diagram. We assume linear solidus and liquidus lines in order to simplify the analysis. α , β and L represent the primary solid phase, peritectic solid phase and the liquid phase, respectively. T_p is the peritectic temperature at which α , β and liquid phases can coexist in equilibrium at the corresponding compositions of C_α , C_β and C_p . The composition of the liquid C_p is usually called the *Peritectic Composition* though Peritectic Point also has also been used to refer to C_β [9]. The range ($C_\alpha \leq C \leq C_p$) is the *Peritectic Range* which is subdivided into two regions as *Hypoperitectic* ($C_\alpha \leq C \leq C_\beta$) and *Hyperperitectic* ($C_\beta \leq C \leq C_p$). When an alloy of initial composition C_0 ($< C_p$) is directionally solidified, the primary α phase solidifies first, followed by the peritectic phase (β).

Typical microstructures described as *band structures* in the Sn-Cd [1] and Pb-Bi [4] systems are shown in Fig. 2 for sample diameters of 3 to 6 mm. Experimental conditions of G/V were used such that planar α or β phases would be stable. The darker phase is the primary α , and the lighter phase is the peritectic β . The actual topology of α and β phases is much more complex than that of the idealized *alternate bands* perpendicular to the growth direction [1-7]. In the Sn-Cd system an extensive band formation has been observed along the growth direction with very small variation in spacing, whereas only transient banding with spacing variations has been observed in the Pb-Bi system. The spacing variation in both these systems does not follow the predictions of the diffusive model [5-7]. Also the bands do not form uniformly over the entire cross-section.

Trivedi [6] proposed an analytical model of *banding* in peritectic systems based on the assumption that the transport of solute is only due to molecular diffusion and occurs only along the growth direction. The corresponding *Banding Cycle* developed in this model is shown schematically in Figure 3. Accordingly, if a melt is solidified from an initially homogeneous composition C_0 , initially the α phase solidifies and grows. The liquid and

solid compositions at the interface vary along the liquidus and solidus lines of α -L equilibrium and tend to approach the steady state solid composition C_0 and α solidus temperature. Before reaching the steady state, however, the secondary phase β may nucleate at the composition C_1^M where the α liquidus line intersects with the β nucleation undercooling line. The solid and liquid compositions at the interface now vary along the solidus and liquidus lines of β -L equilibrium and tend to approach the steady state solid composition C_0 and β solidus temperature. But, before reaching the steady state, the primary phase α may re-nucleate on the solid-liquid boundary of β phase at the composition C_1^m , and the cycle of alternate nucleation and growth of primary and secondary phases may continue leading to alternate bands of α and β . One of the major predictions of the diffusive model [6] is that the banding cycle operates below and above the peritectic temperature if the initial composition of the melt falls inside the *Banding Window* on the phase diagram (Figure 3b). The position and width of the *banding window* is a function of the nucleation undercoolings of the α and β phases for a particular alloy. In Sn-Cd or Pb-Bi systems, the *Banding Window* always falls inside the *Hypoperitectic Region*. Calculation shows that for small but finite undercoolings, a typical *Banding Window* for Sn-Cd is $0.65 \leq C_0 \leq 0.89$ wt %. But, in actual experiments with Sn-Cd alloys, a banded structure has been reported for compositions in the range of 1.0 -1.6 wt% Cd [1, 2, 7], which are in the hyperperitectic composition range. For Pb-Bi system *banding* was observed for compositions within almost the entire two-phase peritectic region [5].

Recently Karma et al. [5] attempted to explain these inconsistencies in terms of convection in the melt in the Pb-Bi system. They realized that the Pb-Bi system must be highly convective due to the rejection of lighter solute at the interface and assumed that the vigorous flow in the melt would cause formation of a *boundary layer* of constant thickness near the interface. Composition variation only in the growth direction and within the thin boundary layer of constant thickness was allowed. The composition outside the layer was assumed homogeneous due to mixing but it increased with time as solidification proceeded.

This model retained the concept of a *banding cycle* and a *banding window* of Trivedi [6], but considered the case where *banding* is transient and caused by the passing of the perfectly mixed bulk composition through the diffusive *banding window* during solidification. For this transient *banding* criterion, the model could predict the occurrence of bands for initial compositions less than the lower limit of the *banding window*. The model could predict the variation of band spacings along the growth direction even for constant imposed growth rate. However, it still could not explain the formation of bands for initial compositions greater than the upper limit of the *banding window*, including the hyperperitectic region. Furthermore, the model fell short by about an order of magnitude in predicting the observed band spacings. Although the model [5] incorporated the effect of convection, the one dimensional analysis failed to capture salient features, such as lateral segregation and inhomogeneity caused by natural convection. In addition, the model did not consider the possibility of convection in the Sn-Cd system due to the rejection of heavier solute at the interface, which may not follow the boundary layer model. However, this model may be applicable to determine the mean banding characteristics only for systems in which extensive convection leads to perfect or almost perfect mixing.

The above discussion clearly shows that neither the diffusive model, nor the boundary layer convective model is operative under the conditions of experiments. Experimental studies by Karma et al. [5] found that usually α bands were interconnected to each other over a considerable distance. By comparing the model with the experimental data, Karma et al. [5] showed that only one nucleation of each phase was occurring so that both the α -phase and β -phase must be continuous. Thus, neither the diffusive nor the convective boundary layer model which assumes repeated nucleation events is operative in experiments. A detailed experimental study by Park and Trivedi [8] confirmed that the band structure observed on a plane of polish (close to the surface) is really a large tree-like structure of the primary α -phase that is surrounded by the peritectic β -phase. This was shown by the successive sectioning of the sample, as shown in Fig. 4. Such branched structures are

laterally stretched out and usually do not extend over the entire cross-section. The axial thickness and the lateral width of the α phase usually decreased along the length of the sample. From now on we shall distinguish any connected branched structure as *oscillating layer structure* as opposed to *separated band structures*.

All earlier experimental studies [1-5, 7] were carried out in ampoules of diameter equal to or greater than 3 mm, in which convection effects could be dominant at low velocities. In order to understand the effect of convection, a systematic experimental study with some control over the fluid flow was recently carried out by Trivedi et al. [10]. In this study the modes and degrees of convection were modulated by carrying out directional solidification in ampoules with decreasing diameters (6 mm to 200 microns inner diameter). By going from 200 microns to 6 mm, one spans a Rayleigh number range of $\sim 10^5$ for a fixed lateral temperature gradient [23]. On implementing this technique for the Sn-Cd system, Park and Trivedi [8] found that the microstructures strongly depended on the diameter of the tube. They observed that in the large hyperperitectic samples, where diffusive bands are forbidden [6], an oscillating structure is observed in which both the primary and peritectic phases are interconnected. In addition, the primary phase forms a large tree-like structure that is surrounded by the peritectic phase, (Fig. 4a-b). This tree-like structure, however, creates an illusion of isolated bands on the polished surface when the depth of polish is not sufficient (Fig. 4a) Such a tree-like structure was shown to disappear when the experiments were conducted under reduced convection conditions in tubes of diameters 0.6 mm or less, (Fig. 4c). Under this condition, in the hyperperitectic region, only one α to β transition is observed consistent with the diffusive band model [6]. Thus, it is evident that convection effects can induce the formation of complex microstructures. To explain this remarkable effect of convection on the shape of the α - β interface, we shall first examine the possibility of convection for the experimental conditions in the Sn-Cd system, and then discuss how the convection affects the interface pattern formation.

III. NATURAL CONVECTION IN THE BRIDGMAN SYSTEM

A vertical Bridgman system consists of crystal and melt contained in a cylindrical ampoule pulled slowly through a vertically aligned furnace, insulator and cooling units. In the simplest analysis, one can assume that the hot and cold zones are isothermal at T_H and T_C and are separated by an adiabatic insulator designed to establish high axial temperature gradient in the liquid at the interface. In a *perfect* vertical Bridgman system, the thermal gradient should be perfectly vertical and positive upwards, and there should not be any lateral temperature gradient. Since, for most fluids the density decreases with increasing temperature, lighter liquid overlays heavier liquid and the density gradient is parallel to the gravity vector. As the binary liquid freezes, solute is preferentially rejected at the interface (for partition coefficient, $k < 1$), so that a solute rich layer forms adjacent to the interface. Since the density of the liquid also depends on the solute concentration, the rejection of solute modifies the density field within this solute layer. If the solute is heavier than the solvent (as in Sn-Cd) then both the solutal and thermal buoyancy forces are parallel to the gravity vector. Under this ideal case of no horizontal variation of temperature, this arrangement is hydro-statically stable (i.e., there is no fluid motion) and the transport of solute must be solely due to molecular diffusion along the growth direction. In this ideal case, the diffusive model of Trivedi [6] may be applicable for the formation of a *banded* structure. On the other hand, if the solute rejected is lighter (as in Pb-Bi), the liquid becomes hydrostatically unstable when certain parameters exceed critical values and *double-diffusive convection* sets in [11-12].

In a *real* vertical Bridgman system, in which the hot and cold zones are separated by the adiabatic insulator, a horizontal temperature gradient always exists in the liquid [13-23], as opposed to the *perfect* Bridgman system with no lateral gradient discussed in the previous paragraph. It is well known that any horizontal temperature difference, however small, will initiate some convective motion [24,25]. Even in the presence of a stabilizing axial gradient, i.e. the melt over the crystal and temperature increasing upwards, the flows induced by radial

temperature gradients can be significant [13-23]. The convective flow in turn makes the composition field laterally nonuniform which gives rise to solutal buoyancy. The complex interactions among the vertical temperature gradient (usually stabilizing), vertical composition gradient (either stabilizing or destabilizing), horizontal temperature gradient and horizontal composition gradient can lead to very complex dynamical behavior in low Prandtl number fluids such as liquid metals ($Pr \sim 0.01$) which is yet to be explored in full detail. However, partial treatments of the problem with one or two gradients in simplified geometries indicated rich varieties of time dependent flow phenomena. In a number of experimental and theoretical studies [26-36] on thermal convection in low Prandtl number fluid ($Pr \sim 0.01$) driven only by horizontal temperature gradient, it has been observed that time periodic, quasi-periodic and chaotic oscillations of temperature and velocity occurred. Thermo-solutal convection in cavities with horizontal thermal and solutal gradients has been the subject of several works in recent days because of its relevance in the crystal growth processes [23, 38-40]. The computational results with low ($Pr = 0.02$) and moderate ($Pr = 0.7, 1$) Prandtl number fluids have demonstrated complex oscillatory flows that depend on the thermal Rayleigh number and the buoyancy ratio (or the ratio of thermal to solutal Rayleigh numbers) for a specific fluid-solute system. Although the above mentioned research work provided considerable exposure to a wide range of dynamical flow phenomena, the prototype systems are far removed from the complexity of the real directional solidification system. In a real vertical Bridgman system, a steady background thermal convection exists even before the start of solidification, driven by the interaction of the vertical and lateral temperature gradients [23]. With the start and progress of solidification, this thermal convection interacts with the solutal buoyancy and leads to complex flow dynamics, especially at large Rayleigh numbers corresponding to solidification in samples of diameter > 3 mm [23, 41-43]. The actual dynamics is completely governed by the Thermal Rayleigh Number [$Ra_T = g\beta_T G_y d^4 / (\nu\kappa)$], Solutal Rayleigh Number [$Ra_S = g\beta_S C_0 d^3 / (\nu\kappa)$], Prandtl number ($Pr = \nu/\kappa$), the aspect ratio (l/d), the Lewis number (Le

= κ/D), the growth rate (V_p) and the ratio of the vertical temperature gradient to the horizontal temperature gradient ($\zeta = G_x/G_y$), where g is the gravitational acceleration; β_T and β_S are the thermal and compositional expansion coefficients, C_0 is the initial composition of the melt, d and l are the diameter and vertical height of the melt column; ν , κ and D are the kinematic viscosity, thermal diffusivity and solute diffusivity respectively. Such a complex problem is not analytically tractable and one has to resort to numerical analysis.

Recently a numerical model has been developed to investigate the characteristics of thermo-solutal convection due to an imposed lateral temperature gradient in a simplified system [41]. In this model, the flow field and its effect on solute redistribution in a differentially heated two dimensional cavity (with imposed lateral temperature gradient between the vertical walls) are calculated. A constant lateral temperature gradient is prescribed between the vertical walls to model the actual radial temperature gradient that exists in all vertical Bridgman systems that employ a three zone heating assembly. The actual lateral temperature gradient for a particular design can only be determined through full scale thermal simulation of the Bridgman Growth process and it turns out to be a complex function of the design variables and also the axial temperature gradient [23]. A full scale simulation of the Bridgman system that takes into account the furnace temperature distribution, heat transfer from furnace to the ampoule, conduction in ampoule and crystal, conduction and convection in the melt, has been undertaken by the authors [43]. However, direct application of a prescribed lateral temperature gradient consistent with the results from the thermal simulation and experimental measurements, considerably simplifies the analysis, yet produces physically relevant results. This numerical analysis of thermo-solutal convection with externally imposed lateral temperature gradient [41] indicated that convection in the melt could be quite significant even in the case of Sn-Cd which has been believed to be convection free [1, 7]. A set of computations were done for a Sn-1.4 wt % Cd alloy with a growth rate of 3.0 $\mu\text{m}/\text{sec}$. A vertically stabilizing temperature gradient of 10.0 K/mm and a horizontal temperature gradient ~ 0.2 K/mm were used. It is found that for tube

diameters of the order of 800 microns or smaller the convective transport of solute is negligible compared to the diffusive transport. For tube diameters of the order of 1.0-2.0 mm the convective transport is of the same order of magnitude as the diffusive transport and the flow is steady. For tube diameters greater than 3.0 mm the convective transport is higher than diffusive transport and the flow is unsteady. The flow in the melt for these samples shows periodic or quasiperiodic oscillatory behaviors. Since most experimental work that observed *banded* structures in the Sn-Cd and Pb-Bi systems were done in ampoules of diameter 3.0 mm or greater [1-5, 7], it is expected that the dynamics fell in the regime of complex time dependent convective transport. We expect that both the intensity and mode of convection (steady or unsteady) must have had a profound effect on the microstructures observed in these experiments. We shall now show that an oscillating tree-like structure can form due to the fluctuation in the composition profile at the interface, which is itself induced by the fluctuating fluid flow.

IV. MECHANISM OF MICROSTRUCTURE DEVELOPMENT

In the experimental studies in different diameter tubes [8, 10], the tube diameter was the only variable that was changed. As the tube diameter was varied from 200 microns to 6 mm, the thermal Rayleigh number changed by approximately five orders of magnitude for a fixed lateral temperature gradient. This causes major change in the strength and modes of convection as discussed earlier. Hence, it strongly indicates that convection was the major cause of layer structure formation. The fundamental concept behind the present theory is that the complex peritectic microstructure development in the convective regime is a result of the steady or time dependent lateral segregation of solute at the interface and the possibility of formation and growth of two phases at the same interface. In the following paragraphs we shall elaborate this concept.

For simplicity we consider solidification inside a two dimensional rectangular vertical slot in which x and y are the vertical and horizontal coordinates. The bottom

horizontal wall is the instantaneous solid-liquid interface growing in the positive x direction, while gravity vector acts in the negative x direction. The vertical walls are rigid solid walls maintained at prescribed temperatures and impervious to mass flux. The temperatures of both the vertical walls increase linearly upwards with a gradient G_x . However a small but finite temperature gradient G_y is assumed to exist between the two vertical walls to model the real experimental imperfection. The horizontal temperature gradient is responsible for initiating the convective flow which is interfered cooperatively (i.e. the thermal and the solutal buoyancies acting in the same direction) or uncooperatively (i.e. the thermal and the solutal buoyancies acting in the opposite directions) with the solute composition gradient after a certain lapse of time. Although the exact dynamics of thermo-solutal convection can be highly complex, the general effect of the flow is to establish a horizontal composition gradient at the interface. For example if we consider flow driven by a horizontal thermal gradient alone, the direction of flow is usually up along the hot wall and down along the cold wall. This establishes an almost parallel flow along the interface (except near the corners) from the cold side towards the hot side. Such a flow causes lateral segregation or nonhomogeneity of solute composition at the interface (and also in the melt). In general, the region near the warmer wall gets richer in solute [23, 41-43, 53]. The schematic liquid composition profiles along the interface are shown in Fig. 5a for three different times, with $\tau_1 < \tau_2 < \tau_3$. The solute profile at τ_1 intersects the peritectic composition C_p at a point $P(\tau_1)$ at a distance $R(\tau_1)$ from the colder wall. At the point $P(\tau_1)$ the three phases are in contact and in local equilibrium. Since the composition of the liquid is greater than the peritectic composition C_p in the region $y > R(\tau_1)$, and the composition of the liquid is less than C_p in the region $y < R(\tau_1)$, the β phase will be present in the region $y > R(\tau_1)$ and the α phase will exist over the region $y < R(\tau_1)$. As solidification proceeds, more and more solute is rejected from the interface and the interface composition increases as shown by the schematic curves for times τ_2 and τ_3 in Fig. 5a. Thus, the point $P(\tau_i)$ gradually moves towards the colder side or the distance $R(\tau_i)$ monotonically decreases with time. Since, the point $P(\tau_i)$ also has a

velocity component in the vertical x direction due to the constant growth rate V_p , the locus of $P(\tau_i)$ will delineate a smooth curve in the solidified sample and appear as a curved interface between the two solid phases α and β , as shown schematically in Fig. 5b. For a cylindrical geometry, this curve will appear as a surface of revolution separating the two solid phases. In order to support our mechanistic model, composition measurements were performed on a sample grown inside a 6 mm ampoule. The microstructure consisted of α growing as a continuous tree-like structure at the center surrounded by the β phase. At a particular axial position the composition is measured at different points from the center to the edge of the sample to obtain the radial composition profile. The solid phase compositions thus obtained, are then converted to the corresponding liquid phase compositions (dividing the α phase composition by k_α , and dividing the β phase composition by k_β). The radial composition profile is plotted in Fig. 6. The α phase spanned ~ 1.2 mm from the center towards the edge where the composition was less than the peritectic composition (C_p). The rest of the cross-section near the edge of the sample was occupied by β phase where the composition was higher than C_p . The high radial segregation and the simultaneous growth of the two solid phases at the same interface are obvious and consistent with the mechanistic model developed here.

During the solidification of large diameter samples (> 3 mm) of binary alloys, the steady convection may become unstable and oscillatory, or quasi-periodic convection may set in [23,41-43]. The velocity, temperature and composition field oscillates in a periodic or quasi-periodic manner, and, hence, the composition profile at the interface may have a complex time-dependent behavior. This, in turn, will cause a periodic or quasi-periodic fluctuating motion of $P(\tau_i)$ in the y direction while being displaced at a constant rate of V_p along the vertical direction. Hence, the locus of $P(\tau_i)$ in the solidified sample will now delineate a curve that may look like *an Oscillating Layered Structure* with arms stretching out in the horizontal direction. This is schematically demonstrated in Fig. 7. The four stages of the layered structure formation are illustrated in this sequence. The solid-liquid

interface remains planar at all times, while the solid-solid interface between α and β (locus of the triple point $P(\tau)$) assumes an oscillating structure. The length and thickness of the arms or layers will depend on the detailed characteristics of the convective fluctuations and the growth velocity. Again in a cylindrical geometry this locus will be a surface of revolution and will appear as a 3 dimensional tree-like structure. We expect to see similar structures in situations where convection is oscillatory, as in ampoules of diameter ~ 6 mm.

The model is for high G/V_p ratio, where the planar interface growth is predicted for both the α and β phases. We thus assume that the interface is planar, and remains planar when the two phases form and grow. We also assume that the curvature of the interface due to convection is negligible. In order to examine the validity of this assumption, experiments were conducted in which the samples were quenched when partial oscillating structure was formed and the shape of the interface was observed [43]. A typical picture is shown in Fig. 8. A planar two-phase interface with α and β growing together was observed in all experiments [43] in accordance with the mechanism proposed here. No appreciable curvature of the interface was observed.

V. COMPUTATIONAL MODEL

The exact details of the flow and its effect on the shape of the α - β interface could be accurately modeled only through full scale numerical simulation of the vertical Bridgman system. This involves multi-scale modeling of heat transfer between furnace, ampoule, melt and solid crystal; and simultaneous computation of thermal, velocity, and composition fields in the melt ; and the phase change during solidification [23]. The method and analysis for the full scale simulation are complex so that a conceptual model is developed here which has the qualitative features of the full scale model and is successful in predicting many of the complex microstructures.

A. Mathematical Model

The present model solves the advection-diffusion equation for solute transport with *prototype flows* to model the advection terms pertinent to steady and unsteady convection [45]. It is assumed that the interface always moves with the constant growth velocity V_p . It is also assumed that the solid-liquid interface always remains planar and perpendicular to the growth direction. Molecular diffusion in the solid phase is neglected. The solute transport equation written in terms of a reference frame fixed at the uniformly moving interface is

$$\frac{\partial C}{\partial t} + (u - V_p) \frac{\partial C}{\partial x} + v \frac{\partial C}{\partial y} = D \left(\frac{\partial^2 C}{\partial x^2} + \frac{\partial^2 C}{\partial y^2} \right) \quad (1)$$

where u and v are the components of fluid velocity along the x and y directions respectively, V_p is the interface velocity and D is the solute diffusivity. The boundary condition at the solid liquid interface is given by the flux balance condition

$$\begin{aligned} \text{at } x = 0, \quad V_p C(k_v - 1) = D \frac{\partial C}{\partial x}, \quad v = \alpha \text{ if } C < C_1^m \\ v = \beta \text{ if } C > C_1^M \end{aligned} \quad (2)$$

The subscript v indicates a specific solid phase. For a single solid phase, nucleation is required to form the other phase. When the liquid composition at any point on the interface falls between C_1^m and C_1^M (see Fig. 3), the phase is selected from the direction of the composition variation at that point. If the composition is increasing from below C_1^m the point remains as α phase until it crosses C_1^M , whereas the point remains as β phase as the composition decreases from above C_1^M until it reaches C_1^m . When two solid phases are present, the condition of equation (2) is modified as: $v = \alpha$ if $C < C_p$, and $v = \beta$ if $C > C_p$.

The boundary condition at the vertical solid walls are the no-flux conditions,

$$\frac{\partial C}{\partial y} = 0 \text{ at } y = d, \text{ and at } y = 0 \quad (3)$$

The boundary condition at the end of the computational domain is given by [11,14-16, 36]:

$$D \frac{\partial C}{\partial x} = V_p (C - C_0), \text{ at } x = L \quad (4)$$

The initial condition is that of a homogeneous melt,

$$C = C_0, \text{ at } t = 0, \text{ for all } x, y \quad (5)$$

B. Convective Velocity Components

The values of u and v are varied to explore how the solute redistribution due to different degrees of convection influences the shape formation of the α - β interface.

B-1: Diffusion Dominated Transport

At the limit of minimal convection ($U_c \ll V_p$, where $U_c = \max |u(x,y), v(x,y)|$) the transport equation takes the form of a one dimensional diffusion equation pertaining to directional solidification [47]. This can be seen by setting u and v equal to zero and dropping the derivatives with respect to y in equation (1).

B-2: Steady Convection

In the case of steady convection, the components u and v are functions of the spatial coordinates x and y only and vary with the Rayleigh Number. The functional forms are obtained from an analytical expression given by Batchelor [24] for convective flow within a two dimensional cavity with differentially heated vertical walls. The solution has a simple closed functional form and is easy to implement in a numerical algorithm. While presenting the results we shall use the parameter U_c/V_p as a measure of the relative degree of convection and diffusion. Proper choice of Rayleigh number in the analytical model [24] is

made so that the convective velocity components have the same order of magnitude as found in the numerical model [41].

B-3 : Unsteady Convection

To model unsteady convection in the melt, a normal mode type finite oscillation [48] is superimposed on the steady state base flows, leading to the forms

$$\begin{aligned} u(x, y, t) &= u_s (1 + \varepsilon \sin 2\pi ft) \\ v(x, y, t) &= v_s (1 + \varepsilon \sin 2\pi ft) \end{aligned} \tag{6}$$

where ε and f are the fractional amplitude and frequency (cycles/sec) of the oscillation, and u_s and v_s are steady base flow components of Batchelor [24]. The values of ε and f commensurate with those observed in the numerical simulation [23,43] are used in this simplified model.

C. Numerical Analysis

The set of equations are solved by the Alternate Direction Implicit (ADI) Finite Difference Method [49,50] on a uniform Cartesian grid. The grid spacings are kept small enough to accurately resolve any sharp concentration gradients. This requires that the cell Peclet numbers satisfy the following conditions at each grid point [51].

$$\begin{aligned} \frac{(u - V_p)\Delta x}{D} &< 0.1 \\ \frac{v\Delta y}{D} &< 0.1 \end{aligned} \tag{7}$$

where Δx and Δy are the grid spacings in x and y directions. The method is unconditionally stable and allows the use of large time steps. However, time steps less than at least one tenth

of the time period of imposed oscillation are used to appropriately resolve the transient effects.

VI. RESULTS

The results are presented mainly in terms of plots of composition profiles, the shape of the α - β interface, and 2D color-coded composition field-maps in the solid phase. The results are classified in three regimes depending on the degree and mode of convection.

A. Diffusive Transport, $Uc/Vp \sim 0$; Limiting Case of Zero Convection

In the case of zero convection, the numerical model closely reproduces the predictions of the diffusive model [6]. A regular *banded* microstructure is observed for initial compositions within the *banding window*. A typical microstructure and the corresponding solid phase composition profile are shown in Fig. 9. The computation was done with $C_0=0.8\%$, $\Delta T_n^\alpha = \Delta T_n^\beta = 0.2$, $V_p = 1.0 \mu\text{m}/\text{sec}$. The typical dynamics involves an initial α phase where composition increases until it reaches $k_\alpha C_l^M$, followed by nucleation and subsequent growth of the β phase until the composition reaches $k_\beta C_l^m$, followed by repetition of these two events. The actual composition profiles from the finite difference models are close to those predicted by the analytical models [5,6]. The reciprocals of the layer thickness (λ_α , λ_β) are plotted against growth velocity in Fig. 10 for $C_0 = 0.8\%$, $\Delta T_n^\alpha = \Delta T_n^\beta = 0.2$. The layer thickness is found to be inversely proportional to the growth velocity. The band spacings also are strong functions of the nucleation undercoolings of individual phases as shown in Fig. 11. During actual experiments, if several potent nucleation sites are present, the undercooling values will not remain constant for each nucleation event, so that a nonuniformly spaced banded structure would result even in a purely diffusive system. The result for diffusive banding is summarized in Fig. 12. The plots are actually 2D maps of composition fields in the solid phase. The composition field

belonging to the α phase is filled with gray to graphically mimic the experimental micrographs. All the computations in this sequence are done with α and β undercoolings of 0.2 and 0.2 K, respectively. For these nucleation undercoolings, the banding window is $0.65 < C_0 < 0.89$. When the initial composition is $C_0=0.8$, finite bands of α and β form (Fig. 12 a). For compositions outside the banding window, only one α to β transition takes place (Fig. 12 b, c), and the solid fraction of α increases with decreasing growth rate.

B. Steady Convection , $Uc/V_p \sim 1-10$

The effect of steady convective flow on the solute redistribution along the interface is illustrated in Fig. 13. The computation is done for $V_p = 4.0 \mu\text{m}/\text{sec}$, $Uc/V_p \sim 10$ and $C_0 = 1.4$ wt %. The instantaneous interface compositions at different time levels are plotted with respect to the lateral coordinate y . The numbers next to the curves indicate the nondimensional time level from the start of solidification. The time scale used for dimensional scaling is $D/(V_p)^2$. The vertical lines $y = 0$ and $y = 0.2$ are the colder and hotter vertical walls, respectively. Hence, the general direction of the flow is counter-clockwise. The lateral solute segregation and the piling up of solute near the hotter wall is obvious from the plots. The horizontal dashed lines $C = 3.9$ and $C = 3.7$ are the $\alpha \rightarrow \beta$ transition composition C_1^M and $\beta \rightarrow \alpha$ transition composition C_1^m respectively. Until $t = 1.5$, the composition at every point on the interface was below C_1^M and hence the surface was completely covered with the α phase. At $t \sim 1.6$ the composition near $y = d$ reaches C_1^M and nucleation and growth of β is initiated. The simultaneous growth of α and β continues until the composition at every point on the interface increases beyond C_p . The locus of the three phase point P that appears as the interface between α and β is plotted in Fig. 14, along with the liquid composition at two end points ($y = 0$ and $y = d$) on the interface. The liquid compositions at $y = d$ and $y = 0$ reached C_1^M and C_p at $x \sim 0.08$ cm and 0.34 cm respectively (Fig. 14b) which appear as the $\alpha \rightarrow \beta$ transition points on Fig. 14a. The effect of steady convection is mainly in establishing curvature on the shape of the α - β interface. The effect

of different degrees of steady convection is summarized in Fig. 15 (a,b,c). All the computations are done with the initial composition $C_0 = 1.4\%$, $V_p = 4.0 \mu\text{m}/\text{sec}$ and α , β undercoolings of 0.1K each. Within the range of $(0.5 < U_c/V_p < 10)$, a higher degree of convection leads to a more pronounced curvature in the $\alpha \rightarrow \beta$ interface and a longer initial α core. This is expected since a stronger steady convection (within the range mentioned) causes greater radial segregation of interface composition and takes longer time between the two end points on the interface to cross the C_1^M line (Fig. 13).

C. Unsteady Convection , $U_c/V_p \geq 100$

The effect of simple oscillatory convection on the $\alpha \rightarrow \beta$ interface is illustrated in Fig. 16 along with the liquid composition at two end points ($y=0$ and $y = d$) at the interface. The computation is done with $C_0=1.4\%$, $V_p = 1.4\mu/\text{sec}$, α and β undercoolings of $0.1 \text{ }^\circ\text{C}$ each, $U_c/V_p = 100$, frequency of oscillation $f = 0.004 \text{ Hz}$, and fractional amplitude $\varepsilon = 0.5$. The composition at $y = d$ reaches C_1^M at $x \sim 0.05 \text{ cm}$ and keeps increasing (Fig. 16 b). The same behavior is observed for other points near $y = d$, though each point had different transition distances. Hence, near the edge $y = d$, the β phase is continuous along the length of the sample (Fig. 16 a). On the other hand, the composition at $y = 0$ shows multiple transitions of $\alpha \rightarrow \beta$ and $\beta \rightarrow \alpha$ as the composition fluctuates above and below C_1^M and C_1^m , respectively, until the composition increases to a value where it does not get below C_1^m thereafter ($x \sim 0.65$). This appears as oscillatory layers of α and β along the length of the sample at $y = 0$ (Fig. 16 a), until continuous growth of β phase completely takes over. Other points between $y = 0$ and $y = d$ show similar behavior but with different phases. The locus of the triple point delineates an oscillatory layered structure where α phase appears to grow as a tree in the continuous β matrix. The layers have the eye shape which is thick at the center and tapers down at the edges. The layers do not extend over the entire cross section and the lateral width and axial thickness gradually decrease along the length of the sample.

In Fig. 17 we summarize the result for oscillating convection. All the computations are done with $V_p = 4.0 \mu\text{m}/\text{sec}$, $U_c/V_p \sim 100$, $\Delta T_n^\alpha = \Delta T_n^\beta = 0.1$, but with different C_0 and frequency of oscillation f . For $C_0=1.2$ (Fig. 17 a), a long and sustained layered structure is observed over the entire domain of interest (4 cm), whereas for $C_0=1.5$ the α layers decay within 1.5 cm of the solidified sample (Fig. 17 b). The effect of the oscillating frequency is shown in Figure 17 c. All the parameters are kept the same as in Fig. 17 (a), while f is changed from 0.005 to .0025 Hz. The increase in the thickness and spacings of layers is obvious.

VII. DISCUSSION

The physical concepts developed in this paper and the subsequent numerical computations provide new insights into the formation of complex microstructures during plane-front solidification of peritectic alloys. Most of the experimental observations are predicted by this model. (i) the α layers are interconnected over a considerable distance along the sample, (ii) the β matrix is continuous, (iii) the layered structure can occur for compositions greater than the upper limit of the *banding window* including the hyperperitectic region, (iv) the α layers do not extend over the entire cross-section of the sample, and (v) the number of finite layers of α depends on the initial composition.

The first of these effects is clearly seen in Fig. 17. All the figures in this sequence show an initial region of continuous α core with oscillating side-branches. Within this region, the planar interface is always occupied by both the α and β phases. This is due to the fact that the interface liquid composition falls on either sides of the peritectic composition due to radial segregation induced by convection. However, the fractional area covered by the respective phases changes with time due to continuous rejection of solute at the interface and convective-diffusive transport. In the case of steady convection, the fractional area occupied by the α phase smoothly decreases to zero until the interface gets completely covered by the

β phase (Fig. 14, 15). For oscillating convection, the fractional area occupied by the α phase undergoes an oscillatory decay. After the initial oscillatory decay to a vanishing α -fraction, the interface is completely covered by the β phase. However, composition fluctuations can again bring the concentration below C_i^m and hence α phase may re-nucleate and grow. In this case, α layers appear as isolated *islands* in the continuous β matrix. It should be noted that the mechanism for the formation of these *isolated islands* is significantly different from the *isolated bands* formed by the diffusive growth [6]. In actual experiments [8], the connectivity of the α phase seems to persist for a much longer distance than that predicted by the present model. This can be due to two reasons. Since, the experiments are done in cylindrical samples, any temperature gradient across the diameter due to imperfection also establishes an angular variation of temperature. This not only causes a swirling component of the convective velocity, but also angular variations of composition, velocity, and temperature. The real three-dimensional nature of the dynamics may be significantly more complex than in the 2D analysis of the present model. The connectivity of the α phase in the angular direction cannot be captured in the present model. The second reason, is perhaps due to the choice of a single mode of oscillation for the entire flow field.

The continuity of the β matrix is obvious from the computed results in Fig. 16 and Fig. 17. These results also demonstrate that complex layered structures can indeed form for initial compositions greater than the maximum composition of the *banding window* including the hyperperitectic region. The α layers did not laterally span across the entire cross-section of the sample due to the two dimensional nature of the solute segregation profile. The number of finite α layers depend on the initial composition. The closer C_0 is to the peritectic composition C_p , the fewer is the number of finite layers formed, since the phase transition from α to β can take place earlier. None of these features observed experimentally, and explained by the present model, were predicted by the existing diffusive [6] and/or boundary layer models [5].

The fundamental difference between the present model and the existing models is in that the previous models explored the inherent oscillatory dynamics of repeated nucleation and growth of two phases, which put stringent conditions on the initial composition. The present model proposes that the complex layered structures observed experimentally and misinterpreted as *discrete bands* [1-5], are the results of oscillating fluid flow. Hence, no strict constraint is necessary for the initial composition, i.e., there is no analog of a banding window.

We have examined the effect of steady and oscillatory convection on the microstructure development in peritectic systems. However, similar mechanisms may be operative in other systems in which the radial composition variation can cause the formation of steeping or another phase, such as an eutectic, near the walls of the ampoule [52-53].

VIII. CONCLUSION

Experimental results in Sn-Cd and Pb-Bi alloys have been presented that show complex microstructure development in the presence of convection. A distinction has been made between *band structures* and *oscillating layered structures*. A physical mechanism for microstructure formation is developed which is later supported by a numerical model that solved the advection-diffusion equation. The advection terms were modeled by *prototype flows*, where the intensity of the flow, the frequency and amplitude of flow oscillations are externally imposed [45]. A rigorous simulation of the Bridgman process, that includes heat transfer from the furnace, conduction through ampoule and crystal, conduction and thermo-solutal convection in melt, and predicts the actual flow patterns and all possible modes of oscillations is now required to quantitatively predict the dominant mode of oscillation, and thus the spacing between the branches under given growth conditions. This rigorous simulation is presently being pursued [43].

The main finding of the present work is that the so called *band structures* observed in experiments [1-5] are actually *oscillating layered structures* which form due to an

oscillatory fluid flow. Two different regimes of convection have been examined: steady convective and unsteady convective regimes, and physical mechanisms that lead to morphological development under these conditions have been developed. In the steady convective regime, the primary α -phase transforms into the peritectic β -phase with a curved $\alpha:\beta$ interface. In the presence of oscillating convection, the model shows the formation of a tree-like shape of the primary phase, as observed experimentally. In the limiting condition of zero convection (or solidification in thin tubes) the present model predicts the formation of a *banded* structure within a narrow range of alloy composition in the hypoperitectic region, in agreement with the diffusive model [6].

ACKNOWLEDGMENT

This research was supported in part by the NASA Microgravity Science and Applications Division under Grant NAG8-1254. This work was supported in part and carried out at the Ames Laboratory, which is operated for the U. S. Department of Energy by Iowa State University, under contract no. W-7405-Eng-82, supported by the director of Energy Research, Office of Basis Energy Sciences. Appreciation is expressed to J. S. Park for providing us with experimental results prior to their publication.

REFERENCES

1. W. J. Boettinger: *Metall. Trans.*, 1974, vol.5, pp. 2023-31.
2. H. D. Brody and S. A. David: *Int. Conf. Solidification and Casting*, Institute of Metals, London, 1977, vol.1, pp144-51.
3. A. P. Titchener and J. A. Spittle: *Acta Metall.*, 1957, vol. 23, pp 497-502.
4. B. C. Fuh, Ph. D Thesis, Iowa State University, Ames, IA, 1984

5. A. Karma, W. J. Rappel, B. C. Fuh, R. Trivedi, *Metall. Mat. Trans.* , 1998, vol. 29A, pp.1457-70
6. R. Trivedi, *Metall. Mat. Trans.*, 1995, vol. 26A, pp. 1583-90.
7. K. Zeishler-Mashl and T. Lograsso, *Metall. Mat. Trans.*, 1997, vol. 28A, pp.1543-52.
8. J. S. Park and R. Trivedi, *J. Cryst. Growth*, 1998, vol.187, pp. 511-515
9. H. W. Kerr and W. Kurz. *Int. Mat. Rev.*, 1996, vol. 41, pp. 129-165.
10. R. Trivedi, H. Miyahara, P. Mazumder, S. Tiwari, submitted to *Met. Trans.*
11. G. B. McFadden, R. G. Rehm, S. R. Coriell, W. Chuck and K. A. Morrish, *Metall. Trans.*, 1984, vol. 15A, pp.2125-37.
12. G. B. Mcfadden and S. R. Coriell, *Phys. Fluids*, 1986, vol. 30, pp. 659-71.
13. R. J. Naumann, *J. Cryst. Growth*, 1982, vol. 58, p. 589
14. C. J. Chang and R. A. Brown, *J. Cryst. Growth*, 1983, vol. 63, pp. 343-65.
15. P. M. Adornato and R. A. Brown, *J. Cryst. Growth*, 1987, vol. 80, pp.155-90
16. D. H. Kim and R. A. Brown, *J. Cryst. Growth*. 1989, vol. 58, pp.609-627.
17. R. A. Brown, *AIChE Journal*. 1988, vol. 34, pp.881-911
18. J. I. D. Alexander, J. Ouazzani, and F. Rosenberger, *J. Cryst. Growth*, 1989, vol. 97, pp.285-302
19. S. Kappurao, S. Brandon, and J. Derby, *J. Cryst. Growth*, 1995, vol. 155, pp.93-102.
20. S. Kaddeche, J. P. garandet, C. barat, H. Ben Hadid, and D. Henry, *J. Cryst. Growth*, 1996, vol. 158, pp. 144-152
21. H. Ouyang and W Shyy, *J. Cryst. Growth*, 1997, vol. 173, pp. 352-366
22. H. Zhang, L. L. Zhang, V. Prasad and D. J. Larson, Jr. *Journal of Heat Transfer*, 1998, vol. 120, pp. 865-873
23. P. Mazumder, PhD Thesis, Iowa State University, Ames, 1999
24. G. K. Batchelor, *Quart. Appl. Math.* 1954, vol. 12, pp 209-33
25. D. J. Tritton, *Physical Fluid Dynamics*, , Oxford Science Publications (1988) p. 35.
26. D. T. J. Hurle, E. Jakeman, C. P. Johnson, *J. Fluid Mech.*, 1974, vol. 64, pp. 565-576

27. M. G. Braunsfurth and T. Mullin, *J. Fluid Mech.*, 1996, vol. 327, pp. 199-219
28. M. A. Azouni , *PhysicoChemical Hydrodynamics*, 1981, vol. 2, pp295-309
29. B. Roux *numerical Simulation of Oscillatory Convection in Low Pr Fluids*, Vieweg, Braunschweig, 1990.
30. A. C. Skeldon, D.S. Riley, K.A. Cliffe, *J. Crystal Growth*, 1996, vol. 162, pp. 95-106
31. K. H. Winters, *Int. J. Numer. Methods Fluids.*, 1988, Vol. 25, pp. 401-414
32. J. P. Pulicani, E.C. Del Arco, A. Randriamampianina, Bontoux and R. Peyret, *Int. J. Numer. Methods Fluids*, 1989, vol. 10, pp. 481-517
33. E. C. Del Arco, J.P. Pulicani, P. Bontoux, *PhysicoChemical Hydrodynamics*, 1989, vol. 11, pp. 681-692
34. R. Selver, Y. Kamotani and S. Ostrach, *Journal of Heat Transfer*, 1998, vol. 120, pp. 108-114
35. C. W. Lan, M. K. Chen and M. C. Liang, *J. Crystal Growth*. 1998, vol. 187, pp. 303-313
36. M. J. Crochet. F. T. Geyling and J. J. V. Schaftingen, *J. Crystal Growth*, 1983. vol. 65. pp. 166-172
37. M. T. Hyun, D. C. Kuo, T. L. Bergman, and K. S. Ball, *Numer. Heat Transfer*, 1995. vol. 27, pp. 639-50.
38. T. L. Bergman and M. T. Hyun, *Int. J. heat Mass Transfer*, 1996, vol. 39, pp. 2883-93
39. T. Nishimura, M. Wakamatsu and A Morega, *Int. J. Heat mass Transfer*, 1998, vol. 41, pp. 1601-11
40. K. Ghorayeb, H. Khallouf, and A. Mojtabi, *Int. J. Heat mass Transfer*, 1999, vol. 42, pp. 629-643
41. P. Mazumder, R. Trivedi, A. Karma 1998, *Proceedings MRS*, eds. E. Ma, M. Atzmon, P. Bellon, R. Trivedi, vol. 481, pp. 39-44
42. P. Mazumder. R. Trivedi, in *Fluid Flow Phenomena in Metals Processing*, eds. N. El-Kaddah, D. G. C. Robertson, S. T. Johansen, and V. R. Voller, 1999, TMS
43. P. Mazumder, R. Trivedi, to be submitted to *J. Fluid Mechanics*

44. J. S. Park and R. Trivedi, Unpublished work, 1997, Iowa State University, Ames, IA.
45. S. H. Davis, in: *Handbook of Crystal Growth*, 1994, Ed. by D. T. J. Hurle, North Holland, Amsterdam, pp. 861-97.
46. J. C. Heinrich, *Comp. Meth. App. Mech. and Engg.*, 1988, vol. 65, pp. 65-88
47. W. A. Tiller, K. A. Jackson, J. W. Rutter and B. Chalmers, *Acta Metall.*, 1953, vol. 1, pp. 428-37.
48. H. Schlichting *Boundary Layer Theory*, McGraw Hill, 1979, Toronto
49. D. W. Peaceman and H. H. Rachford, *J. Soc. Indust. Appl. Math.* 1956, vol 3, p 28.
50. L. Lapidus and G. F. Pinder, *Numerical solution of partial differential equations in science and engineering*, John Wiley & Sons, New York, (1982).
51. C. A. J. Fletcher, *Computational Techniques for Fluid Dynamics*, 1 (1988) 293.
52. J. D. Verhoeven, J.T. Mason and R. Trivedi *Metall. Trans.* , 1986, vol. 17. pp.991-1000
53. R. Trivedi, P. Mazumder, Tiwari S, submitted to *Met. Trans.*

FIGURE CAPTIONS

Figure 1: Schematic Peritectic Phase Diagram.

Figure 2: Typical *band* structures observed upon directional solidification of peritectic alloys (a) Sn-Cd [1] (b) Pb-Bi [5].

Figure 3: One dimensional diffusive model for discrete banding [6] showing: (a) nucleation undercooling and the critical liquid compositions at which transition from one phase to the other take place; (b) *banding cycle* and *banding window*.

Figure 4: Microstructures of directionally solidified Sn-1.4% Cd alloy. (a) Observation of an apparent *banded* structure on a longitudinal section taken below but close to the surface. Sample diameter = 6mm. (b) An oscillating layered structure of α surrounded by β closer to the center. Sample diameter = 6mm. (c) A single α to β transition in a sample of diameter 0.6mm. [8].

Figure 5 : A mechanism of nonplanar interface formation between primary and peritectic solid phases due to solute-segregation along the interface, while the solid-liquid interface remains planar (a) Liquid composition profiles at three time levels. (b) Formation and growth of β - phase from the warmer wall due to the increase of composition beyond the peritectic composition.

Figure 6: Radial liquid composition profile across the sample. The measured solid compositions are then converted to the corresponding liquid phase compositions (dividing by k_α and k_β). The composition profile clearly shows the significant radial segregation across the sample.

Figure 7: A mechanism of *oscillating layered structure* formation due to oscillating segregation profiles at the interface. The four figures represent four different stages of the layered structure formation. The solid-liquid interface is still planar, however the solid-solid interface between primary and peritectic phase fluctuates due to the oscillation of interface composition about the peritectic composition.

Figure 8 : Quenched interface during solidification of Sn-Cd (1.4%) binary alloy. α (darker) and β (lighter) phases are growing together at the same planar interface. The interface doesn't show any appreciable curvature due to convection.

Figure 9 : Prediction of *Band structure* in Sn-0.8%Cd alloys under Diffusive growth conditions, $\Delta T_n^\alpha = \Delta T_n^\beta = 0.2^\circ\text{C}$, $V_p = 1 \mu\text{m}/\text{sec}$. The solid composition profile oscillates between $k_\alpha C_1^M$ and $k_\beta C_1^m$. Discrete bands of α and β repeatedly nucleate and grow in response to the oscillating cycle.

Figure 10 : Linear relationship between the reciprocals of band widths and growth rate indicate that band widths are inversely proportional to growth rate.

Figure 11 : Variation of Band widths as function of nucleation undercoolings as illustrated by axial composition profiles along the sample. $V_p = 2 \mu\text{m}/\text{sec}$, $C_0 = 0.8\%$.

Figure 12 : Summary of Diffusive Bands as functions of initial composition and growth rate (a) $C_0 = 0.8\%$, $V_p = 4 \mu\text{m}/\text{sec}$. (b) $C_0 = 0.9\%$, $V_p = 4 \mu\text{m}/\text{sec}$ (c) $C_0 = 0.9\%$, $V_p = 2 \mu\text{m}/\text{sec}$.

Figure 13: Temporal development of composition profiles at interface during solidification. The numbers next to the curves indicate the nondimensional time after the start of solidification. The warmer wall ($y=0.2$) gets richer in solute content due to counter-clockwise convective flow.

Figure 14 : Effect of steady convection on microstructure and composition field. (a) Curved interface development between α and β phases due to lateral solute segregation at the interface (b) Axial composition profile along the edges of the solidified sample The colder wall is at $y=0$ and the warmer wall is at $y=d$.

Figure 15: Summary of the effect of steady convection on curved interface formation between α and β phases. $C_0 = 1.4\%$, $V_p = 4 \mu\text{m}/\text{sec}$, $\Delta T_n^\alpha = \Delta T_n^\beta = 0.1$ (a) $U_c/V_p = 0.2$. (b) $U_c/V_p = 2.0$ (c) $U_c/V_p = 6.0$.

Figure 16 : Effect of oscillatory convection on microstructure and composition field. (a) Oscillating interface development between α and β phases due to oscillatory solute

segregation at the interface (b) Axial composition profiles along the edges of the solidified sample The colder wall is at $y=0$ and the warmer wall is at $y=d$.

Figure 17: Summary of the effect of oscillatory convection on oscillating layered structure formation between α and β phases. $V_p=4\mu\text{m}/\text{sec}$, $\Delta T_n^\alpha=\Delta T_n^\beta=0.1$, $U_c/V_p=52.0$ (a) $C_0=1.2\%$, $f=0.005$ cycles/sec, $\varepsilon=0.7$. (b) $C_0=1.5\%$, $f=0.005$ cycles/sec, $\varepsilon=0.7$ (c) $C_0=1.2\%$, $f=0.0025$ cycles/sec, $\varepsilon=0.7$.

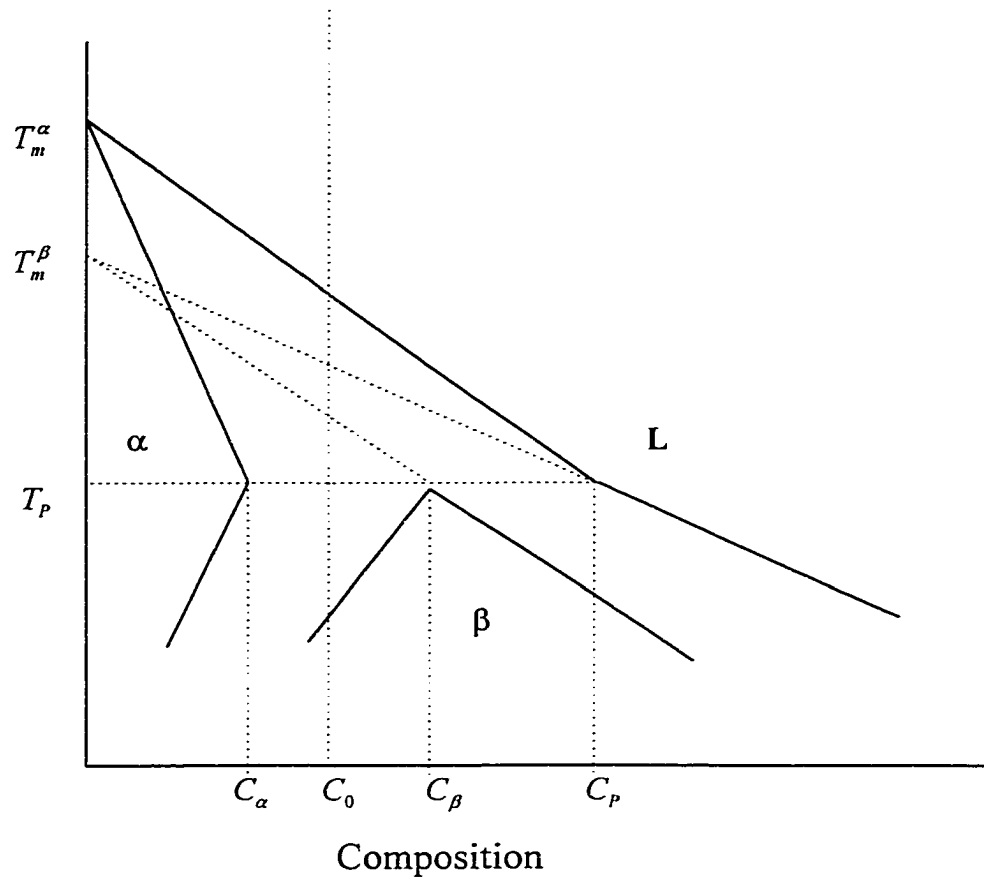


Figure 1: Schematic Peritectic Phase Diagram

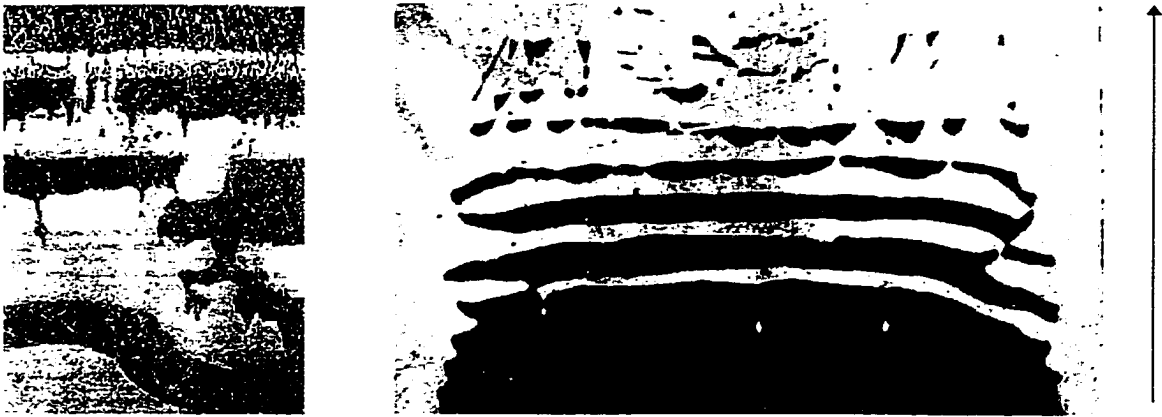


Figure 2: Typical *Band* structures observed on directional solidification of peritectic alloys (a) Sn-Cd [1] (b) Pb-Bi [5]. The arrow shows the growth direction.

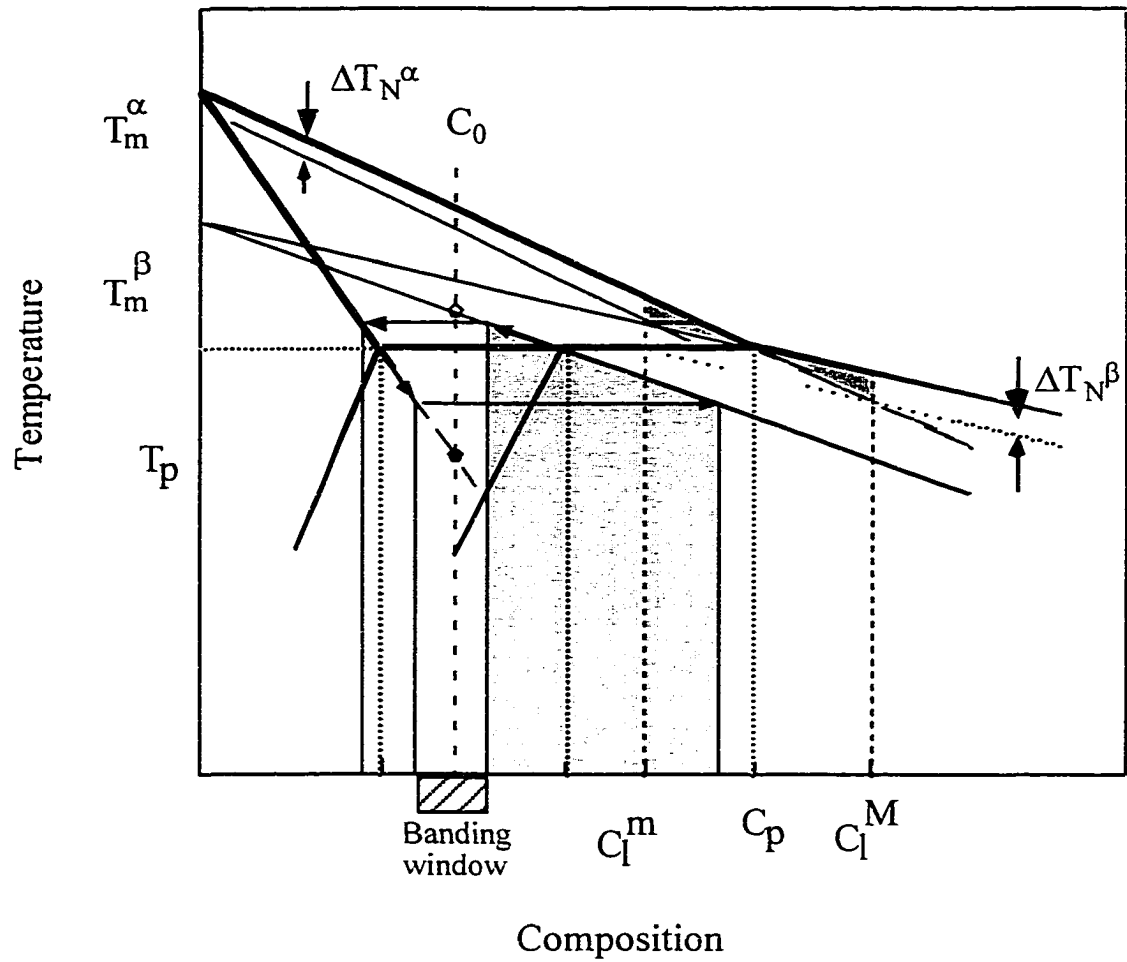


Figure 3: One dimensional diffusive model for discrete banding [6]. Nucleation undercoolings (ΔT_N^α , ΔT_N^β) and the critical liquid compositions (C_l^m , C_l^M), at which transition from one phase to other phase take place, and the *banding cycle* and the *banding window* are shown.

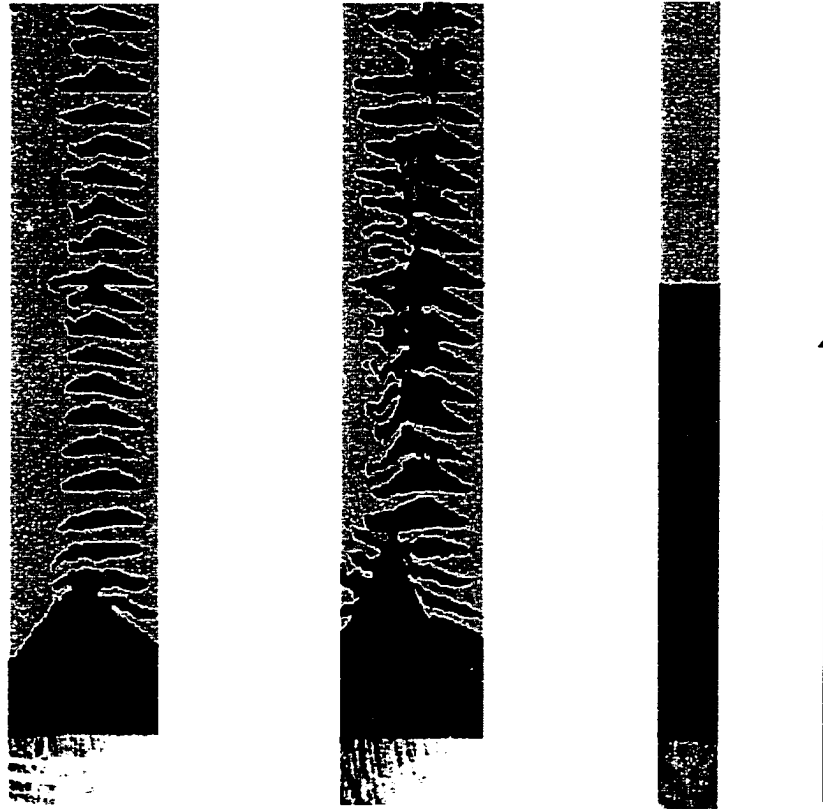


Figure 4: Microstructures of directionally solidified Sn-1.4% Cd alloy. The arrow shows the growth direction. (a) Observation of an apparent *banded* structure on a longitudinal section taken below but close to the surface. Sample diameter = 6mm. (b) An oscillating layered structure of α surrounded by β closer to the center (c) A single α to β transition in a sample of diameter 0.6 mm [8]

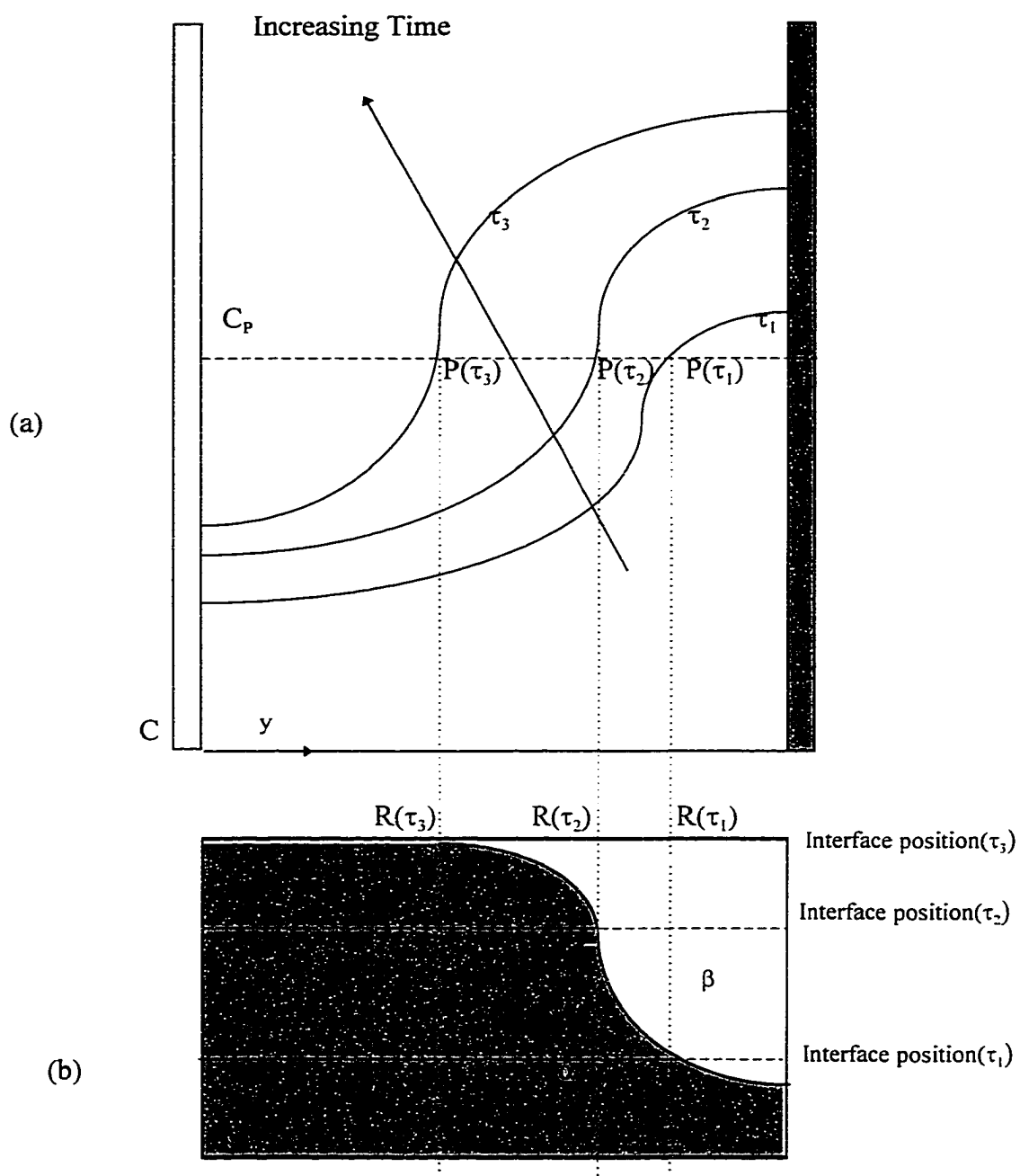


Figure 5: Mechanism of nonplanar interface formation between primary and peritectic solid phases due to solute segregation at interface, while the liquid-solid interface remains planar. (a) Liquid composition profiles at three time levels (b) formation and growth of β phase from the warmer wall due to increase of composition beyond the peritectic composition.

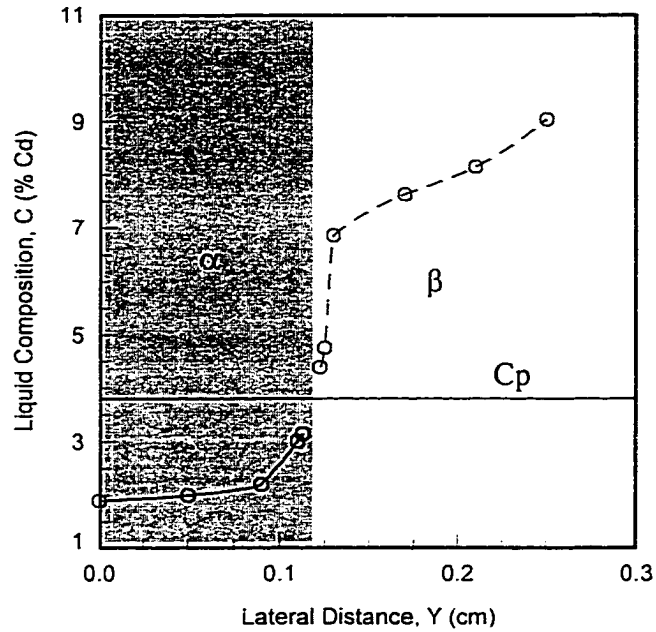


Figure 6: Lateral liquid composition profile across the sample. The measurement is done on a cross-section of the solidified sample. The measured solid compositions are then converted to the corresponding liquid phase compositions (dividing by k_α and k_β respectively). The composition profile clearly shows the significant lateral segregation across the sample.

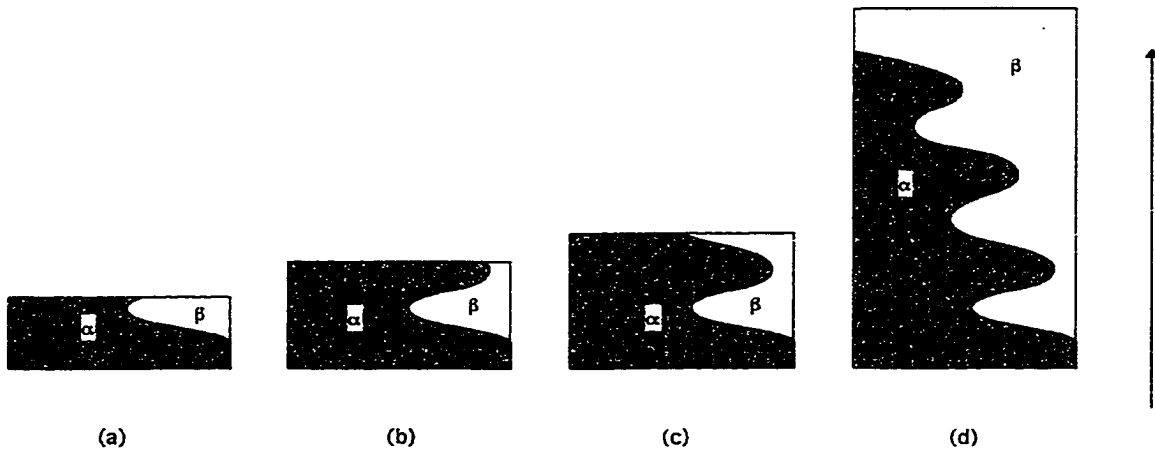


Figure 7: Mechanism of oscillating layered structure formation due to oscillating segregation profile at the interface. The four figures represent four different stages of the layered structure formation. The solid-liquid interface is still planar; however, the solid-solid interface between primary (α) and peritectic (β) phases fluctuates due to oscillation of interface composition about the peritectic composition (C_p). The arrow shows the growth direction.



Figure 8: Quenched interface during the directional solidification of a Sn-Cd (1.4%) binary alloy [44]. Primary α (darker) and peritectic β (lighter) phases are growing simultaneously at the same planar interface. The interface does not show any appreciable curvature. The arrow shows the growth direction. The diameter of the sample is 6 mm.

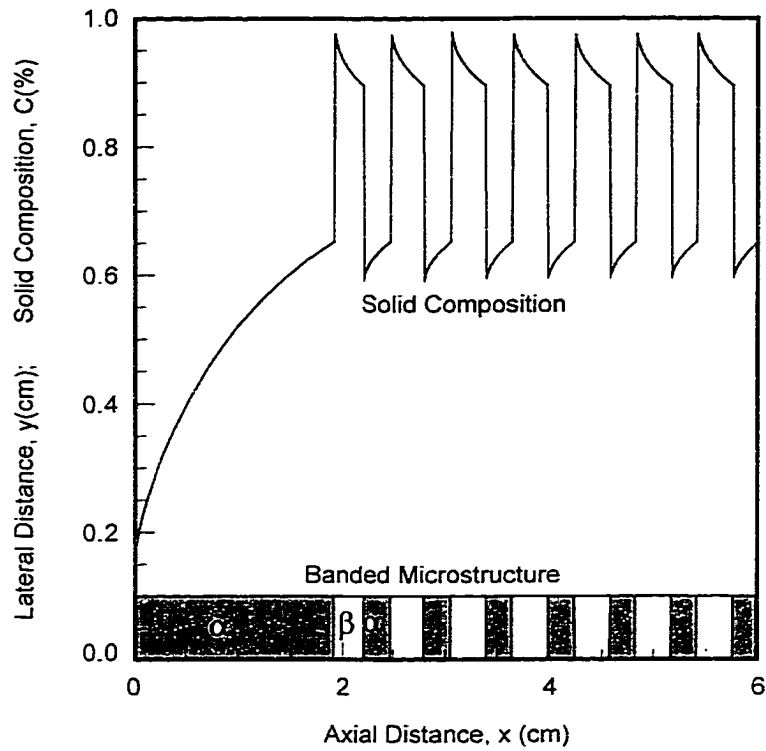


Figure 9: Prediction of *band structure* in Sn-0.8%Cd alloys under diffusive growth conditions, $\Delta T_n^\alpha = \Delta T_n^\beta = 0.2^\circ\text{C}$, $V_p = 1\ \mu\text{m}/\text{sec}$. The solid composition profile oscillates between $k_\alpha C_1^M$ and $k_\beta C_1^m$. Discrete bands of α and β repeatedly nucleate and grow in response to the oscillating cycle.

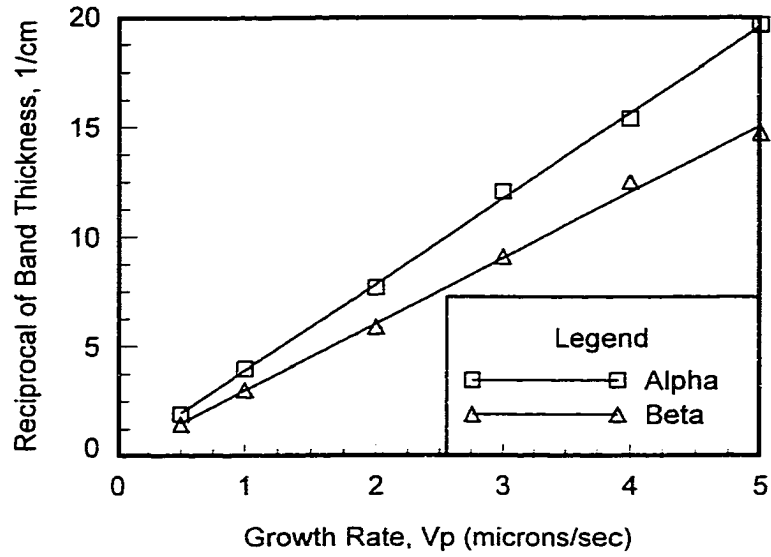


Figure 10: Linear relationship between the reciprocals of band widths and growth rate indicate that band widths are inversely proportional to growth rate.. $C_0 = 0.8 \%$, $\Delta T_n^\alpha = \Delta T_n^\beta = 0.2^\circ\text{c}$

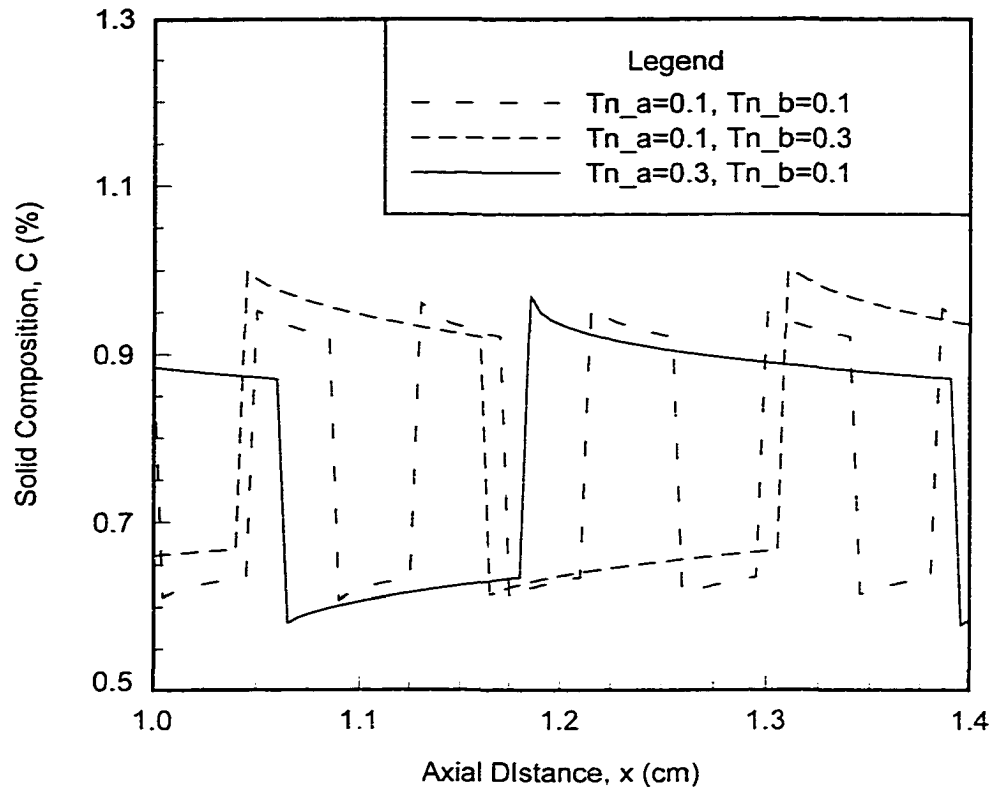


Figure 11: Variation of band widths as a function of nucleation undercoolings as illustrated by the axial composition profiles along the sample. $V_p = 2 \mu\text{m}/\text{sec}$, $C_0 = 0.8\%$.

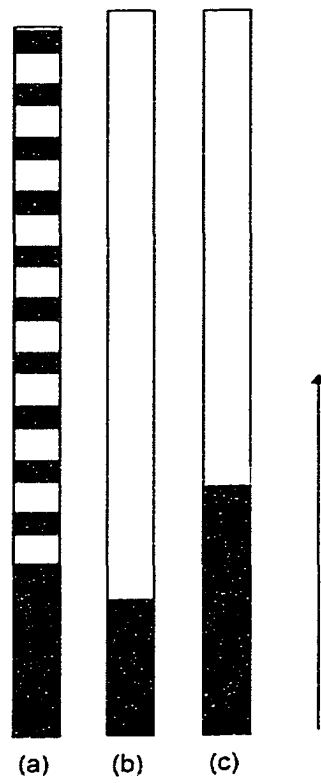


Figure 12: Summary of diffusive bands as functions of initial composition and growth rate (a) $C_0=0.8\%$, $V_p=4\ \mu\text{m}/\text{sec}$. (b) $C_0=0.9\%$, $V_p=4\ \mu\text{m}/\text{sec}$ (c) $C_0=0.9\%$, $V_p=2\ \mu\text{m}/\text{sec}$. The arrow shows the growth direction.

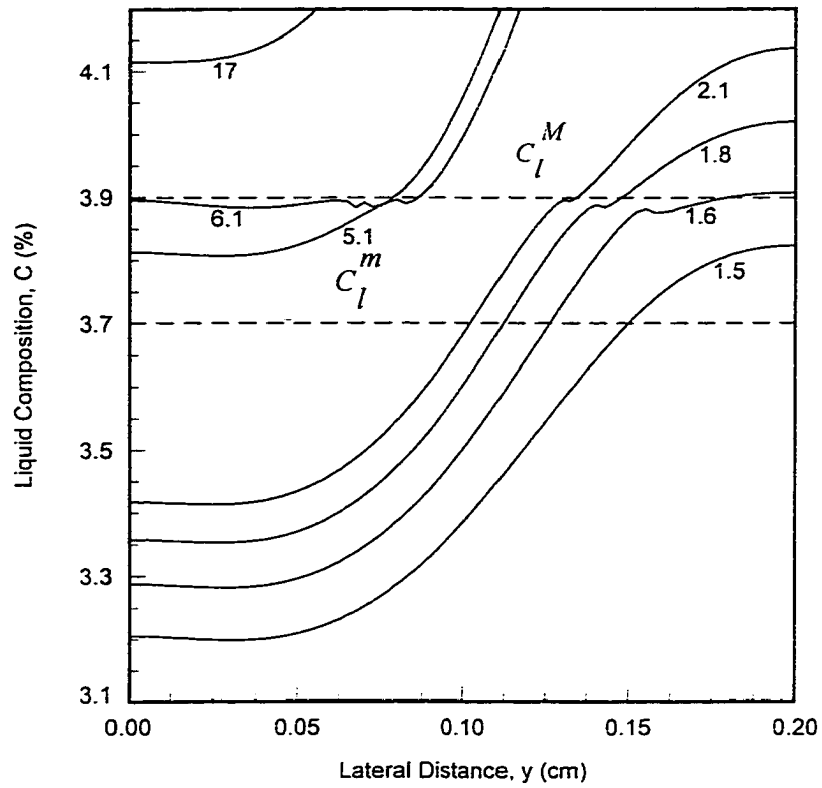


Figure 13: Temporal development of composition profiles at the interface during solidification. The numbers next to the curves indicate the nondimensional time after start of solidification. The warmer wall ($y=0.2$) becomes richer in solute content due to the counter-clockwise convective flow.

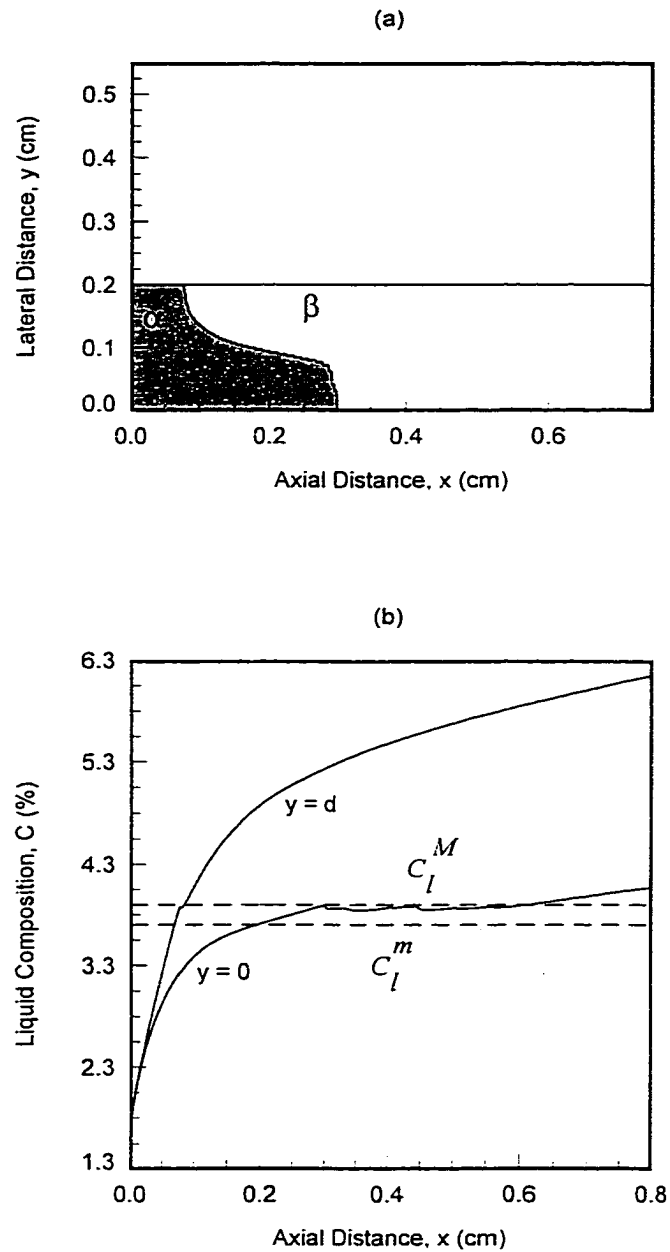


Figure 14: Effect of steady convection on the microstructure and composition field. (a) Curved interface development between α and β phases due to lateral solute segregation at the interface (b) Axial composition profile along the edges of the solidified sample. The colder wall is at $y=0$ and the warmer wall is at $y=d$.

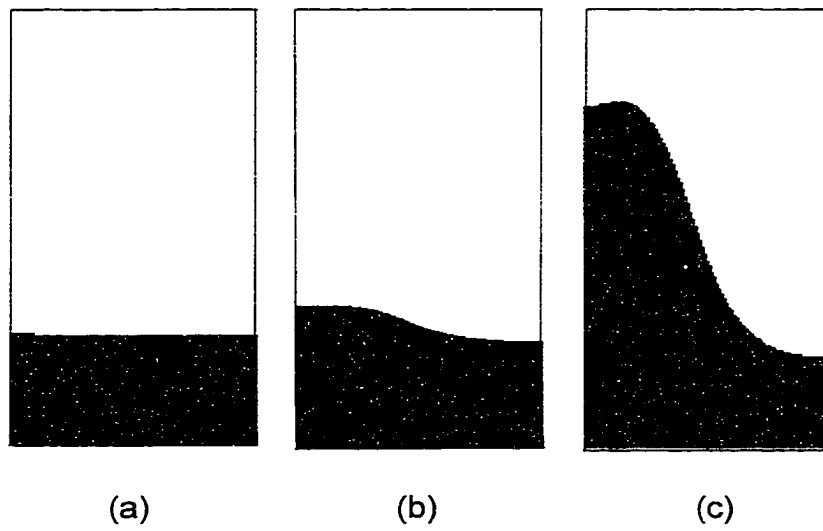


Figure 15: Summary of the effect of steady convection on curved interface formation between α and β phases. $C_0=1.4\%$, $V_p=4\mu\text{m}/\text{sec}$, $\Delta T_n^\alpha=\Delta T_n^\beta=0.1$ (a) $U_c/V_p=0.2$ (b) $U_c/V_p=2.0$ (c) $U_c/V_p=6.0$.

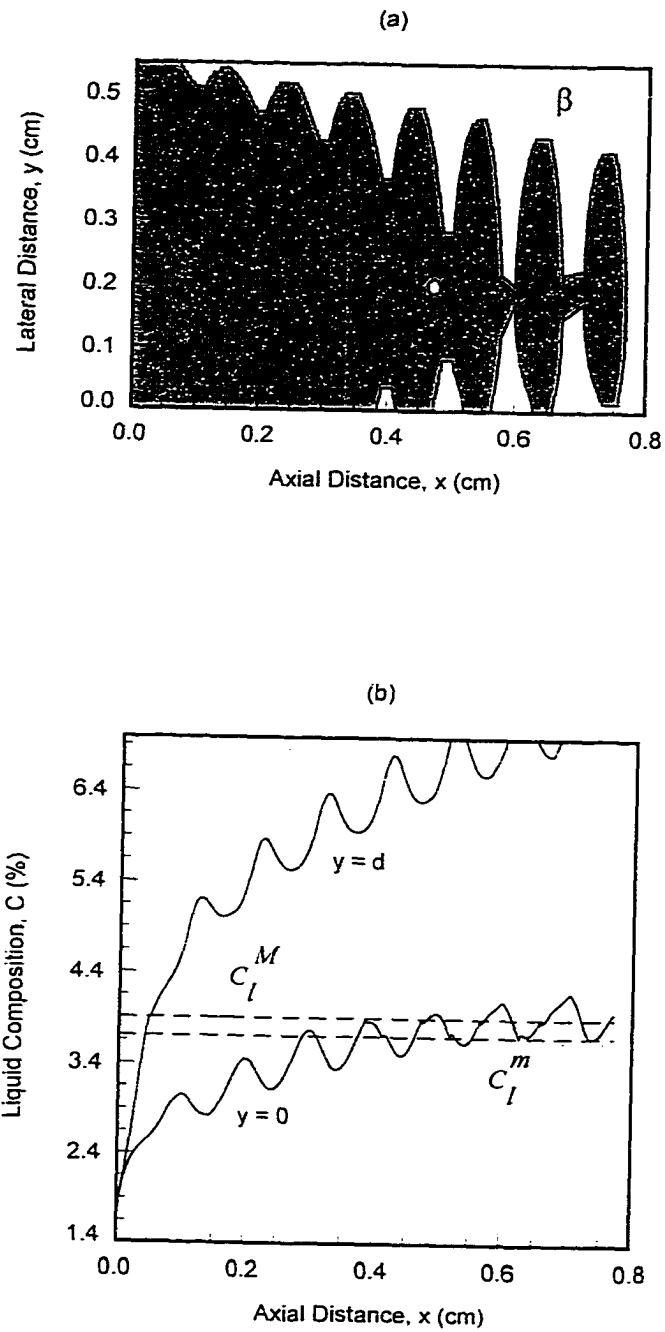


Figure 16: Effect of oscillatory convection on the microstructure and composition field. (a) Oscillating interface development between α and β phases due to oscillatory solute segregation at the interface (b) Axial composition profile along the edges of the solidified sample. The colder wall is at $y=0$ and the warmer wall is at $y=d$.

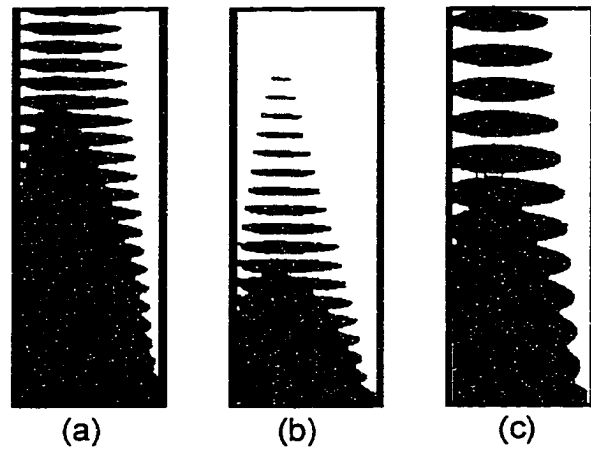


Figure 17: Summary of the effect of oscillatory convection on oscillating layered structure formation between α and β phases. $V_p=4 \mu\text{m}/\text{sec}$, $\Delta T_n^\alpha=\Delta T_n^\beta=0.1$, $U_c/V_p=52.0$ (a) $C_0=1.2\%$, $f=0.005$ cycles/sec, $\varepsilon=0.7$. (b) $C_0=1.5\%$, $f=0.005$ cycles/sec, $\varepsilon=0.7$ (c) $C_0=1.2\%$, $f=0.0025$ cycles/sec, $\varepsilon=0.7$.

CHAPTER 3: MECHANISMS OF LAYER STRUCTURE FORMATION IN PERITECTIC ALLOYS

A paper published in MRS Symposium Proceedings, Volume 481, 1998

P. Mazumder*, R. Trivedi** and A. Karma***

Ames Laboratory US-DOE, Iowa State University, Ames, IA 50011

*Department of Mechanical Engineering, prantik@iastate.edu

**Department of Material Science and Engineering, trivedi@ameslab.gov

*** Department of Physics, Northeastern University, Boston, MA

Abstract

The mechanisms of layer structure formation in the two phase region of peritectic systems are discussed. Under diffusive growth conditions, a banded structure is predicted within a narrow composition range in the hypoperitectic composition. Experimental studies show the formation of an oscillatory structure in the hyperperitectic region. It is shown that this structure is induced by convection in the melt, and it is a novel structure in which a large single tree-like structure of primary phase is surrounded by the peritectic phase. Basic ideas of convection that lead to this tree-like morphology are described.

Introduction

Several experimental studies in the two-phase region of peritectic systems have shown the development of a layered structure in which layers of primary and peritectic phases form alternately along the growth direction [1-3]. Analytical models have recently been developed to explain the mechanism of layer structure formation under the assumption of diffusive growth [4] or strong convective growth which can be described by the boundary layer model [5]. Although these models offered insight into the inherent oscillatory

dynamics of repeated nucleation and growth of two phase solids for idealized situations, they could not explain many of the salient features observed in actual experiments.

A conceptual analytical model of *banding* in peritectic systems was first proposed by Trivedi [4] for diffusive growth in which the change in phases occurred when appropriate nucleation undercooling was reached. The basic concept of Banding Cycle under diffusive growth conditions is illustrated in Fig. 1. According to this model if a melt is solidified from an initially homogeneous composition C_0 , initially the α phase will form and grow, and will tend to approach steady-state condition corresponding to the α -solidus temperature of the alloy, shown as the filled circle in Fig. 1. However, before reaching the steady state, the peritectic β - phase will nucleate when the α -liquidus line intersects the undercooling line for the β -phase nucleation. The solid and liquid compositions at the interface will now vary along the solidus and liquidus lines of β -L equilibrium and tend to approach the steady state solid composition, C_0 , at the β -solidus temperature, shown as an open circle in Fig. 1. But, before reaching the steady state, the primary α -phase may again nucleate on the solid-liquid boundary of β phase when the β liquidus line intersects the undercooling line for the α -phase nucleation. This cycle of alternate nucleation and growth of primary and secondary phases may continue leading to alternate bands of α and β . The major predictions of this diffusive banding model are: the banding cycle will operate below and above the peritectic temperature, the banding window exists only for a narrow composition range, and the band width will scale inversely with velocity. The *Banding Window* for composition always falls on the *Hypoperitectic Region*. Calculations show that for small but finite undercoolings a typical *Banding Window* for Sn-Cd is $0.6 \leq C_0 \leq 0.9\%$.

Several experimental studies in the Sn-Cd system have reported band formation in hyperperitectic composition which is not supported by the diffusive model. Figure 2 shows the composition ranges predicted by the diffusive model [4] and the composition range over which banding has been observed experimentally [1 - 3]. On modeling band structure formation in the Pb-Bi system, Karma et. al.[5] realized that Pb-Bi system must be highly

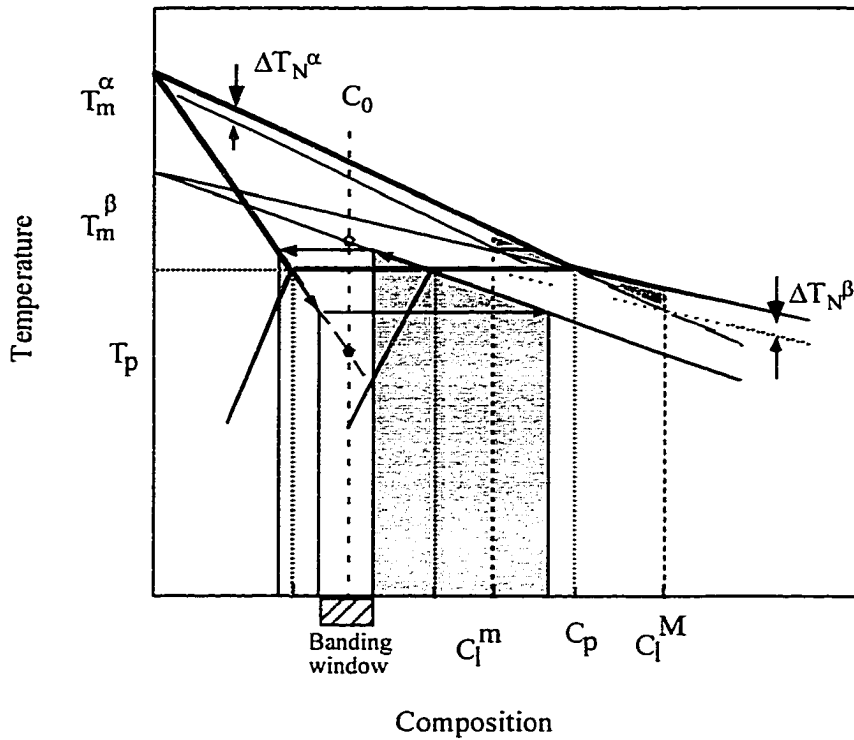


Fig. 1. A schematic peritectic diagram showing the banding cycle.

convective due to the rejection of lighter solute at the interface and assumed that the vigorous flow in the melt would cause formation of a boundary layer of constant thickness near the interface. This model retained the concept of *banding cycle* and *banding window* of the diffusive model [4] but developed the criterion for *banding* as passing of the perfectly mixed bulk composition through the banding composition window predicted by the diffusive model. This modified model could predict occurrence of bands for initial compositions less than the lower limit of the *banding window*. However, it still could not explain the formation of bands for initial compositions greater than the upper limit of the *banding window*. The model fell short by about a factor of five in predicting the band spacing. Although an attempt was made to model the effect of convection, the one dimensional analysis inadvertently submerged the salient features such as lateral segregation and inhomogeneity caused by

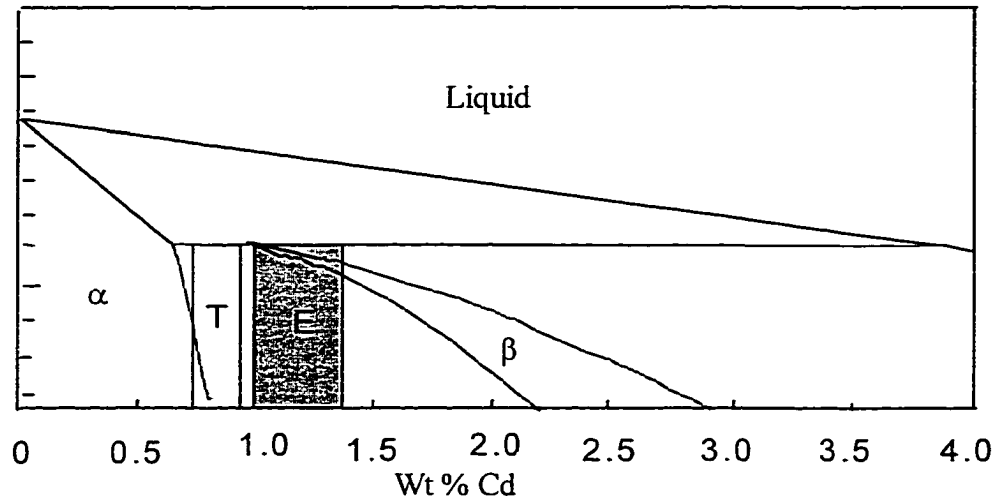


Fig. 2. Phase diagram of the Sn-Cd system showing the banding window predicted by the diffusive model (lightly shaded region, T), and the composition range for which banding is observed experimentally (darkly shaded region, E).

convection. Furthermore, the model did not consider the possibility of natural convection that will be present in the Sn-Cd system due to the rejection of heavier solute at the interface.

Experimental Results

Recently, Park and Trivedi [8] have carried out systematic experimental study by reducing convection through solidification in tubes of small diameters. They observed that in the composition range where the diffusive model predicts band formation a banded structure develops. On the other hand, in large samples, where convection effects are important, a new oscillating structure is observed in which both the primary and peritectic phases are interconnected, and the primary phase forms a large single tree-like structure that

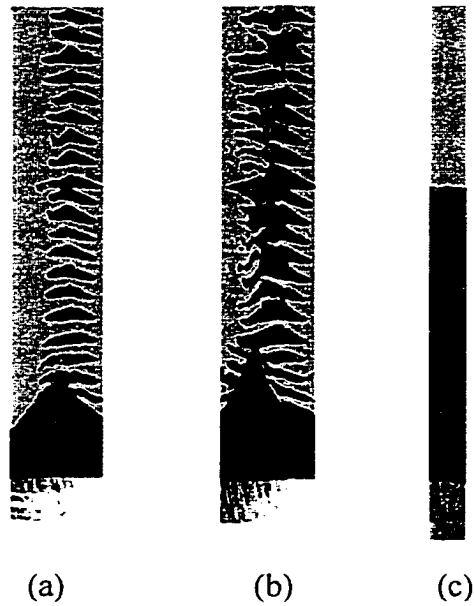


Fig. 3. Microstructures of directionally solidified Sn-1.4 wt % Cd alloy at $V = 3.0 \mu\text{m/s}$ and $G = 13.5 \text{ K/mm}$. (a) Observation of a banded structure on a longitudinal section taken below the surface. Sample diameter = 6 mm. (b) A tree-like structure of α surrounded by β on a section closer to the center. Sample diameter = 6 mm. (c). A single α to β transition in a sample of diameter 0.6 mm. [6].

is surrounded by the peritectic phase, Fig. 3a. Such a tree-like structure was shown to disappear when the experiments were carried out under reduced convection conditions in tubes of diameters 0.6 mm or less, Fig. 3b, indicating that these structural differences might have been caused by convection in fluid. In this paper we shall briefly introduce basic ideas on the role of convection in oscillatory structure formation.

Theoretical Model for Convection Induced Oscillatory Microstructure

In the vertical Bridgman system used in directional solidification, in which the hot and cold zones are isothermal at T_H and T_C and are separated by the adiabatic insulator

designed to establish high axial temperature gradient at the interface, a radial temperature gradient always exists in the liquid [7] which will initiate some convective motion [8]. Even in the presence of a stabilizing axial gradient, i.e. the melt over the crystal and temperature increasing upwards and heavy solute rejected at the interface, the flows induced by horizontal temperature gradient can be extremely intense [7]. The convective motion in turn makes the composition field laterally nonuniform and this gives rise to solutal buoyancy. The actual dynamics of thermo-solutal convection can be extremely complex, and regimes of flow encompass steady minimal convection to intense chaotic convection. However the general effect of the flow is in establishing a horizontal concentration gradient at the interface. The concentration of solute gets higher near the vertical walls, thereby initiating the formation and growth of the β -phase near and from the walls. This leads to a coupled growth of α and β phases at the same interface, with α growing near the center and surrounded by β . However, for steady convection, the α -phase slowly disappears due to continuous increase in interface composition beyond peritectic composition. When steady convection becomes unstable, oscillatory convection sets in [9, 10]. In this case, α and β phases show oscillatory coupled growth in response to composition fluctuations above and below the peritectic composition at the interface. This should appear as an oscillatory structure on the vertical section of the solidified sample.

For mathematical modeling, we consider vertically upward solidification of a binary liquid of initial composition C_0 (in % solute) inside a two dimensional rectangular cavity. The bottom horizontal wall is the instantaneous no-slip rigid solid-liquid interface. The upper stress-free boundary is solute conserving. The vertical walls are rigid solid walls maintained at prescribed temperatures and impervious to mass flux. The temperatures of both the vertical walls increase linearly upwards with a gradient G_v . However, a small but finite temperature gradient is imposed between them to model the real horizontal temperature gradient. The system of coupled nonlinear equations written in coordinate system fixed with the uniformly moving solid-liquid interface include Boussinesq

approximated Navier-Stokes equations, and the heat and solute transport equations. These equations are completely described by thermal and solutal Rayleigh numbers, the ratio of vertical to horizontal temperature gradients, the Peclet number based on growth rate, the partition coefficients for the two phases, the Prandtl number, the Lewis number and the aspect ratio. Numerical calculations have been carried out for conditions characteristic of solidification of Sn-1.3 wt % Cd at a growth rate of 3.0 $\mu\text{m/s}$ in tubes of inner diameter 0.6 mm -6.0 mm. The average interface compositions for $Ra_T = 0.07$, $Ra_s = 1.5$ (for 0.6 mm tube), and $Ra_T = 200$, $Ra_s = 1440$ (for 6.0 mm tube) are plotted in Fig. 4a. which show a steady and an oscillatory developments, respectively. The dashed line, C_p , is the peritectic liquid composition. In Fig. 4b, the concentrations at three different locations on the interface for 6 mm diameter tube are plotted. The composition near the hotter and colder walls ($y=1$ and $y=0$) fluctuates either above or below C_p , while all the points in-between fluctuate about C_p . The color-coded concentration maps in the solid are plotted in Fig. 5 corresponding to the two cases considered above. The microstructure in 0.6 mm tube is diffusion-controlled and shows a sharp transition from α to β phase corresponding to the point where C_{av} , intersects C_p , in Fig. 4a. However, for the second case, i.e. 6.0 mm diameter tube, the oscillating segregation profile at the interface gives rise to an oscillatory coupled growth of both the phases. This leads to a tree-like microstructure as shown in Fig. 4b in which the profiles are assumed symmetric around the middle axis. The arms of the α -phase may appear as isolated bands on a partially polished sample. In conclusion, a numerical model of convection is developed which shows that the oscillatory microstructures observed in experiments form due to the presence of oscillating convection in the melt.

Acknowledgment

This research was supported in part by the NASA Microgravity Science and Applications Division under Grant NAG8-1254. This work was carried out in part at the Ames

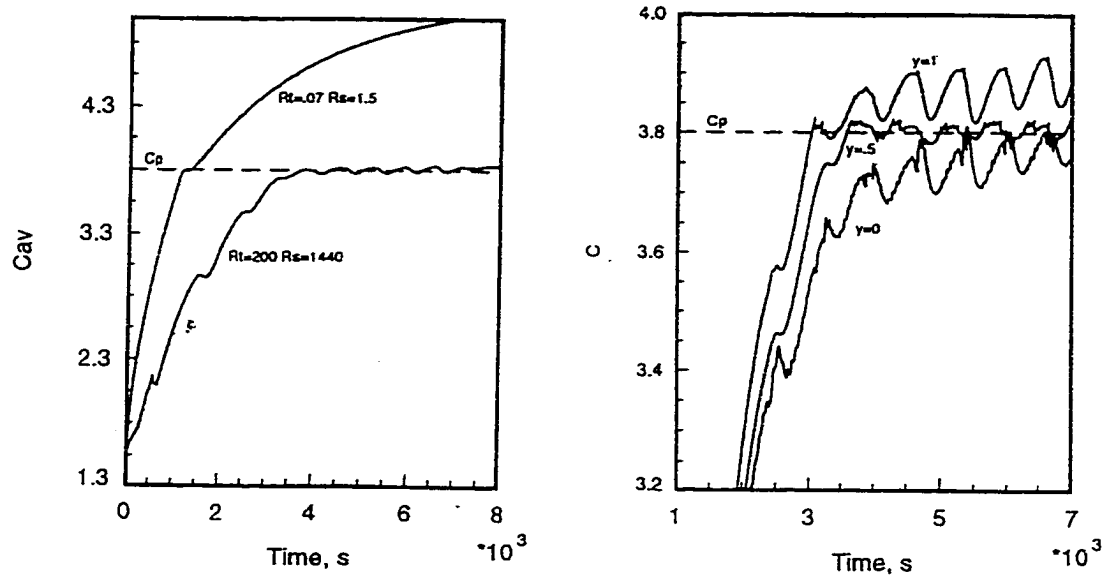


Fig. 4. Numerical results of (a) average concentration variation along the interface as a function of time. (b) Interface composition variation with time at three different locations along the interface, $y=0$ (center), 0.5 and 1.0 (wall).

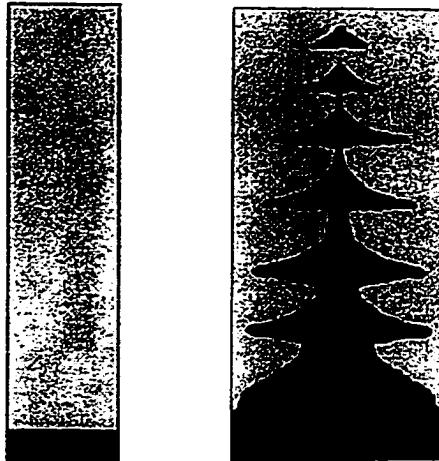


Fig. 5. The results of the numerical model showing the formation of an oscillatory microstructure in presence of an oscillatory convection. The microstructure characteristics show all the features observed in experiments [7,8].

Laboratory, which is operated for the U. S. Department of Energy by Iowa State University, under contract no. W-7405-Eng-82, supported by the director of Energy Research, Office of Basis Energy Sciences. Appreciation is expressed to J. S. Park for providing us with experimental results prior to their publication.

References

1. W. J. Boettinger Metall. Trans, **15**, p. 2023 (1974).
2. H. D. Brody and S. A. David, in Int. Conf. On Solidification and Casting, Sheffield, U.K., Institute of Metals, London, **1**, p. 139 (1977)
3. K. Zeishler-Mashl and T. Lograsso. Metall. Mater. Trans. **28A**, 1543. (1997).
4. R. Trivedi, R. Metall. Trans, **26A**, 1583 (1995).
5. A. Karma, W-J. Rappel, B. C. Fuh and R. Trivedi Metall. Mat. Trans. (in press)
6. J. S. Park and R. Trivedi. J. Cryst. Growth (in press)
7. C. J. Chang and R. A. Brown, J. Crystal Growth. **63**, p 343 (1983) .
8. G. K. Batchelor, Quart. of Appl. Math., **12**, p209 (1954).
9. P. G. Drazin and W, H, Reid, Hydrodynamic stability, Cambridge .
10. T. G. L. Shircliffe, Nature (1967) 489.

CHAPTER 4: THE EFFECT OF CONVECTION ON DISORDER IN PRIMARY CELLULAR AND DENDRITIC ARRAYS

A manuscript submitted to *Met. Trans. A*

R. Trivedi*, P. Mazumder** and S. N. Tewari#

*Ames Laboratory U. S. Department of Energy and Department of Materials Science and Engineering, Iowa State University, Ames, IA 50011

** Department of Mechanical Engineering, Iowa State University, Ames, IA 50011

#Department of Chemical Engineering, Cleveland State University, Cleveland, OH

ABSTRACT

Directional solidification studies have been carried out to characterize the spatial disorder in the arrays of cells and dendrites. Different factors that cause array disorder are investigated experimentally and analyzed numerically. In addition to the disorder resulting from the fundamental selection of a range of primary spacing under given experimental conditions, a significant variation in primary spacing is found to occur in bulk samples due to convection effects, especially at low growth velocities. The nature of convection that leads to an array disorder is examined through directional solidification studies in two different alloy systems, Pb-10 wt pct Sn and Al-4.1 wt pct Cu. The modes of convection are significantly different in these systems due to the solute being heavier than solvent in the Al-Cu system and lighter in the Pb-Sn system. In vertically upward solidification, an intense fluid motion occurs in the Pb-Sn system due to double diffusive convection. Fluid motion in both the systems also occurs due to the radial temperature gradient that is always present in Bridgman growth. Numerical models are developed to characterize fluid motion in these two

systems, and the results of the model are compared with the experimental data. Experimental observations of higher disorder and solute segregation in a weakly convective Al-Cu system than that in a highly convective Pb-Sn system are explained by the numerical model.

1. INTRODUCTION

One of the important microstructural length scales of directionally solidified alloys is the primary spacing or the periodicity of the cellular and dendritic structures. This periodicity often controls the microsegregation profiles and governs the formation of a second phase in the intercellular or interdendritic regions, and consequently controls the properties of the material. Several theoretical and experimental studies have thus been carried out to relate primary spacing with processing conditions of growth rate and temperature gradient [1-5]. Although average spacing is most often reported in the literature, experimental studies show that a significantly broad spectrum of primary spacing is present. This disorder in spacing can occur due to two factors: a weak spacing selection criterion which causes a range of spacing to be present and the effect of convection in large or bulk samples.

Fundamental studies on distribution of primary spacing under diffusive growth conditions have been carried out theoretically as well as experimentally. Warren and Langer [2] have developed a diffusive boundary layer model that predicted that primary dendrite spacing would not have a unique value under given growth conditions. Rather, a band of primary spacing would be stable. A similar result was obtained by Hunt and Lu [3] through a numerical solution of the primary spacing problem. Both these approaches assume that initially a perfect arrangement of cells or dendrite is present with a definite spacing. They have not analyzed how the simultaneous presence of all stable spacing in a given sample will alter the spacing distribution.

Detailed experimental studies have been carried out in thin samples of a transparent material in which primary spacing is controlled by the diffusion process [5]. These studies

have confirmed the presence of a finite range of spacing under given growth conditions. In contrast to the small disorder observed in diffusive growth, experimental studies in bulk metallic and organic systems have clearly shown the presence of a highly disordered spatial arrangement of cells or dendrites, and convection effects have been assumed to be responsible for this large disorder [4]. The effect of convection on the disorder in spatial arrangement of cells or dendrite was observed by comparing the primary dendrite arrays formed under 1g and μg conditions for the same growth conditions [6]. A result of one microgravity experiment [6] showed a more regular array of dendrites with a much larger primary spacing. However, only a few dendrites were present in the sample processed under μg conditions, so that no quantitative analysis of the primary spacing disorder under diffusive growth conditions could be carried out.

For primary spacing studies, larger diameter samples in the range of 3.0 - 7.0 mm are generally used to obtain sufficient number of primary cells or dendrites required for a proper statistical analysis. However, as the size of the sample increases, the possibility for convection increases. In fact, for the Al-Cu system, convective transport can become greater than or equal to the diffusive transport under 1g conditions for sample diameters greater than 3 mm [7,8]. The presence of convection can not only influence the average spacing value but also alter the distribution of primary spacing about the average value. The array disorder is governed by the intensity and specific modes of convection present in the system, so that it is necessary to carry out quantitative analysis that will couple the nature of convection with the array disorder. A proper quantitative understanding of the effect of convection on the disorder in spacing is important since the properties of a material depend not only on the average spacing but also on the extent of disorder in primary array that will locally influence the mushy zone length and segregation profiles.

In this paper we shall examine quantitatively the effect of convection on an array disorder. We shall first present experimental data on primary spacing distribution, and then analyze these data by using the results of a numerical model of convection. Experiments have been carried out in two alloy systems, Pb- 10 wt % Sn and Al- 4.1 wt % Cu. These two

systems were selected since the density variation due to the solute field is different in these systems so that they exhibit different modes of convection. In the Pb- Sn system, the rejected solute at the interface is lighter than the solvent which can result in a significant fluid motion due to double diffusive instability [9]. In contrast, in the Al- Cu system, the rejected solute at the interface is heavier, and will give rise to a negative density gradient in the liquid at the interface which will result in no fluid motion in absence of other destabilizing forces. Experimental results, however, showed that the disorder in the Al-Cu system was significantly greater than that in the Pb-Sn system. In addition, the disorder was found to remain over a wide range of velocity examined. Although vertical thermal and solute gradients do not cause fluid motion in the Al-Cu system, convection can still be present in this system if there is any thermal gradient in the radial direction since there is no threshold for convection in presence of a radial temperature or concentration gradient [10,11]. In fact, a radial temperature gradient is always present in Bridgman growth in which the hot and cold chambers are separated by an insulating region [7, 12-17]. A detailed numerical analysis of convection is carried out for both the systems to characterize the fluid motion and the composition profiles. The results of this numerical model on convection in these two systems will be presented in this paper. and it will be shown that the mode of convection in the Al-Cu leads to higher radial segregation and hence to higher disorder in the primary spacing distribution.

2. EXPERIMENTAL STUDIES

A. Microstructures

Directional solidification experiments were carried out in the Al-4.1 wt pct Cu and Pb-10 wt pct Sn alloys using the sample preparation procedure and directional solidification equipment described previously [18]. For Al-Cu alloys, 6 mm ID recrystallized alumina tubes were used, whereas 7 mm ID quartz tubes were used for Pb-Sn alloys and the melt

column was about 20 cm. Long. The total sample length was about 30 cm. Precast Al-4.1 wt pct Cu and Pb-10 wt pct Sn samples were remelted and directionally solidified in a flowing argon atmosphere. Directional solidification was carried out by raising the thermal assembly at a fixed rate, keeping the sample tube fixed, so as to avoid any possibility of fluid motion due to the irregular motion of the sample. The furnace assembly was moved at rates ranging from 0.70 to 44.0 $\mu\text{m/s}$.

Four different velocities were examined for each alloy system, as shown in Table 1, and these velocities were selected to obtain both cellular and dendritic arrays, and to examine the effect of convection with velocity. For Al - 4.1 wt % Cu alloys, the samples were directionally solidified at velocities of 5.5, 11.0, 22.0 and 44.0 $\mu\text{m/s}$. The temperature gradient was 14.0 K/mm. The transverse cross-sections of the directionally solidified samples are shown in Fig. 1, which show a cellular structure at two lower velocities, a transition to dendritic microstructure at 22.0 $\mu\text{m/s}$, and a fully dendritic structure at 44.0 $\mu\text{m/s}$. Transverse sections in the mushy zone, 100 μm behind the quenched tip, were used for the primary arm spacing measurements.

The Pb-10 wt % Sn alloys were directionally solidified at velocities of 2.5, 3.5, 4.0 and 8.0 $\mu\text{m/s}$, at $G = 11.0$ K/mm. The microstructures were cellular at growth speeds of 2.5 and 3.5 $\mu\text{m/s}$, a transition to dendritic microstructure at 4.0 $\mu\text{m/s}$, and fully dendritic structure at 8.0 $\mu\text{m/s}$. A typical transverse section of the cellular structure is shown in Fig. 2.

A comparison of transverse microstructures of directionally solidified Pb-10 wt % Sn and Al-4.1 wt % Cu alloys shown in Fig. 3, clearly illustrates the significant difference in array disorder in these two systems. In the Pb-Sn alloys, the array distribution shows that the macroscopic interface, i.e., the positions of tips, is aligned with an isotherm. In contrast, the cells in the Al-Cu alloys were observed to cluster in the center and the macroscopic front showed a significant curvature in the center.

B. Primary Spacing Analysis

The average primary spacing is generally determined from a transverse cross-section by counting the number of cells or dendrites present in a circular region of fixed diameter. Then, by assuming a hexagonal, square or random distribution, the average primary spacing value is calculated [19]. The actual value of primary spacing is thus influenced by the distribution assumed for calculations. Note that the actual distribution is neither regular nor random, so that such a method gives ambiguous results. Another common method in the literature for characterizing primary spacing is to measure a large number of nearest neighbor distances and then obtain the average value. One of the problems in this method is to identify the nearest neighbors when the distribution has a significant disorder. In order to examine this method, we have determined the distribution of spacing between two points from the array of points that represent the center of mass of each cell. In principle, one should obtain peaks that correspond to the first, second, third, etc. nearest neighbor spacing. From this distribution, the nearest neighbor spacing could be determined. The experimental data on the distribution of the distances between the points is shown in Fig. 4. Note that all the patterns are significantly disordered so that it is not possible to distinguish between the nearest and the second nearest neighbor spacing. Consequently, any attempt to visually select nearest neighbors to calculate spacing distribution or average spacing will be in error. We shall thus analyze primary spacing by using two different methods: (i) the minimum spanning tree (MST), and (ii) the weighted Wigner-Seitz (W-S) method to characterize the average spacing and the disorder in spacing, as described by Billia et al. [19].

In the MST and W-S methods, the array is first characterized by a set of points. To obtain a set of points, the transverse microstructures, shown in Figs 1 and 2, were first digitized and photo-enhanced to obtain well-defined cell or dendrite boundaries. A binary image was then produced in which the cell/dendrite interiors were white and the cell or dendrite boundaries were black, as shown in Fig. 5. The first step in the image analysis was to determine the coordinates of the centers of each cell/dendrite and their surface area. The

center of the cell or dendrite was taken as the *center of mass* of all the pixels in the cell or dendrite. Once the coordinates of the centers were determined, the distributions of these points in two-dimensional space were analyzed by using the minimal spanning tree method [19], and the weighted Wigner-Seitz method [19].

In the minimum spanning tree (MST) method, the order in the distribution of a set of points in space is characterized in terms of the mean distance, m , and the standard deviation, σ . The histogram of the edge length is plotted and the value of m and σ are determined. The pair of (m, σ) value is then compared with the calculated pair of values based on the perfect arrangement and on arrangement in which known Gaussian noise is introduced. The (m, σ) results of the minimal spanning tree for cellular and dendritic structures for the Pb-Sn samples, corresponding to the four velocities examined, are shown in Fig. 6. The circle and triangle symbols, respectively, correspond to the Al-Cu and Pb-Sn. Note that two different regions in one Pb-Sn alloy were analyzed to test the reproducibility of results for a given growth condition. The filled circles in this figure are the values for directionally solidified Pb-30 wt pct Tl alloy ($G_1=45 \text{ K cm}^{-1}$, $V = 1.1 \text{ cm h}^{-1}$), reported by Billia et al. [19]. Experimental results are compared with the theoretical values for a hexagonal and a square lattice. Note that a random distribution is predicted when $m=0.65$ and $\sigma=0.30$, since the disordered values of square and hexagonal arrangements meet at that point. Our experimental results show that the arrangement for the Al-Cu and Pb-Sn cells and dendrites is closer to a hexagonal array with a significant disorder in the arrangement.

The most accurate method to quantitatively analyze the primary spacing data is the weighted Wigner-Seitz method described by Billia et al. [19]. In this method, the transverse micrograph is analyzed by drawing no flux lines between the neighboring cells or dendrites thereby forming polygonal shapes around each cell or dendrite. By this method one obtains an array of polygons, each of which contains an original cell or dendrite. The polygons will be hexagonal for a perfect hexagonal array, whereas polygon sides will differ from six when any disorder is present. The weighted Wigner-Seitz construction gives us additional

information on the number of cells, number of nearest neighbors, the area of each cell and the number and length of each side of the cell.

The experimental results for the Al-Cu samples are shown in Fig. 7. The variation in gray levels in the figure corresponds to the pairs of 5-7 and 4-8 sided polygons. Fig. 8 and 9 show the frequency of polygons of different sides for the Pb-Sn and Al-Cu alloys. There does not appear to be a significant difference between the distributions of cells and dendrites, either for Pb-Sn or Al-Cu alloys. A maximum in the distribution is observed for six-sided cells, confirming the MST result that the distribution is a disordered distribution around the hexagonal arrangement. Note that a perfect hexagonal arrangement would give only six sided cells. A wider distribution showing the presence of 2 to 9 sided cells indicates that a significant randomness is present in the arrangement of cells or dendrites. The average values of Wigner-Sietz diameter is shown in Fig. 10 as a function of velocity.

The primary spacing distribution was found to be more random in the Al-Cu than in the Pb-Sn system. A statistical analysis of the Pb-Sn and Al-Cu samples (Table-2) shows that distribution for Al-Cu (5.62 ± 1.46) is more random than Pb-Sn (5.91 ± 0.82). The median and mode is 6 for Pb-Sn alloys and 5 for Al-Cu alloys. Statistical analysis of number of cell/dendrite sides in Pb-Sn and Al-Cu alloys was carried out using the ANOVA single factor analysis and t-test of the combined data for the Pb-Sn and Al-Cu specimens which show that the standard deviation and means are significantly different in the two systems, as shown in Table 2. The above results seem to be counter-intuitive since highly convective Pb-Sn system shows lower disorder than weakly convective Al-Cu system. In order to understand the role of convection on the observed disorder in primary spacing, we shall carry out a numerical analysis of convection and establish the nature of convection that leads to the disorder in cellular/dendritic arrays.

3. NUMERICAL MODELING

Melt convection due to thermal and compositional gradients in the liquid can lead to lateral segregation of solute across the interface [7, 12-17]. This inhomogeneity in solute concentration along the solid:liquid interface is a major source of disorder in primary spacing. It is thus expected that a greater disorder in spacing should be observed when thermosolutal convection in the melt causes larger lateral solute segregation. In this section we shall present a numerical analysis of convection for the Pb-Sn and the Al-Cu systems to assess how the modes of convection present in these systems would influence primary spacing disorder. The model is a first approximation in that the convection effect is examined for a fixed interface.

Experiments were carried out with solidification occurring in the direction opposite to the gravity vector. Since the vertical temperature gradient is positive, it is stabilizing and it does not cause fluid motion by itself. However, the advancing solid-liquid interface is also rejecting solute such that the vertical concentration gradient is negative, i.e. the solute concentration decreases with increasing distance from the interface. For the Pb-Sn system, the rejected solute is lighter than the solvent and hence the effect of concentration gradient is opposite to that of the temperature gradient. The net density gradient, which is a combination of the individual effects may be positive or negative. If the net gradient is positive, i.e. heavier liquid resides over lighter liquid, then a well-known Rayleigh-Benard convection can set in when the density gradient exceeds a critical value. Even if the net density gradient is negative, i.e., lighter liquid over heavier liquid, double diffusive instability can set in when certain parameters cross their critical values due to disparate diffusivities of solute and heat [9]. In either case, the flow in the Pb-Sn system is found to be intense and highly unsteady.

In contrast, for the Al-Cu system, the rejected solute is heavier and hence the vertically negative concentration gradient is also stabilizing similar to the vertical temperature gradient and hence no fluid flow should occur in the absence of other driving

forces. However, the design of the Bridgman system always leads to a radial temperature gradient due to mismatch of thermal boundary conditions along the outer surface of the ampoule wall, and the differences in thermal conductivities of the solid crystal, the liquid melt and the ampoule [7,12-14,16]. The presence of the radial temperature gradient, however small, always causes convection [10,11]. The intensity and mode (steady, periodic, quasi-periodic or chaotic) of convection depends on the degree of radial temperature gradient established in the system. For the Al-Cu system, the buoyancy force due to radial segregation of solute acts opposite to the thermal buoyancy. This tends to damp the convection, and leads to low intensity flow. Through numerical modeling we will demonstrate that the low intensity convection in the Al-Cu system causes higher radial segregation than the high intensity convection in the Pb-Sn system. The numerical simulations described here solve a complete two-dimensional model for heat transfer, melt convection and solute transport in a prototype of the vertical Bridgman crystal growth system. This complex transport problem is solved by the finite difference method using Alternate Direction Implicit integration [21,22]. The model is briefly described below, and a detailed mathematical treatment is given elsewhere [7, 16,17].

A. Model

The simulations presented here are for the analysis of thermo-solutal convection, heat and mass transfer and solidification in a two dimensional prototype of the vertical Bridgman system shown schematically in Fig. 11. The model includes heat transfer in melt and crystal contained in a two dimensional ampoule that is surrounded by a moving Bridgman furnace which consists of hot and cold zones separated by an insulated region. The field variables, velocity, pressure, temperature and solute composition, are described in a dimensionless coordinate reference frame (x,y) that is fixed with the lower end of the sample as shown in Fig. 11. Variables are put in dimensionless form by scaling the coordinates (x,y) and lengths with the inner width of the ampoule, d , time t with the scale for

heat diffusion d^2/α_l , velocity $\mathbf{u}(x,y,t)$ with the characteristic velocity of heat diffusion α_l/d , where α_l is thermal diffusivity of the melt. The dimensionless composition and temperature fields are defined as

$$c = \frac{C - C_0}{C_0} \quad (1)$$

$$\theta = \frac{T - T_C}{T_H - T_C} \quad (2)$$

where T_H and T_C are the characteristic temperatures of the isothermal hot and cold zones of the furnaces. The two-dimensional time-dependent equations describing convection, and heat and solute transport are

$$\frac{\partial \mathbf{u}}{\partial t} + (\mathbf{u} - \mathbf{v}_p) \cdot \nabla \mathbf{u} = -\nabla p + \nabla^2 \mathbf{u} + \frac{1}{\text{Pr}} \left[Ra_s c - Ra_T (\theta - \theta_0) \right] \quad (3)$$

$$\nabla \cdot \mathbf{u} = 0 \quad (4)$$

$$\frac{\partial c}{\partial t} + (\mathbf{u} - \mathbf{v}_p) \cdot \nabla c = \frac{1}{Le} \nabla^2 c \quad (5)$$

$$\frac{\partial \theta}{\partial t} + (\mathbf{u} - \mathbf{v}_p) \cdot \nabla \theta = \nabla^2 \theta \quad (6)$$

where θ_0 is a reference temperature. The dimensionless groups that appear in the equations are defined in table 3. The heat transport equations in the solidified crystal and ampoule are

$$\frac{\partial \theta}{\partial t} + \mathbf{v}_p \cdot \nabla \theta = \frac{\alpha_s}{\alpha_l} \nabla^2 \theta \quad (7)$$

$$\frac{\partial \theta}{\partial t} + \mathbf{v}_p \cdot \nabla \theta = \frac{\alpha_a}{\alpha_l} \nabla^2 \theta \quad (8)$$

where α_s and α_a are the thermal diffusivities of the solid crystal and the ampoule respectively.

The boundary conditions on the velocity field on the ampoule and at the melt/crystal interface specify that there is no slip relative to the solid surfaces. Along the ampoule inner wall, the continuity of the heat flux and the temperature between melt, crystal and ampoule are specified. The vertical ampoule walls are impervious to mass flux. The temperatures at the bottom and the top surfaces are prescribed according to measured experimental data. Isothermal temperatures equal to those of the hot and cold zones are possible to prescribe at these boundaries. But, this needs careful selection of the length of the computational domain. Using smaller computational domains than those required for the temperature in the liquid and solid to gradually reach the isothermal furnace temperatures and fixing the temperatures at the furnace temperatures can lead to unrealistically high axial and radial temperature gradients [7,16,17]. Proper care is necessary for physically realistic simulation while describing the thermal boundary conditions and fixing the lengths of the computational domain in the absence of experimental data [7,16,17]. The solid-liquid interface is continuously rejecting solute and the boundary condition is

$$\frac{\partial c}{\partial x} = -v_P Le(1+c)(1-k), \quad (9)$$

in which k is the partition coefficient.

The outer surfaces of the ampoule are assumed to exchange heat with the surrounding furnace according to Newton's law of cooling,

$$\frac{\partial \theta_a}{\partial y} = -Bi_c (\theta_\infty - \theta_a), \quad \text{in cold zone}$$

$$\frac{\partial \theta_a}{\partial y} = -Bi_a (\theta_\infty - \theta_a), \quad \text{in adiabatic zone}$$

$$\frac{\partial \theta}{\partial y} = -Bi_h (\theta_\infty - \theta_a), \quad \text{in hot zone}$$

where Bi_h and Bi_c and Bi_a are the nondimensional heat transfer coefficients, or the Biot Numbers in the hot, cold and adiabatic zones respectively, θ_∞ is the furnace temperature distribution obtained by direct measurement [7, 23]. The proper choice of the heat transfer coefficients is done through regression analysis of computed axial and radial temperature profiles with measured experimental data.. The set of partial differential equations is solved using second order Finite Difference Schemes, with Alternate Direction Implicit integration [19, 20]. Local grid refinement is used for the concentration field in the Pb-Sn system to resolve the thin boundary layers adjacent to the solid walls.

B. Numerical Results

Only the salient results germane to the effect of convection in axial and lateral segregation of solute and its effect on the disorder of cellular spacing are presented in this section. The details of the structure and nature of flow and thermal field in response to variation of design and processing parameters will be described in a separate paper [17].

The convection induced disparate disorder in Pb-Sn and Al-Cu systems could be best illustrated by the lateral composition profiles. The lateral composition profiles at the advancing solid-liquid interface for both the systems are plotted in Fig. 12 for different stages of time. The numbers immediately above the curves indicate the time in seconds from the start of solidification. The low intensity convection in the Al-Cu system causes a large variation in solute concentration across the interface. The composition varies smoothly across the entire cross-section without showing any boundary layer type characteristic at the side walls. This suggests that the stability characteristic must be different for different points on the interface and a significant disorder in spacing may result. In contrast, in Pb-Sn

system the solute concentration is significantly homogeneous over the most of the cross-section of the interface. Hence, in this region the stability characteristic should be relatively uniform for different points, and that should lead to lower disorder than that in Al-Cu system. A thin boundary layer type region is observed near the side walls for Pb-Sn system, where the concentration sharply rises. This is a consequence of intense convection in the Pb-Sn melt, which causes more uniform mixing. Using *Quasi-Steady State Models* earlier investigators observed that for a given furnace-ampoule combination the amount of compositional non-uniformity (or radial segregation) was a non-linear function of Rayleigh number [12-15, 24]. The most important result of these calculations has been to demonstrate that between the diffusion-controlled and complete mixing limits for solute transport in the melt lies a region of poor mixing which leads to large segregation of solute across the interface.

The flow in the Al-Cu system is found to be steady and weak due to the dampening effect of the solute field. This flow leads to a solute transport that is almost diffusion dominated along the axial length. This is illustrated in Fig. 13. The axial concentration profiles in the melt are plotted in Fig. 13a along the edge and the centerline. The concentration at the interface didn't reach the steady state composition (23 %) till this time. However, the asymptotic decay of the concentration to its initial value far downstream of the interface clearly suggests a diffusion-dominated transport. This conclusion is bolstered in the accompanying plot of axial solute segregation profiles along the length of the solidified sample (Fig. 13b). The calculated curves along the edge and the centerline are compared to the one-dimensional analytical model by Tiller et. al. [25] and good agreement is observed. However, this low intensity flow is responsible for causing large lateral segregation as observed in Fig. 12. This apparently puzzling behavior of large lateral segregation, along with a diffusion type axial segregation is consistent in terms of degrees of mixing caused by lateral temperature gradients and the solutal damping of the flow caused by rejection of heavier solute. Similar, phenomena have been observed experimentally by Capper et. al. [26] for HgCdTe system, which were later explained through numerical modeling [13].

The flow in the Pb-Sn system is found to be intense and highly unsteady due to the rejection of lighter solute at the interface. This fluid motion leads to a convection dominated solute transport along both the lateral and axial directions. This is illustrated in Fig. 14. The axial concentration profiles in the liquid melt are plotted in Fig. 14a along the wall and the centerline. Except for a thin boundary layer type region adjacent to the interface, the melt composition is almost uniform over the entire length of the melt due to vigorous mixing in the melt. The calculated axial segregation profiles in the solidified sample are compared to the diffusion model [25] in Fig. 14b. A high frequency and small amplitude fluctuation is observed due to the quasi-periodic fluid flow. The large departure of the calculated segregation profiles from the diffusion profile is clear. The intense convection suppresses the growth rate of concentration profile along the sample length. A constant boundary layer model type theory [27] could be applied to model the axial segregation behavior. However, such a simplified model is not useful while trying to understand the lateral segregation behavior and its effect on the spacing disorder, especially in a system with poor mixing as in the Al-Cu system.

4. DISCUSSION

We shall first discuss the experimental results on the disorder in the spacing distribution, and then focus on the theoretical aspects of convection that can give rise to disorder in the cellular array. Finally we shall discuss how convection effects give rise to the disorder in the spatial arrangement of cells and dendrites.

A. Experimental Results

Experimental results show that a disorder in the array is present in both the Al-Cu and the Pb-Sn systems. Although the amount of convection is significant in the Pb-Sn system, our results show that the arrays are predominantly hexagonal, as seen in the

histograms of the number of sides of Wigner-Seitz polyhedra. For all velocities, the peak corresponds to a six-sided polyhedron. Also, the MST results show the mean value to be 89% of the perfect hexagonal array, although the standard deviation is found to be 0.15, which is only half of the value for random distribution. In contrast, the distribution of cells and dendrites in the Al-Cu system was found to be significantly more random than in the Pb-Sn system. The Wigner-Seitz construction showed peak at either 5 or 6, and significantly wider distributions of number of sides were observed, e.g. the number of sides varies from 2 to 9. Also, the MST results, shown in Fig. 5, indicated a larger disorder from the perfect hexagonal array. Since convection is stronger in the Pb-Sn system compared to that in the Al-Cu, array disorder is not directly related to convection effects. We shall thus examine the role of convection in giving rise to a disorder in the array.

B. Convection Effects

Due to nonhomogeneous nature of the thermal boundary conditions, lateral temperature gradients always exist in a vertical Bridgman system. Through experimental measurements and numerical modeling, it is observed that a 2-4° C temperature difference can exist between the center and the edge of Al-Cu sample [7]. The convective flow driven by this radial temperature gradient may not be intense, especially in the presence of axially stabilizing solute gradient, but causes significant lateral segregation in large samples (~ 6.0 mm diameter). However, the axial segregation profiles do not deviate significantly from the diffusive model (Fig. 13b) and no significant macrosegregation is expected once steady state is reached. On the contrary, the intense convection in the Pb-Sn system due to the destabilizing solute gradient tends to produce large macrosegregation in the axial direction [Fig. 14]. The same trend is shown by the experimental data of composition profiles in both the systems. The measured axial composition profiles in both the Al-Cu and Pb-Sn system are shown in Fig. 15. While the macrosegregation is almost insignificant in the former system, it is large in the latter. This is due to disparate levels of mixing in the two systems as

discussed in the section on Numerical Results. It is to be noted that the experimental results are for the cellular growth at high growth rate ($2.0 \mu\text{m/s}$ for Pb-Sn, and $2.8 \mu\text{m/s}$ for Al-Cu) while the computations were done for a planar front at low growth rate ($1.0 \mu\text{m/s}$). Hence, a steady state profile was quickly attained in the experiments on Al-Cu, whereas the computed data were still in the initial transient while approaching the steady state. No steady state can be attained when the melt is vigorously mixed since the well mixed bulk composition is always increasing with time, and this is illustrated in both the measured and computed results (Fig. 14, 15).

In the numerical model, the effects of convection and the morphology of the interface are decoupled. This approximation, however, seems to be valid when the curvature of the interface is not very large [7]. A rigorous model, however, needs to be developed which couples convection with interface morphology. Such a model is quite complicated, although a basic framework has recently been developed by Xang, Beckermann and Karma [28] using the phase field approach.

C. Array Disorder

There are three major causes for the disorder in the spatial arrangement of cells or dendrites: (1) The spacing selection criterion in the diffusive regime predicts a range of spacing that can be exhibited in an array, (2) the effect of fluid flow in the liquid, and (3) the shape of the interface dictated by the fluid motion through the variation in temperature and composition along the radial direction. For most experiments carried out in 5 mm. tube, the last two effects have been found to be dominant so that we shall discuss how these effects give rise to a disorder in the array.

We shall now examine the effect of fluid velocity on an array disorder. It should be emphasized that fluid velocity will influence the value of primary spacing, but the disorder arises primarily from the local variation in composition and temperature at different cells or

dendrites in an array. Thus, the disorder will be small not only when the fluid motion is very small, but also when the fluid motion is very large so that good mixing leads to almost uniform concentration distribution across the interface.

As we discussed earlier, the fluid motion is not vigorous in the Al-Cu system as compared to that in the Pb-Sn system. However, in the Al-Cu system, the presence of radial concentration gradient at the interface causes the macroscopic interface to become curved i.e. protrude at the center, Fig. 3a. This instability has been observed earlier in systems with denser solute, and it is often referred to as the steeping effect [29,30]. The presence of curvature of the solidification front gives rise to varying thermal and solute conditions at different cell or dendrite tips in an array. Because of the lateral flow of solute due to convection, the composition in the liquid near the interface increases from the center to the side wall. This variation in composition would give rise to variation in spacing in the radial direction. In order to show the effect of radial composition variation on primary spacing, average primary spacing is measured at different locations along the radial direction. Also, the composition in the solid near the cell or dendrite tip is measured for different cell/dendrites in an array. A systematic variation in primary spacing as function of tip composition in the solid is observed, as shown in Fig. 16. These results establish that the decrease in primary spacing from the center to the wall is due to the variation in composition cause by convection. Since the nearest neighbor distances will vary in radial direction, the nearest neighbor interactions are not symmetric so that the cell/dendrite distribution becomes non-uniform, which is reflected as a disorder in the MST construction. Thus, the disorder in primary spacing, observed in the Al-Cu system, is due to the curvature of the interface caused by the convection that gives rise to segregation of solute in the radial direction.

5. CONCLUSIONS

The arrangement of cellular and dendritic arrays in directionally solidified Pb-Sn and Al-Cu alloys have been analyzed by using the minimal spanning tree and the weighted

Wigner-Seitz approaches. It is found that the arrangement of cells and dendrites corresponds to a disordered hexagonal array. Experimental results on array disorder are characterized by the mean value and standard deviation, as well as by characterizing the histogram of the nearest neighbor cells and dendrites. More disorder is found in vertically stable fluid in the Al-Cu system than the highly convective Pb-Sn system. It is shown that the disorder does not depend on the extent of fluid motion, but it depends on the radial inhomogeneity that causes the interface to become macroscopically curved, as in the case of Al-Cu alloys. The effect of convection in these two systems has been examined numerically, and the results have been correlated to the observed disorder in primary spacing.

ACKNOWLEDGEMENTS

This work was supported by NASA microgravity research, Division of Materials Science, grant # NASA NCC8-98. Authors would like to acknowledge H. Jamgotchian and J. T. Mason for help in the statistical analysis of the results, and H. Song and V. M. Kumar for help with the directional solidification work.

REFERENCES

1. M. C. Flemings, *Solidification Processing*, McGraw-Hill, (1975).
2. J. A. Warren and J. S. Langer, *Phys. Rev.*, 1990, vol. 42A, p. 3518
3. J. D. Hunt and S. Lu, *Metall. Mat. Trans. A*, 1996, vol. 27 A, p.611
4. S. N. Tewari and R. Shah, *Metall. Mat. Trans.*, 1996, vol. 27A, pp.1353-1362.
5. S. H. Han and R. Trivedi, *Acta Metall. Mater.*, 1994, vol. 42, pp. 25-41
6. M. D. Dupouy, D. Camel and J.J. Favier, *Acta Metall.* 1989, vol. 37, p. 1143.
7. P. Mazumder, Ph. D. Thesis, Iowa State University, 1999.
8. R. Trivedi, H. Miyahara, P. Mazumder and S. N. Tewari, *Materials Trans.* 1999, (Submitted)

9. S. R. Coriell, M. R. Cordes, W. J. Boettinger, R. F. Sekerka, *J. Crystal Growth*, 1980, vol. 49, p.13
10. G. K. Batchelor, *Quarterly of Applied Mathematics*, 1954, vol.12, no. 3, p209
11. D. J. Tritton, *Physical Fluid Dynamics*, , Oxford Science Publications (1988)
12. P. M. Adornato and R. A. Brown, *J. Crystal Growth*, 1987, v 80, p 155
13. D. H. Kim and R. A. Brown, *J Crystal Growth*, 1989, v 96, p 609
14. D. H. Kim and R. A. Brown, *J Crystal Growth*, 1991, vol. 114, pp. 411-34
15. C. J. Chang and R. A. Brown , *J. Crystal Growth*, 1983, v 63, p 343
16. P. Mazumder and R. Trivedi, in *Fluid Flow Phenomena in Metals*, The Materials Society, Warrendale, PA, 1999.
17. P. Mazumder and R. Trivedi, to be submitted to *J. Fluid Mech*.
18. S. N. Tewari and R. Trivedi, *Microgravity Sci. Technol.:* 1991, vol. 4, pp. 240-244.
19. B. Billia, H. Jamgotchian and H. Nguyen Thi: *Metall. Trans. A*, 1991, vol. 22A, pp. 3041-3050.
20. D. G. McCartney and J. D. Hunt, *Metall. Trans. A*, 1984. vol. 15, p. 983.
21. W. Peaceman and H. H. Rachford, *J. Soc. Indust. Appl. Math*, 1956, vol. 3, p. 28.
22. L. Lapidus L and G. F. Pinder, *Numerical solution of partial differential equations in science and engineering*, John Wiley & Sons, New York, (1982).
23. E. Simsek and P. Mazumder, Unpublished work. Iowa State University, Ames, IA, 1998.
24. R. A. Brown, *AIChE Journal*, 1988, vol. 34, p 881.
25. W. A. Tiller, K. A. Jackson, J. W. Rutter and B. Chalmers, *Acta Metall.*, 1953, vol. 1, p. 428
26. P. Capper, C. L. Jones, E. J. Pearce and M.J.T. Quelch, *J Crystal Growth*, 1983, vol. 62, p. 487
27. J. A. Burton, R. C. Prim and W. P. Slichter, *J. Chem. Phys*, 1953, v 21, p 1987.
28. Xang, C. Beckermann and A. Karma, unpublished work, University of Iowa, (1998).

29. J. D. Verhoeven, J.T. Mason and R. Trivedi: *Metall. Trans. A*, 1986, vol. 17, pp. 991-1000.
30. M.H. Burden, D.J. Hebditch and J.D. Hunt: *J. Cryst. Growth*, 1973, vol. 20, pp. 121-24.

Table 1. Growth parameters for directionally solidified Pb-10 wt pct Sn and Al-4.1 wt pct Cu alloys.

Alloy Specimen	Velocity ($\mu\text{m/s}$)	Thermal Gradient (K/mm)	W-S Diameter (μm)	Morphology
1. Pb-10 wt pct Sn	2.5	11.0	122	Cell
2. Pb-10 wt pct Sn	3.5	11.0	135	Cell
3. Pb-10 wt pct Sn	4	11.0	142	Cell to dendrite
4. Pb-10 wt pct Sn	8	11.0	130	Dendrite
1. Al-4.1 wt pct Cu	5.5	14.0	97	Cell
2. Al-4.1 wt pct Cu	11	14.0	106	Cell
3. Al-4.1 wt pct Cu	22	14.0	163	Cell to dendrite
4. Al-4.1 wt pct Cu	44	14.0	161	Dendrite

Table 2. Statistical analysis of number of cell/dendrite sides in Pb-Sn and Al-Cu alloys.

(a) t-Test: Two samples assuming unequal variances.

	Pb-Sn	Al-Cu
Mean	5.91	5.62
Variance	0.68	2.14
Median	6	5
Mode	6	5
Count	536	609

Table 3. Dimensional Groups and their characteristic values used in simulation

Group	Symbol	Definition	Values	
			Al-Cu	Pb-Sn
Thermal Rayleigh Number	Ra_T	$\frac{g\beta_T(T_H - T_C)d^3}{\alpha_l\nu}$	10000	7000
Solutal Rayleigh Number	Ra_S	$\frac{g\beta_S C_0 d^3}{\alpha_l\nu}$	4000	-70000
Prandtl Number	Pr	ν/α_l	0.013	0.009

FIGURE CAPTIONS

Fig. 1. Transverse microstructures of directionally solidified for Al-4.1 wt pct Cu alloys at velocities: (a) 5.5 (b) 11.0 (c) 22.0 and (d) 44.0 $\mu\text{m/s}$. $G = 14.0 \text{ K/mm}$

Fig. 2. Transverse microstructures of directionally solidified Pb-10wt% Sn alloy at different velocities: (a) 2.5 (b) 3.5 (c) 4.0 and (d) 8.0 $\mu\text{m/s}$. $G = 11.0 \text{ K/mm}$

Fig. 3. Longitudinal cross-sections of deirectionally solidified alloys: (a) Al-4.1 wt % Cu, $V_p=5.5 \mu\text{m/s}$, $G = 14.0 \text{ K/mm}$. (b) Pb- 10 wt % Sn alloy, $V = 2.0 \mu\text{m/s}$. $G = 11.0 \text{ K/mm}$, and Al-4.1 Cu wt pct alloy, $V = \mu\text{m/s}$ and $G = 14.0 \text{ K/mm}$. The macroscopic interface is almost flat for the Pb-Sn alloy, whereas a steeping effect observed in the Al-Cu alloy.

Fig. 4. A representative histogram of spacing between cells (or dendrites) including the nearest and higher order spacing for directionally solidified Al-4.1 wt pct alloy directionally solidified at $V = 11.0 \mu\text{m s}^{-1}$

Fig. 5. A typical binary image of a transverse cross-section of a directionally solidified alloy. The construction of a minimal spanning tree is shown for a cellular array in Al - 4.1 wt pct Cu alloy, directionally solidified at 5.5 $\mu\text{m/s}$ and $G = 14.0 \text{ K/mm}$.

Fig. 6. The (m, σ) diagram for the distribution of cellular and dendritic arrays in the Pb-10 wt pct Sn (squares), Al-4.1 wt pct Cu (circles) and Pb-30 wt pct Tl (triangles)^[8] alloys. The filled symbols correspond to the dendrites and the open symbols to the cells. Theoretical lines for hexagonal (thick line) and square array (thin line) as a function of disorder are also shown for comparison. The numbers, adjacent to the symbols, are the sample identification numbers given in Table-1.

Fig. 7. Representative examples of the modified Wigner-Seitz construction showing the nearest neighbor cells and dendrites in Al-10 wt pct Cu system. Different gray levels show the presence of 5-7 and 4-8 sides of polygons. The results are for velocities: (a) 5.5, and (b) 44.0 $\mu\text{m/s}$.

Fig. 8. Histogram of nearest neighbor of polygons in the Wigner-Seitz construction for Pb-Sn alloys directionally solidified at velocities: (a) 2.5 (b) 3.5 (c) 4.0 and (d) 8.0 $\mu\text{m s}^{-1}$.

Fig. 9. Histogram of nearest neighbor of polygons in the Wigner-Seitz construction for Al-Cu alloys directionally solidified at velocities: (a) 5.5, (b) 11.0, (c) 22.0 and (d) 44.0 $\mu\text{m s}^{-1}$.

Fig. 10. The variation in the average diameter of W-S cells as a function of velocity in the Al-Cu system.

Fig. 11 : Computational Model of the Vertical Bridgman System.

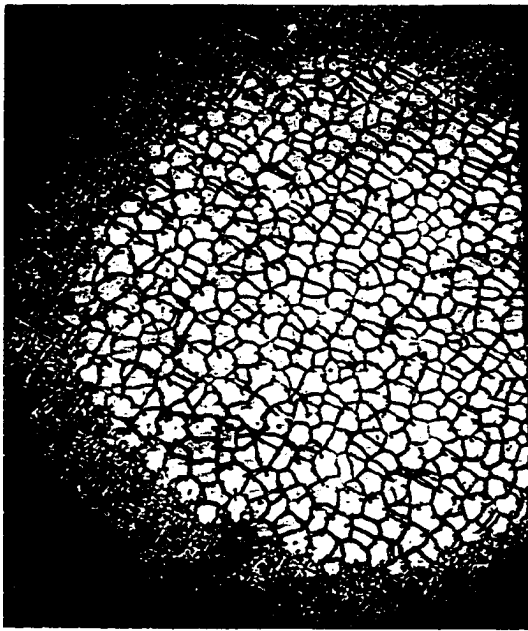
Fig. 12. Lateral composition profiles at different time levels (seconds) from the start of solidification. (a) Al-4% Cu (b) Pb-10% Sn. The low intensity convection in Al-Cu system causes higher lateral segregation than in Pb-Sn system.

Fig. 13: Almost diffusion dominated axial solute profiles in Al-4% Cu system. (a) Solute profile in liquid ahead of the interface (b) Axial segregation profiles along the length of solidified sample.

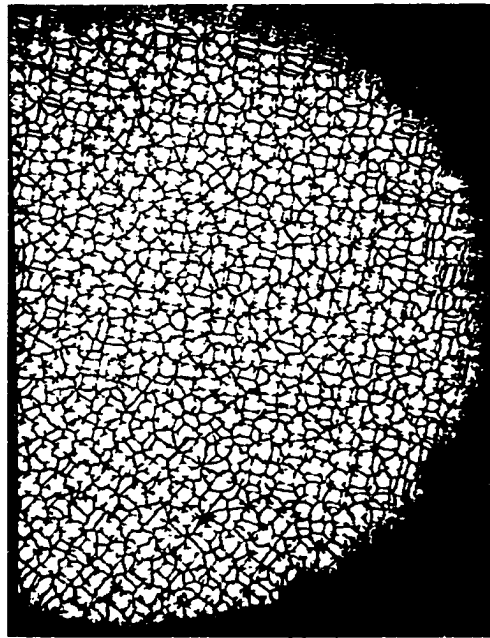
Fig. 14: Almost perfectly mixed axial solute profiles in Pb- 10% Sn system. (a) Solute profile in liquid ahead of the interface shows a thin boundary layer type characteristic outside of which the melt is almost perfectly mixed due to vigorous convection. The uniform melt composition, however, is much higher than the initial solute composition (10%) (b) Axial segregation profiles along the length of solidified sample along the edge and the center. The actual profiles deviate considerably from the diffusive model [25]

Fig. 15: The variation of primary spacing with composition at the center of cells or dendrite for a microstructure that exhibits the steeping effect. Al-4.0 wt pct alloy, directionally solidified at $1.83 \mu\text{m/s}$ at $G = 14.0 \text{ K/mm}$.

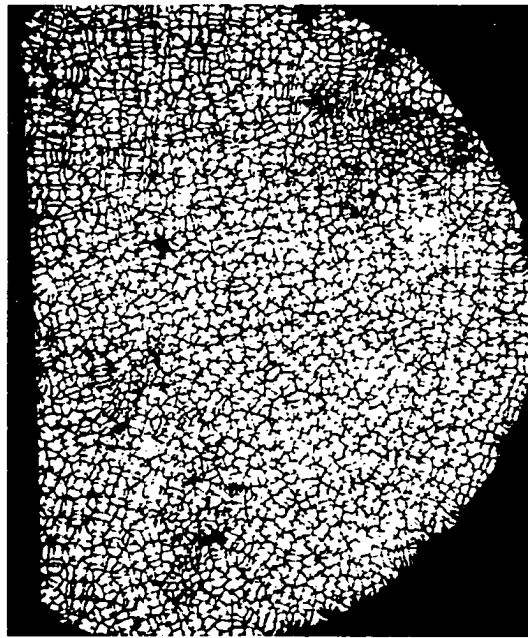
Fig. 16: Axial segregation profiles in the Al-4.1 wt% Cu and Pb- 10 wt% Sn systems. The Al-Cu system shows no significant macrosegregation, while Pb-Sn shows large macrosegregation.



(a)



(b)



(c)

Fig. 1. Transverse microstructures of directionally solidified for Al-4.1 wt pct Cu alloys at velocities: (a) 5.5 (b) 11.0 (c) 22.0. $G = 14.0$ K/mm.

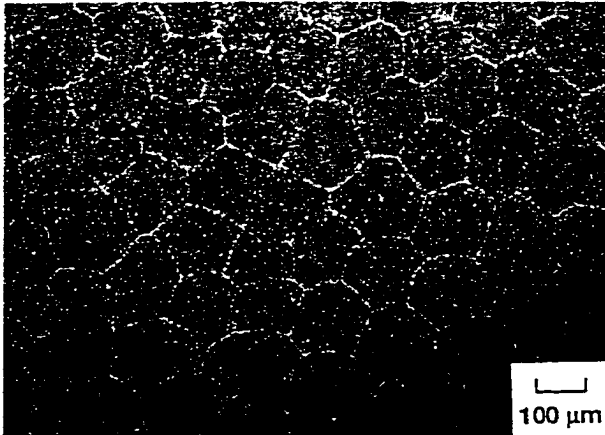
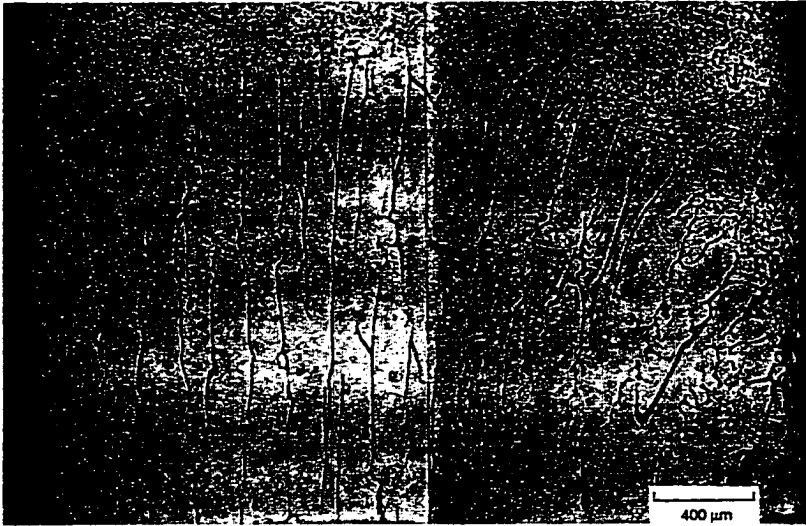
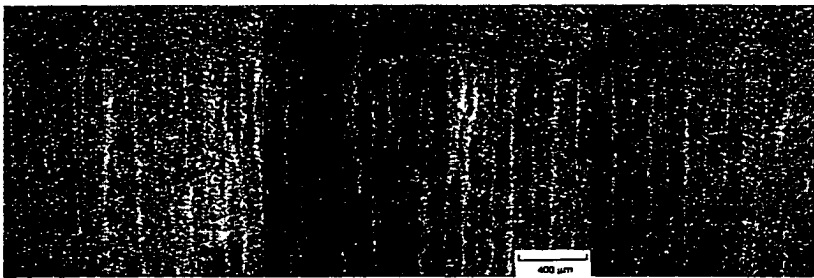


Fig. 2. Typical transverse section of cellular structures in directionally solidified Pb-10wt% Sn alloy at $2.5 \mu\text{m/s}$. $G = 11.0 \text{ K/mm}$



(a)



(b)

Fig. 3. Longitudinal cross-sections of directionally solidified alloys: (a) Al-4.1 wt % Cu, $V_p=5.5 \mu\text{m/s}$, $G = 14.0 \text{ K/mm}$. (b) Pb- 10 wt % Sn alloy, $V = 2.0 \mu\text{m/s}$, $G = 11.0 \text{ K/mm}$, and Al-4.1 Cu wt pct alloy, $V = \mu\text{m/s}$ and $G = 14.0 \text{ K/mm}$. The macroscopic interface is almost flat for the Pb-Sn alloy, whereas a steeping effect observed in the Al-Cu alloy.

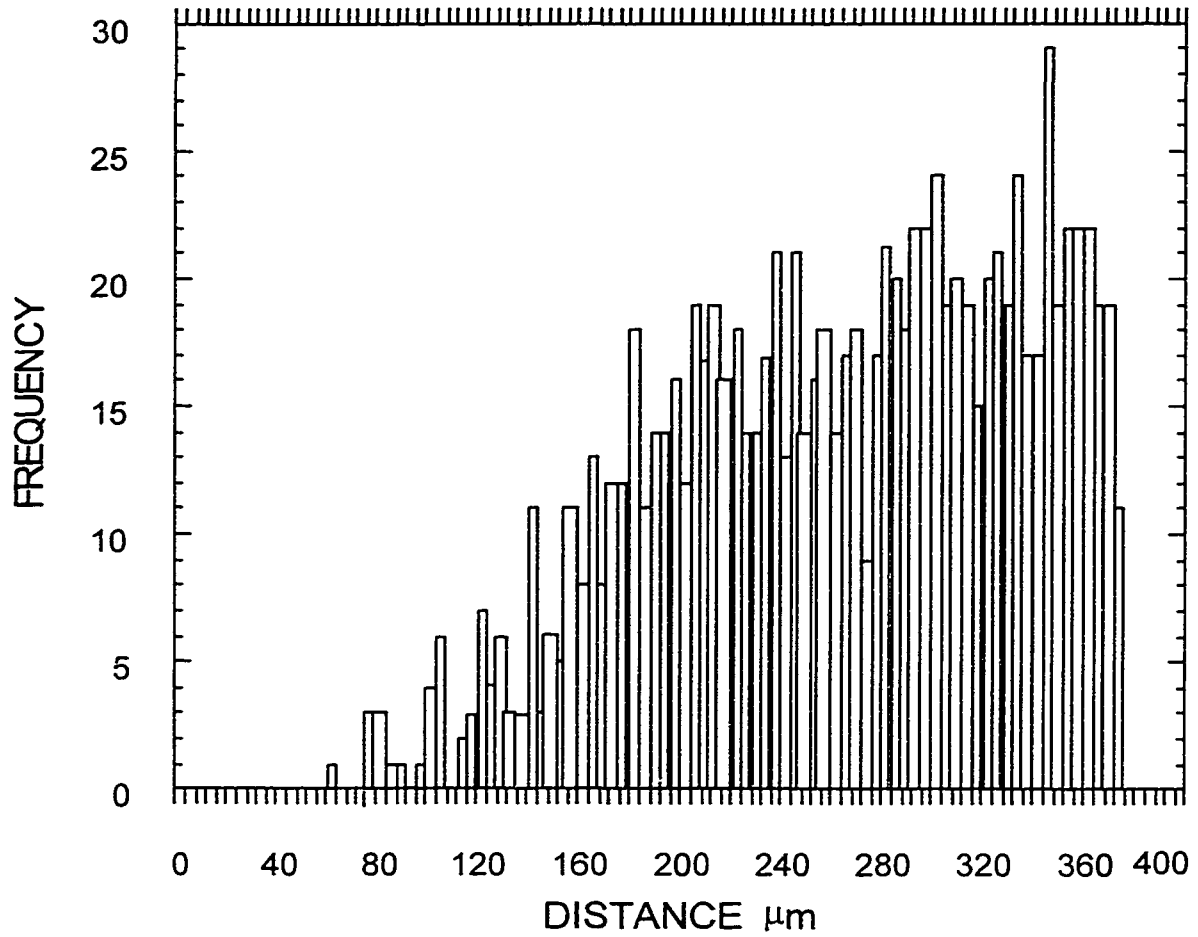


Fig. 4. A representative histogram of spacing between cells (or dendrites) including the nearest and higher order spacing for directionally solidified Al-4.1 wt pct alloy directionally solidified at $V = 11.0 \mu\text{m s}^{-1}$

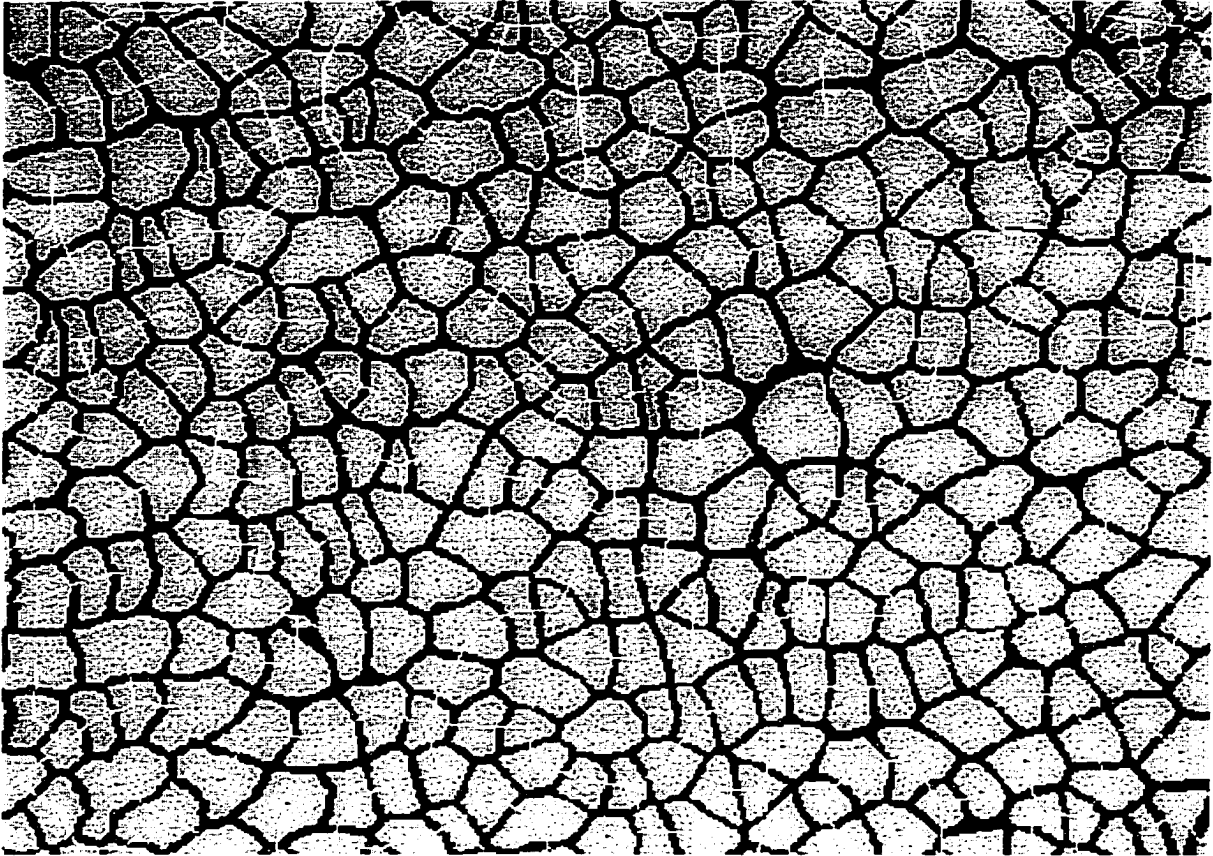


Fig. 5. A typical binary image of a transverse cross-section of a directionally solidified alloy. The construction of a minimal spanning tree is shown for a cellular array in Al - 4.1 wt pct Cu alloy, directionally solidified at $5.5 \mu\text{m/s}$ and $G = 14.0 \text{ K/mm}$.

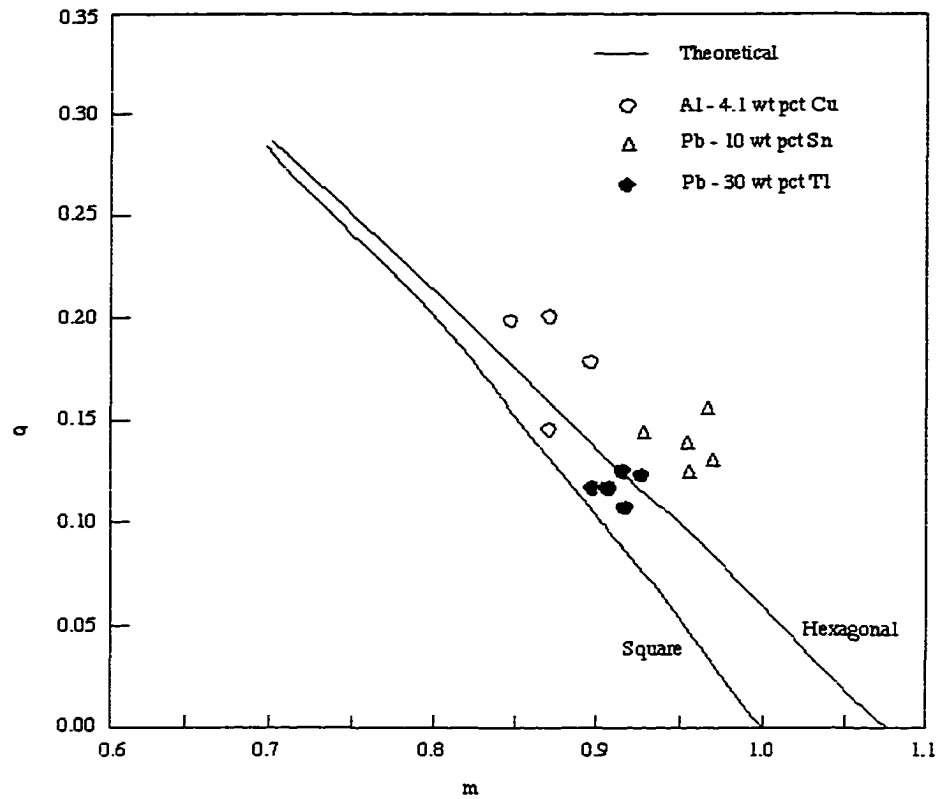


Fig. 6. The (m, σ) diagram for the distribution of cellular and dendritic arrays in the Pb-10 wt pct Sn (squares), Al-4.1 wt pct Cu (circles) and Pb-30 wt pct Tl (triangles)^[8] alloys. The filled symbols correspond to the dendrites and the open symbols to the cells. Theoretical lines for hexagonal (thick line) and square array (thin line) as a function of disorder are also shown for comparison. The numbers, adjacent to the symbols, are the sample identification numbers given in Table-1.

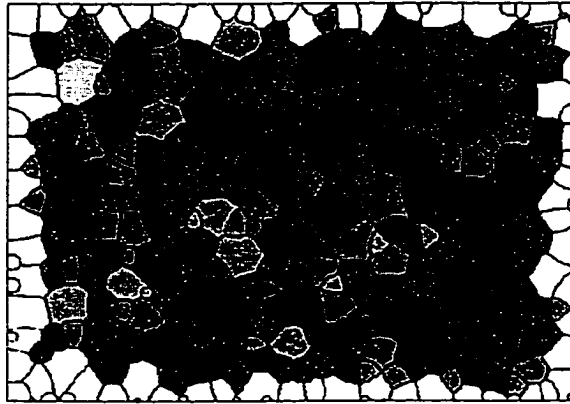


Fig. 7. Representative examples of the modified Wigner-Seitz construction showing the nearest neighbor cells and dendrites in Al-10 wt pct Cu system. Different gray levels show the presence of 5-7 and 4-8 sides of polygons. The results are for velocities: (a) 5.5, and (b) 22.0 $\mu\text{m/s}$.

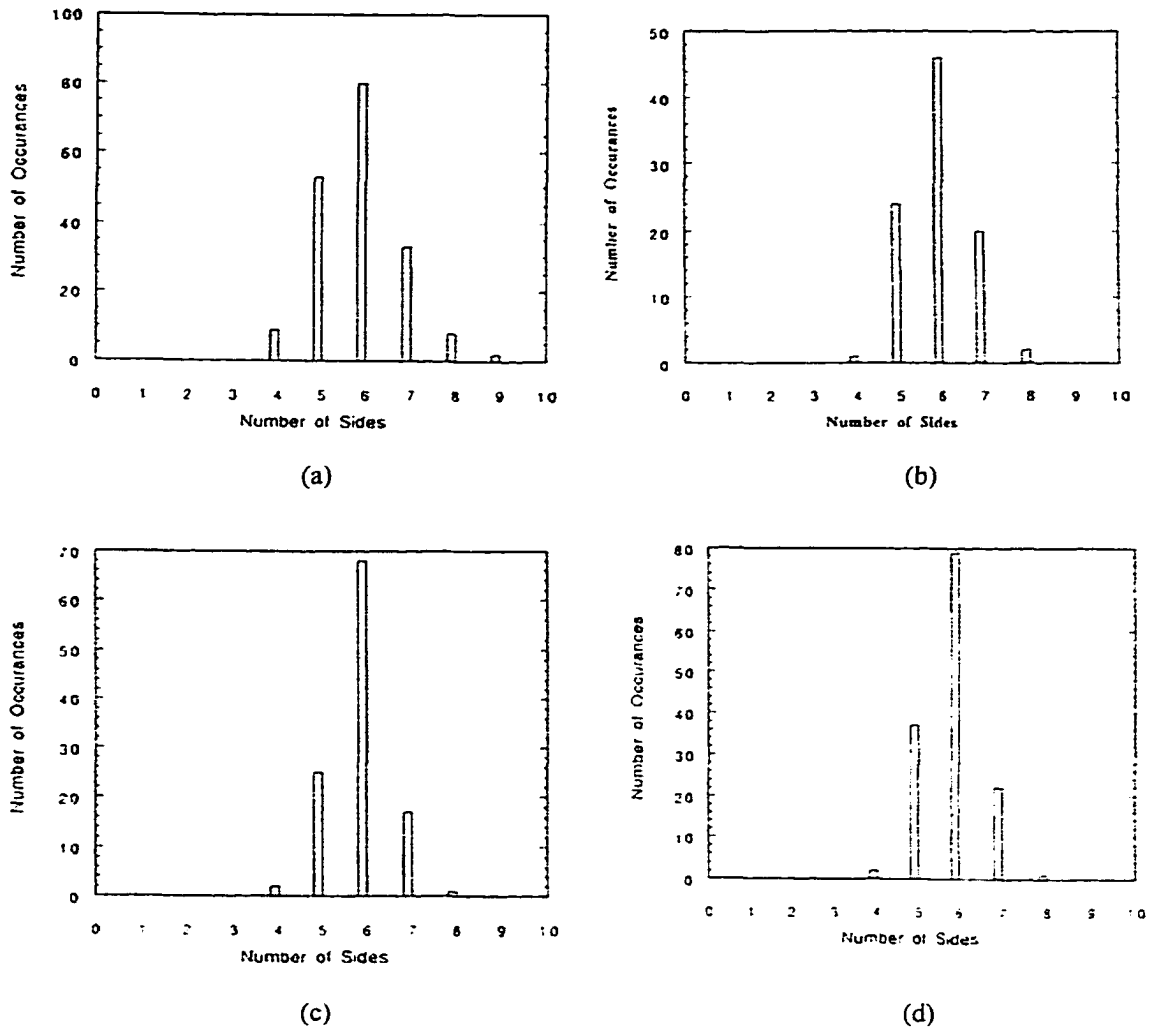


Fig. 8. Histogram of nearest neighbor of polygons in the Wigner-Seitz construction for Pb-Sn alloys directionally solidified at velocities: (a) 2.5 (b) 3.5 (c) 4.0 and (d) 8.0 $\mu\text{m s}^{-1}$.

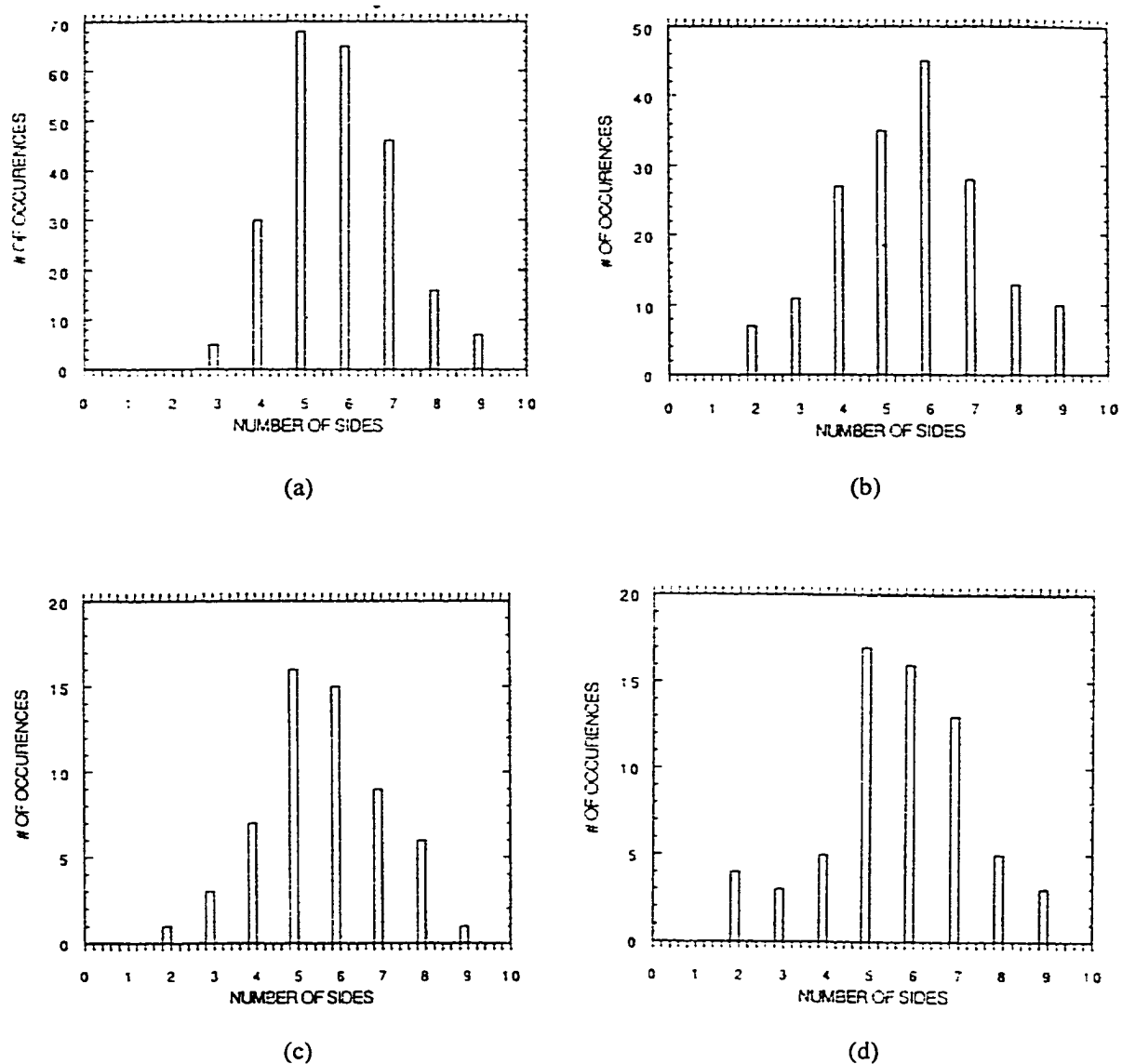


Fig. 9. Histogram of nearest neighbor of polygons in the Wigner-Seitz construction for Al-Cu alloys directionally solidified at velocities: (a) 5.5, (b) 11.0, (c) 22.0 and (d) 44.0 $\mu\text{m s}^{-1}$.

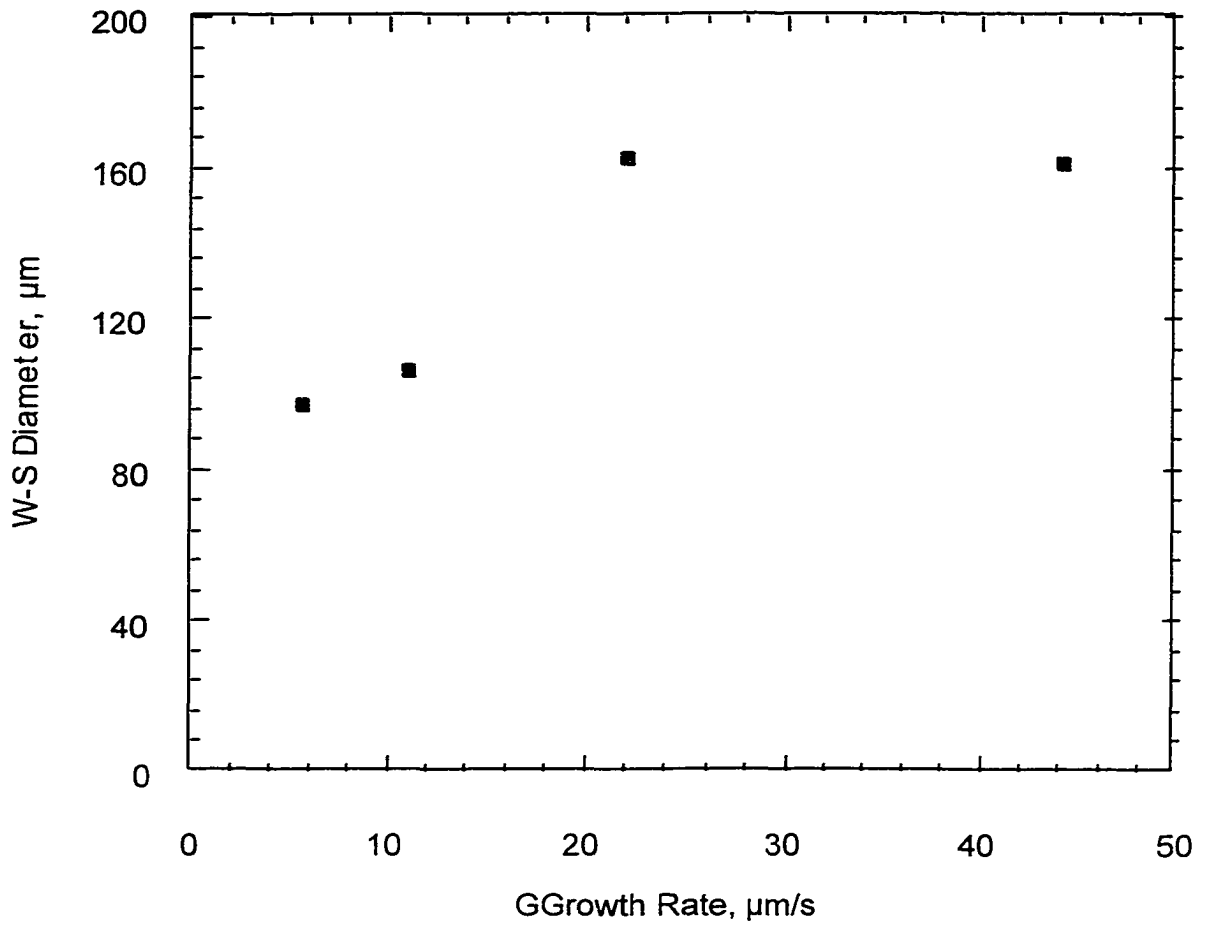


Fig. 10. The variation in the average diameter of W-S cells as a function of velocity in the Al-10 wt % Cu system.

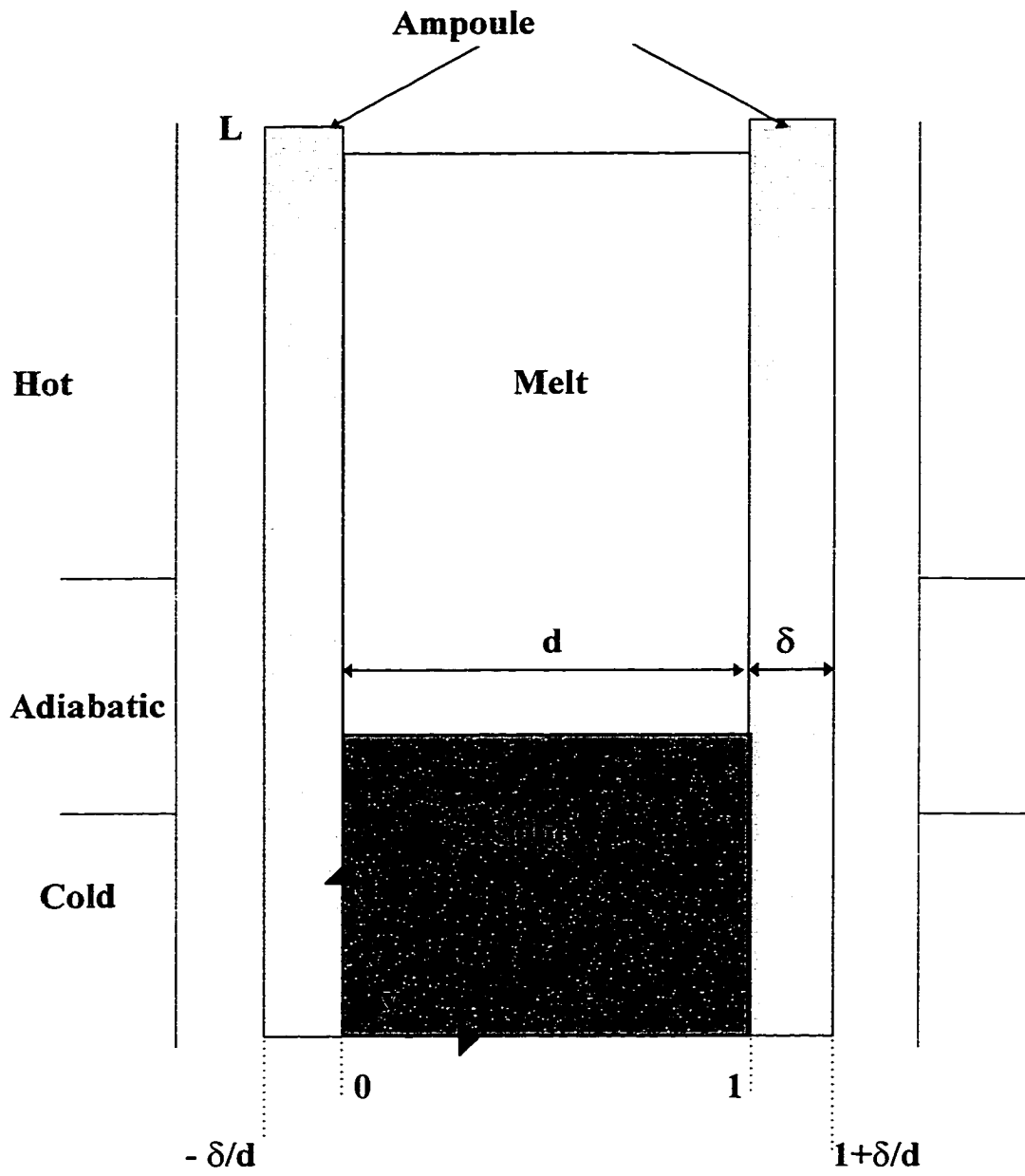


Fig. 11. Computational model of the vertical Bridgman System

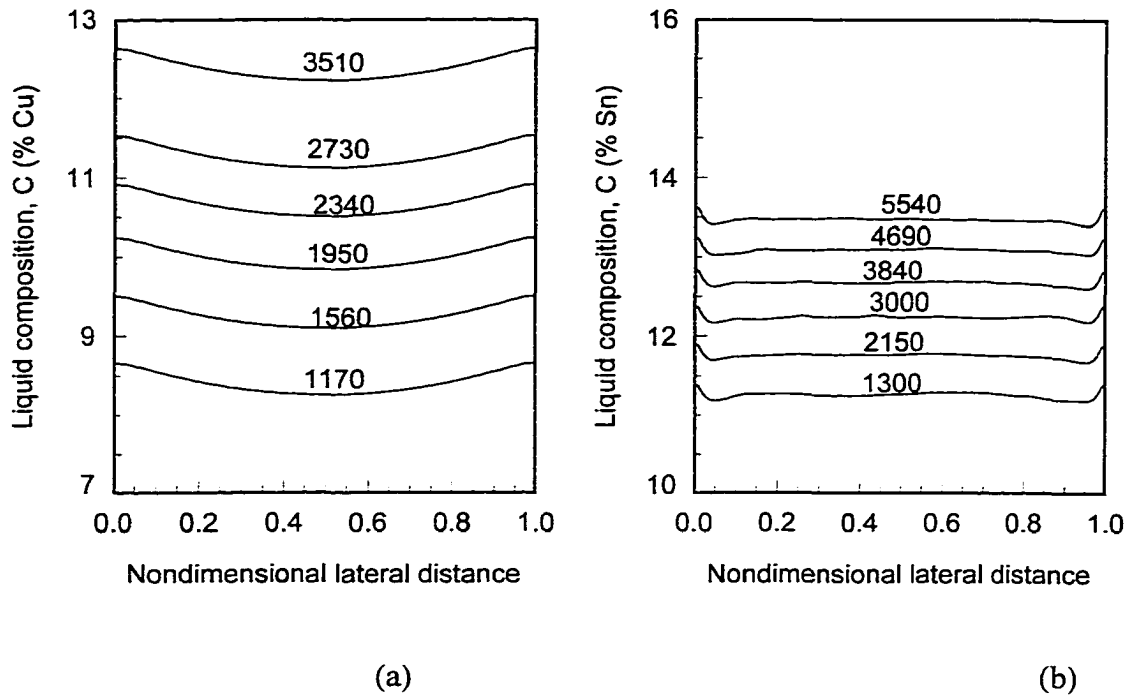
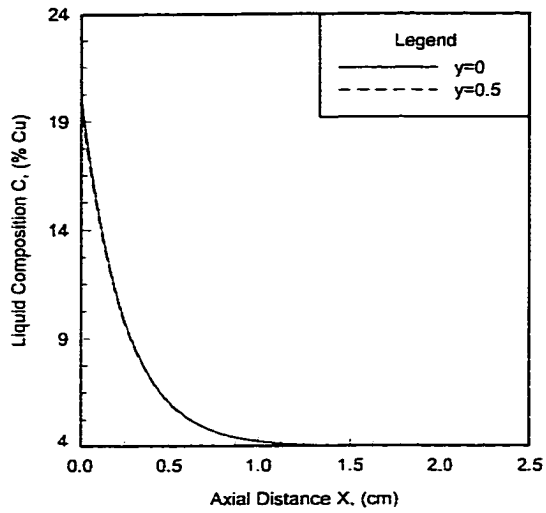
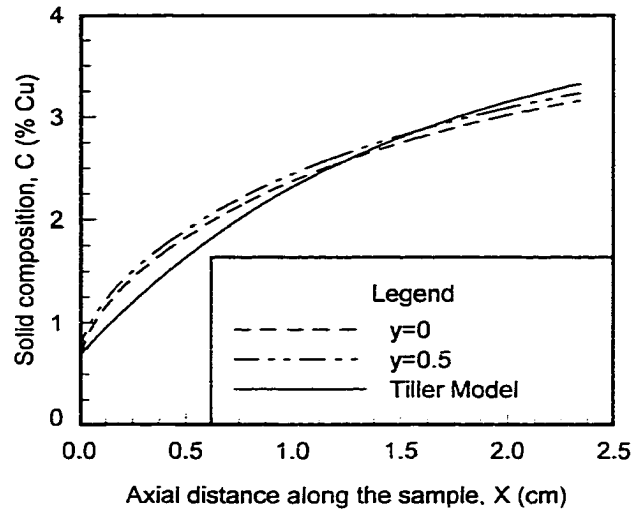


Fig. 12. Lateral composition profiles at different time levels (seconds) from the start of solidification. (a) Al-4% Cu (b) Pb-10% Sn. The low intensity convection in Al-Cu system causes higher lateral segregation than in Pb-Sn system.



(a)



(b)

Fig. 13. Almost diffusion dominated axial solute profiles in Al-4% Cu system. (a) Solute profile in liquid ahead of the interface (b) Axial segregation profiles along the length of solidified sample. The actual profiles along the edge and the center of the sample, are close to the diffusive model [25]

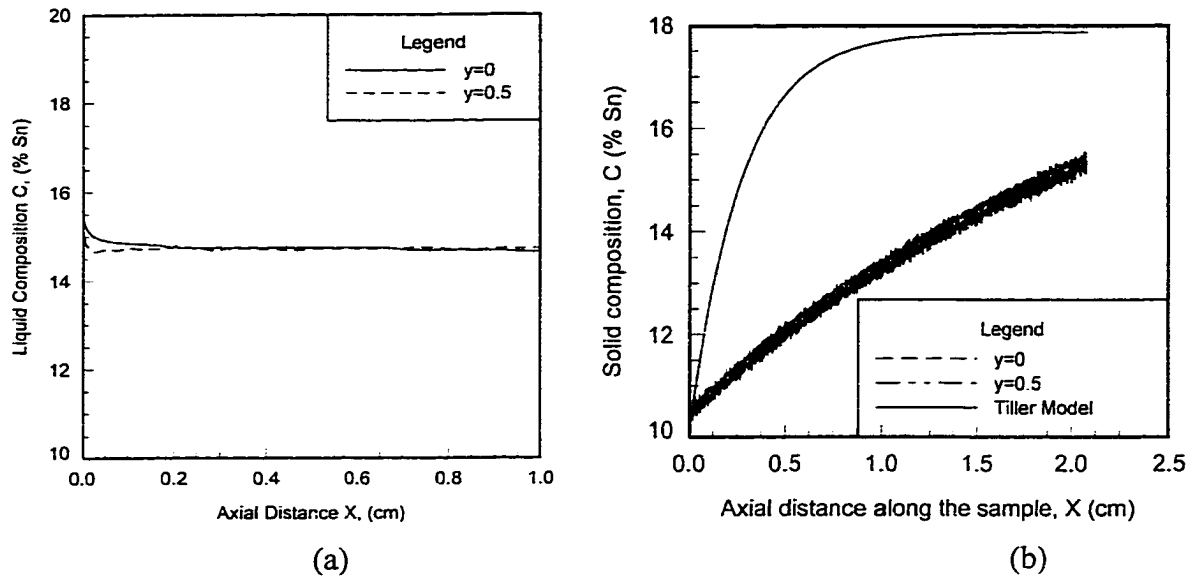


Fig. 14. Almost perfectly mixed axial solute profiles in Pb-10%Sn system. (a) Solute profile in liquid ahead of the interface shows a thin boundary layer type characteristic outside of which the melt is almost perfectly mixed due to vigorous convection. The uniform melt composition, however, is much higher than the initial composition (10 %) (b) Axial segregation profiles along the length of solidified sample along the edge and the center. The actual profiles along the edge and the center of the sample deviate considerably from the diffusive model [25]

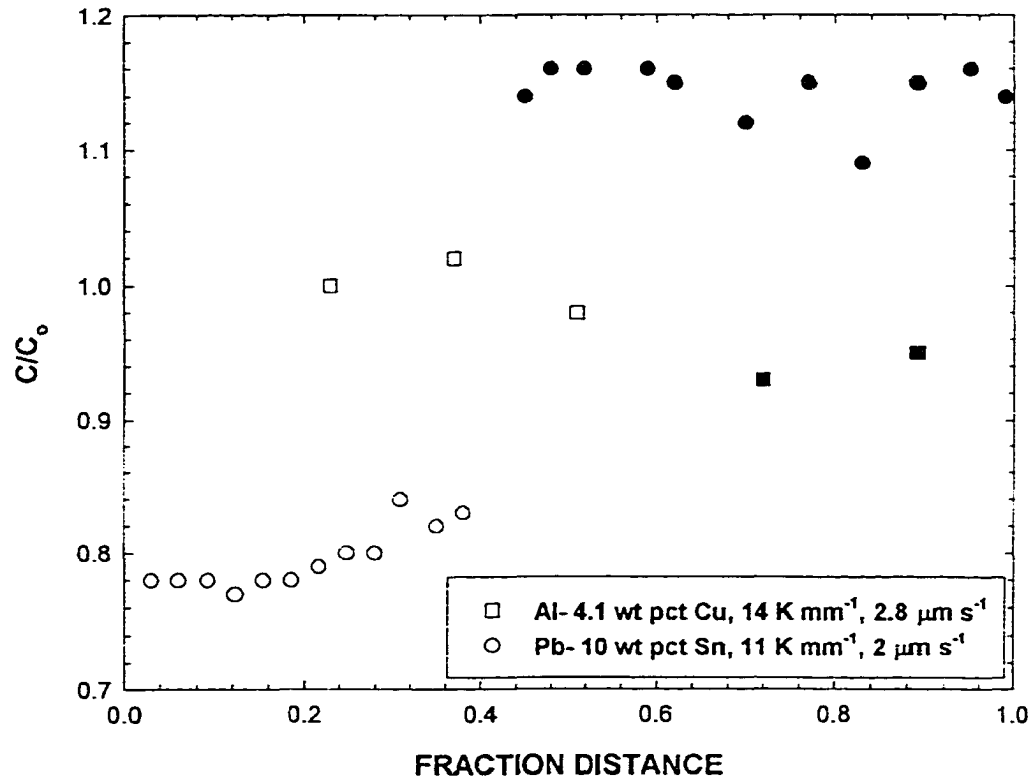


Fig. 15. Axial segregation profiles in the Al-4.1 wt% Cu and Pb- 10 wt% Sn systems. The Al-Cu system shows no significant macrosegregation, while Pb-Sn shows large macrosegregation.

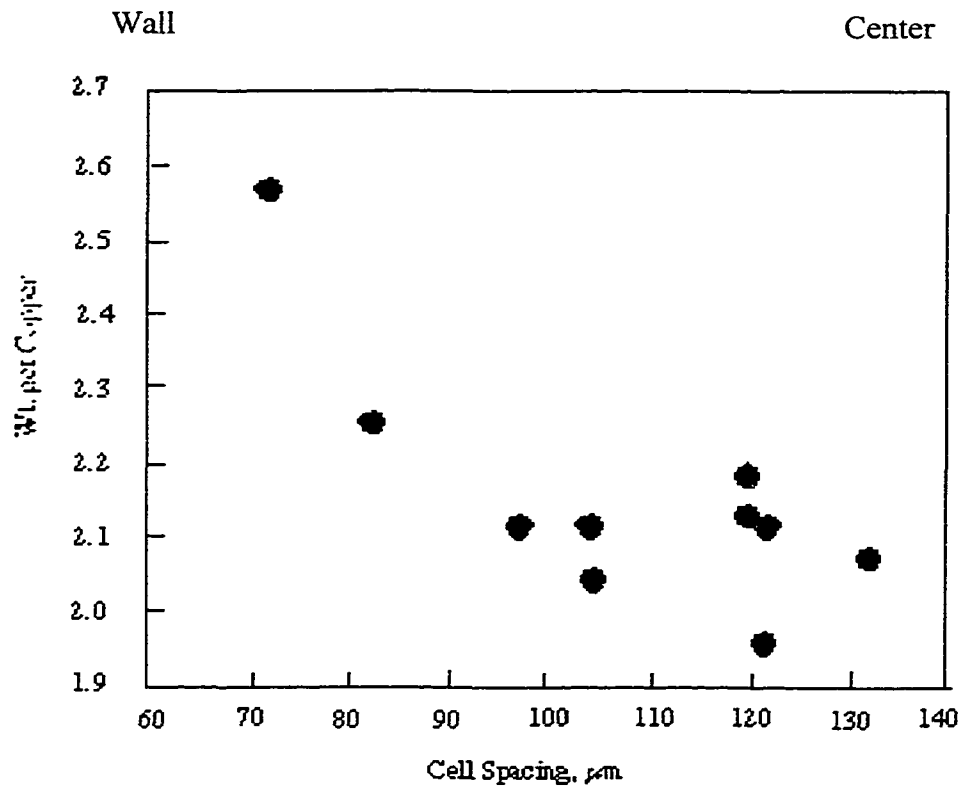


Fig. 16. The variation of primary spacing with composition at the center of cells or dendrite for a microstructure that exhibits the steeping effect. Al-4.0 wt pct alloy, directionally solidified at $1.83 \mu\text{m/s}$ at $G = 10.0 \text{ K/mm}$.

CHAPTER 5: UNSTEADY THERMO-SOLUTAL CONVECTION IN VERTICAL
BRIDGMAN SYSTEM AND PATTERN FORMATION IN SOLID PHASE :
MODELING, DYNAMICS AND MICROSTRUCTURE EVOLUTION

A manuscript to be submitted to *Journal of Fluid Mechanics*

P. Mazumder, R. Trivedi

Ames Laboratory, US-DOE, Iowa State University, Ames, IA 50011

* Department of Mechanical Engineering, prantik@iastate.edu

ABSTRACT

Direct numerical simulation of the thermo-solutal convection during the solidification of binary alloys is carried out. A finite-difference analysis is used for dynamic modeling of a two-dimensional prototype of the vertical Bridgman system that takes into account heat transfer in the melt, crystal, and the ampoule; melt flow and solute transport. Actual temperature data from experimental measurements are used for accurately describing the thermal boundary conditions. The simulations are restricted to an alloy system that rejects heavier solute in the melt during solidification. The complex interaction of vertical and lateral gradients of temperature and concentration leads to a range of complex spatio-temporal dynamics in the melt. The flow transitions and the nonlinear evolution following the transitions are carefully monitored. At high Rayleigh numbers, *intermittent oscillation-relaxation* convection is observed, and a physical mechanism is presented. The spatio-temporal dynamics of the flow and mass transfer are coupled with the phase change, and are found to be directly related to the spatial patterns observed experimentally in the solidified alloys. For hyper-peritectic Sn-Cd alloys, the unsteady convection gives rise to a new class of microstructure in which a tree-like primary phase in the center of the sample is embedded in the surrounding peritectic plane.

1. INTRODUCTION

A myriad of semiconductor and metal alloys are processed every day by directionally solidifying a multi-component melt using the vertical Bridgman technique. Single crystals of II-VI materials e.g. CdTe, HgCdTe used for detectors, II-V materials e.g. GaAs, InP used in opto-electronic devices and integrated circuits (Brown 1988), nickel-based super alloys used for fabrication of turbine blades, to name a few, are the materials processed by these techniques. The final properties of these materials strongly depend on the processing conditions and the phase diagram parameters of the multi-component alloys. It has been well established that there is an immediate need for understanding the fundamental transport processes, especially the fluid flow effects, in order to have better control and predictability of the final microstructures, solute/dopant field, stress fields, and hence the thermo-mechanical, electrical and optical properties of the solid crystals (Rosenberger 1979, Trivedi 1989, Brown 1992). This realization led to a large number of theoretical and numerical studies in the past fifteen years to predict and analyze the convective flow in the melt due to temperature and concentration gradients that exist and develop during solidification. The volume of work can be classified in two major categories based on the directions of the buoyancy terms. (1) The first category deals with the *double diffusive* convection due to vertical temperature and concentration gradients in the melt, with the former having a stabilizing effect and the latter having destabilizing effect on the density stratification (Coriell et al. 1980, McFadden et al. 1984, 1985, 1987, Heinrich 1988, Le Marec et al. 1996). This situation arises when the solute rejected from the interface in the melt is lighter than the solvent. (2) The second category deals with convection driven by the radial temperature gradient that always exists in the vertical Bridgman system (Chang and Brown 1983, Kim and Brown 1989, 1991). Even when the solute rejected is heavier than the solvent, the convection driven by the radial thermal gradient is found to be significant and causes considerable solute segregation in the sample. The modeling of the second case is particularly challenging since the driving force for convection (radial temperature gradient)

is not known a priori, and to be determined through the analysis. Although, significant advances have been made on both the modeling and understanding of the flow phenomena in both the geometries, there has not been much effort to couple the microstructure that develops in the solid crystals with the complex transport processes, especially unsteady convection. Only recently an attempt has been made to directly correlate the oscillation of double diffusive convection in alloys that reject lighter solute with the non-homogeneity in dopant concentration or striations in the crystals (Guerin et al. 1998). On the other hand, for alloys that reject heavier solute in the melt, no attempt has been made to explore the flow transitions, nonlinear evolution of the flows following the transitions, and their effects on the micro-structure formation in the solid crystals. In fact, it has been concluded from the limited range of work on these alloys that the flow in the melt always gets monotonically damped due to the resistance offered by the solute field to the thermal convection. However, in the present work we will demonstrate that although the strength of the mean flow may get dampened due to the solutal effect in these systems, the complex interaction of the thermal and solutal buoyancies can contribute to rich complexity in the spatio-temporal dynamics of the melt that was not achieved by the thermal convection alone. The spatio-temporal dynamics in the melt flow is found to give rise to a new class of microstructures, termed as *oscillating layered microstructure* in the two-phase peritectic alloys. The impetus behind this work is the recent experimental finding that the microstructure in two-phase peritectic alloys depend strongly on the sample diameter (Park and Trivedi 1998) and the subsequent physical mechanism proposed by Mazumder et al. (1999), in terms of oscillating fluid flow.

In section 2, we present a comprehensive review of the relevant literature on the modeling and analysis of melt convection in the vertical Bridgman system, and the status of understanding of the so called *banded microstructure* in peritectic alloys.

2. BACKGROUND

In this section we review the relevant research done on the fluid flow phenomena in the vertical Bridgman system, as well as the layered structure formation in peritectic systems.

2.1 Convection in Vertical Bridgman System

2.1.1 Double Diffusive Convection in Vertical Configuration Due to Unstable Solute Gradient

Coriell et al. (1980) and McFadden et al. (1985a, 1985b, 1986) pioneered the quantitative analysis of thermo-solutal convection during upward solidification of binary alloys when the solute rejected at the interface was lighter than the solvent, leading to a vertically destabilizing solute gradient in the presence of a vertically stabilizing temperature gradient. This situation corresponds to the classic *double diffusive* configuration (Veronis 1968, Turner 1973, Turner 1985, Moore and Weiss 1990), where a no-flow equilibrium solution is possible for the equations of motion. However, this base static state becomes unstable above the critical values of the appropriate Rayleigh numbers, and double-diffusive convection sets in, even though the net density decreases vertically upwards. Through linear stability analysis and numerical modeling, the critical solutal Rayleigh numbers were identified as functions of the solidification velocity for fixed temperature gradients (Coriell et al. 1980, McFadden et al. 1985a,b, 1986). For a narrow solutal Rayleigh number range, the flow was found to be time periodic. After this pioneering work, numerous studies were done on thermo-solutal convection in vertical solidification of binary alloys with a lighter solute in a heavier solvent (Le Marec et al. 1996 a,b, Heinrich 1988). Although, these studies could be related to systems where the melt is solutally unstable (e.g. Pb-Sn, Pb-Bi) and the dominant driving force for convection is the solutal buoyancy, the models cannot explain the

flow processes in alloys where the solute rejected is heavier than the solvent (e.g. Al-Cu, Sn-Cd). However, it's been experimentally observed that convection effects were present even in these systems where the solute is heavier than the solvent (Trivedi et al. 1999, Capper et al. 1983, Klaren et al. 1980, Rouzad et al. 1985, Tewari and Trivedi 1991, Tewari et al. 1993, Tewari and Shah 1996, Tewai 1986, 1988, 1990, Park and Trivedi 1998, Karma et al. 1998). The driving force for convection in these samples is the radial temperature gradient that always exists in all Bridgman systems due to its design (heating and cooling from side) and imperfections. The analytical solution of the heat conduction equation with boundary conditions as in Bridgman system (cooling zone and heating zone separated by an adiabatic zone), clearly showed that a significant lateral temperature gradient existed in the sample due to the nature of the boundary conditions (Naumann 1982). The magnitude of the gradient depends on the heat transfer coefficients or the Biot numbers between the furnace and the sample, and the thermal conductivity of the ampoule and sample material.

2.1.2 Convection in Vertical Configuration Due to Radial temperature Gradient

Chang and Brown (1983) first carried out the pioneering simulation where the thermal convection due to the lateral temperature gradient is considered. The prototype model considered vertical solidification of a binary alloy with zero solutal buoyancy inside a cylindrical ampoule. The temperature field was prescribed along the edge of the sample and consisted of isothermal hot and cold zones separated by an adiabatic zone. This is equivalent to assuming that there is no resistance to heat transfer between the furnace and the sample, or the overall heat transfer coefficient between the furnace and the sample is infinite, so that the temperature of the furnace is directly impressed on the ampoule wall. The calculations demonstrated intense convection even in the presence of a vertically stabilizing temperature gradient, driven by large radial temperature gradient near the adiabatic-hot junction. The radial temperature gradient is a consequence of the nonuniform temperature distribution along the ampoule boundary. The temperature in the melt is found to be greater near the

wall and lower at the center, and this temperature gradient leads to toroidal steady flows where the flow is up along the warmer wall and down along the cooler center. The radial segregation at the interface was found to be as large as 60% of the mean composition at certain cases.

Adornato and Brown (1987) improved this model by considering the finite thickness of the ampoule, finite heat transfer coefficient between the ampoule and the furnace, and the positive solutal buoyancy (the rejected solute is heavier than the solvent). Due to nonzero resistance to heat transfer between the furnace and the ampoule wall, the temperature of the furnace is hence not directly impressed on the outer ampoule wall, and instead is modeled by Newton's law of cooling. This difference in the heat transfer environment decreased the axial temperature gradient significantly, and substantially changed the flow features in the melt. Instead of the single toroidal cell flowing down along the centerline and up along the ampoule wall as seen previously (Chang and Brown 1983), there were two axially stacked counter-rotating cells, with the cell nearest to the interface moving downwards along the wall and up along the centerline. The model could predict the steady state (or quasi-steady state) interface shape, thermal, flow and solute field in the melt. It was found that the radial segregation was a nonlinear function of the thermal Rayleigh number and the maximum segregation occurred where the diffusive and convective rate of transport were the same order of magnitude. Inclusion of the solutal buoyancy, or positive solutal Rayleigh number seemed to damp the thermal convection. For certain combinations of thermal and solutal Rayleigh number and the growth rate, sideways diffusive instability was observed due to interaction of the lateral temperature gradient with the stabilizing axial solute gradient as predicted by Hart (1983)

The success of these models inspired a large number of numerical studies of the vertical Bridgman system (Carlson et al. 1984, Ouyang and Shyy 1996, 1997, Ouyang et al. 1997, Kaddeche et al. 1996, Kappurao et al. 1995 a, 1995b, Kim and Brown 1989, 1991, Brown and Kim 1991, Brown 1992). These models closely simulated the real Bridgman system, taking into account the heat transfer from the furnace to the ampoule of finite

thickness, conduction through the ampoule and the solid crystal, and conduction and convection in the melt. However, most of these models were restricted to steady and/or quasi-steady state analysis of either only thermal convection, or both thermal and solutal convections only in a narrow Rayleigh number range for few specific semi-conductor alloys. Although in a few cases the initial transient and the transient effects due to finite sample size have been explored for the same materials, the flow instabilities and transition of steady convection to oscillatory or chaotic convections have not been investigated. Moreover, since the alloys with specific thermo-physical characteristics were considered, the results could not be generally applied to other systems. For example, it was consistently reported that the generic structure of the flow in the system consisted of two toroidal cells stacked over each other, which rotated in opposite sense. We found in the present study, that this was due particularly to the lower thermal conductivity of the solid than the liquid for the semiconductor alloys considered, and hence could not be generalized. For alloys in which the solid phase has a higher thermal conductivity than the liquid phase, the counter-rotating cells are replaced by co-rotating cells stacked over each other (counter-clockwise arrows showing the sense of rotation in the lower cells). We showed that this causes lateral segregation at the interface in a sense opposite to that has been predicted earlier, and these facts will be elaborated upon in section 5.

2.2 Layered Structure Formation in Peritectic Alloys

Several experimental studies in the two-phase region of peritectic systems have shown the development of a so called *banded microstructure* in which *discrete* bands of primary (α) and peritectic (β) phases seemed to form alternately along the growth direction (Boettinger 1974, Brody and David 1977, Titchener and Spittle 1975, Fuh 1984, , Zeishler-Mashl and Lograsso 1997, Karma et al. 1998). A conceptual analytical model of *discrete banding* in peritectic systems was first proposed by Trivedi (1995) based on one

dimensional diffusive theory of directional solidification (Tiller et al. 1953). According to this model, a cycle of alternate nucleation and growth of primary and secondary phases can occur leading to alternate bands of α and β . The physical mechanism behind this alternate banding is that neither solid phase (α or β) can grow in steady state since the α (β) phase can nucleate and grow before the growing β (α) phase can reach its steady state. However, for this cyclic mechanism to occur, the initial composition of the alloy must be within a *banding window* which is a function of the phase diagram variables and the nucleation undercoolings of both the solid phases (see Fig. 1). The *banding window* always falls on the *hypoperitectic region* (C_α to C_β), and for small but finite undercoolings a typical window for Sn-Cd is $0.6 \leq C_0 \leq 0.9\%$ as shown by the lightly shaded region on the Sn-Cd phase diagram (Fig. 1). If the initial composition of the alloy is on the left side of the banding window ($< 0.6\%$ for Sn-Cd), only the α phase will grow and it will reach its steady state after sufficient length of solidification. If the initial composition is on the right of the banding window ($> 0.9\%$ for Sn-Cd), initially an α phase will grow until the β phase nucleates and grows towards its steady state value. Several experimental studies in the Sn-Cd system have reported band formation in *hyperperitectic region* (C_β to C_p) which is not supported by the diffusive model. Fig. 1 shows the composition ranges predicted by the diffusive model (Trivedi 1995) and the composition range over which banding has been observed experimentally (Boettinger 1974, Brody and David 1977, Zeishler-Mash 1997). While modeling *band structure* formation in the Pb-Bi system, Karma et al. (1998) realized that Pb-Bi system could be highly convective due to the rejection of lighter solute at the interface and assumed that the vigorous flow in the melt would cause the formation of a concentration boundary layer of constant thickness near the interface. This model retained the concept of the *banding cycle* and *banding window* of the diffusive model (Trivedi 1995) but developed the criterion for *banding* as passing of the perfectly mixed bulk composition through the banding window predicted by the diffusive model. This modified model could predict occurrence of bands for initial compositions less than the lower limit of the *banding window*, that is for $C_\alpha < C_0 < C_\beta$.

However, it still could not explain the formation of bands for initial compositions greater than the upper limit of the *banding window*, particularly in the hyperperitectic range. The model fell short by about a factor of five in predicting the band spacing. Although an attempt was made to model the effect of convection, the one dimensional analysis inadvertently submerged the salient features such as lateral segregation and inhomogeneity caused by convection. Furthermore, the model did not consider the possibility of natural convection that will be present in the Sn-Cd system due to the rejection of heavier solute at the interface.

Recently, Park and Trivedi (1998) have carried out a systematic experimental study of simultaneous solidification of multiple samples of diameters varying from 200 microns to 6 mm in order to gradually reduce and calibrate the effects of melt convection, if present, on *band formation*. The authors reported that the solidification microstructure of a sample of initial composition in the *hyperperitectic region* varied with the sample diameter. In thin samples (diameter less than 800 microns) only an α to β transition took place at a sharp and flat interface in agreement with the diffusive model. The corresponding microstructure is shown in Fig. 2a, where the darker and lighter regions are the α and β phases respectively. On the other hand, in large samples (diameter 6.0 mm), for the same composition and same experimental conditions as in the thin sample, a complex two-phase microstructure was observed, Fig. 2b and 2c. On a plane of polish close to the surface of the sample, the microstructure appeared as discrete islands of α in the continuous β matrix, Fig. 2b. However, on a plane of polish through the center of the sample, the microstructure appears as an oscillating structure in which both the primary and peritectic phases are interconnected, and the primary phase forms a large single tree-like structure that is surrounded by the peritectic phase, Fig. 2c. The discrete islands of the α phase in Fig. 2b are hence the projections of the α branches of the continuous tree like structure on the plane of the polish.

The formation of this intriguing tree-like structure in large samples have recently been explained by Mazumder et al. (1999) in terms of convection in the melt. The

fundamental concept behind the physical mechanism proposed by the authors is that the complex tree-like microstructure in the large samples is a result of the time dependent segregation of solute at the solidification interface due to unsteady convection in the melt and the possibility of simultaneous growth of both the solid phases. A simple model has been developed where the advection-diffusion equation for solute transport was solved, with *prototype flows* to model the effect of zero, non-zero steady, and non-zero oscillating convection. This simplified model supported the mechanistic model developed by the authors, and proved that oscillatory convection in the melt, if present, could give rise to two-phase oscillatory microstructure in the peritectic alloys. This tree-like structure, called *oscillatory layered structure* hereupon, is distinguished from the *band structure* based on their fundamentally different formation mechanisms. The latter is formed due to the inherent oscillatory dynamics of repeated nucleation and growth of the two solid phases only if the initial composition is within a narrow *banding window* (Trivedi 1995, Karma et al. 1998). On the other hand, convection induced oscillatory layered structures could form for any initial composition within the entire two-phase region. In the limiting condition of zero convection (in thin tubes) the model showed only α to β transition for hyperperitectic alloys, and discrete bands for alloys of composition in the banding window (Mazumder et al. 1999, Mazumder 1999). Although it was shown that oscillatory convection, if present, could produce oscillatory microstructure, no attempt has been made to investigate the flow dynamics which requires rigorous modeling and analysis of the transport processes in the vertical Bridgman system. In addition to prove that unsteady convection would indeed be present during the solidification of large samples (6 mm diameter) of peritectic alloys, a rigorous model is needed to predict the actual flow dynamics (steady, periodic, quasi-periodic, non-periodic) that is necessary for the quantitative prediction of the layer thickness and spacing.

3. OBJECTIVE

The objective of the present paper is two-fold. (1) We will first develop a physically realistic numerical model of the vertical Bridgman system that will accurately simulate the thermal field in the ampoule, melt and the crystal. This is absolutely necessary since the details of the transport processes and the final microstructure of the material grown out of the melt depend strongly on the thermal field. Through direct numerical simulation of the constitutive transport equations, visualization of the instantaneous thermal, solutal, flow, and vorticity fields, and analysis of the time series plots we will investigate in detail the flow dynamics and transitions associated with thermo-solutal convection. Although any alloy system with any initial composition could be simulated with the model developed here, we will restrict our attention to Sn- 1.3 % Cd. The entire range of Rayleigh numbers corresponding to the solidification of Sn-Cd alloy in tubes of diameter 0.2 to 6 mm will be considered. It will be shown that for conditions equivalent to solidification inside a 6 mm diameter tube, the flow in the melt is indeed unsteady and shows *intermittent oscillation-relaxation* behavior. A physical mechanism for the intermittent flow behavior will be presented. (2) In the second phase we will couple the time dependent flow and hence the time dependent solute segregation at the solid-liquid interface with the microstructural pattern that will develop in the solid sample. The formation of oscillating α layers in response to the dominant modes of flow oscillation will be illustrated which will support the conceptual mechanistic model developed earlier (Mazumder et al. 1999)

4. MATHEMATICAL FORMULATION

The simulations presented here are for the analysis of thermo-solutal convection, heat transfer, and directional solidification in a two-dimensional prototype of the vertical

Bridgman system shown schematically in Fig. 3. The prototype includes a binary melt and crystal contained in a two dimensional ampoule that is surrounded by a moving Bridgman furnace. The furnace consists of hot and cold zones separated by an adiabatic zone of finite thickness. Directional solidification takes place as the furnace assembly is moved upwards with a constant speed V_p . In a real growth system, and in the absence of significant convection, the vertical velocity of the interface asymptotically reaches the steady state velocity V_p with a time constant $\sim D / (k V_p^2)$ where D , and k are the solute diffusivity, and partition coefficient for the phase diagram (Smith et al. 1953). With convection, the time to reach steady state may differ from that with diffusion only, and will strongly depend on the nature of convection. In addition, the lateral temperature and solute gradient may induce curvature in the advancing solid-liquid interface. In the case of oscillating convection, the interface may fluctuate back and forth and may lead to periodic melting and freezing (Muller and Ostrogorsky 1994). In order to capture the details of the solid-liquid interface shape and dynamics, the interface needs to be treated as a free boundary and tracked numerically. This demands excessive numerical costs and computational resources if one needs to simulate both the unsteady convection and the free interface propagation. Since, we focus on the time dependent convection and its effect on microstructure development, we do not consider the curvature of the interface and assume that the interface is moving with the constant speed V_p . This also helps to decouple the effect of only transient convection from the effects of complex interactions of convection and dynamics of the deformable interface, on the microstructure development. In particular, the assumption of negligible curvature of the interface is satisfactory, especially for Sn-Cd samples, due to very high axial temperature gradient achieved in these samples, since the maximum deflection of the interface (the vertical distance between the center and the edge of the sample) scales with the ratio of lateral temperature gradient to the axial temperature gradient. The quenching experiment done to visualize the interface shape (Mazumder et al. 1999) bolstered the fact that the

interface remains flat for all practical purposes as long as the pulling velocity is lower than the critical velocity for plane front instability (Mullins and Sekerka 1963).

The field variables, velocity, pressure, temperature and solute composition, are described in a dimensionless coordinate reference frame (x,y) that is fixed with the interface as shown in Fig. 3. Variables are put in dimensionless form by scaling the coordinates (x,y) and lengths with the inner width of the ampoule 'd', time t with the scale for heat diffusion d^2/α_l , velocity $v(x,y,t)$ with characteristic velocity of heat diffusion in liquid α_l/d , where α_l is the thermal diffusivity of the liquid. The dimensionless composition and temperature fields are defined as

$$c = \frac{C - C_0}{C_0} \quad (1)$$

$$\theta = \frac{T - T_C}{T_H - T_C} \quad (2)$$

where T_H and T_C are the characteristic temperatures of the hot and cold zones of the furnace. The maximum and minimum temperatures in the hot and cold zones of the furnace are usually taken as these reference temperatures.

Convection in the binary melt is driven by density gradients due to both the temperature and the concentration gradients. The density variation due to temperature and concentration variation can be simply approximated through the following linear relationship (Turner 1973, Tritton 1988)

$$\rho(C, T) = \rho_0 [1 - \beta_T(T - T_0) + \beta_S(C - C_0)] \quad (3)$$

where the reference density ρ_0 is that of the melt at some reference temperature T_0 and concentration C_0 . The terms β_T and β_S are the thermal and solutal expansion coefficients for

the melt. For most metals, the density of the melt decreases with temperature and hence β_T is positive. However, the density can decrease or increase with increasing concentration depending on the binary alloy, and β_S could be either positive or negative. For the Sn-Cd system, the rejected solutes are heavier than the solvent, and hence β_S are positive. The two-dimensional time-dependent Boussinesq approximated Navier-Stokes equations describing the fluid flow are

$$\frac{\partial u}{\partial t} + (u - v_p) \frac{\partial u}{\partial x} + v \frac{\partial u}{\partial y} = -\frac{\partial p}{\partial x} + \left[\frac{\partial^2 u}{\partial x^2} + \frac{\partial^2 u}{\partial y^2} \right] + \frac{Ra_T}{Pr} \left[N c - (\theta - \theta_0) \right] \quad (4)$$

$$\frac{\partial v}{\partial t} + (u - v_p) \frac{\partial v}{\partial x} + v \frac{\partial v}{\partial y} = -\frac{\partial p}{\partial y} + \left[\frac{\partial^2 v}{\partial x^2} + \frac{\partial^2 v}{\partial y^2} \right] \quad (5)$$

The continuity equation :

$$\frac{\partial u}{\partial x} + \frac{\partial v}{\partial y} = 0 \quad (6)$$

where u, v and p denote the nondimensional velocity components in the x and y directions and pressure, θ_0 is a reference temperature, and N is the buoyancy ratio defined as

$$N = \frac{Ra_S}{Ra_T} = \frac{\beta_S C_0}{\beta_T (T_H - T_C)} \quad (7)$$

The thermal (Ra_T) and solutal (Ra_S) Rayleigh numbers are defined as

$$Ra_T = \frac{g\beta_T(T_H - T_C)d^3}{\nu\alpha_l}$$

$$Ra_S = \frac{g\beta_S C d^3}{\nu\alpha_l}$$

where, ν is the kinematic viscosity of the melt. Pressure can be eliminated from equations (3) and (4) through cross differentiation and subtracting the resulting expressions (Tritton 1988).

Defining vorticity (ω) and stream-function (ψ) as

$$\omega = \frac{\partial v}{\partial y} - \frac{\partial u}{\partial x} \quad (8)$$

$$u = \frac{\partial \psi}{\partial y} \quad (9 \text{ a})$$

$$v = -\frac{\partial \psi}{\partial x} \quad (9 \text{ b})$$

the resulting set of equations become

$$\frac{\partial \omega}{\partial t} + (u - v) \frac{\partial \omega}{\partial x} + v \frac{\partial \omega}{\partial y} = \left[\frac{\partial^2 \omega}{\partial x^2} + \frac{\partial^2 \omega}{\partial y^2} \right] + \frac{1}{Pr} \left[-N \frac{\partial \theta}{\partial y} + Ra \frac{\partial \theta}{\partial y} \right] \quad (10)$$

$$\frac{\partial^2 \psi}{\partial x^2} + \frac{\partial^2 \psi}{\partial y^2} = -\omega \quad (11)$$

The solute and heat transport equations in the melt are

$$\frac{\partial c}{\partial t} + (u - v_p) \frac{\partial c}{\partial x} + v \frac{\partial c}{\partial y} = \frac{1}{Le} \left(\frac{\partial^2 c}{\partial x^2} + \frac{\partial^2 c}{\partial y^2} \right) \quad (12)$$

$$\frac{\partial \theta}{\partial t} + (u - v_p) \frac{\partial \theta}{\partial x} + v \frac{\partial \theta}{\partial y} = \left(\frac{\partial^2 \theta}{\partial x^2} + \frac{\partial^2 \theta}{\partial y^2} \right) \quad (13)$$

The dimensionless groups that appear in the equations are defined in Table 1. The heat transport equations in the solidified crystal and ampoule are

$$\frac{\partial \theta}{\partial t} + v_p \frac{\partial \theta}{\partial x} = \frac{\alpha_s}{\alpha_l} \left(\frac{\partial^2 \theta}{\partial x^2} + \frac{\partial^2 \theta}{\partial y^2} \right) \quad (14)$$

$$\frac{\partial \theta}{\partial t} + v_p \frac{\partial \theta}{\partial x} = \frac{\alpha_a}{\alpha_l} \left(\frac{\partial^2 \theta}{\partial x^2} + \frac{\partial^2 \theta}{\partial y^2} \right) \quad (15)$$

where α_s and α_a are the thermal diffusivities of the solid crystal and the ampoule, respectively.

The velocity boundary conditions on the ampoule and at the melt/crystal interface specify that there is no slip relative to the solid surfaces. The concentration and temperature boundary conditions at the interface are obtained from conservation of mass, energy, and continuity of temperature. Since the interface is not allowed to deform, all the usual solidification boundary conditions can not be satisfied. In particular, it is not required to equate the interface temperature to the equilibrium temperature (McFadden et al. 1984), which was found to have insignificant effect on the onset and nature of convection from linear stability analysis (McFadden et al. 1984). The composition boundary condition on the advancing solid-melt interface is

$$\frac{\partial \bar{x}}{\partial x} = -v_p \text{Le} (1+c) (1-k) \quad (16)$$

where, k is the partition coefficient. The thermal boundary conditions at the interface are

$$-\kappa_s \left. \frac{\partial \theta}{\partial y} \right|_s = -\kappa_l \left. \frac{\partial \theta}{\partial y} \right|_l; \quad \theta_s = \theta_l \quad (17)$$

The latent heat effect is neglected in the heat flux balance condition of equation (17) since it is a much smaller compared to the conduction flux terms (Flemings 1974, Kurz and Fisher 1984). The vertical ampoule walls are impervious to mass flux. Along the ampoule inner wall the continuity of the heat flux and the temperature between the melt, crystal and ampoule are specified.

$$\begin{aligned} -\kappa_s \left. \frac{\partial \theta}{\partial y} \right|_s &= -\kappa_a \left. \frac{\partial \theta}{\partial y} \right|_a; \quad \theta_s = \theta_a \\ -\kappa_l \left. \frac{\partial \theta}{\partial y} \right|_l &= -\kappa_a \left. \frac{\partial \theta}{\partial y} \right|_a; \quad \theta_l = \theta_a \end{aligned} \quad (17)$$

The outer surfaces of the ampoule are assumed to exchange heat with the surrounding furnace according to Newton's law of cooling,

$$\begin{aligned} \frac{\partial \theta}{\partial y} \Big|_a &= -Bi_c (\theta_\infty - \theta_a), \quad \text{in cold zone} \\ \frac{\partial \theta}{\partial y} \Big|_a &= -Bi_a (\theta_\infty - \theta_a), \quad \text{in adiabatic zone.} \end{aligned} \quad (18)$$

$$\frac{\partial \theta_a}{\partial y} = -Bi_h (\theta_\infty - \theta_a), \quad \text{in hot zone}$$

where Bi_h and Bi_c and Bi_a are the nondimensional heat transfer coefficients, or the Biot Numbers in the hot, cold and adiabatic zones respectively. The proper choice of the heat transfer coefficients is done through regression analysis of computed axial and radial temperature profiles with measured experimental data. The details are given in the result section.

4.1 Boundary Condition at Top and Bottom Surfaces

The boundary conditions for heat transfer at the top and bottom surfaces (i.e. at $x = 0$ and $x = H$) are not easy to define and need special care. The most popular practice is to let the temperature equilibrate with the local temperatures of the furnace (Chang and Brown 1983, Adornato and Brown 1987, Kim and Brown 1989, 1991). But, this requires careful selection of the length of the computational domain. Using shorter computational domains than those required for the temperature in the liquid and solid to gradually reach the isothermal furnace temperatures can lead to unrealistically high axial and radial temperature gradients. These points will be discussed with supporting results in the following section.

4.2 Grid System and Numerical Scheme

Special care was taken to properly resolve all the length scales associated with the different transport processes. Due to the small mass diffusivity of the melt, the solute layers are extremely thin compared to the thermal and momentum length scales. Two different grid systems were used to accurately resolve the length scales. The thermal and flow fields were solved on a grid system that used 107 nodes in the radial direction (covering the sample and

the ampoule walls on both sides) and 61 nodes in the axial direction per unit distance. The concentration field was solved on a grid system with 161 nodes in the radial direction (in the melt only) and 301 nodes in the axial direction per unit distance. This means that the grid for concentration calculation was five and two times finer than the thermal and flow field grid in the axial and lateral directions respectively. Uniform mesh spacing was used over the entire computational domain for both the grid systems. Sensitivity of the numerical solutions to mesh spacings are conducted by comparing the solutions from the grid system mentioned with yet finer grid arrangement. The finest grid system had 213 nodes in the radial direction (covering the sample and the ampoule walls on both sides) and 121 nodes in the axial direction for unit distance to solve thermal and velocity quantities, and 321 by 501 nodes per unit distance along radial and axial directions to compute the concentration field. Almost perfect agreement between the solutions from the two grid systems was achieved for all values of Ra_T . The grid spacings are chosen such that all the cell Reynolds numbers and cell Peclet numbers (mass and thermal) were much smaller than unity throughout the computations (Fletcher 1991), or

$$\begin{aligned} (u - v_p) \Delta x \ll 1, \quad v \Delta y \ll 1 \\ (u - v_p) Le \Delta x_c \ll 1, \quad v Le \Delta y_c \ll 1 \end{aligned} \tag{19}$$

where Δx and Δy are the grid spacings for calculation of thermal and flow fields, and Δx_c and Δy_c are the grid spacings for the concentration grid. Although, ADI method for two dimensional problems are unconditionally stable, time steps of $\Delta t = 0.1, 0.05, 0.01,$ and 0.001 are used to test the stability and accuracy of the solutions. It was found that time step independent solution was obtained for $\Delta t \leq 0.01$ and hence $\Delta t = 0.01$ is used for all the computations.

The partial differential equations (10), (12), (13), (14) and (15) were discretized by a second order alternate direction implicit (ADI) finite difference scheme (Peaceman and Rachford, 1956; Lapidus and Pinder 1982). The tri-diagonal system of algebraic equations

that arise while sweeping along each direction (x or y) were directly solved using Thomas algorithm (Fletcher 1991). The Poisson equation (11) was solved using a fast elliptic solver FISHPAK developed by NCAR (National Center for Atmospheric Research).

5. BENCHMARKING WITH PUBLISHED RESULTS

In order to gain confidence in the present mathematical and numerical model we needed to benchmark the model with existing numerical results. However, to the author's knowledge this is the first work where the unsteady convection is explored in a vertical Bridgman system where both the axial temperature and solute gradients are stabilizing. We hence could not make an exact comparison between our entire model with others. However, comparison of the results of the present numerical model with the existing results for diverse systems with various different conditions gave very good agreement. These are listed in this section.

5.1 Case Study 1: Steady State Convection in Differentially Heated Square Cavity Filled With Air, $Pr = 0.71$

de Val Davis and Jones (1983) organized a symposium for benchmarking the codes for calculating natural convective flows inside differentially heated square cavities. One vertical wall was maintained at a higher temperature than the other vertical wall. The bottom and top horizontal walls were insulated. The cavity was filled with air, $Pr = 0.71$. The value of stream function at the center of the cavity, the maximum value of stream function and its location, the maximum value of velocity components on mid-planes were produced by thirty researchers. Our computational results for this system agreed closely with the compiled results and are compared with two independent results in Table 1. The stream function at the center of the square cavity, the maximum stream function, the maximum u and v on the mid plane and their locations are presented for different thermal Rayleigh numbers.

5.2 Case Study 2: Oscillatory Convection in Low Prandtl Number Fluid Inside Rectangular Cavity

Recently, benchmark studies of two-dimensional unsteady convection of low Prandtl number fluids ($Pr = 0$ and 0.015) in a differentially heated horizontal cavity (ratio of horizontal length to vertical height = 4) was carried out in the GAMM workshop (Roux 1989). Using widely diverse numerical techniques (finite difference, finite volume, finite element, spectral method), a group of scientists provided accurate determination of the onset of oscillations, period doubling, quasi-periodic behaviour, reverse transition, and hysteresis loops, for a wide range of Grashof numbers. Our computations for the same problem, were in excellent agreement with the results provided by the workshop. The critical Grashof numbers for various flow bifurcations, and the spatial and temporal dynamics of the flow following each instability almost exactly reproduced the published results. The time history of one such solution is compared with the results by Behnia and de Vahl Davis (1989) in Fig. 4. The details of the conditions can be found in Roux (1989) and are not repeated here. The plot of axial and lateral velocity components, and the stream function at fixed locations show initial singly periodic oscillations up to time 1.10 and settling of the flow towards a steady value. The agreement between the two computations is very close.

5.3 Case Study 3: Transient Thermo-Solutal Convection of Pb-Sn Alloy in a Differentially Heated Square Cavity

In the previous case studies, we considered steady and oscillatory convections due to horizontal thermal gradients only. In this study, we calculate two-dimensional thermosolutal convection in Pb-Sn melt induced by horizontal temperature and concentration gradients, and compare our results with those by Bergman and Hyun (1996). The system considered is a two-dimensional square cavity. The top and bottom of the cavity were insulated, while the

left and right faces were held at uniform cold and hot temperatures, respectively. The left and right walls are maintained at Sn-rich (light) and Pb-rich (heavy) uniform concentrations. Hence, thermal buoyancy leads to a thermally driven core (TDC) with counterclockwise circulation, and a solutal-driven boundary layer (SDBL) adjacent to the walls with clockwise circulation. Bergman and Hyun (1996) carried out their numerical simulation using the spectral method, and obtained solutions of high accuracy over a wide range of thermal and solutal Rayleigh numbers, which we could reproduce very closely with our finite difference model. The comparison of one set of calculations is shown in Fig. 5, where the predicted concentration and stream function fields are plotted at four different time levels from the start of the flow. The details of the parameters can be found in Bergman and Hyun (1996, Fig. 2).

5.4 Case Study 4: Quasi-Steady Directional Solidification of Hg-Cd-Te Alloys

So far we considered steady and unsteady thermal convection, and thermo-solutal convection in simple square or rectangular geometries where the boundary conditions on the walls were precisely prescribed. In this section, we consider vertical solidification of Hg-Cd-Te alloys in a 2D ampoule and compare the results with axisymmetric calculations of Adornato and Brown (1987). The models took into account the finite heat transfer between the furnace and the ampoule, the conduction in the ampoule and solid crystal, and conduction-convection in the melt. A set of results on the steady state thermal, flow and solute fields calculated by Adornato and Brown (1987), is shown in Fig. 6, for $Ra_T = 5 \times 10^7$. The interface is slightly concave upwards, the generic structure of the flow is bi-cellular where the upper and lower vortices are moving in counter-clockwise and clockwise directions, respectively, and the solute field is such that the central region is richer in solute. The corresponding plots obtained by the present model is shown in Fig. 7 b. The present model is based on the assumption of a flat interface moving with constant velocity V_p , and hence is fixed with respect to the thermal assembly throughout the calculation. Moreover,

the present model is for a two dimensional geometry, as opposed to Adornato and Brown's (1987) axisymmetric geometry. Nevertheless, the agreement between the two models is remarkably close. We also compared our model with a two dimensional model by Alexander et al. (1989), and the quantitative agreement between the results is almost perfect.

6. EFFECT OF THERMAL CONDUCTIVITIES OF SOLID AND LIQUID ON THE THERMAL, FLOW AND SEGREGATION PATTERNS

For most real materials the thermal conductivities in the liquid and solid phases are not equal. The difference in thermal conductivities in the two phases lead to different axial thermal gradients in the two phases at the interface. Assuming that the heat flow is uniaxial at the interface, it can be derived that the axial gradients are inversely proportional to the conductivities of each phase due to the continuity of heat flux, provided the latent heat effect is small. The difference in thermal conductivities among the phases and the ampoule material also leads to the lateral temperature gradient near the interface. The magnitude and the direction of this temperature gradient depend on the relative values of the conductivities, or K_s/K_L for a fixed ampoule material. Most metallic semiconductors have higher conductivity in the liquid ($K_s/K_L < 1$) while most metallic alloys have higher conductivity in the solid phase ($K_s/K_L > 1$).

Previous investigators consistently reported that the generic structure of the convection pattern in a Bridgman system consisted of two axially stacked counter-rotating torroidal cells, with the cell nearest to the interface moving downward along the wall and up at the centerline (Adornato and Brown 1987, Kim and Brown 1989, 1991, Brown and Kim 1991). The mismatch between the thermal boundary condition at the hot-adiabatic junction led to a lateral temperature gradient in that region such that the fluid near the ampoule was hotter than the fluid near the center, and hence the flow was up along the wall and down along the centerline in the upper cell. In contrast, in the region of melt adjacent to the interface, the fluid was hotter near the centerline than the material near the ampoule, and

hence the lower cell moved up along the centerline. The authors attributed this fact to the “particular combination of the long gradient zone and the different, but comparable, thermal conductivities between melt, crystal and ampoule” (Adornato and Brown 1987). We however, found that this fact was actually due to the lower thermal conductivity of the solid than that of the liquid for the alloys (Ga-Ge, Hg-Cd-Te) under consideration. However, when the solid has a higher thermal conductivity than the liquid, as in the case of most metallic alloys, a significantly different result is obtained. The radial temperature gradient in the region near the interface changes sign if the solid has higher thermal conductivity than the liquid. In this case both the cells rotate in the same sense (up along the wall) with a thin layer of almost stationary liquid between them. In order to illustrate this point and to benchmark our numerical model, we carried out a simulation of GaGe growth in Boron-Nitride tube at exactly the same condition as in Adornato and Brown (1987), at $Ra_\tau = 5 \times 10^7$ (as defined by Adornato and Brown 1987) for two cases. In the first case all the variables and parameters are the same as that of Adornato and Brown (1987). The thermal conductivity of the solid phase is smaller than that of the liquid phase, $K_s=0.17$, $K_L=0.39$. In the second case, we used $K_s=0.39$, $K_L=0.17$. The temperature difference between the edge and the center of the sample is plotted along the sample length in Fig. 7a for the two cases. For ($K_s/K_L < 1$) the center is hotter than the edge near the interface. In this case the radial temperature profile at the interface is convex upwards (not shown). For ($K_s/K_L > 1$) the temperature near the edge is higher than that in the center, and the temperature profile at the interface is concave upwards. This difference will also lead to opposite curvatures in the solid liquid interface. For the former case the interface will be concave upwards (for most metallic alloys, Al-Cu, Pb-Bi) and for the latter case, it will be concave downwards as observed for semi-conductor materials. However, the lateral temperature gradient near the hot-adiabatic junction has the same sign for both the cases, since it is set solely by the mismatch in boundary condition at the junction and also the difference in thermal conductivities between the melt and the ampoule. However, the temperature gradient is higher at that junction when the thermal conductivity of the ampoule ($K_A = 0.26$) is greater

than that of the melt, that is for $K_L=0.17$. In Fig. 7 b and 7 c we plot the temperature, flow and solute fields for the two cases. The results in Fig. 7 b reproduce the thermal, flow and concentration fields, Fig. 5,7,9 of Adornato and Brown (1987) with $K_L=0.39$ and $K_S=0.17$. In Fig. 7 c, we plot the thermal, flow and solute fields with $K_L=0.17$ and $K_S=0.39$. The curvature of the isotherms near the interface changes sign. The counter-rotating cells are now replaced by two co-rotating cells and that significantly alters the composition field. The segregation profile makes the region near the ampoule wall richer in solute than in the center, unlike the previous case.

7. THERMAL CHARACTERIZATION: DETERMINATION OF BOUNDARY CONDITIONS AND BIOT NUMBERS

The temperature distribution in the melt, crystal and the ampoule can be accurately predicted if the temperature distribution on the outer surface of the ampoule is precisely known. In many cases the outer boundary temperature distribution is fixed by equating it to the furnace temperature profile. This is equivalent to assuming zero thermal resistance or infinite heat transfer coefficient or Biot number between the furnace and the ampoule wall. However, in real situations, the heat transfer coefficient or Biot number is finite and the temperature of the furnace is not directly impressed on the outside wall of the ampoule. Another existing method (Adornato and Brown 1987, Kim and Brown 1989, 1991), and also used in this work is to model the interaction between the ampoule and the furnace by Newton's law of cooling and using appropriate Biot number as in equation 18. However, the temperature distribution on the outer surface, and the axial and radial temperature gradients in the sample strongly depend on the choice of the Biot numbers. Hence, for physically realistic modeling, the appropriate selection of Biot number becomes extremely important. The boundary conditions for heat transfer at the top and bottom of the ampoule are also not easy to define. One common method was to equilibrate these boundary temperatures with the local furnace temperatures (Adornato and Brown 1987, Kim and

Brown 1989). However, the latter needs careful selection of the length of the computational domain. Using a smaller domain than that required for the temperature in the liquid and solid to asymptotically equilibrate with the local furnace temperatures may lead to over-predicted axial and radial temperature gradients. The above points, that is the importance of the choice of Biot numbers and computational domain, are exemplified in Fig. 8. The axial temperature profiles along the melt and crystal center are plotted for two different Biot numbers ($Bi = 10$ and 0.4) and two different axial domain ($X_m = 4$ and 20). Higher Biot numbers and smaller computational domain usually lead to higher axial temperature gradient. This is also associated with higher radial temperature gradient (not shown in the picture). The proper selection of Biot numbers can only be made through matching of computed and measured temperature profiles. The temperature measurement also suggests a judicious choice of the computational domain. We measured the axial temperature profiles along the centerline of the sample (both in solid and liquid), the outer surface of the ampoule and the furnace using three thermo-couples as shown in Fig. 9 (Simsek and Mazumder 1998). The measured temperature distribution in the furnace is used as the thermal boundary condition for θ_x in equation 18. Computed temperature profiles are compared with the experimental data and the closest match yielded the right choice of Biot numbers. It is to be noted that even after ~ 10 ampoule diameter (6 cm) the temperature in the melt did not equilibrate with that of the furnace.

8. BACKGROUND OR BASE FLOW

Prior to the initiation of solidification, natural convection in the melt already exists due to the radial temperature gradient that arises as a result of the furnace-ampoule assembly. We call this preexisting thermally driven flow *background or base flow*. Although the base flow is initiated solely by the radial temperature gradient, its intensity and dynamics are set by the combined effects of the vertical and radial temperature gradients. The radial

temperature gradient drives the vortices up along the warmer side walls and down along the cooler center, while the vertical temperature gradient (usually much larger than the horizontal temperature gradient) tends to dampen the flow. For precise scaling of the thermal convection with respect to the two thermal gradients, one needs to use a Rayleigh number based on the horizontal temperature gradient and a ratio of the vertical to horizontal temperature gradients. However, in a complex simulation of the vertical Bridgman system, both the radial and vertical temperature gradients are unknown prior to the simulation. The Rayleigh number based on the maximum vertical temperature difference between the hot and cold zones of the furnaces hence may not be a proper scaling parameter for the intensity of the base flow (Adornato and Brown 1987). However, since the horizontal temperature gradient is proportional to the vertical temperature gradient (Adornato and Brown 1987, Mazumder 1999), a Rayleigh number based on the horizontal temperature gradient will be proportional to the Rayleigh number based on the vertical temperature difference. Hence, an informative scaling relationship can still be expected between the intensity of the convection and Ra_T . It is important to characterize the base flow so that the effects of the interaction of solutal and thermal buoyancies during the course of the solidification could be studied separately. We computed the base flows for $10 < Ra_T < 10^8$, $V_p=0$ and $N = 0$ (or $Ra_S=0$). The flows were found to be steady over the entire range of Ra_T considered. The time evolution of the stream function ψ_c at a fixed location C ($x=0.55$, $y=0.25$), and the stream lines of the flow for various Ra_T are shown in Fig. 10 and 11. The steady states are reached beyond short initial transients that depend on the values of Ra_T . However, the order of magnitude of the initial transient is within $\sim O(1)$, that is the time scale for heat diffusion (d^2/α_l). The generic structures of the flow for all Ra_T are similar and consist of two co-rotating vortices or cells stacked on each other on each side of the central axis (Fig. 11). The bi-cellular structure develops due to the non-uniformity of the lateral temperature gradient along the length of the sample. Due to the nature of the thermal boundary conditions, the lateral temperature gradients are localized near the solid-liquid interface and the hot-

adiabatic junction as also been observed by Adornato and Brown (1987), Kim and Brown (1989, 1991). The lateral temperature differential in the central region of the adiabatic zone is very small and hence the flow is very weak there. The lower cells are driven by the radial temperature gradient near the interface. However, the upward flow in the lower cells turn around near the center of the adiabatic zone since there is not enough upward buoyancy present to drive the fluid against the vertical temperature gradient. The upper cells are driven by the lateral temperature gradient near the adiabatic-hot junction. For $Ra_T > 10^6$, another pair of vortices appear near the top surface of the melt. This is due to the fact that an artificial boundary is placed at that location where the flow is forced to turn around or the vertical velocity component is forced to vanish. For large Ra_T , the high shear developed in this region may cause the formation of the third vortex. For quantitative analysis of the flow intensity as a function of Ra_T , we plotted three quantities with respect to Ra_T in Fig. 12. The three quantities are the stream function ψ_c at C, the positive maximum of the stream function in the melt ψ_{max} , and the maximum of the vertical velocity component of the melt convection u_{max} . ψ_{max} corresponds to the stream function value at the center of the lower cell. All the three quantities vary linearly with the Rayleigh number, up to $Ra_T \sim 5000$. This suggests that in that range, the nonlinear advection terms in the Navier-Stokes equation are small, and steady state is achieved through a balance of the buoyancy term and the viscous term (Tritton 1988). Order of magnitude balance between the two terms then suggest that the fluid velocity in the melt should scale linearly with the thermal Rayleigh number Ra_T , and the same holds for the stream functions. The regressed functional relations obtained from these calculations are

$$\psi_c = 5.5 \times 10^{-6} Ra_T \quad (19a)$$

$$u_{max} = 3.23 \times 10^{-5} Ra_T \quad (19b)$$

Until $Ra_T \sim 10^6$, the plots of ψ_c and ψ_{max} coincided as the center of the lower vortex (where the stream function is a maximum) coincided with the point C. For $Ra_T > 10^6$ the center of the lower vortex gradually moves closer towards the side wall due to the formation of boundary layers along the walls and hence ψ_c and ψ_{max} diverge. Beyond $Ra_T = 2000$, the flow starts to deviate from linearity. At high Rayleigh numbers the nonlinear inertial terms are important, and a balance between the inertia and buoyancy gives a quadratic variation of velocity and stream function with Rayleigh number (Tritton 1988). The lateral profiles of vertical velocity components and the temperature at $x = 0.55$ (horizontal plane through point C in Fig. 11) are shown in Fig. 13 for $Ra_T = 10^4$, 5×10^4 , 10^5 , and 10^6 . Positive and negative values of u represent upwards and downwards directions respectively. The velocity profiles show the formation of boundary layers beyond $Ra_T = 5 \times 10^4$. It is well established through these analyses of the base flows that only thermal convection due to radial and vertical temperature gradients does not give rise to oscillatory flow in the range of thermal Rayleigh number considered. Any aspect of flow oscillation hence should be explored in terms of the interaction of thermal and solutal buoyancies.

9. THERMO-SOLUTAL CONVECTION DURING SOLIDIFICATION

The calculations of directional solidification coupled with thermo-solutal convection are started for each Ra_T once the thermally driven background flow attains steady state. The effect of solidification is primarily in injecting continuous (but not necessarily constant) flux of solute from the bottom horizontal surface into the melt that is in a state of steady convection. For, Sn-Cd alloys the solute (Cd) is heavier than the solvent (Sn). The buoyancy ratio N for initial composition $C_0 = 1.3$ wt % Cd is 0.0238. It is clear from equation (10) that the solutal buoyancy term acts in the opposite direction to the thermal buoyancy term, or acts as a restoring force that tries to dampen the flow. However, the interaction of the thermal and solutal buoyancies can lead to a spectrum of dynamical behaviour, ranging from

damped steady convection, to damped oscillatory convection to damped convection with intermittent bursts, to chaotic intermittent convection, depending on the Rayleigh number. The complex dynamics of the thermo-solutal convection depend strongly on both the thermal Rayleigh number Ra_T and the buoyancy ratio N and the growth rate V_p . Since, we are restricted to Sn-Cd binary alloys in this paper, the buoyancy ratio remains fixed at $N = 0.0238$, and we will mainly investigate the effect of Ra_T on the flow dynamics. In other words, Ra_T is the bifurcation parameter for our study. This will enable us to estimate both the strength and the dynamics of the melt convection in tubes of various diameters as used in solidification experiments on Sn-Cd samples (Park and Trivedi 1998).

All the following calculations were done with $V_p = 4$ microns/seconds and $N = 0.0238$ in the following sections unless otherwise mentioned.

9.1 Steady State Thermo-Solutal Convection For Small Ra_T

For, $0 < Ra_T \leq 22000$, the thermo-solutal convection in the melt asymptotically reaches steady state. The time evolution of the stream functions at C ($x = 0.55$, see Fig. 11) for $Ra_T = 10000$ and 15000 is shown in Fig. 14. The dotted straight lines are the corresponding steady state values of the thermally driven background flows at the two Ra_T values. The salient observations from these plots are that, the strength of the convection gets damped by the solute buoyancy since it acts as a restoring force, and the time series plot shows time scales widely disparate from the time scale for thermal convection alone. The transient development of the flow, solute and vorticity fields in the melt within two sample width from the interface are displayed in Fig. 15. The entire region is within the adiabatic zone. In order to gain insight into the transient process of vorticity field development, the profile of lateral concentration gradient $\partial c/\partial y$ at $x = 0.55$ (shown by the dotted line in the first plot of Fig. 15) is also shown, since that is the term that attributes to the readjustment of the vorticity field from the background flow (clearly seen from equation 10). At $t = 0$ the

situation corresponds to steady state background convection driven by thermal convection only. The contours of stream function, vorticity and concentration in the melt at the beginning of solidification, $t = 0$ are shown in Fig. 15. The negative vorticity (perpendicular out from the plane of the paper) contours are plotted with solid lines and the positive vorticity (perpendicular into the plane of the paper) contours are plotted with broken lines. The flow is symmetric about the vertical center line, and the vorticity field on the left of the center is a mirror image of that on the right hand side. Considering the right domain only, the thermal gradient $\partial\theta/\partial y$ produces negative vorticity in the bulk of the melt, except in the wall region where the no slip condition produces vorticity of opposite sign (positive) to that of the bulk flow. The vertical separatrix between the regions of positive and negative vorticity is almost vertical and parallel to the wall, and must be the loci of the point where the vertical velocity is a local maximum. Similarly, the horizontal separatrix is the loci of the local minima in the lateral velocity component. At $t = 0$, the melt concentration is homogeneous and the lateral concentration gradient is zero everywhere. At $t = 20$, a thin concentration boundary layer is discernible on the horizontal and vertical walls, with high lateral concentration gradients while the central region is still homogeneous. Between $t = 20$ and 60, the solute boundary layer turns around and flows downward along the center. Although the downflow of the solute layer is not captured in the concentration contours due to its small value, the small non-zero concentration gradient near the center can be clearly seen in the profile of lateral concentration gradient. The flow field reaches a new steady state after $t \sim 2000$, during which the vorticity and solute fields readjust themselves through diffusion and advection. Closed vorticity loops of opposite signs immediately above the lower roll cells indicate that weak region of counter-rotating cells exist between the upper and lower roll cells. These cells are not captured in the stream-line plots due to their low strength. Another interesting feature is that the vertical dimension of the lower cells have reduced from the beginning of solidification. This is because the vertical dimensions of the roll cells are set by the maximum height the heated fluid could rise along the walls before

turning around at a location where the density of the rising fluid equals the average density of the fluid at that location. In contrast to the base flow, during solidification the rising fluid is heavier in solute content than the bulk fluid at any location, and hence can rise to a shorter height.

The axial concentration profiles in the melt ahead of the interface along $y=0, 0.25$ and 0.5 are shown in Fig. 16 and compared with the one dimensional steady state model by Tiller et al. (1953). In contrast to Burton et al.'s model (1953), the boundary layer thickness is not constant along the lateral direction, but varies substantially from the center to the sides of the sample. Moreover, the boundary layer model is based on the phenomena that the convection induced boundary layer is thinner than the diffusive boundary layer. The concentration profiles of Fig. 16, shows that although the boundary layer thickness along the center is much smaller than the diffusive boundary layer, the boundary layer thickness near the edge is much bigger than the diffusive boundary layer since the general direction of the flow is upwards near the edge. Moreover, outside the boundary layer the composition is not uniform over the entire melt, but shows step like structures which represent two vertical cells. The compositions are approximately uniform within the steps or the cells except for thin regions of high gradients at the interface and between the cells. Moreover, at location $y = 0.25$ the concentration can increase upwards at certain range, since solute rich liquid is brought over the solute free fresh melt at the core. At higher Ra_T this gets more pronounced and almost the entire top half of the lower cell gets unstably stratified with solute. This situation may lead to double diffusive convection of fingering type (Chen and Chen 1997).

9.2 Oscillatory Convection For $Ra_T > 23,000$

The thermo-solutal convection smoothly reaches steady state for $Ra_T < 23,000$ without showing any fluctuation. For $Ra_T \geq 23,000$ complex time dependent phenomena have been observed that depends on the Rayleigh number. For $22500 \leq Ra_T \leq 24,500$ a

transient periodic oscillation is observed to be superimposed on the mean flow (time dependent) during the approach toward the final steady state. One such plot is shown in Fig. 17 a, where the variation of ψ_c with time is shown for $Ra_T = 23000$. The amplitude of oscillation is too small to be discerned in this scale of plot. However, a local magnification of the time series $425 < t < 675$ clearly shows small amplitude fluctuations superposed on the mean flow. The oscillations slowly grow, reach a maximum amplitude and then decay. Similar behavior is observed for $Ra_T = 24500$, as shown in Fig. 17c. It is difficult to analyze this behavior in the sense of bifurcation phenomena, since the behavior is in the transient regime, whereas the traditional approach in bifurcation studies is to investigate only the long-time behavior of the dynamical systems. Since, we are interested in the microstructure development in the crystals, we need to carefully consider all the details of the transient behaviour as well. In this paper we will attempt to explore the nature of the transient dynamics following the methods used for dynamical studies of asymptotic states. In the absence of stable oscillatory flow with constant amplitude, we will use the maximum amplitude of oscillation (A) observed in the time series as the order parameter, and investigate its response to the thermal Rayleigh number, Ra_T , which is the bifurcation parameter. The square of A is plotted against Ra_T , in Fig. 18, and a linear relation is obtained. The behavior is parallel to a supercritical Hopf bifurcation where the amplitude of the oscillatory solution or the radius of the limit cycle is proportional to the square root of the distance of the bifurcation parameter (here Rayleigh number) from its critical value for the onset of the bifurcation. The amplitude is found to vary with the Rayleigh number as

$$A \propto \sqrt{Ra_T - Ra_T^{cr1}} \quad (20)$$

Extrapolating the straight line to $A = 0$, yields a critical Rayleigh number $Ra_T^{cr1} = 22321$. It must be noted that although the behavior of the transient oscillation appears similar to a supercritical Hopf bifurcation, it must be distinguished from the latter since Hopf bifurcation

is defined as a bifurcation between steady stable solution and stable periodic solution, or a bifurcation from a fixed point to a stable limit cycle in the phase space. Another interesting feature of the oscillatory flow is the value of the frequency of oscillation and its variation with time. For all $22500 < Ra_T < 24500$, the frequency of oscillation at the onset is found to be $f = 0.13$. For $Ra_T = 23000$, the frequency is maintained from the growth till the decay of the oscillation as illustrated by the frequency-power spectrum plot in Fig. 19 a. For $Ra_T = 24500$, the frequency of oscillation at the growth is $f = 0.13$ which is maintained till $t \sim 600$. From $t = 600$ to $t = 700$ two frequencies are present in the time series, $f = 0.13$ and $f = 0.26$, with the former decaying and the latter growing. For $t > 710$, the second frequency $f = 0.26$ is the only frequency present with decaying amplitude. The frequency-power spectrum of the entire oscillatory range thus shows two distinct peaks, at $f = 0.13$ and $f = 0.26$. The physical mechanism for these low amplitude oscillations is perhaps an internal wave often encountered in stratified fluids and needs further study for full understanding. The prediction and analysis in terms of the natural frequency of stratified fluids, also known as Brunt-Varsala frequency (Turner 1985, Tritton 1988), is difficult due to the complex interaction between horizontal and vertical gradients of temperature and concentration. Moreover, the unsteady development of the solute gradient field with the course of solidification contributes to the difficulty in analysis.

Between $Ra_T = 24500$ and $Ra_T = 26000$, the flow dynamics seems to undergo a drastic change. The time series of ψ_c for $Ra_T = 26000, 28000, 35000, 40000, 50000$ and 70000 are shown in Fig. 20. At $Ra_T = 26000$, the amplitude of oscillations is almost two order of magnitude greater than that for $Ra_T = 24500$. The variation of the maximum amplitude (A) with Ra_T over the range $23000 \leq Ra_T \leq 70000$, is shown in Fig. 21. The first four data points correspond to the Ra_T values in Fig. 19 (23225, 23500, 24000, 24500), for which a linear relationship between A and $\sqrt{Ra_T - Ra_T^{cr1}}$ is already found (equation 20). The abrupt jump to a much larger amplitude at $Ra_T = 26000$ resembles a bifurcation of subcritical type for A , and indicates that the large amplitude oscillations may be generated

by a mechanism different from the low amplitude oscillations observed for $22321 \leq Ra_\tau \leq 24500$. The structure of the time series for $Ra_\tau = 26000$, is that oscillations grow rapidly in amplitude over a short interval ($t \sim 400-550$), then decay to a non-oscillatory mean flow that monotonically approaches the steady state value. The time series has the structure of a single wave packet that occurs during the entire time span. In this case the steady state occurs after a long transient and is not shown in these plots. For $Ra_\tau = 28000$, the time series is similar to that for $Ra_\tau = 26000$, except the wave packet shows more irregularity during the growth process, and the time duration during which the amplitude grows gets shorter. The period over which the oscillation decays is longer than in the previous case and is followed by a couple more wave packets with very weak amplitudes (shown with the arrows) before approaching the steady state. For $Ra_\tau = 35,000$, the first wave packet includes a growth process that shows abrupt increase in the amplitude within a very short time followed by small amplitude oscillatory decay. The same phenomena tends to repeat itself generating more wave packets, but decays due to dissipation. The long time behaviour resembles a quasi-periodic behaviour where a high frequency oscillation is modulated by a slowly varying oscillation. It appears that the high frequency oscillation is rather regular, while the low frequency oscillation is very irregular. For $Ra_\tau > 40000$, the time series shows an interesting phenomena. The growth process is similar to the previous case, that is, it consists of a short phase of abruptly increasing amplitudes. However, during the period of decay the flow is not oscillatory and monotonically decreases until oscillation starts again. The structure is of an *intermittent oscillation-relaxation* type and persists for a considerable period that depends on the Ra_τ . The higher the Ra_τ , the longer does the intermittent oscillation-relaxation survive before it gets dissipated. The long term behaviour for both 40000 and 50000 shows similar quasi-periodic behavior as in 35000, that is, a dominant high frequency modulated by a slowly varying oscillation of irregular frequency. For $Ra_\tau = 70000$ the intermittent oscillation-relaxations are stable and survive throughout the duration of computation. Two highly disparate time scales are observed in the time series. The interval

between the intermittent bursts is in the range of 100-300 time units, whereas the time period of the high frequency oscillation is of the order of 2 time units. This is clearly shown in Fig. 22, which is a blow up of the time series for $Ra_T = 70000$. It must be noted that though two distinct *time scales* are present, the actual periodicities are highly irregular, or in other words the frequency-power spectrum does not show only two distinct peaks (not shown).

9.3 Vortex Shedding, Intermittent Oscillation-Relaxation

We have discussed so far the time traces of stream function that increasingly gets complex as the Rayleigh number is increased. In addition the direct simulations give access to the instantaneous features of the flow and temperature and solute fields that give some insight into the dynamics of chaotic thermo-solutal convection and the physical mechanisms involved. In this section we will investigate the mechanism of the intermittent oscillation-relaxation observed for $Ra_T = 70000$. The snapshots of concentration and vorticity fields in the melt within two unit distances from the interface at various time steps that include three cycles of high frequency oscillation ($t = 111$ to $t = 118.5$) and one cycle between two successive intermittent bursts ($t = 111$ to $t = 190.5$) are shown in Fig. 23. The time levels are identified on the time series plot in Fig. 22 by cross marks. The positive vorticity field is color coded with red and yellow, while the negative vorticity field is color coded with green and blue, with red representing stronger positive vorticity and blue representing stronger negative vorticity. In addition the positive iso-vorticity contours are plotted. The first plot in the sequence is for $t = 0$, or at the start of solidification. The vorticity field/contour is for steady thermal convection driven by the radial temperature gradient and resemble the first plot of Fig. 15. At $t = 101$, a complex boundary layer structure formed on the side walls. We will concentrate only on the right hand side of the plots, without any loss of generality, since the flow fields are symmetric about the central axis. The positive vorticity boundary layer that remained thin and attached to the side wall for the base flow ($t = 0$), seemed to form a tongue like feature that intruded into the zone where the fluid is turning around. The time

series plot in Fig. 22 shows that the flow was still monotonically decreasing at that time ($t = 101$). At $t \sim 108$, the time series shows the onset of small amplitude oscillation. From $t = 110$ till $t = 113$, the snapshots show that the positive vorticity tongue elongates and shrinks giving rise to one small amplitude oscillation in the time series. This oscillation is perhaps due to the instability of the vorticity boundary layer, and should be distinguished from the international oscillations characteristic of stratified flows. Between, $t = 114.5$ and $t = 115$, the instability of the vorticity layer becomes strong enough to shed a vortex from the wall boundary layer into the melt. This is clearly seen from the closed positive vorticity contour adjacent to the tongue. This suggests that a vorticity maxima has been created into the melt which is an indication of vortex separation (Lugt 1978). At $t = 115.5$, the separated vortex is advected further from the wall with the liquid that is turning around at that region. However, the tongue of positive vorticity is continuous and still contains the separated vortex. At $t = 116$, the separated vortex is completely isolated from the tongue of positive vorticity which snaps back to a thinner boundary layer on the wall. The space between the boundary layer of positive vorticity along the wall and the separated vortex is occupied by liquid with negative vorticity. From $t = 116$ till $t = 117$, the separated vortex gets sheared and advected by the local velocity field, resulting in a continuously deforming plume like structure that flows downward along the center. The rapid shearing of the vortex leads to its breaking at $t = 117.5$, and gets entrained and dissipated into the core of the roll vortex with negative vorticity. However, at $t = 117.5$, the side wall vorticity layer sheds another vortex that follows the similar dynamics at $t = 118$ and 118.5 as seen earlier. These dynamics lead to large amplitude oscillations in the time series between $t = 114$ and $t = 119$, which is probably dominated by the growth, shedding, advection and shearing of isolated vortices from the wall layer. However, the strength of the instability decreases and the oscillation decays to the non-oscillatory relaxation regime, where the flow monotonically decreases. The snapshot at $t = 165$ shows the similar structure as $t = 101$. At $t = 190$, the vortex is separated again and advects inwards at $t = 190.5$.

10. MECHANISM OF LAYERED STRUCTURE FORMATION

It has been proposed by Mazumder et al. (1999) that oscillatory convection in the melt, *if present*, could lead to oscillatory layered structure formation in peritectic alloys. The direct simulation presented in this paper, has conclusively shown that complex time-dependent convection indeed develops during the solidification of Sn - Cd binary alloys for $Ra_T > 22231$. In this section we will couple the convection effects in the melt to the microstructure formation in the solid phase and explain the experimental observations by Park and Trivedi (1998), where they found that only $\alpha \rightarrow \beta$ transition takes place in thin tubes (0.4 mm), whereas oscillatory layered structure formed in large tubes (6mm), under the same experimental conditions in peritectic alloys of initial composition in the hyper-peritectic region.

10.1 Thin Tubes, $\alpha:\beta$ Transition at Flat Horizontal Interface

The thermal Rayleigh number corresponding to a tube of diameter 0.4 mm is $Ra_T = 21$, which produces very low level of convection. Moreover, in the experiments the thin tubes were actually immersed in the melt inside the large tube. Hence the lateral temperature gradient is also very small in thin tubes, since the thermal boundary condition along the outer wall of the thin tube does not encounter any abrupt change, as in the outer tube. For such low Ra_T , and such arrangement, the direct simulation showed that the level of convection is almost negligible in thin tube immersed in the melt, and the mass transfer is mainly dominated by molecular diffusion along the axial direction. This also suggests that the lateral segregation of solute is insignificant in these samples. The axial composition profiles (liquid phase composition) along the sample length is shown in Fig. 23. The dark solid line represents the computed profiles in the sample along $y = 0$ (edge) and $y = 0.5$ (center), and shows almost zero lateral segregation. The profiles are compared to the one

dimensional diffusive model by Tiller et al. (1953) computed for both the solid phases (α and β). Until the peritectic composition $C_p = 3.8\%$ (see Fig. 1), the α phase solidifies and grows from the liquid, and hence the concentration profile approaches the diffusive profile for α . At and beyond C_p , the secondary β phase solidifies from the liquid, and hence the concentration profile shows an abrupt change in shape, and approaches the diffusive profile for β . Since the concentration is uniform along the radial direction at the interface, all the points on the interface simultaneously transform from α to β phase at the same axial location, and hence the α : β interface is flat and perpendicular to the growth direction at the axial location where the liquid composition just crossed C_p (neglecting the nucleation barrier). This is illustrated in Fig. 23 b, which is essentially a phase map of the solidified sample. The region occupied by the primary α phase is covered with darker shade and the area occupied by the secondary β phase is covered by the lighter shade to mimic the experimental micrographs. A sharp α : β transition is predicted in the small tubes as also observed in the experiments Fig. 2 c.

10.2 Large Tubes (~ 6mm), Oscillatory α : β :L Triple Point Motion and Layered Structure Formation.

The tree-like oscillating layered structures (Fig. 2 b) observed in hyper-peritectic Sn-Cd alloys were for sample (or ampoule) size 6 mm (Park and Trivedi 1997). The thermal Rayleigh number corresponding to this ampoule size is $\sim 70,000$, which suggests that the dynamics of double-diffusive convection in the melt during the growth of these samples were highly unsteady. In fact, our direct numerical simulation has conclusively shown the presence of large amplitude relaxation-oscillation type behaviour. Although, we explored in details the solute and vorticity fields in the melt ahead of the interface, we have not so far explored the effect of these oscillations on the solute segregation profiles in the solidified material or the micro-structure pattern formations. From the calculations of Fig. 23 it is

evident that the oscillating solute fields in the melt adjacent to the interface will also cause oscillatory concentration profiles at the freezing interface. Through a simple semi-analytical model, Mazumder et al. (1999) have previously demonstrated that imposition of an oscillating convective velocity in the melt leads to corresponding oscillating concentration profile (or lateral segregation profiles) at the interface, that can lead to oscillatory tree-like structure formation in the solidified material. The variation of ψ_C and the corresponding variation of the liquid phase concentration at two points ($y = 0$ and 0.5 , edge and center) on the solidifying interface with time are shown in Fig. 25. It is evident that the concentration at the interface oscillates in response to the large amplitude relaxation-oscillation of the melt flow. The frequency of the concentration fluctuation is directly related to the frequency of the occurrence of the intermittent oscillation-relaxation of flow. The Fig. 25 b shows that the concentration near the edge is much higher than that in the center due to convection induced lateral segregation. Since, the peritectic composition is $C_p = 3.8$ wt %, the liquid at the edge will be freezing as the secondary β phase after the concentration at those locations exceeds 3.8 % , whereas the liquid near the central region still freezes as the primary α phase since the concentration at those locations is below 3.8 % . This is the fundamental mechanism of the patterned interface formation between the two solid phases in response to convection in the melt. This idea is more clearly demonstrated in Fig. 26 and Fig. 27 where we show the mechanism of formation of one α layer in the continuous β matrix. One cycle of oscillation and eight snapshots of the instantaneous lateral concentration profiles at the interface with the corresponding microstructure near the interface are shown in Fig. 27. The eight instants on the concentration time series are identified in Fig. 26. At 996.9 seconds from the start of solidification, the lateral concentration profile at the interface looks like the first plot in Fig. 27 b. The horizontal line represents the peritectic composition ($C_p=3.8$ wt % Cd). Below the concentration profile we plot the color coded phase map of the solid phase with dark shade for α phase, and light shade for β phase. The top horizontal line for each phase maps represent the instantaneous solid-liquid solidification boundary that is growing

in the vertical direction with a constant speed V_p . Since the liquid in the region near the two edges (or warmer solid walls) has concentration higher than the peritectic composition, the β phase solidifies in that region, whereas the central region is still occupied by the α phase due to the liquid composition being lower than the peritectic composition in that region. It is thus possible to achieve a *simultaneous* growth of both the solid phases at the same interface solely due to the segregation caused by the fluid flow effect. This *simultaneous* growth in the peritectic alloys is distinguished from the *coupled* growth observed in the eutectic alloys (Jackson and Hunt 1966), since a direct coupling of the diffusion fields (the solute rejected by the primary phase is intercepted by the secondary phase) of the two solid phases exist in the latter case in the absence of any convection.

At 1044.4 seconds, the concentration profile moved upwards due to continuous rejection of solute from the interface and thereby reduced the α fraction on the interface. If the convection remained steady and small, this increase or upward movement of the concentration profile would continue and this will lead to gradual vanishing of the α phase at and after the time when the concentration profile moves completely over the peritectic composition (Mazumder et al. 1999). However, due to fluctuations of the flow, the concentration near the edges of the sample decreases (point 3 on Fig. 26) and this brings the concentration below C_p from their previous values above C_p . This is particularly significant for the locations near the triple point, that is where the two solid phase and the liquid phase co-exist (compare the concentration profiles at 1044.4 seconds and 1091.9 seconds near the triple point). This leads to an increase in the area fraction of the α phase on the advancing interface and this continues till the composition at the interface starts to increase again thereby decreasing the α fraction (between 1091.3 and 1139.3 seconds). The decrease in α fraction continues until 1281.8 seconds after which the same event of increasing the α fraction starts (1329.3 seconds). Thus at the end of the cycle one branch-like α layer has developed. This entire phenomena repeats itself and leads to the formation of multiple branches of α layers that appears like an oscillating tree like structure embedded in the

secondary β matrix as shown in Fig. 28. For a cylindrical geometry, if observed from the top (from the liquid side onto the interface), the cross-section will appear as two concentric circles. The inner circle is the primary α phase embedded in the outer circle of β phase, and the radius of the inner circle will oscillate with time or growth direction.

10.3 Effect of Growth Rate (V_p) on Layer Thickness and Spacings

The diffusive model (Trivedi 1995) predicted that the spacing and the thickness of the discrete α and β bands should scale with the inverse of the pulling velocity V_p , or

$$\lambda \propto \frac{1}{V_p} \quad (21)$$

where λ is the generic symbol for spacing or thickness of individual solid phases. The experimental measurements done by Zeishler-Mashl and Lograsso (1997) have indicated that the spacings followed the following scaling behaviour.

$$\lambda \propto \frac{1}{\sqrt{V_p}} \quad (22)$$

This disagreement is due to the fact that the band structures observed by Zeishler-Mashl and Lograsso (1997) were actually the projections of the oscillatory layered structure that formed due to convection in the melt. The formation mechanism of these structures is due to the oscillating fluid flow as described in section 9.2, and hence their length scales should be related to the frequency of the flow fluctuation and pulling velocity as

$$\lambda \propto \frac{1}{f} V_P = \tau V_P \quad (23)$$

where f and τ are the frequency and time-period of the most dominant mode of flow oscillation that is responsible for the layered structure formation. In Fig. 28 a, we show the variation of flow oscillation with three different pulling velocities $V_p = 3, 4,$ and 5 microns/sec, as used in experiments (Zeishler-Mashl and Lograsso 1997, Park and Trivedi 1998). The time period between successive intermittent burst shows a general trend to decrease with increasing V_p , although the periods are not strictly constant for each run. At least 4 time periods for each V_p were measured and plotted against V_p in Fig. 28b. A linear trend is found despite the dispersions of τ for each V_p . However, the dispersion seems to decrease with higher velocity. The scaling between τ and V_p is found to be

$$\tau \propto V_P^{-1.46} \quad (24)$$

Hence, the scaling between spacing and velocity from (23) is

$$\tau \propto V_P^{-.46} \quad (25)$$

which agrees well with the experimental observation.

Acknowledgment

This research was supported in part by the NASA Microgravity Science Applications Division under Grant NAG8-1254. This work was supported in part and carried out at the Ames Laboratory, which is operated for the U. S. Department of Energy by Iowa State University, under contract no. W-7405-Eng-82, supported by the director of Energy Research, Office of Basic Energy Sciences.

REFERENCES

- Adornato P. M. and Brown R. A. 1987, *J. Crystal Growth*, v 80, p 155
- Alexander J. I. D., Ouazzani J., and Rosenberger F., 1989, *J. Crystal Growth*, v 97, p 285
- Azouni M. A. 1981, *PhysicoChemical Hydrodynamics*, v 12, p 295
- Batchelor G. K. 1954, *Quarterly of Applied Mathematics*, v.12, p209
- Behnia M., and de Vahl Davis G. 1989, in *Notes on Numerical Fluid Mechanics*, v 27, p 11
- Bergman T. L. and Hyun M. T. 1996, *Int. J. Heat Mass Transfer*, v 39, p 2883
- Brown R. A. 1988, *AIChE Journal*, v 34, p 881
- Brown R. A. and Kim D. H. 1991, *Journal of Crystal Growth*, v 109, p 50
- Brown R. A. 1992, in *Heat and Mass Transfer in Materials Processing*, eds.. Tanasawa I and Lior N, p 137
- Burton J. A., Prim R. C., Slichter W. P. 1953, *J. Chem. Phys.* v 21, p 1987
- Capper P., Jones C. L., Pearce E. J. and Quelch M. J. T. 1983, *J Crystal Growth*, v 62, p 487
- Carlson F. M., Fripp A. L., Crouch R. K. 1984, *J. Crystal Growth*, v 68, p 747
- Chang C. J. and Brown R. A. 1983, *J. Crystal Growth*, v 63, p 343
- Chen C. F., and Chen F. 1997, *J. Fluid Mech.*, v 352, p 161
- Coriell S. R., Cordes M. R., Boettinger W. J., Sekerka R. F. 1980, *J. Crystal Growth*, v 49, p13
- de Vahl Davis G., and Jones I. P. 1983, *International Journal for Numerical Methods in Fluids*, v 3, p 227
- Flemings, M.C. 1974, *Solidification Processing*, McGraw Hill, New York
- Fletcher C. A. J. 1991, *Computational Techniques for Fluid Dynamics*, v 1
- Gill A. E. 1974, *J. Fluid Mech.*, v 64, p 577
- Guerin R., Le Marec C., Haldenwang P. 1998, *J. Crystal Growth*, v 194, p 247
- Hart J. 1972, *J. At. Sci.* , v29, p 687

- Hart J. 1983, *J. Fluid Mech.*, v 132, p 271
- Heinrich J. C. 1988, *Comp. Meth. App. Mech. and Engg.*, v 65
- Huppert E. 1976, *Nature*, v 263, p 20
- Hurle D. T. J., Jakeman E., Johnson C. P. 1974, *J. Fluid Mech.*, v 64, p 565
- Jackson K. A., and Hunt J. D. 1966, *Trans. Metall. Soc. AIME*, v 236, p1129
- Kaddeche S., Garandet J. P., Barat C., Ben Hadid H., Henry D. 1996, *J. Crystal Growth*, v 158, p 144
- Kappurao S., Brandon S., Derby J. J. 1995, *J. Crystal Growth*, v 155, p 93
- Kappurao S., Brandon S. and Derby J. 1995, *J. Crystal Growth*, v 155, p 103
- Karma A., Rappel W. J., Fuh B. C., Trivedi R. 1998, *Metall. Mat. Trans.*, v 29A, p 1457
- Kim D. H. and Brown R. A. 1989, *Journal of Crystal Growth*, v 96, p 609
- Kim D. H. and Brown R. A. 1991, *Journal of Crystal Growth*, v 109, p 50
- Klaren C. M., Verhoeven J. D. and Trivedi R. 1980, *Metal. Trans. A*, v 11, p 1853
- Kutz W., and Fisher D. J. 1984, *Fundamentals of Solidification*, Trans Tech Publications, USA
- Lapidus L and Pinder G. F. 1982. *Numerical solution of partial differential equations in science and engineering*, John Wiley & Sons, New York
- Laure P. and Roux B. 1987, *CRAS Ser. II*, v 305, p1137
- Le Marec C., Guerin R., Haldenwang P. 1996, *J. Crystal Growth*, v 169, p 147
- Le Marec C., Guerin R., Haldenwang P. 1996, *Phys. Fluids*
- Lugt H. J. 1978, *Vortex Flow in Nature and Technology*, John Willey & Sons, NY, p 74
- Mason J. T., Verhoeven J. D. and Trivedi R. 1982, *J. Crystal Growth*, v 59, p 516
- Mazumder P. 1999, Ph.D. Thesis, Iowa State University, Ames
- Mazumder P., Trivedi R., and Karma A. 1999, submitted to *Met. Trans A*
- Mazumder P., Trivedi R., Karma A. 1998, *MRS Proc.*, v 481, p 39
- Mazumder P. Trivedi R. 1999, in *Fluid Flow Phenomena in Metals Processing*, eds. El-Kaddah N., Robertson D. G. C., Johansen S. T., Voller V. R., TMS, p 459

- Mazumder P. 1999, Unpublished work, Ames Laboratory, IA 50011
- McFadden G. B., Rehm R. G., Coriell S. R., Chuck W. and Morrish K. A. 1984, *Met. Trans.*, v A15, p 2125
- McFadden G. B., Coriell S. R., Boisvert R. F. 1985, *Phys. Fluids*, v 28, p 2716
- McFadden G. B., Coriell S. R. 1987, *Phys. Fluids*, v 30, p 659
- Moore D. R. and Weiss N. O. 1990, *Phil. Trans. R. Soc. Lond. A* , v 121
- Muller G. and Ostrogorsky A. 1994, in *Handbook of Crystal Growth*, v 2b, p 709
- Muller A. and Wiehelm M. 1964, *Z. Naturf. A* , v 19, p 254
- Mullins W. W., and Sekerka R. F. 1963, *J. Appl. Phys.*, v 34, p 323
- Naumann R. J. 1982, *J. Crystal Growth*, v 58, p 589
- Ouyang H. and Shyy W. 1996, *Int. J. heat and Mass Transfer*, v 39, p 2039
- Ouyang H., Shyy W., Levit V. I., Kaufman M. J. 1997, *Int. J. heat and Mass Transfer*, v 40, p 2293
- Ouyang H. and Shyy W. 1997, *J. Crystal Growth*, v 173, p 352
- Park J. S. and Trivedi R. 1998, *J. Cryst. Growth*, v 187, p 511
- Peaceman D. W. and Rachford H. H. 1956, *J. Soc. Indust. Appl. Math.* v 3, p 28
- Rosenberger F. 1979, *Fundamentals of Crystal Growth*, Springer, New York
- Roux B. 1989, *Numerical Simulation of Oscillatory Convection in Low Pr Fluids*, Vieweg, Braunschweig
- Rouzaud A., Camel D., Favier J. J. 1985, *J. Crystal Growth*, v 73, p 73
- Simsek E., and Mazumder P. 1998, Unpublished work, Ames Laboratory, Ames, Iowa
- Smith V. G., Tiller W. A., Chalmers B. 1955, *Can. J. Physics*, v 33, p 723
- Tewari S. N. and Trivedi R. 1991, *Int. J. Microgra. Res.*IV/4, p 240
- Tewari S. N., Shah R. and Chopra M. A. 1993, *Metall. Trans.*, v 24A, p 1661
- Tewari S. N. and Shah R. 1996, *Metall. Trans.*, v 27A, p 1353
- Tewari S. N. 1986, *Metall. Trans.*, v 17A, p 2279
- Tewari S. N. 1990, *Mat. Sci. Eng. A*, v 130, p 219

- Tewari S. N. 1988, *Metall. Trans.*, v 19A, p 1351
- Tewari S. N. and Chopra M. A. 1990, *Int. J. Microgra. Res.*III, p 99
- Tiller W. A., Jackson K. A., Rutter J. W. and Chalmers B. 1953, *Acta Metall.*, v1, p 428
- Tritton D. J. 1990, *Physical Fluid Dynamics*, Oxford Science Publications
- Trivedi R., Mazumder P., Tewari S. N. 1999, submitted to *Met. Trans A*
- Trivedi R., Miyahara H., Mazumder P., Tewari S. N. 1999, submitted to *Met Trans. A*, 1999
- Trivedi R., Liu S, Mazumder P., Simsek E. 1999, submitted to *J. Mater. Sci.*
- Trivedi R. 1989, "Directional Solidification of Alloys", in *Principles of Solidification and Materials Processing*, eds. R. Trivedi, J. Majumdar, J. A. Sekhar, p 33
- Trivedi R, Miyahara H, Mazumder P, Tewari S N 1999, Unpublished work. Ames Laboratory, Ames, Iowa
- Tritton J. 1988, *Physical Fluid Dynamics*. Oxford Science Publications. p. 35
- Turner J. S. 1985, *Ann. Rev. Fluid Mech.* v 17, p 11
- Turner J. S. 1973, "Buoyancy Effects in Fluids". Cambridge University Press, London
- Veronis G. 1968. *J. Fluid Mech.* v 34. p 315
- Zeishler-Mashl K., and Lograsso T. 1997. *Metall. Mater. Trans.*, v 28A, p 1543

Table 1: Dimensional Groups and their characteristic values used in simulation

Terms	Symbol	Definition	Values for Sn-Cd system
Thermal Rayleigh Number	Ra_T	$\frac{g\beta_T(T_H - T_C)d^3}{\alpha_l\nu}$	0 - 10^8
Solutal Rayleigh Number	Ra_S	$\frac{g\beta_S C_0 d^3}{\alpha_l\nu}$	0 - 2.38×10^6
Buoyancy ratio	N	$\frac{Ra_S}{Ra_T} = \frac{\beta_S C_0}{\beta_T(T_H - T_C)}$	0.0238
Prandtl Number	Pr	ν/α_l	0.01
Lewis Number	Le	α_l/D	10.000

Table 2. Comparison of Solutions of Steady State Thermal Convection Inside Differentially Heated Square Cavity Filled With Fluid of $Pr = 0.71$

$Ra = 10^3$

First Author	Ψ_{mid}	Ψ_{max}	u_{max} , @ $y =$	v_{max} , @ $x =$
Mazumder	1.176	1.176	3.7, @ 0.175	3.653, @ 0.8125
de Vahl Davis	1.174	1.174	3.697, @ 0.178	3.649, @ 0.813
Upson 1	1.1754	1.1754	3.7040, @ 0.166	3.656, @ 0.812

$Ra = 10^4$

First Author	Ψ_{mid}	Ψ_{max}	u_{max} , @ $y =$	v_{max} , @ $x =$
Mazumder	5.083	5.083	19.6, @ 0.1125	16.207, @ 0.825
de Vahl Davis	5.081	5.081	19.64, @ 0.119	16.2, @ 0.823
Upson 1	5.0753	5.0753	19.675, @ 0.1187	16.193, @ 0.822

$Ra = 10^5$

First Author	Ψ_{mid}	Ψ_{max}	u_{max} , @ $y =$	v_{max} , @ $x =$
Mazumder	9.1695	9.6833	68.898, @ 0.0625	34.835, @ 0.85
de Vahl Davis	9.121	9.624	68.68, @ 0.066	34.81, @ 0.855
Upson 1		9.6206	68.896, @ 0.0663	34.62, @ 0.856

$Ra = 10^6$

First Author	Ψ_{mid}	Ψ_{max}	u_{max} , @ $y =$	v_{max} , @ $x =$
Mazumder	16.370	16.780	224.807, @ 0.0375	65.1465, @ 0.85
de Vahl Davis	16.41	16.84	221.28, @ 0.038	64.96, @ 0.85
Upson 1		16.707	220.64, @ 0.0316	64.593, @ 0.85

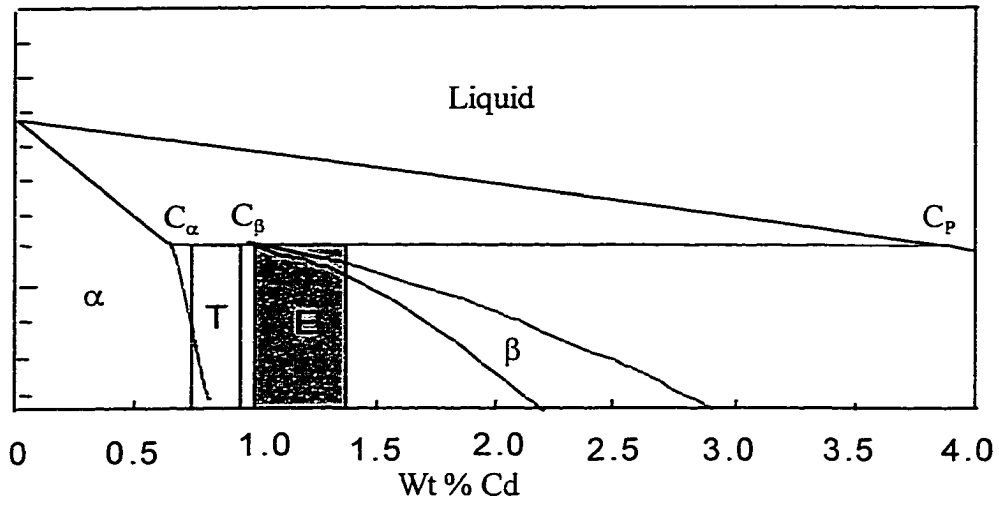


Fig. 1: Phase diagram of the Sn-Cd system showing the banding window predicted by the diffusive model (lightly shaded region, T), and the composition range for which banding is observed experimentally (darkly shaded region, E).

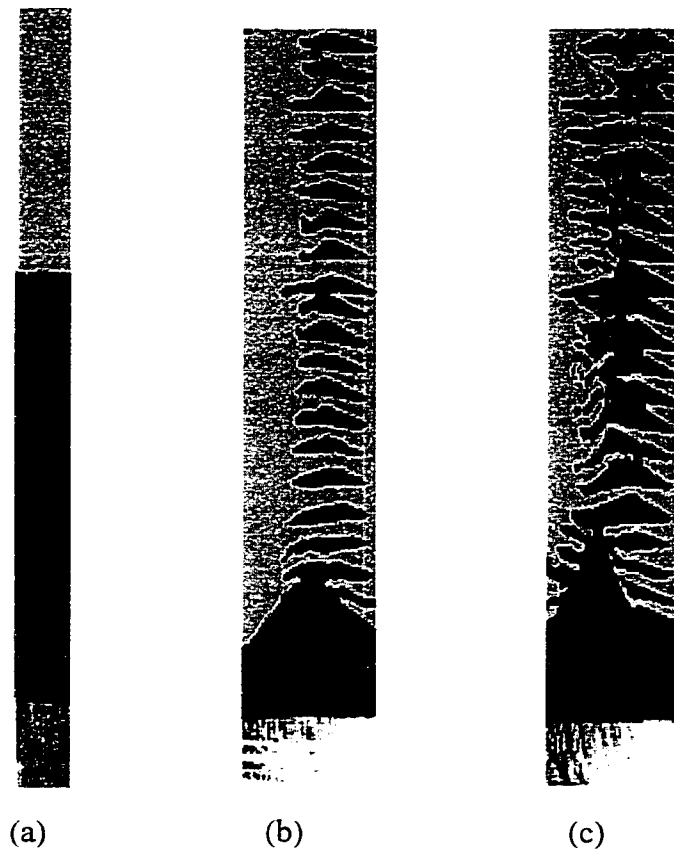


Fig. 2: Microstructures of directionally solidified Sn-1.4 wt % Cd alloy at $V = 3.0 \mu\text{m/s}$ and $G = 13.5 \text{ K/mm}$. (Park and Trivedi 1998) (a). A single α to β transition in a sample of diameter 0.6 mm. (b) Observation of isolated α bands on a longitudinal section taken close to the surface. Sample diameter = 6 mm. (c) A tree-like structure of α surrounded by β on a section closer to the center of the same sample as in (b)

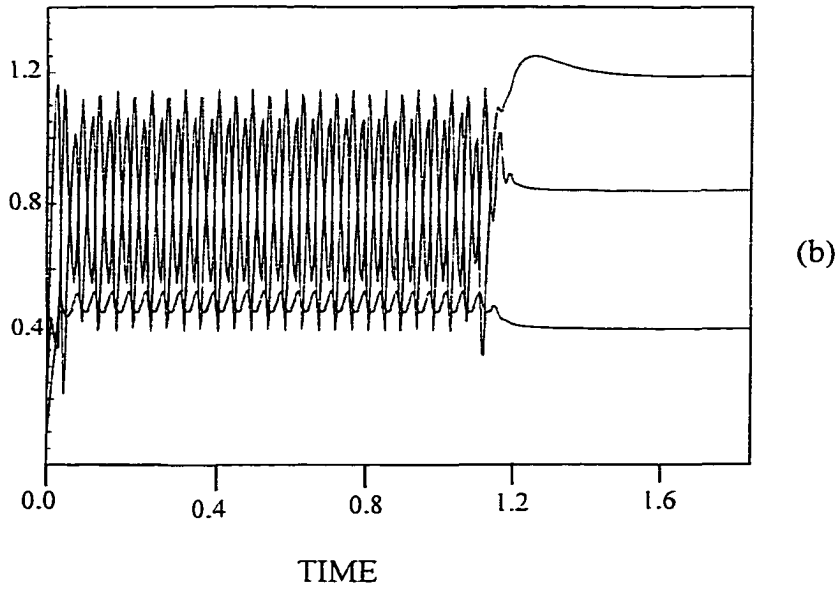
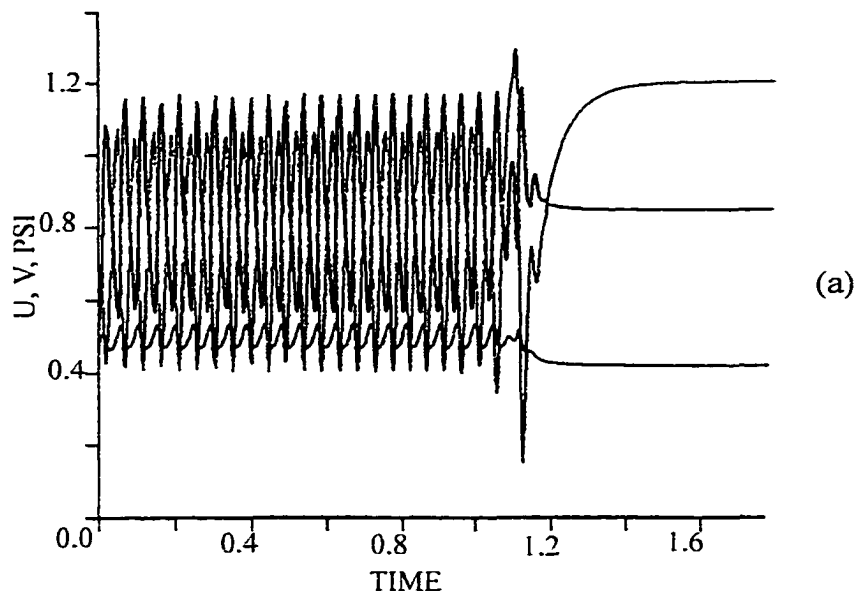


Fig. 4: Time history of the solution for $R - R$, $Gr = 40,000$, $Pr = 0.0$ (a) Behnia and G. de Vahl Davis (b) Present

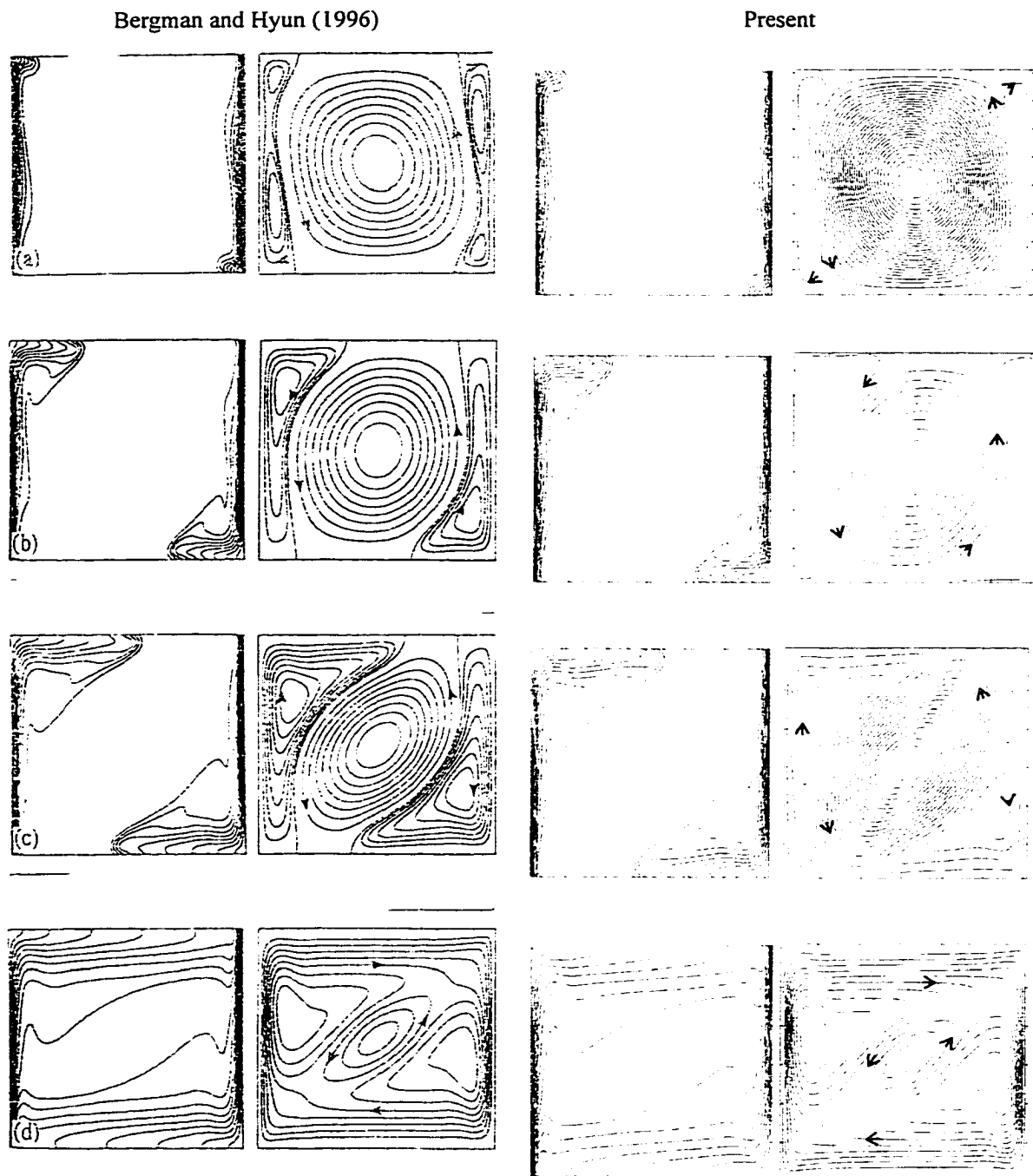


Fig. 5: Comparisons between present computation and Bergman and Hyun's (1995) results. Predicted concentration and stream function distributions for $Ra=100$, $N=-10$ at : (a) $t=0.3$ (b) $t=0.75$ (c) $t=1.35$ (d) $t=3.15$

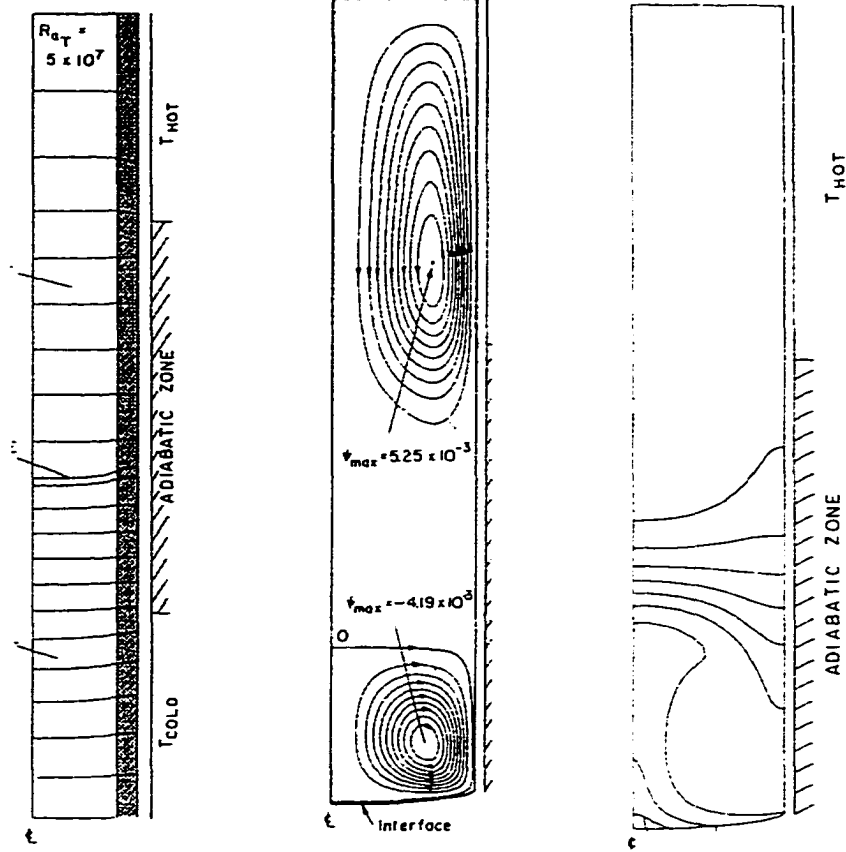


Fig. 6: Steady state thermal, flow and solute field computed by Adornato and Brown (1987)

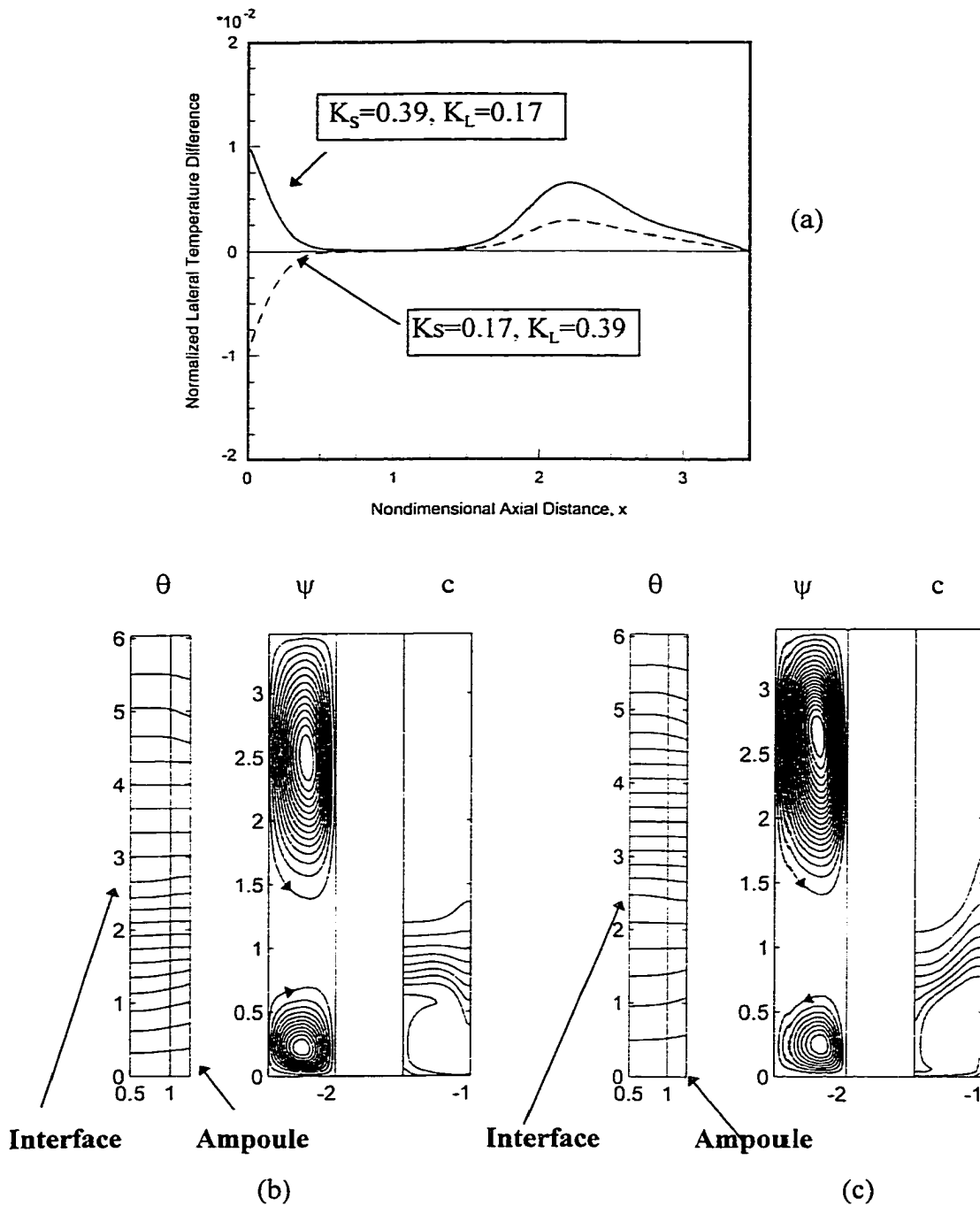


Fig. 7: Effect of relative thermal conductivities of Solid and Liquid on the thermal, flow and concentration field. (a) Temperature difference between the edge and the center of the sample along the axial length. For $K_S < K_L$, the center is hotter than the edge near the interface. For $K_S > K_L$, the edge is hotter than the center near the interface. (b) $K_L=0.39$ and $K_S=0.139$. (c) $K_L=0.17$ and $K_S=0.139$

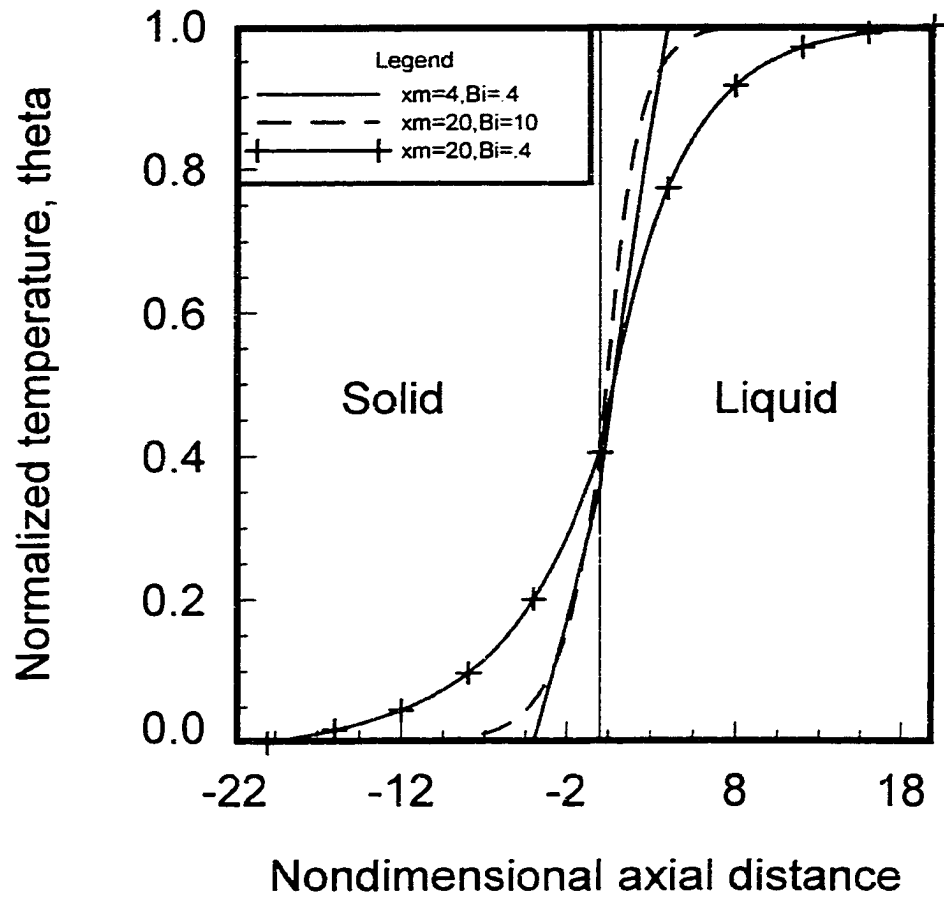


Fig. 8: Effect of Biot number and the length of the computational domain on the axial temperature profile of Bridgman system.

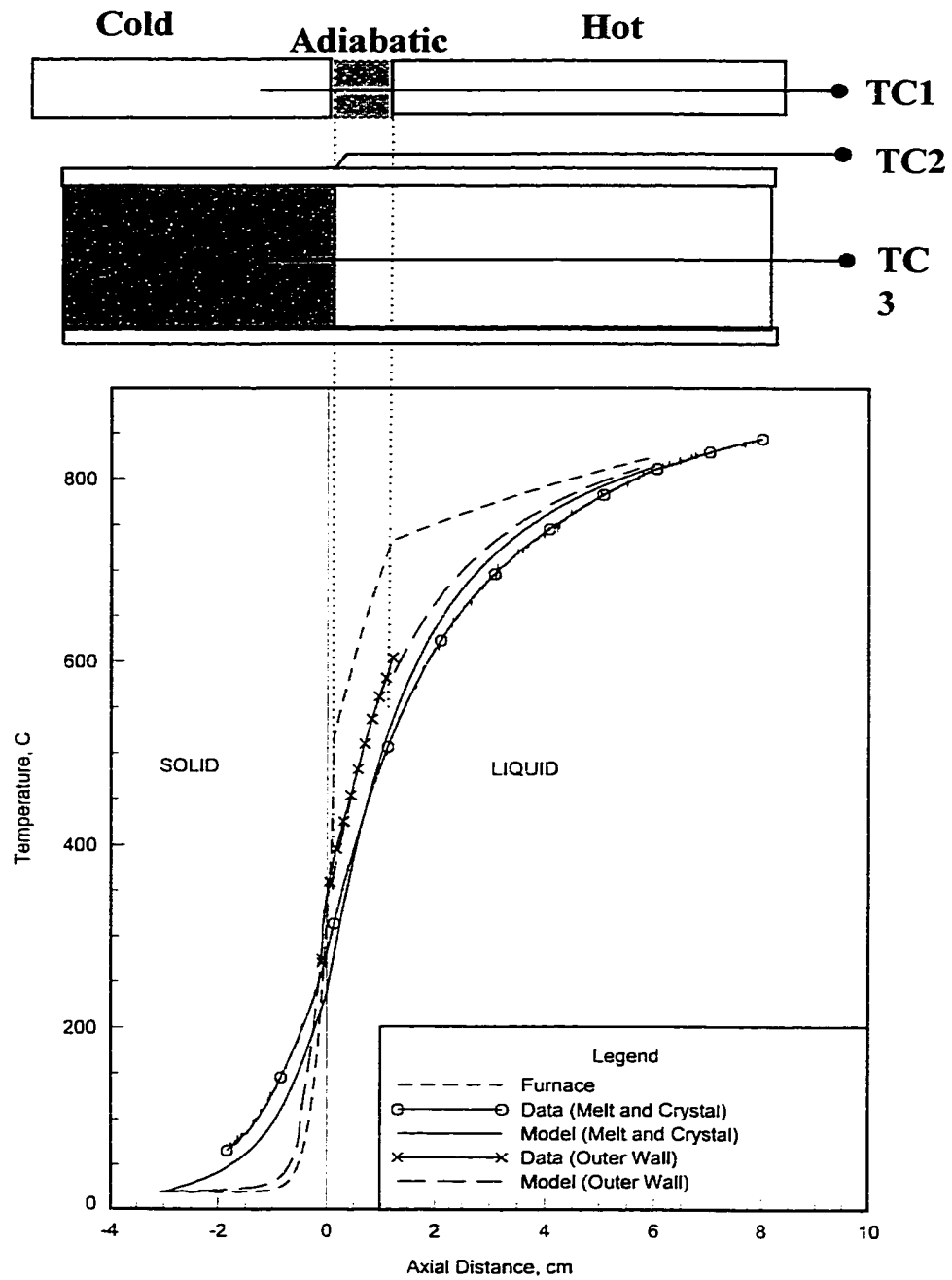


Fig. 9: The axial temperature profiles along the furnace, the outer wall of the ampoule and the sample (both solid and melt) are measured by Thermocouples TC 1-3. The computed axial temperature profiles along the outer wall and the centerline of the sample (solid and melt) are compared. System : Sn-Cd binary alloy in Quartz ampoule (6mm id, 1 mm thickness).

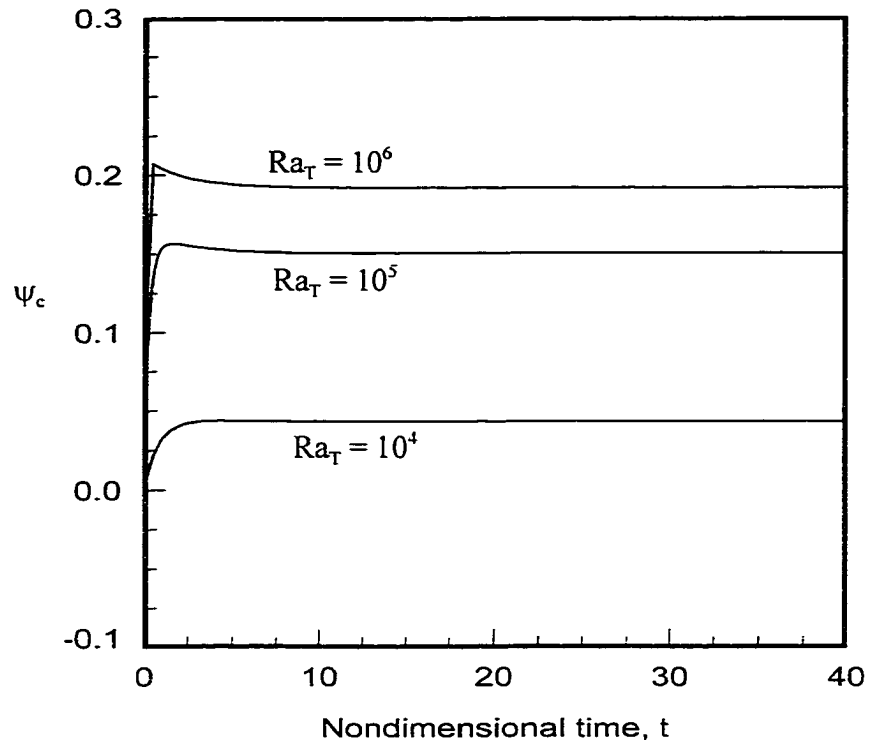


Fig. 10: Time variation of the stream function at point C ($x = 0.55$, $y = 0.25$ see Figure 11), for thermal Rayleigh numbers, $Ra_T = 10^4$, 10^5 , 10^6 .

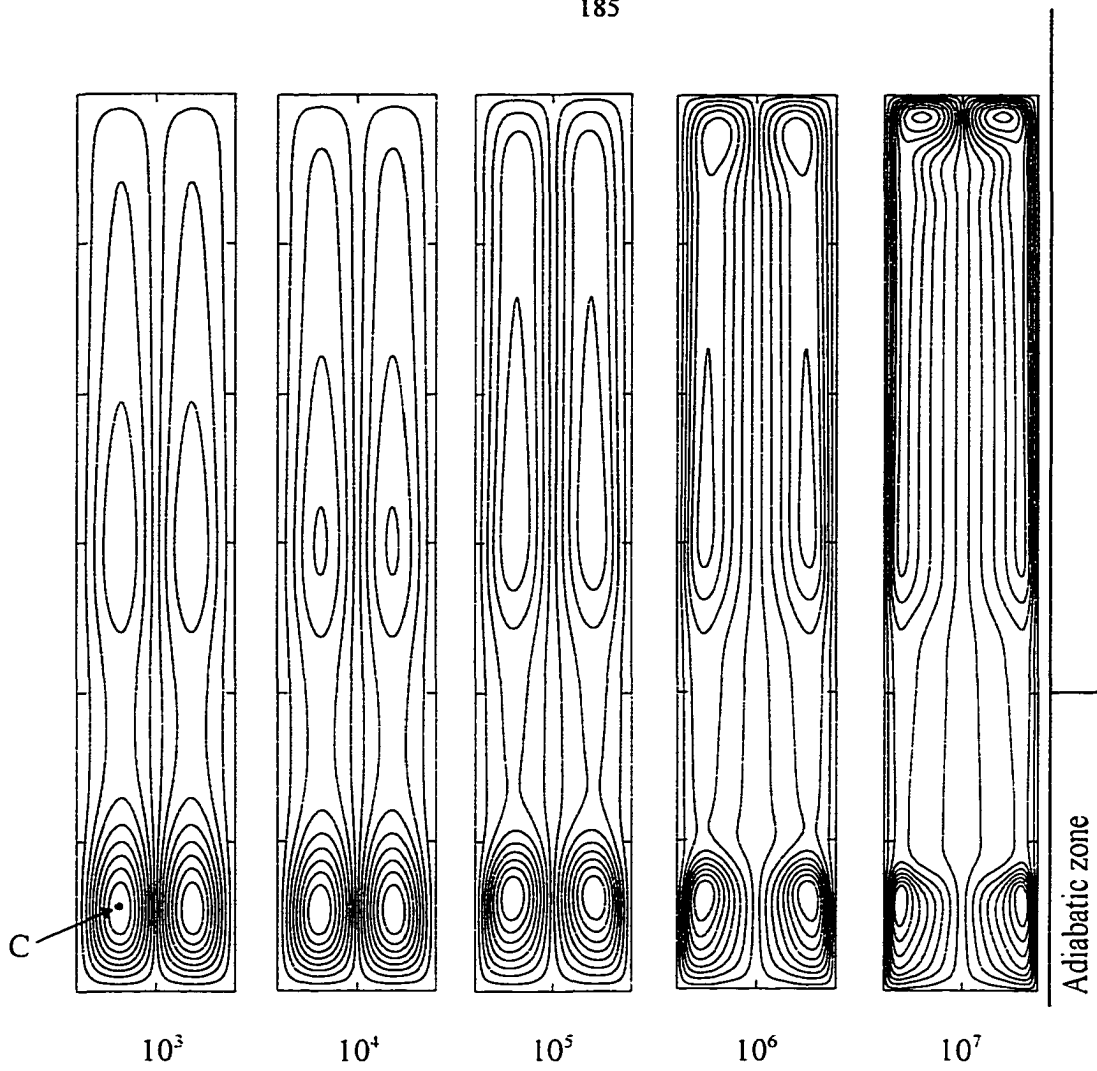


Fig. 11: Steady state base flows in the Sn-Cd melt driven by lateral temperature gradient prior to solidification. The flows are computed with $V_p = 0$, $N = 0$, and $Ra_T = 10^3, 10^4, 10^5, 10^6$, and 10^7 .

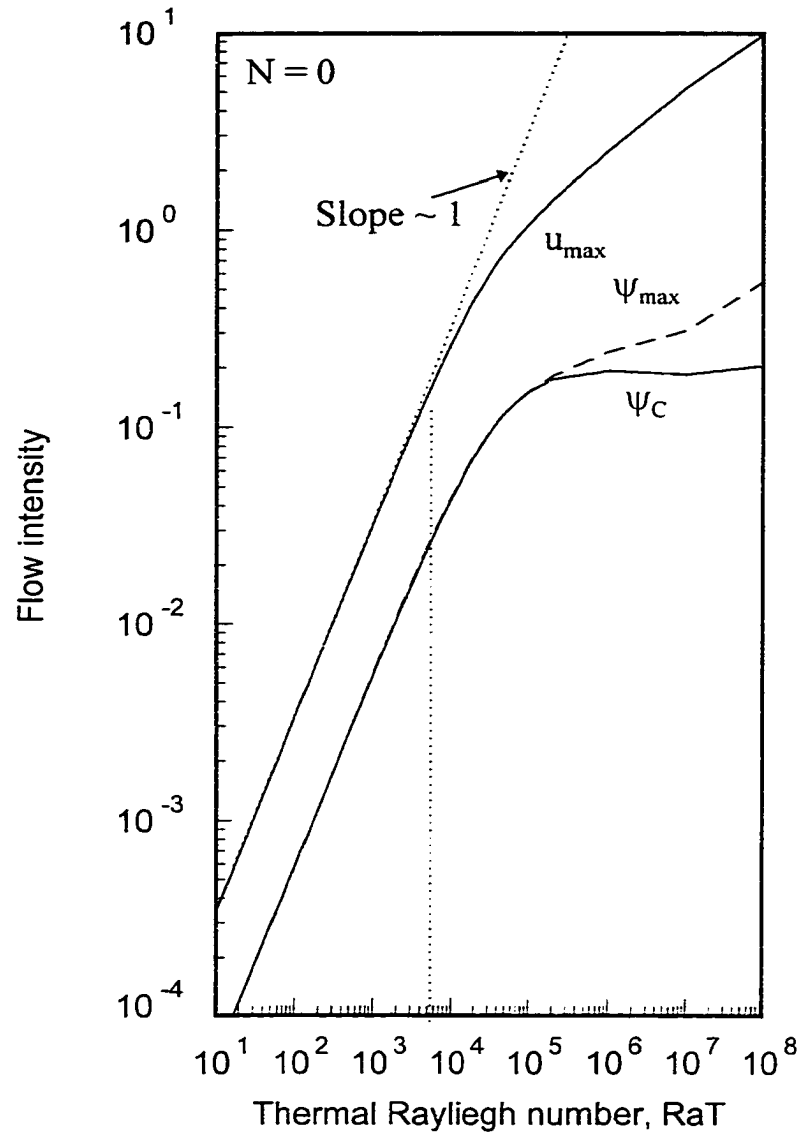


Fig. 12: Variation of stream function ψ_c at the point C ($x=0.55$, $y=0.25$, see figure 11), maximum of stream function in the melt ψ_{max} , and maximum of vertical velocity component u_{max} in the melt as a function of thermal Rayleigh number Ra_T for the base flow. $V_p = 0$, $N = 0$

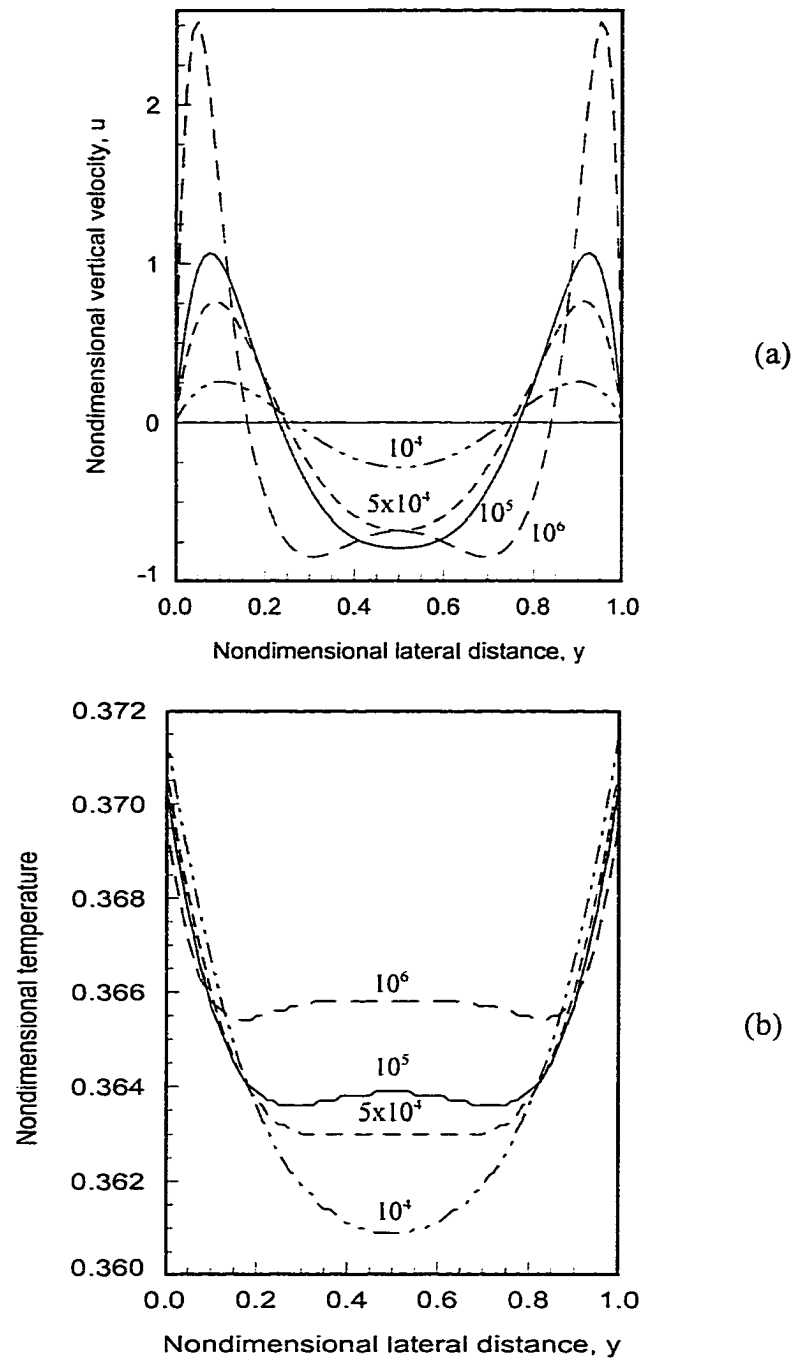


Fig. 13: Lateral profiles of velocity and temperature at $x = 0.55$, for baseflow with $Ra_T = 10^4$, 5×10^4 , 10^5 , 10^6 . (a) nondimensional vertical velocity component, u , (b) normalized temperature.

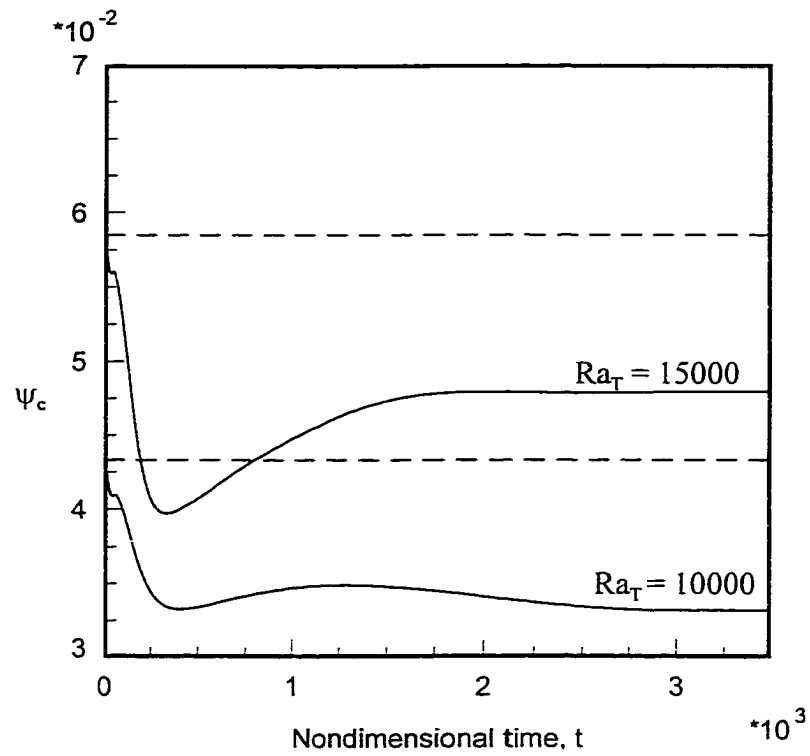


Fig. 14: Variation of ψ_c with time during solidification of Sn-1.3 % Cd alloy for $Ra_\tau = 10,000$ and $15,000$. The dotted lines are the respective steady state values of ψ_c for the background flow with $v_p = 4.0$ microns/sec and $N = 0.0238$. The rejection of heavier solute dampens the convection, and after the initial transients the flows reach steady states weaker than the corresponding thermal convection.

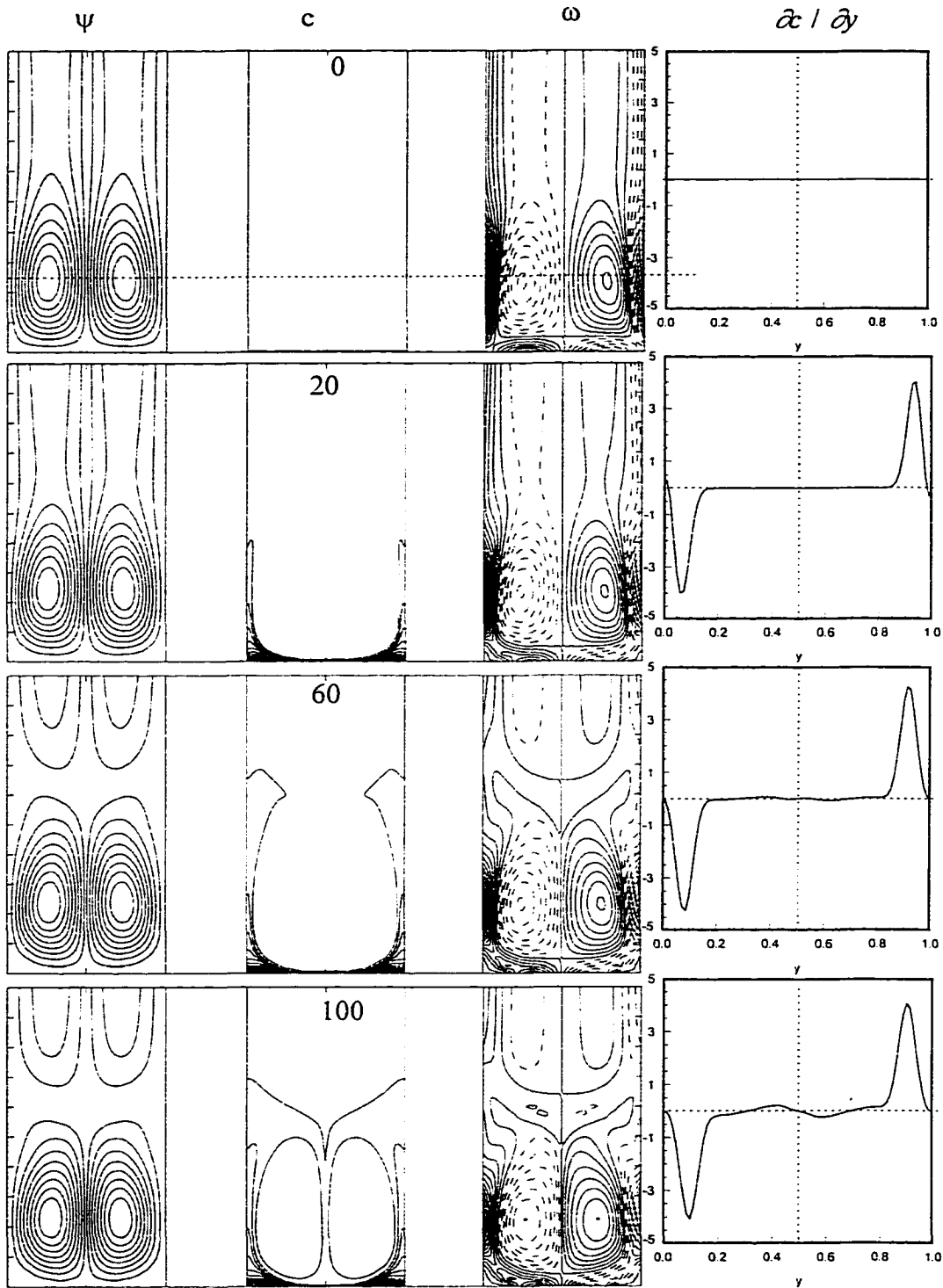


Fig. 15: Snapshots of flow, solute, vorticity fields in the melt, and the lateral profile of lateral concentration gradient at $x = 0.55$

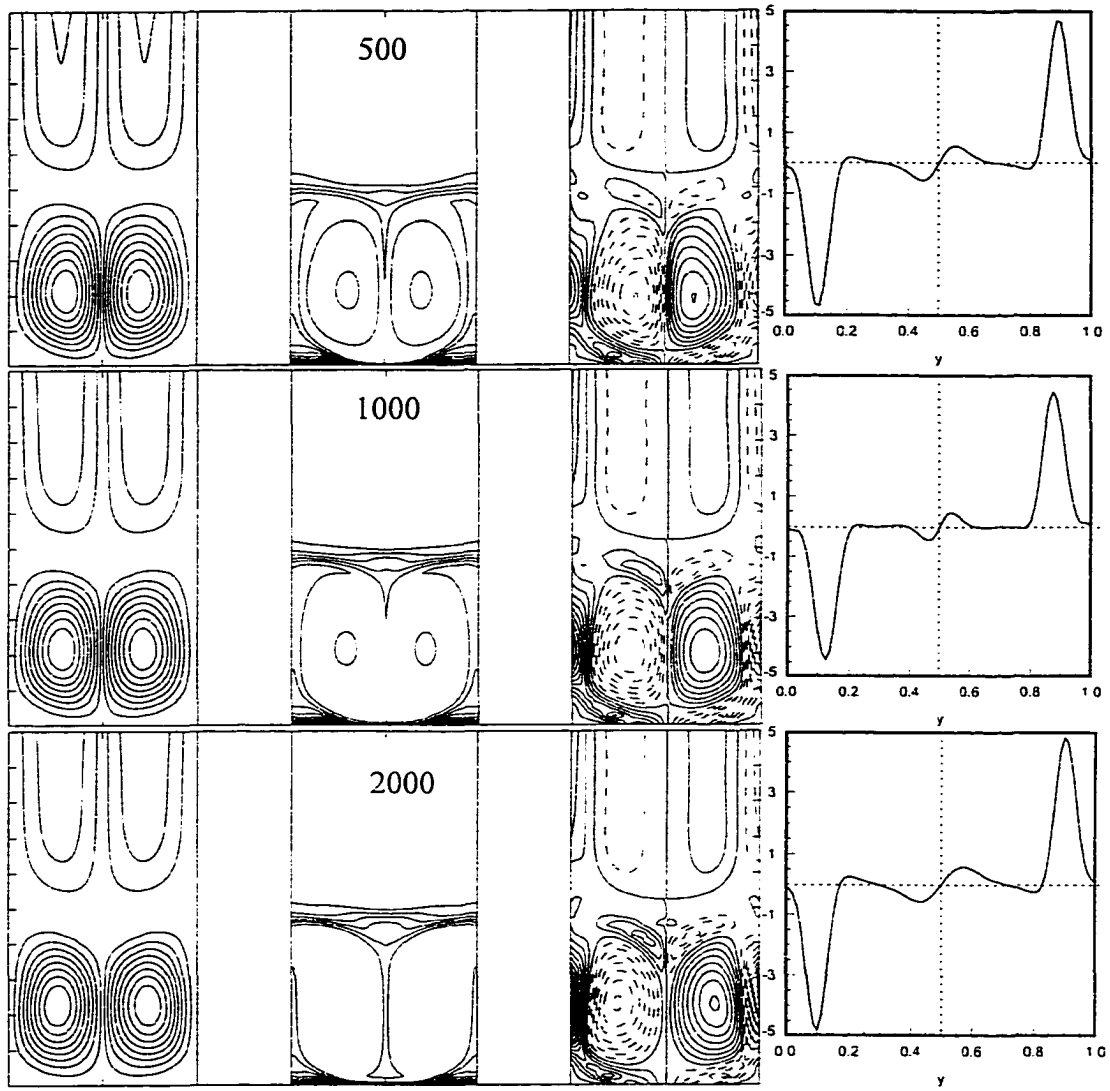


Fig. 15: Continued

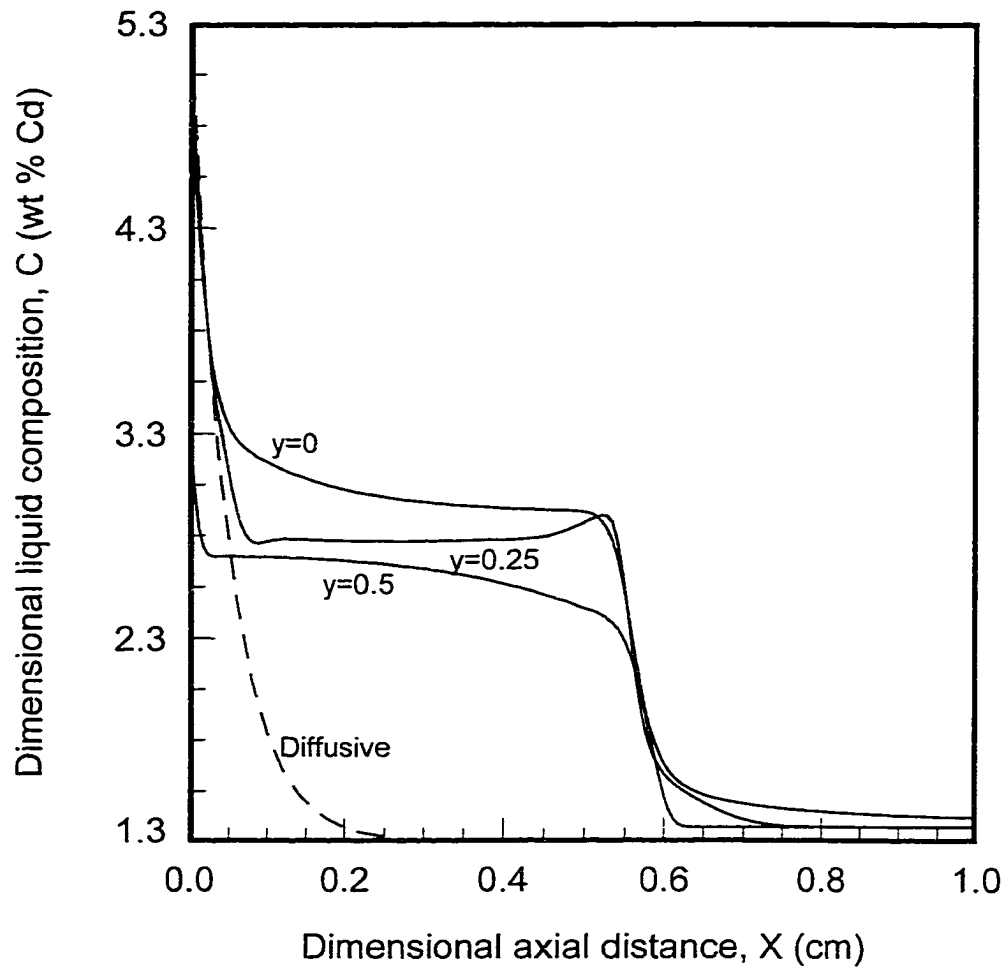


Fig. 16: Steady state axial composition profiles along $y = 0$, $y=0.5$. The dotted curve is the corresponding steady state profile with one dimensional diffusion model (Tiller et al. 1953). $Ra_T = 15000$, $V_p=4$ microns/sec.

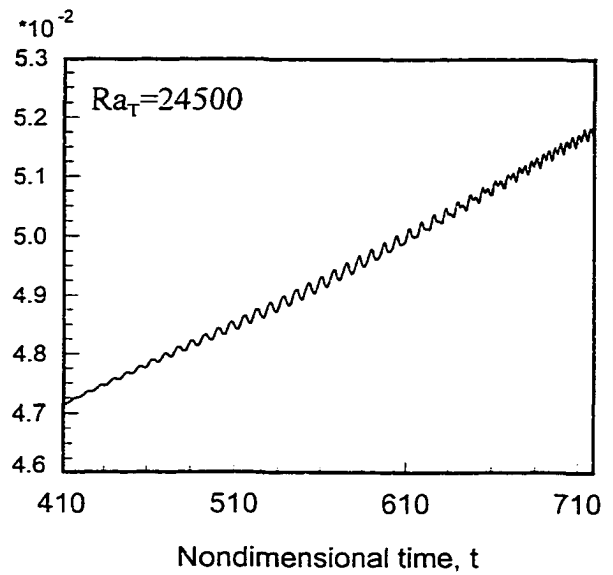
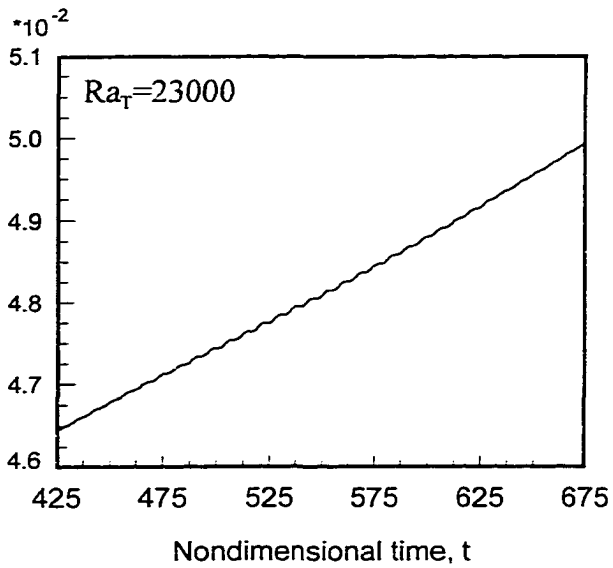
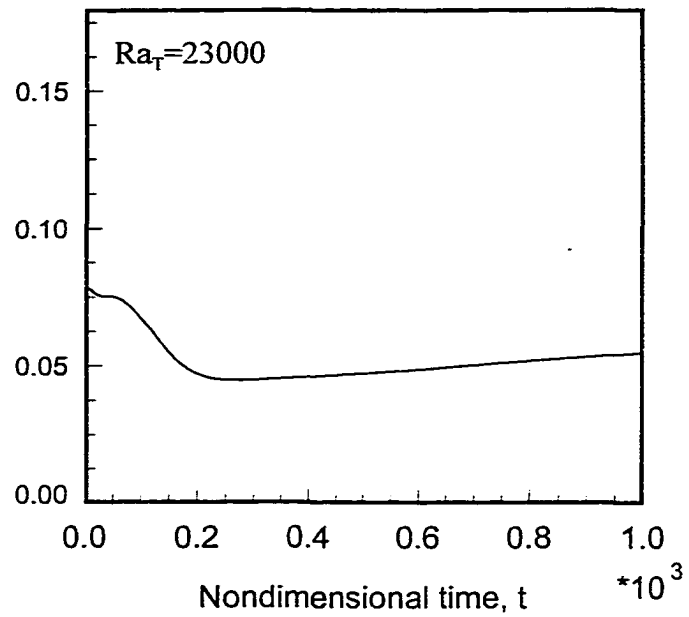


Fig. 17: Growth and decay of small amplitude oscillation during the development of steady state flows. (a) Long time behavior that submerges the oscillation (b) enlargement of the oscillatory regime (c) $Ra_T = 24500$

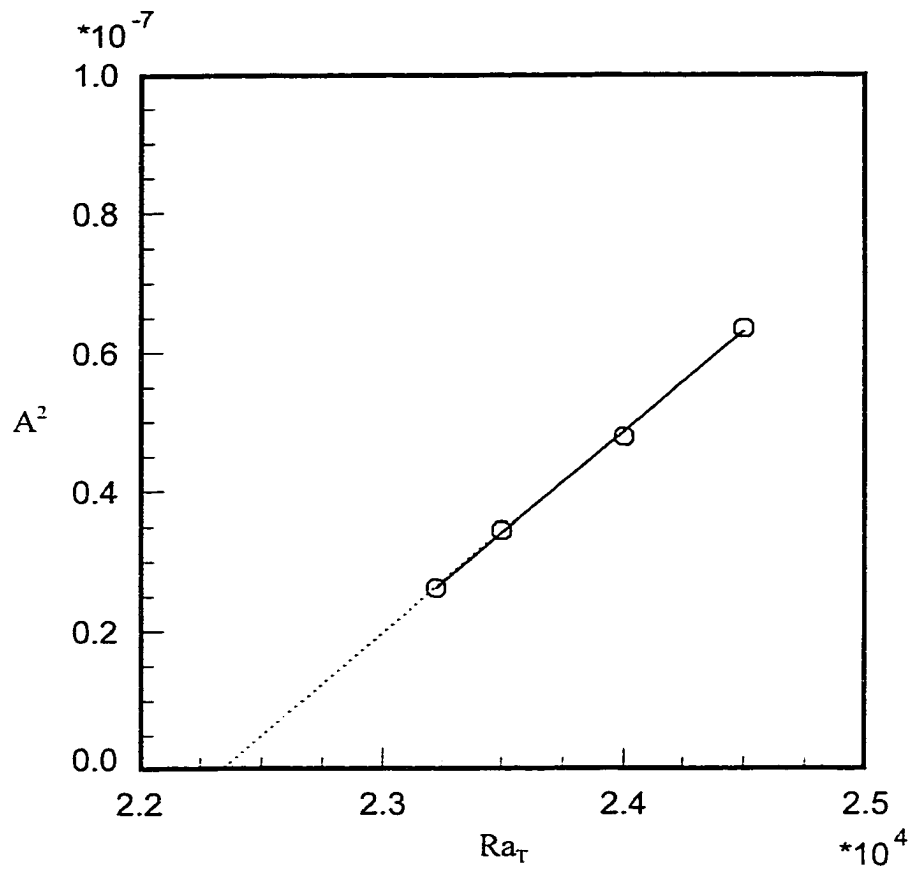


Fig. 18: Square of the maximum value of the oscillatory amplitude with Ra_T shows supercritical behavior.

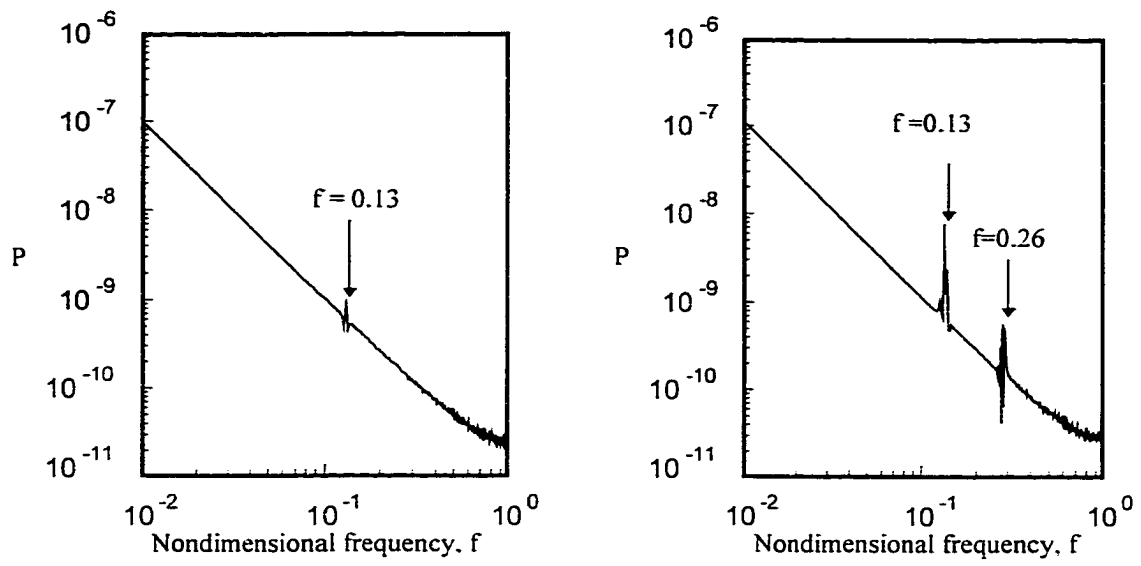


Fig. 19: Frequency (f) - Power (P) spectrum of time series of ψ_C of Fig. 18 (a) $Ra_T=23000$ (b) $Ra_T=24500$

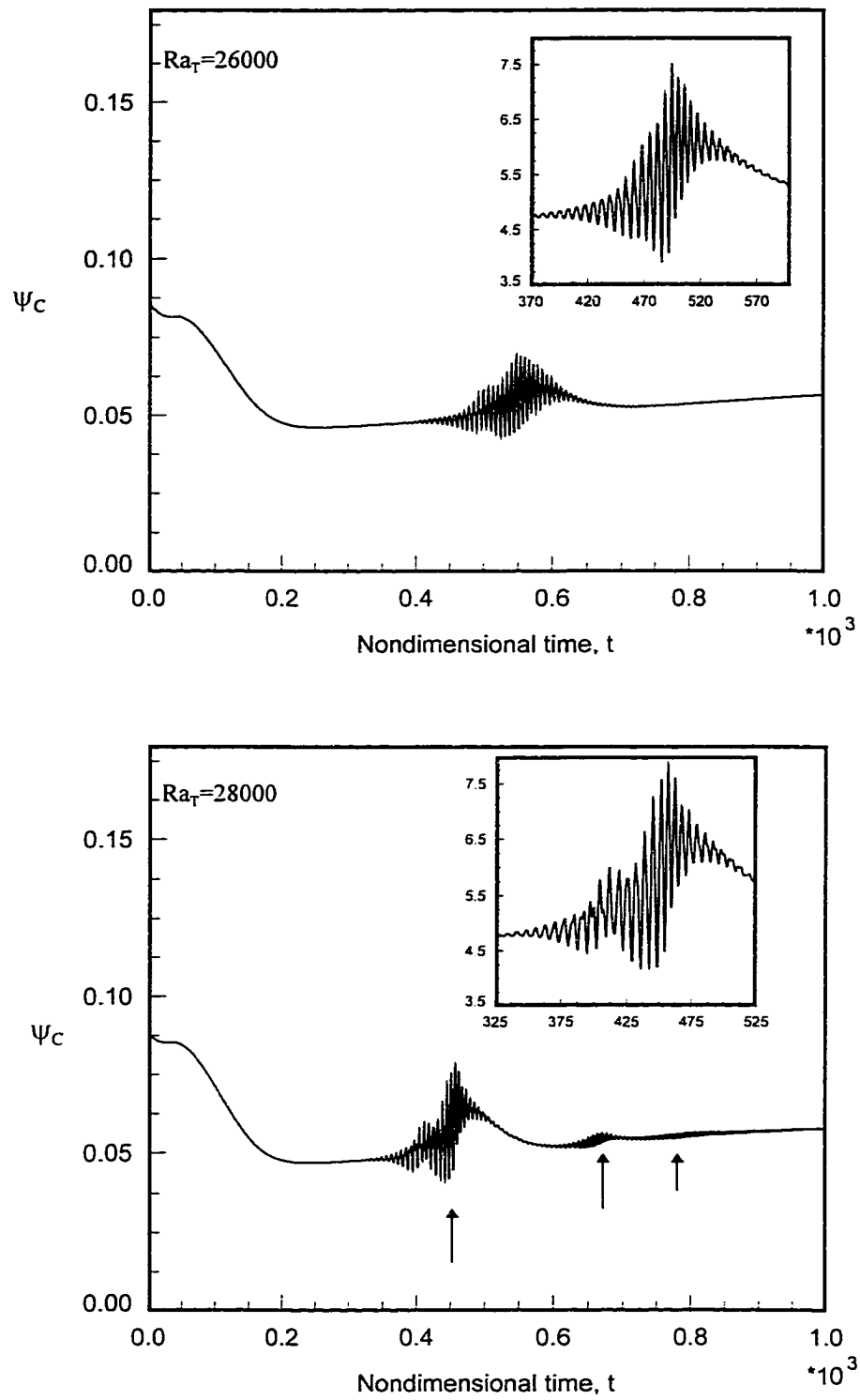


Fig. 20: Time series of ψ_c as function of increasing Ra_τ . $N = 0.0238$, $V_p = 4$ microns/sec.

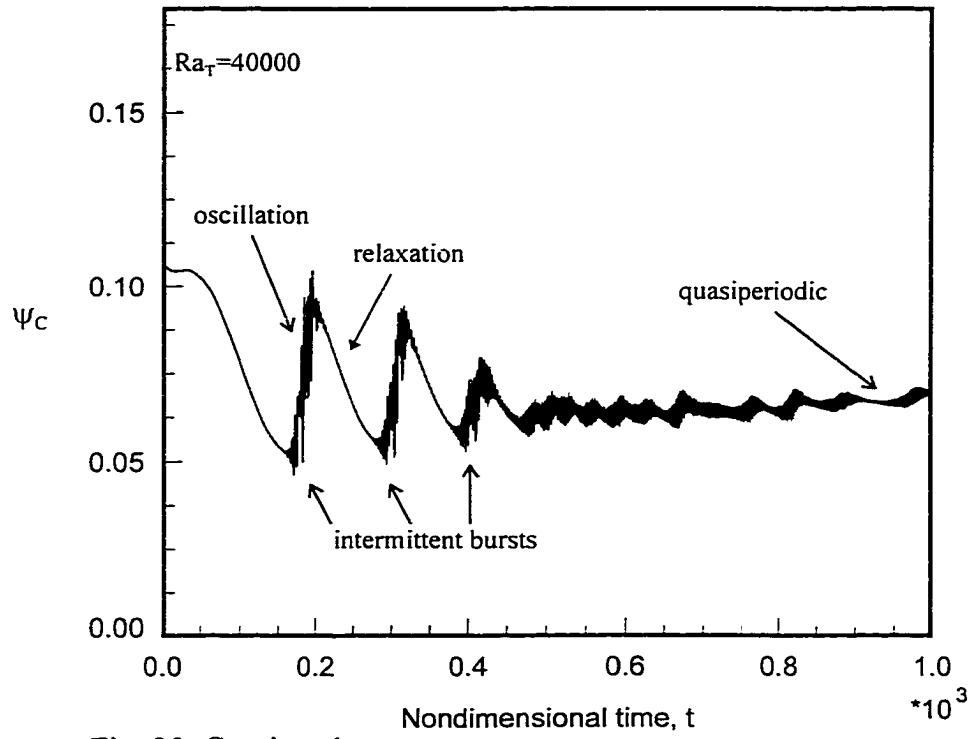
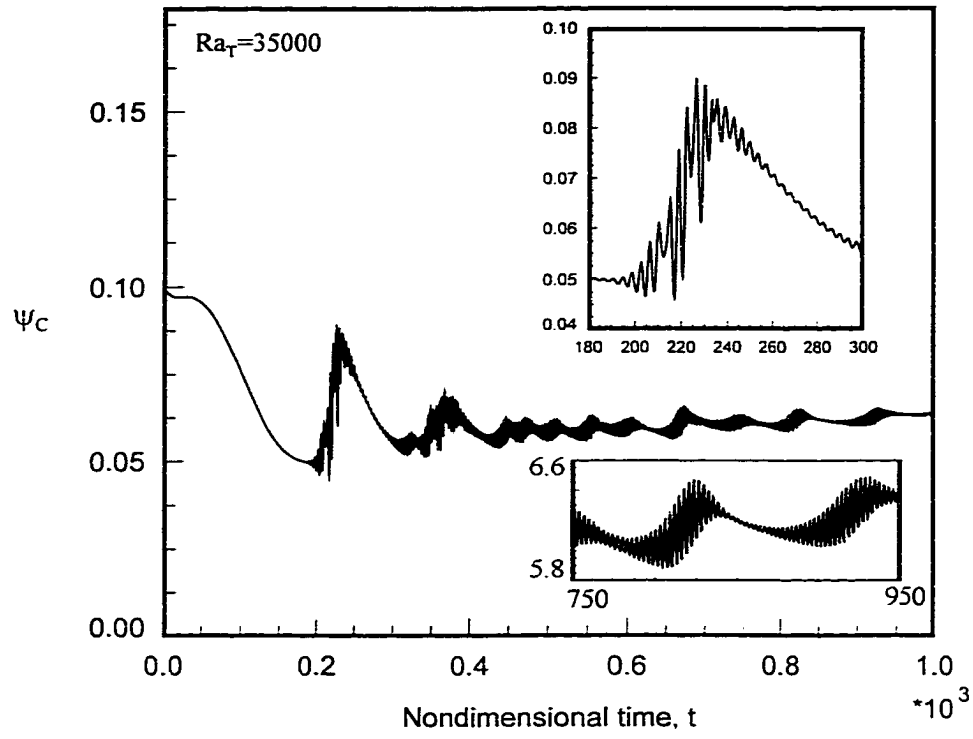


Fig. 20: Continued

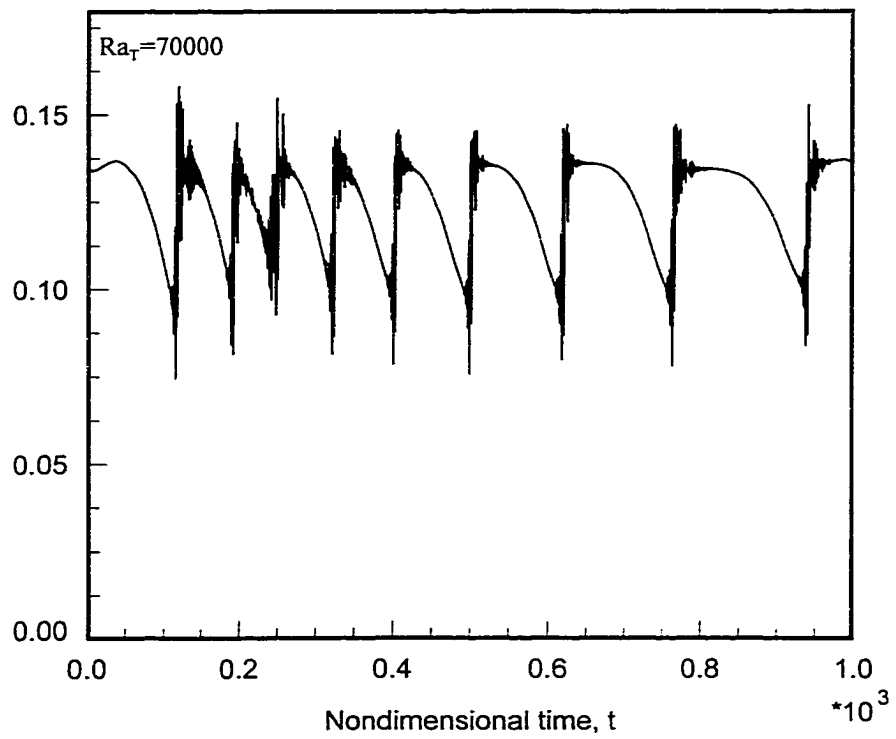
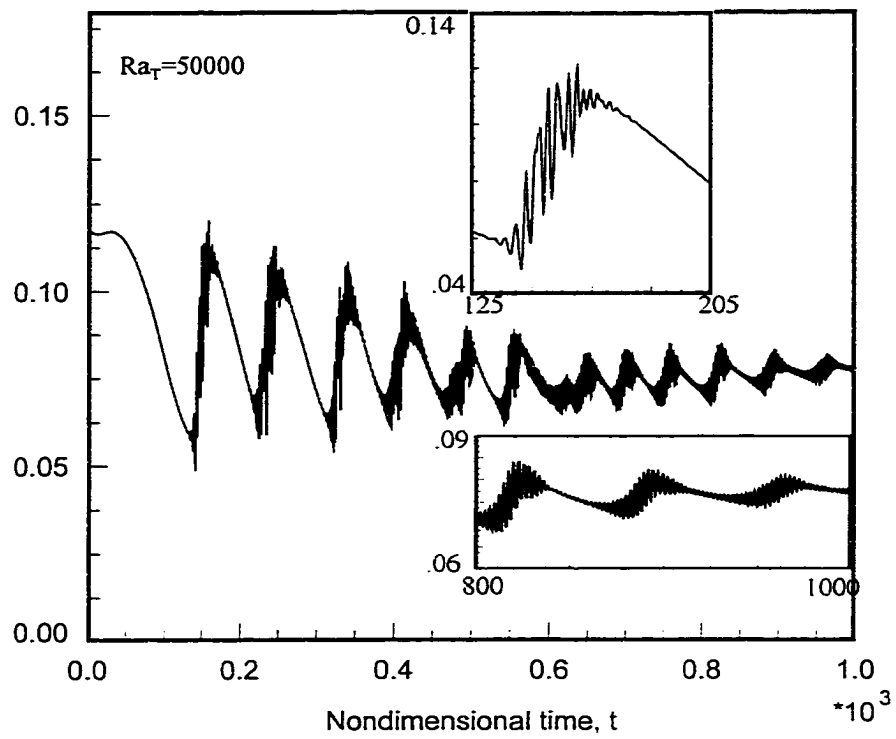


Fig. 20: Continued

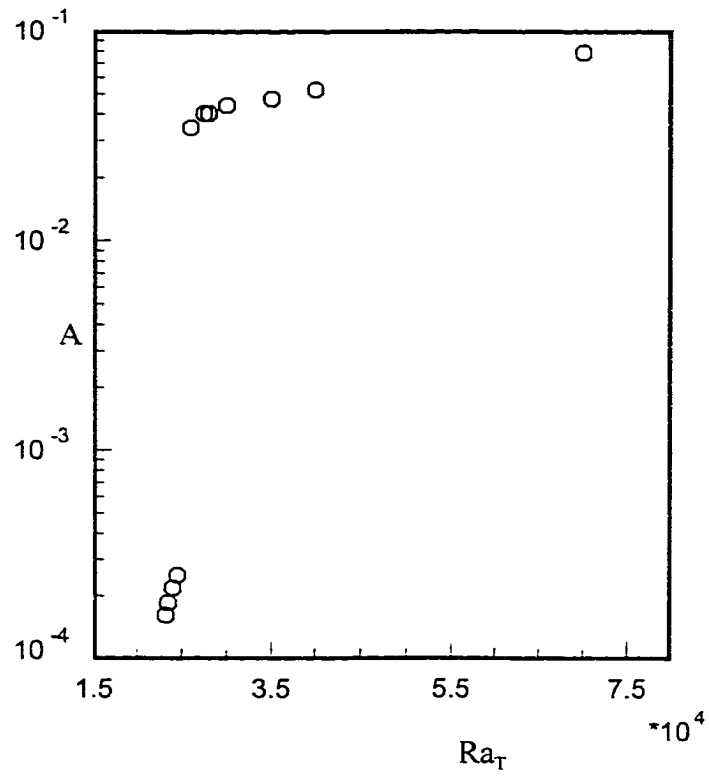


Fig. 21: Variation of maximum amplitude (A) of oscillation with thermal Rayleigh number (Ra_T)

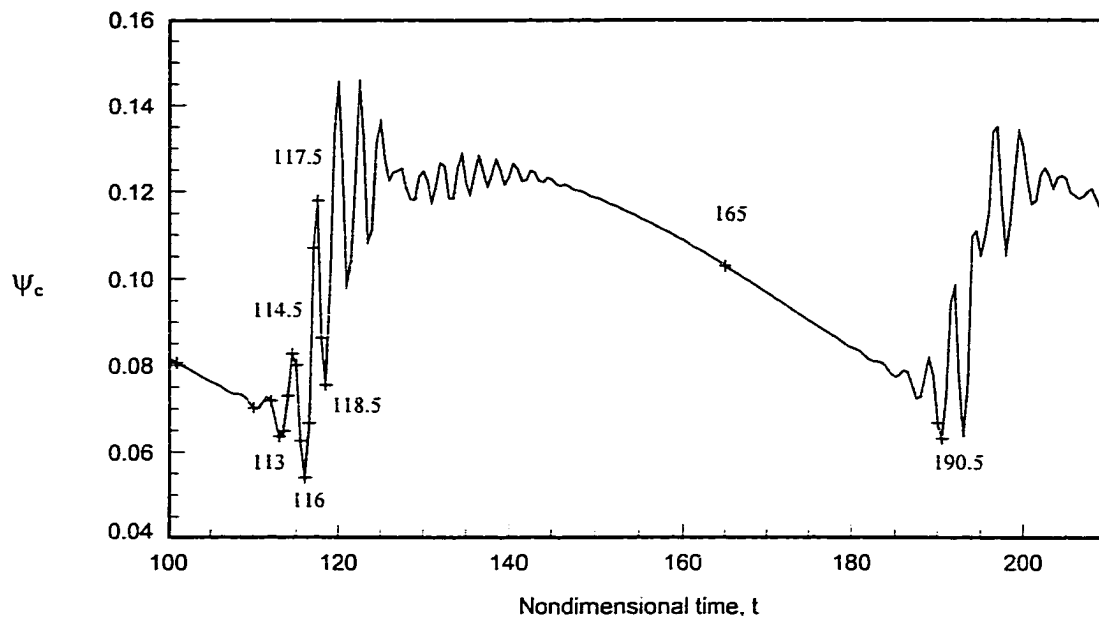


Fig. 22: Time series of ψ_c for $Ra_T = 70000$ and the time levels at which the snapshots of vorticity and concentration fields are shown in Fig. 23.

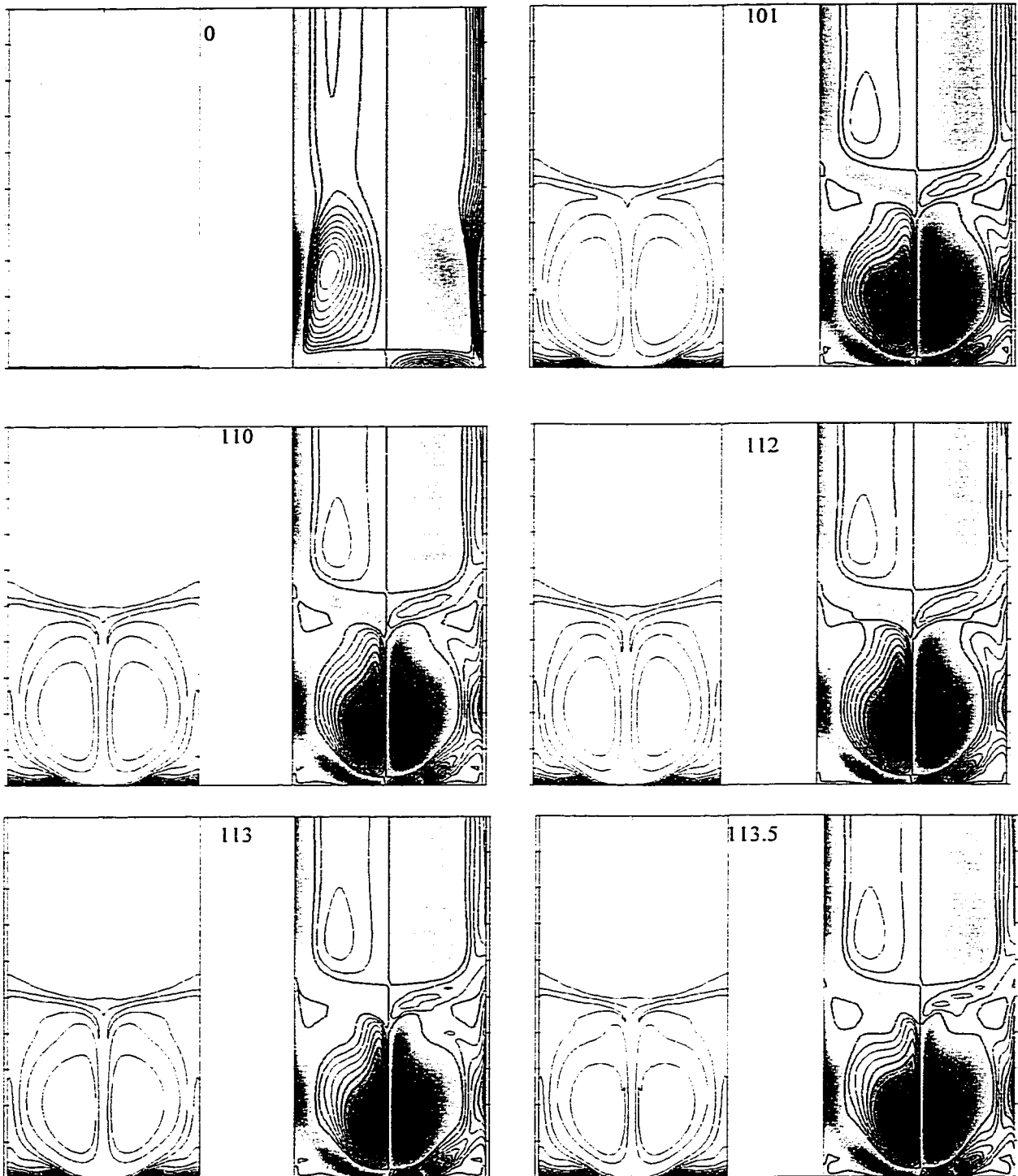


Fig. 23: Snapshots of concentration and vorticity fields at various time steps. The contours for positive vorticity are drawn. Blue shade represents negative vorticity. Red, yellow shade represents positive vorticity.

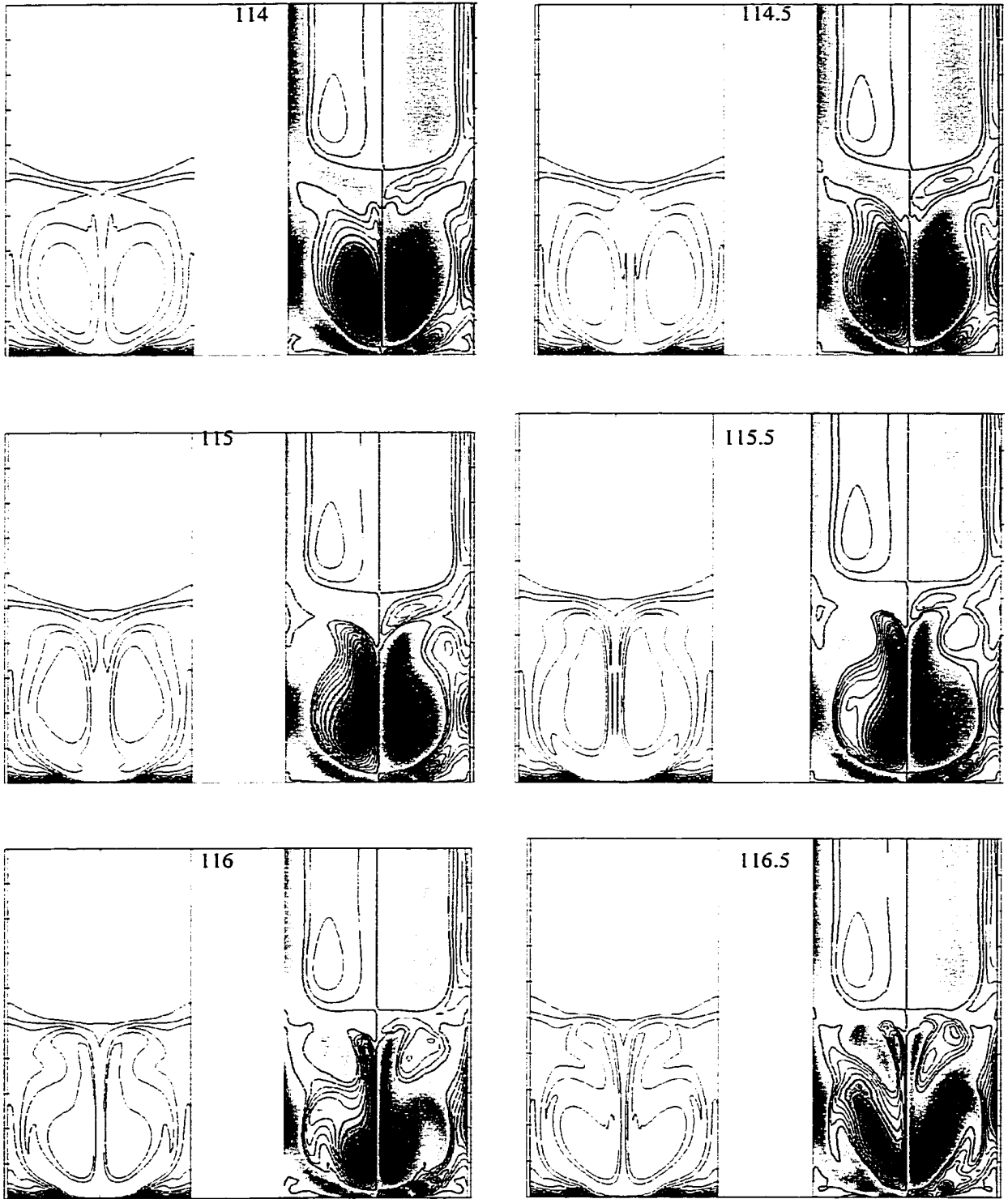


Fig. 23: Continued

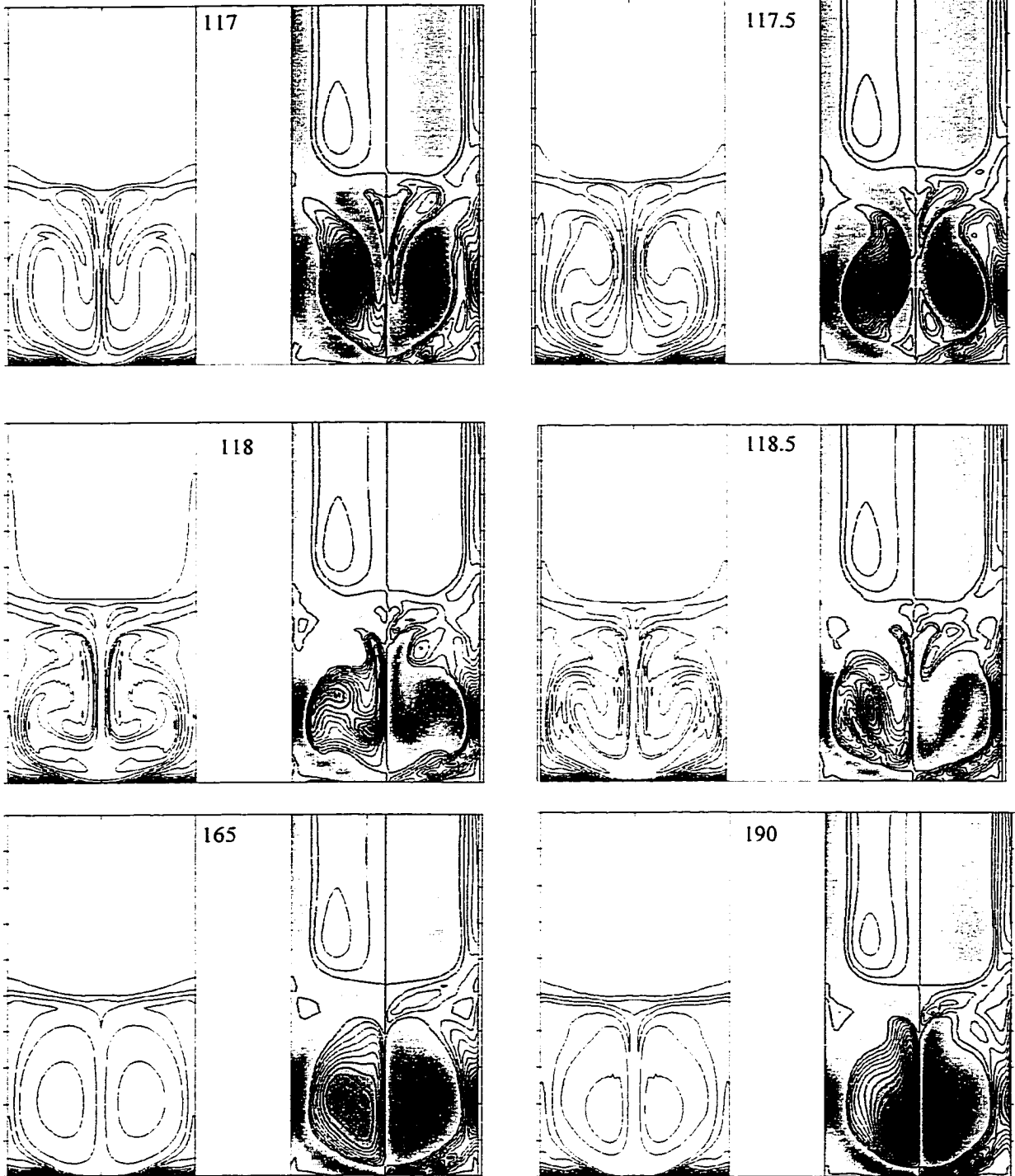


Fig. 23: Continued

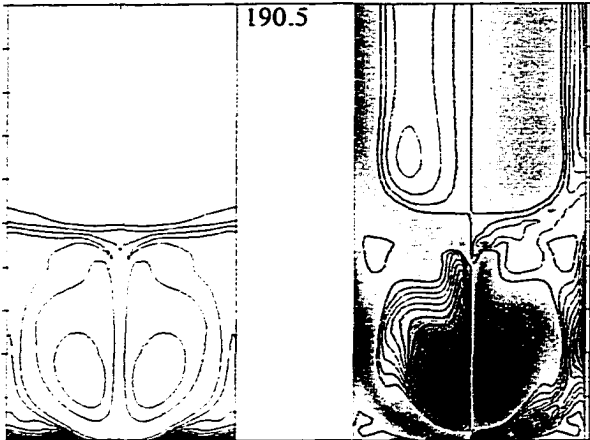
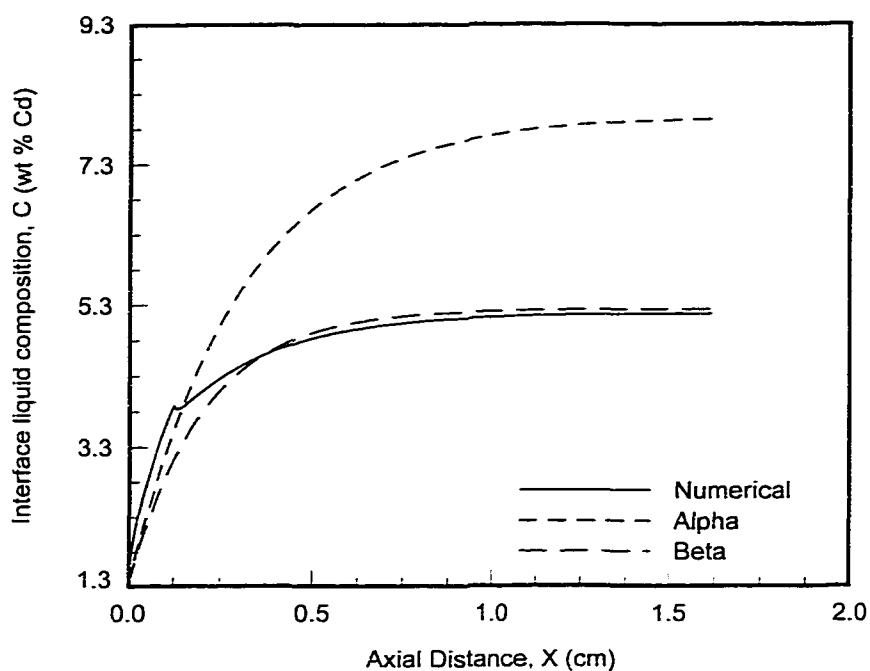


Fig. 23: Continued



(a)



(b)

Fig. 24: Solidification of Sn-1.3% Cd in 400 micron diameter sample. $V_p = 4$ microns/sec, $Ra_T = 21$ (a) Axial concentration profile along the sample length. The solid line is the computed liquid phase concentration profile across the centerline and the edge of the sample. The dotted lines are the concentration profiles for the diffusive growth of primary α and secondary β phases from the diffusive model (Tiller et al. 1953). The computed profile initially approaches the α profile until the peritectic composition ($C_p = 3.8\%$) and then follows the β profile. (b) The microstructure of the solidified sample shows a sharp α (darker phase) to β (lighter phase) transition at $x = 1.25$ cm, where the liquid composition crosses the peritectic composition. The figure is not to scale. The lateral dimension is to represent 400 microns.

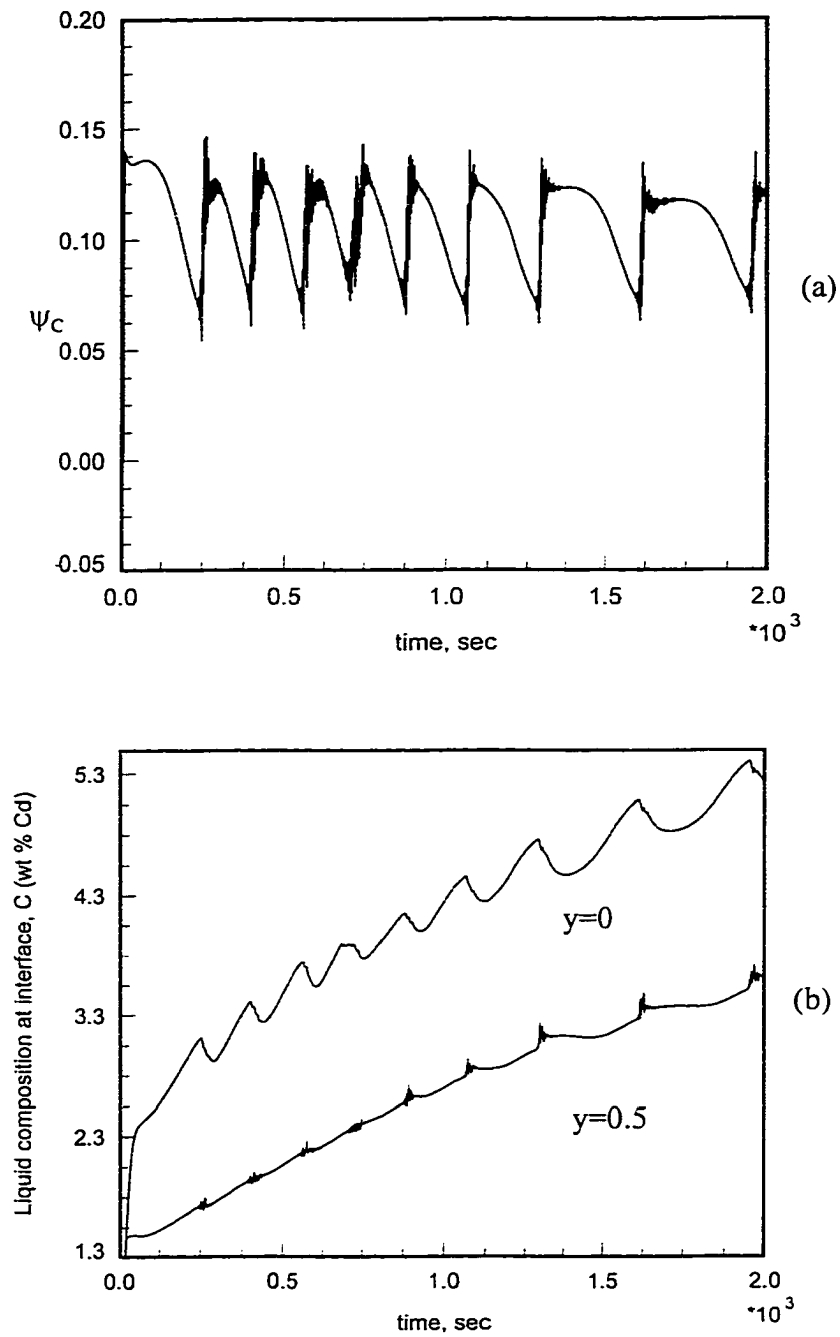


Fig. 25: (a) Variation of ψ_C with time (b) Variation of liquid phase Cd composition at two locations on the solidifying interface with time. The two locations are the sample edge ($y=0$) and the sample center ($y=0.5$)

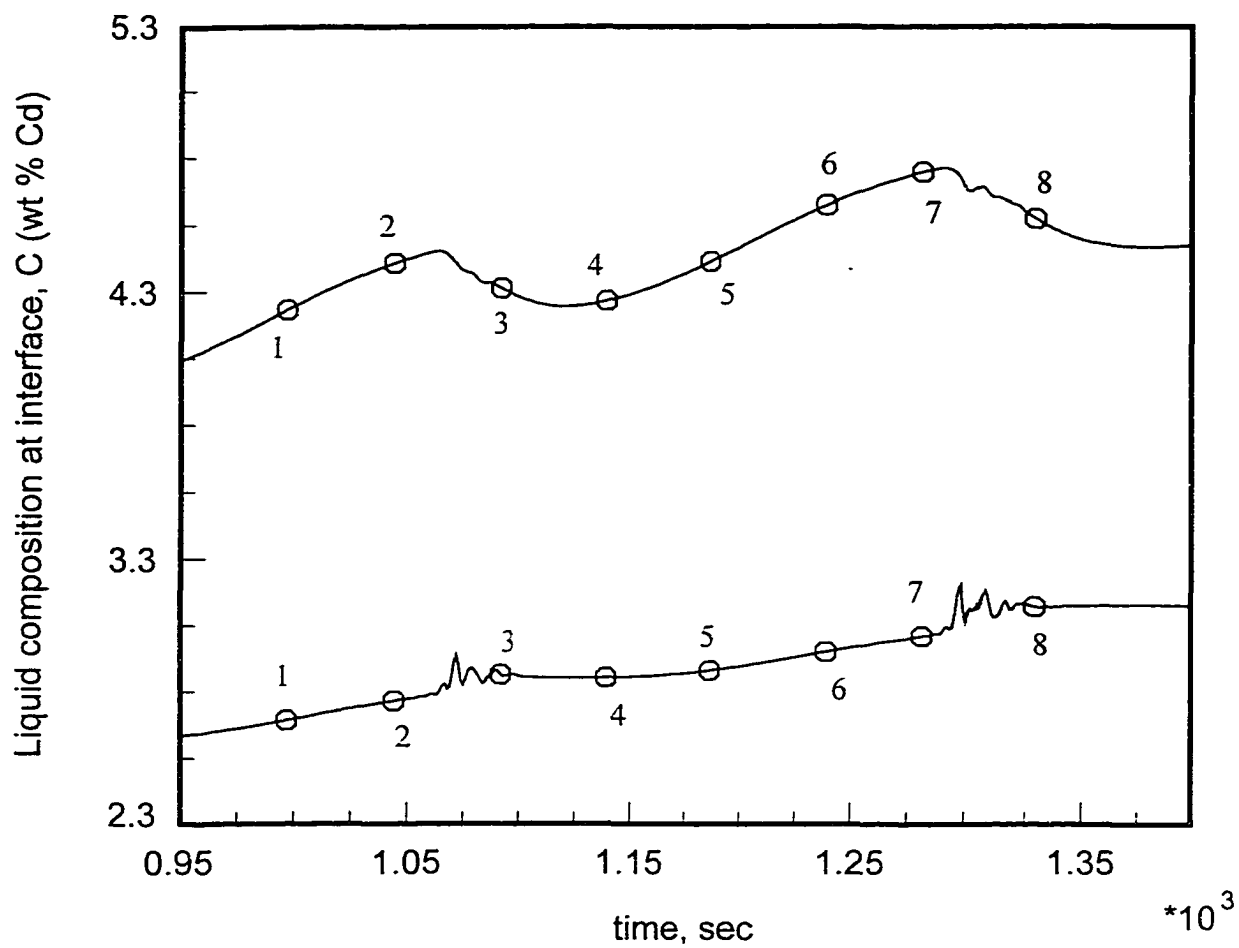


Fig. 26 : Time locations on concentration fluctuations at the interface at which the snapshots of concentration profiles and phase maps are presented in Fig. 27.

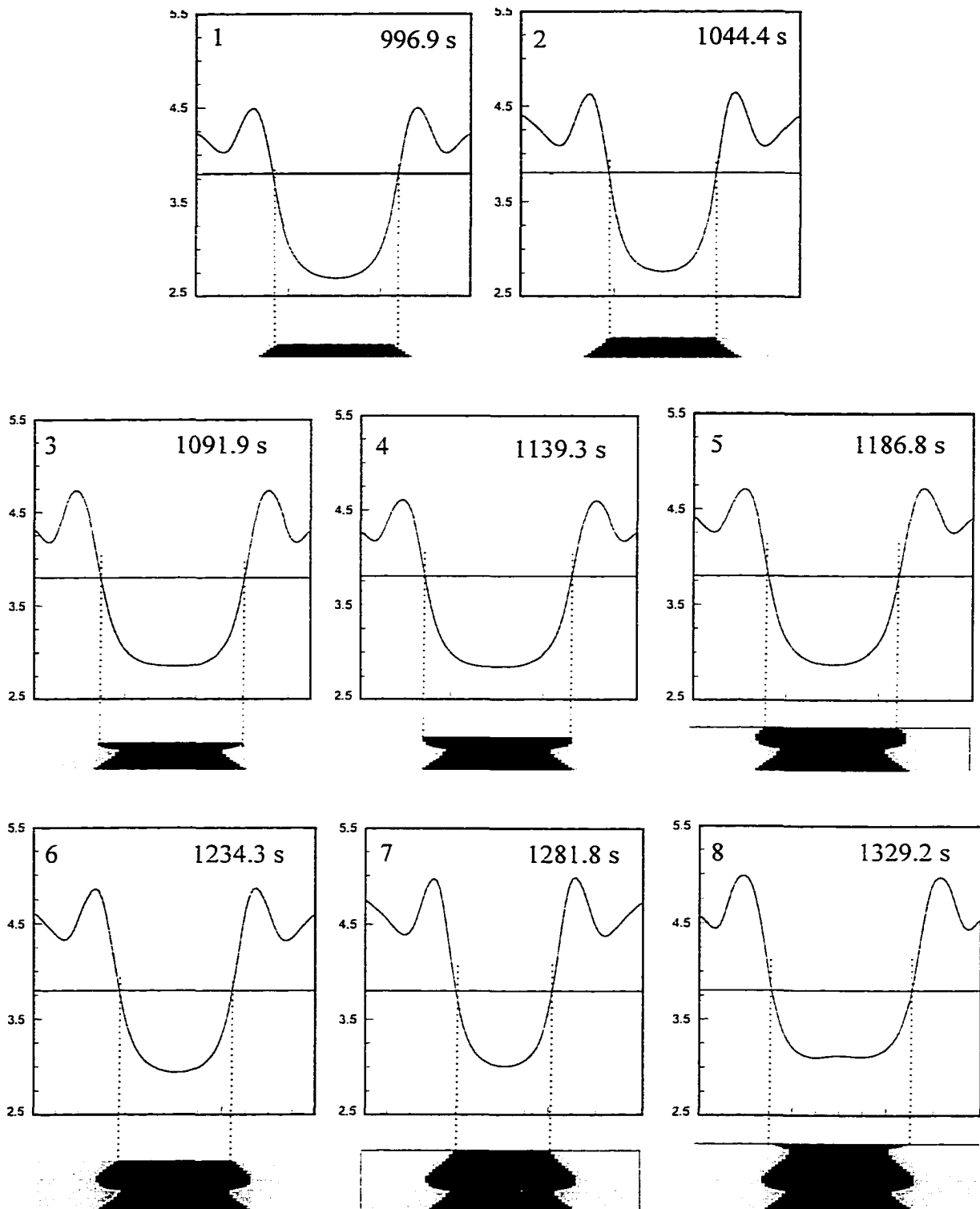


Fig. 27: Snapshots of concentration profiles at interface and phase maps in the solid.

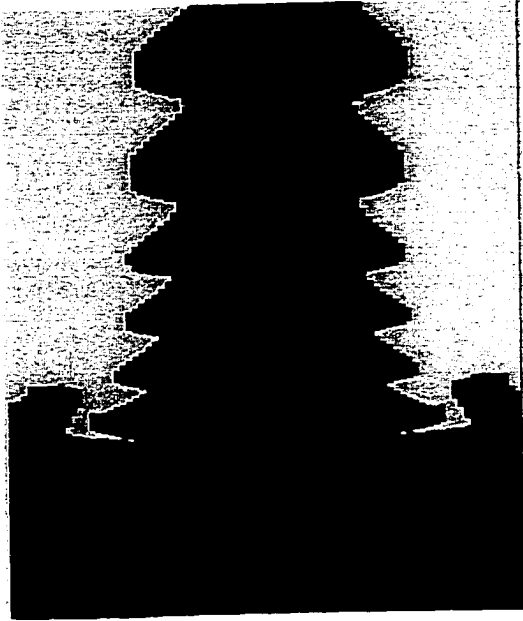
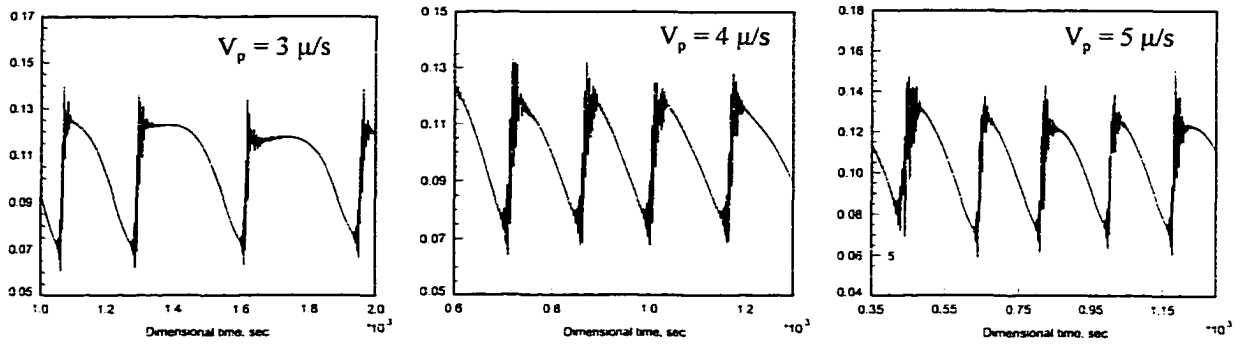
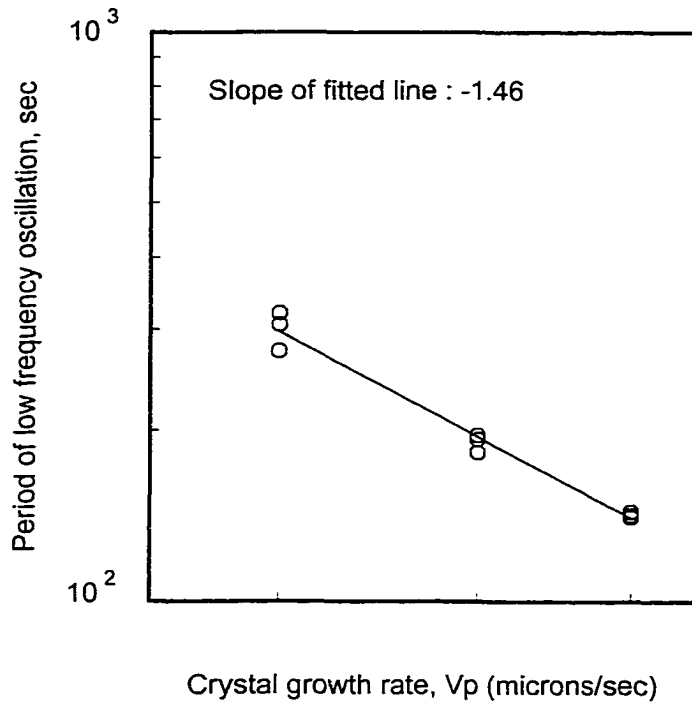


Fig. 28: Oscillatory layered structure in Sn-1.3% Cd alloy predicted with direct numerical simulation. The solidification is for sample of diameter 6.0 mm and $V_p = 4$ microns/sec.



(a)



(b)

Fig. 29: (a) Time series of ψ_C for $V_p = 3, 4, 5$ microns/sec. $Ra_T = 70,000$ (b) Variation of time period between successive intermittent bursts with V_p .

CHAPTER 6: GENERAL CONCLUSIONS

The transport aspects (heat, mass and momentum transfer) of directional solidification and their effects on the microstructure and solute field developed in the solidified crystals are investigated in this thesis. The work includes mechanistic or physical modeling, direct numerical simulation, and experiments. The salient points observed and claimed in the thesis are detailed below.

1. Layered Structure Formation in Sn-Cd Peritectic System

- A novel *physical mechanism* is proposed for the oscillatory layered structure formation in Peritectic alloys which proposes that oscillatory convection in the melt, if present, can create oscillatory microstructure.
- With simple conceptual model it is proved that the previous experimental studies (1974-1995) misinterpreted layered structure as band structure.

2. Direct Numerical Simulation of Thermo-Solutal Convection in Directional Solidification

- The first direct numerical simulation is carried out for the thermo-solutal convection in vertical Bridgman system with vertically stabilizing concentration and temperature gradients.
- A physically realistic model of thermal interaction between the furnace and the sample is developed using integrated measurement and computation.
- The *base flow* prior to the onset of solidification is found to be steady up to the maximum Rayleigh number considered (10^8).
- Steady state thermo-solutal convection is observed for $Ra_T < 22,300$

- Supercritical Hopf type bifurcation to short-lived periodic oscillation is observed for $22,320 \leq Ra_T \leq 24,500$.
- A subcritical bifurcation is observed between $Ra_T = 24,500$ and 25000.
- For $Ra_T > 30,000$ intermittent oscillation-relaxation is observed. The higher the Ra_T , the longer does the oscillation-relaxation survive.
- Instability of the vorticity boundary layers on the side walls and periodic vortex shedding dominates the dynamics of oscillation-relaxation at the highest Ra_T considered (70000).
- Coupling of the oscillatory dynamics with solidification shows the formation of tree-like oscillatory layered microstructure and supports the conceptual model developed.
- An inverse scaling law between the length scale of layers and crystal growth rate is observed that agrees with experimental observation.

3. Convection and Spacing Selection in Al-Cu / Pb-Sn

- Directional solidification studies are carried out to characterize the effects of convection on primary spacing distribution (cellular, dendritic) in Al-Cu and Pb-Sn alloys.
- Higher disorder in spacing distribution is observed in weakly convective Al-Cu, than that in highly convective Pb-Sn alloys.
- Direct simulation explained that weak convection in Al-Cu alloys causes poor mixing and high lateral segregation of solute at the interface, while intense convection in Pb-Sn alloys causes good mixing and small lateral segregation of solute at the interface, and hence the apparently puzzling experimental observation.
- It is predicted from computation that a microgravity level of 10^{-3} g or ampoule diameter of ≤ 1 mm for terrestrial experiments is required to establish diffusion dominated transport during directional solidification of Al-Cu alloys.
- A novel experimental system is developed based on this prediction that substantiated the numerical results.

ACKNOWLEDGEMENTS

I wish to express my sincere gratitude to the following individuals who have made this work possible:

My major professors, Dr. Richard H. Pletcher and Dr. R. Trivedi, for their guidance and support.

My committee members, Dr. Joseph M. Prusa, Dr. James C. Hill, Dr. Palaniappa A. Molian, Dr. Srinivas Garimella, and Dr. Iver Anderson for their service on the committee and critical reviews of the thesis.

Dr. Alain Karma, and Dr. Surendra Tewari for their time and valuable suggestions.

The past and present members of the solidification group, Dr. J. S. Park, Dr. H. Miyahara, Dr. Ralph Napolitano, Dr. S. H. Liu, and Mr. E. Simsek, for their cooperation and friendship.

Susan Knott and Rosalie Enfield, for their continuous support and help with the official work.

My family and all my friends, especially Rachel Phillips, Ravikant Avancha, Sambit Basu and Arun Sood, for their support and encouragement during the most trying periods.

This research was supported in part by the NASA Microgravity Science and Applications Division under Grant NAG8-1254 and NCC 898. This work was supported in part and carried out at the Ames Laboratory under contract no. W-7405-Eng-82 with the US Department of Energy. The United States government has assigned the DOE Report number IS-T 1883 to this thesis.